Multifunctional carbon nanotube networks for energy storage applications

Pichamon Sirisinudomkit

A Thesis submitted for the degree of Doctor of Philosophy and the Diploma of Imperial College London

Department of Materials

Imperial College London

London, SW7 2AZ, UK

Supervisor:

Prof. Milo S.P. Shaffer

Declaration

I, the author Pichamon Sirisinudomkit, hereby declare that the work in this Thesis is entirely my own, and any other knowledge support from other works have been referenced appropriately. The research was performed in the Department of Materials and Department of Chemistry at Imperial College London, South Kensington campus and White city campus, London, UK. I declare that no portion of work referred in this Thesis has been submitted previously for the reward of a degree at this or any other university or other institute of learning.

Pichamon Sirisinudomkit

London, 2022

Abstract

Efficient electrochemical energy storage is a central challenge for the 21st century. Single-walled carbon nanotubes (SWCNTs) are attractive for energy storage applications owing to their excellent electrical conductivity, stability, and surface area.[1, 2] This Thesis focuses on the fabrication of multifunctional supercapacitors from SWCNTs, specifically maximising gravimetric and volumetric performance in full devices by systematically optimising the nanostructures of electrodes and separator. Strong inter-tube van der Waals interactions typically drive the formation of 'bundles' that reduce electrochemical performance.[3, 4] This work creates the first examples of SWCNT buckypapers using reductive methods to minimise rebundling ("nanotubide buckypapers"). The nanotubide anions are generated using sodium naphthalide as a charging agent. The carbon and sodium concentrations control the dissolution process, as well as the microstructure and electrochemical performance of the resulting electrodes. The nanotubide buckypapers were optimised in three-electrode system, then assembled to form full symmetric supercapacitors. With an ionic liquid electrolyte, the energy and power densities reached 2.2 mWh/cm^{3}and 8.3 W/cm^3, respectively, normalised by total volume of the device. The use of an ultrathin bacterial cellulose (BC) film (7 microns) as a separator lowered resistive loses and maximised volumetric performance.

The reductive chemistry provides a further opportunity to limit rebundling, by covalently cross-linking the individualised SWCNT anions.[5, 6] The cross-linking reaction with p-diiodobenzene (DIB) was explored as a function of reagent concentration and stoichiometry. Cross-linking generally improves the gravimetric performance and enhances rate capability at high scan rate. The performance of the most successful cross-linked nanotubide electrodes was then extended by varying the electrode thickness, to find the optimum balance between maximising the active material and its rate performance; ionic transport limitations were found to dominate at SWCNT loadings above 2.8 mg/cm^2 (55 microns).

In order to increase energy density, a redox active polymer, polypyrrole (PPy), was hybridised with the cross-linked nanotubide buckypapers (CNBs) via electrodeposition. By adjusting the electrodeposition potential and pulse sequence, it was possible to generate

idealised coatings of PPy throughout the CNB. The introduction of PPy increased the specific energy to 63 Wh/kg, compared to 28 Wh/kg for the pure CNB, in three-electrode measurements using 1 M sulphuric acid as the electrolyte. The optimised hybrid electrode was combined with a pure electrochemical double layer electrode to form an asymmetric device. To balance the overall capacitance, a new design was developed by sandwiching one positive hybrid electrode (PPy-CNB) between two negative electrodes (CNBs). Whilst acting as an active electrode, CNBs have significant mechanical strength (~20 MPa) and Young's modulus (~0.3 GPa), indicating potential importance in the field of structural energy storage. Although mechanical and electrochemical performance typically conflict, the addition of PPy was found to enhance both aspects.

Acknowledgements

First and foremost I would like to thank myself for being able to accomplish this important task of my life. This PhD degree not only developing my scientific knowledge but also improving me to be a mature person. I cannot deny that I have experienced both happiness and suffering during these four years. However, as people always say no pain no gain so it is. I will remember all happiness part as if it is my treasure and the emotional suffering part will be counted as a life lesson. I want to put 100+ thumb up emoji here to congratulate myself and tell myself that "You are always doing great so stop worrying too much".

To my supervisor, Professor Milo Shaffer, I would like to thank you for your continual help, guidance and support. It has been an honour to work with you throughout my time at Imperial College London. I want to thank you a lot for always listening to my idea and encouraging me to do new stuff. You may not know it but because you always open to discuss so, it helps me a lot to gain my confidence.

Additionally, I would like to acknowledge the financial support from the Ministry of Higher education, Science, Research and Innovation, Royal Thai Government. Without their support I wouldn't be able to achieve this degree.

I also thank to Dr.Koon-Yang Lee for the supply of BC nanopaper that I used as the separator in my research studies.

To my family, my mom, my dad and my sisters who have supported me emotionally as well and financially throughout my whole life. I could not have succeeded this far without three of you. I also want to thank to my little brothers "Kreab" and "Poon" for being my emotional support on all these years.

More generally, I would like to thank to all members in the Nanostructured Hierarchical Assemblies and Composites Group (NanoHAC) for helping and encouraging me during these 4 years; Specifically thanks to Noelia, Evgeny, Kalpana, Adriana, Yuhan, Jakyung and Dave A(Anthony) for always helping me and always being there for me whenever I have difficult time not only about the research but also about life stuff. My thesis will not be able to complete without your help. To the rest, I am so

thankful to have good friends like you all; Sandy, Heather, Hugo, Shirley, Wonjun, Joe, Gabriel, Tommaso, Dave S(Stringer), Dave B(Buckley), Hinchun, Chris, Alex and Hannah. The time that I spend with you all during these 4 years are the most memorable moments in my PhD. I can't imagine doing a PhD without your companion. I really love you all and I promise our friendship will not end here. We will continue to share our good memories together and let make the trip to Thailand.

To my Thai friends; Firstly, Park, P mind, P Pin and P Fon who are my besties. My life in UK will not be this much fun and memorable without four of you. To Park and P mind, who can imagine that three of us who studied in the same research group since undergraduate year would also continue doing PhD together in UK. You both are lecturer now as I will be. Thanks to both of you for always helping and listening to me every time not only about electrochemistry knowledge but also life problems. To P Pin and P Fon, I really thank to both of you for always taking care of me like your youngest sister. I do enjoy a lot when we hung out mostly every weekend and every evening whenever I want to go somewhere you both never refuse to go with me. I can't wait to see you both again in Thailand. Of course I can't forget to mention my ICL Thai gangs, Krai, Fah, P Meaw, P L, P Sung, P Arm, P Joice, Nhamkhang for being a foodie buddies.

ในโอกาสนี้ขอขอบคุณบุคคลสำคัญที่สุดในชีวิต ครอบครัว ป๊า คุณแม่ พี่แพร์ที่คอยสนับสนุนทั้งด้านการเงินและคอยให้กำลังใจและเข้าใจพีชอย่างสม่ำเสมอ อยากบอกว่าทุกคนคือส่วนสำคัญที่มากที่สุดที่ทำให้พีชผ่านพันทุกอุปสรรคในชีวิตไปได้ ไม่ใช่แค่เรื่องเรียนแต่รวมถึงทุกเรื่องๆ ถ้าไม่มีทั้งสามคนพีชคงไม่ได้มายืนถึงจุดนี้ พีชสัญญาว่าต่อไปจะเข้มแข็งไม่ว่าจะมีอุปสรรคอะไร และอยากขอบคุณข้าวเกรียบและข้าวปุ้น น้องชายทั้งสองของพี่ที่เป็นกำลังใจเสริมให้พี่เสมอ ถึงเกรียบพี่หวังว่าเกรียบจะมีความสุขดีอยู่ที่ไหนสักแห่ง

最后想感谢我最爱的三位歌手 BamBam、**井胧和曹**杨，**感**谢你们的声音陪我度过写论文的时光。 你们的歌你们的作品给我带来了快乐, **希望你**们的未来越来越好，继续创作优秀的作品，**我会一直支持你**们!

Table of contents

List of publications

In preparation

Hybridising PPy-nanotubide buckypapers for multifunctional structural supercapacitors: P. Sirisinudomkit, N. Rubio and M. S. P. Shaffer (**in preparation**).

Published

Reductive processing of single-walled carbon nanotubes for high volumetric performance supercapacitors : P. Sirisinudomkit, E. Senokos, N. Rubio and M. S. P. Shaffer (2021) Materials Advances DOI: 10.1039/D0MA00898B.

Real-time mechanistic study of carbon nanotube anion functionalisation through open circuit voltammetry : A. J.Clancy, P. Sirisinudomkit, D. B. Anthony, A. Z. Thong, Jake L. Greenfield, M. K. Salaken Singh and M. S. P. Shaffer (2019), Chemical Science 10(11): 3300-3306. DOI: 10.1039/C8SC04970J

Conferences

05/2021 **Modified Single-walled carbon nanotubes for the new generation of energy storage applications.** P. Sirisinudomkit, E. Senokos, N. Rubio and M. S. P. Shaffer (Material Energy for webinar 2021) at Imperial College London.

09/2019 **Real-time mechanistic study of carbon nanotube anion functionalisation through open circuit voltammetry.** P. Sirisinudomkit, A. J.Clancy, D. B. Anthony, A. Z. Thong, Jake L. Greenfield, M. K. Salaken Singh and M. S. P. Shaffer. NT19 (National Conference on SElectrochem 2019) at Imperial College London.

07/2019 **Real-time mechanistic study of carbon nanotube anion functionalisation through open circuit voltammetry.** P. Sirisinudomkit, A. J.Clancy, D. B. Anthony, A. Z. Thong, Jake L. Greenfield, M. K. Salaken Singh and M. S. P. Shaffer. NT19 (International Conference on the Science and Application of Nanotubes and Low-Dimensional Materials) at Würzburg, Germany.

07/2018 **Cross-linked single-walled carbon nanotubes and polytriazine-imide for energy storage applications.** P. Sirisinudomkit, N. Rubio, M. S. P. Shaffer. Graphene Study 2018 at Hjortviken, Hindås, Sweden.

04/2018 **Cross-linked single-walled carbon nanotubes and polytriazine-imide for energy storage applications.** P. Sirisinudomkit, N. Rubio, M. S. P. Shaffer. Chem on Tube 2018 at Biarritz, France

List of equations

Equation number	Name	Equation	Page
Equation 3.19	The electrochemical double layer capacitance	$i_c = v \times C_{dl}$	84
Equation 3.20	The ECSA	$ECSA = \frac{C_{dl}}{C_s}$	84
Equation 3.21	The ultimate tensile stress	$\sigma_t = \frac{F_{max}}{A_{CSA}}$	85
Equation 3.22	The strain	$\epsilon = \frac{\Delta x}{L}$	85
Equation 3.23	The tensile tensile modulus of elasticity	$E_t = \frac{\sigma}{\in}$	85
Equation 6.1	Mass balance	$\frac{m_+}{m_-} = \frac{C_{s-}V_-}{C_{s+}V_+}$	181
Equation 6.2	Area ratio	$\frac{A_+}{A_-} = \frac{m_+\rho_{A+}}{m_-\rho_{A-}}$	181

List of tables

List of figures

List of symbols and abbreviations

General			
CNT	Carbon nanotube	BC	Bacterial cellulose
SWCNT	Single-walled carbon nanotube	CNB	Cross-linked nanotubide buckypaper
CVD	Chemical vapour deposition	Q	Electrical charge
WE	Working electrode	ΔV	Working potential
RE	Reference electrode	i	Current
CE	Counter electrode	**ν**	Potential scan rate
PPy	Polypyrrole	C	Capacitance
at%	Atomic mass percentage	Z′	The real part of impedance
RBMs	Radial breathing modes	Z″	The imaginary part of impedance
I_D/I_G	Intensity ratio of Raman D to G bands	τ_0	The relaxation time
σ_t	Stress	f_0	The response of frequency at the maximum point of the energy curve
ϵ	Strain	E	Energy density
E_t	The tensile tensile modulus of elasticity	P	Power density
m	mass	t	Time
ρ	Density	1P_1N	The normal structural cell device (1 positive electrode with 1 negative electrode)
$t_{on}\_t_{0V}$	Electrodeposition period and resting period	1P_2N	The new structural cell device (1 positive electrode with 2 negative electrodes)

Chemicals			
Na	Sodium	NaNp	Sodium naphthalide
DMAc	N,N-dimethylacetamide	DMF	Dimethylformamide
DIB	Diiodobenzene	KCl	Potassium chloride
H_2SO_4	Sulphuric acid	[EMIM][TFSI]	Ethyl-methyl-Imidazolium bis(trifluoromethylsulfonyl)-imide
PTFE	Poly(tetrafluoroethylene)	P_2O_5	Phosphorus pentoxide
Characterisation techniques			
SEM	Scanning electron microscopy		
FT-IR	Fourier transform - infrared spectroscopy		
TGA	Thermogravimetric analysis		
XPS	X-ray photoelectron spectroscopy		
BET	Brunauer-Emmet-Teller method		
CV	Cyclic voltammetry		
EIS	Electrochemical impedance spectroscopy		
GCD	Galvanostatic charge-discharge		

1. Introduction

Carbon-based materials have excellent chemical and physical properties, which are abundant and available in bulk, making them suitable electrodes for supercapacitors.[7] Amongst the large family of carbon materials, single-walled carbon nanotubes (SWCNTs) are of specific interest owing to their outstanding electron transport, high elastic modulus, tensile strength and outstanding electrical and thermal properties.[1, 2] The synthesis of SWCNTs controls their geometry and dimensions, influencing their intrinsic properties and their assembly into larger structures. Strong $\boldsymbol{\pi - \pi}$ interactions between SWCNTs cause agglomeration and reduce the active surface area leading to poor electrochemical performance. Therefore, each SWCNT must be separated as much as possible within a given electrode material, in order to maximise their electrochemical efficiency. Various methods have been proposed to individualise/disperse SWCNTs for application, including intense sonication or other methods involving mechanical shear. However, these approaches tend to both shorten SWCNTs and degrade their intrinsic properties by damaging the carbon conductive framework.[8] Additionally, SWCNTs generally explored for supercapacitor electrodes with excellent performance in gravimetric when normalised to active material only and its volumetric performance in whole device is still not quite yet explored. For real application, the SWCNT electrode architecture must be designed to maximise both gravimetric and volumetric performance along with a good mechanical performance to maximise the utilisation of the materials.[9] The present work aims to address these problems by individualising SWCNTs via a reductive charging process (forming 'nanotubide' anions) and produce highly individualised free standing SWCNT electrode for supercapacitors with high gravimetric and volumetric electrochemical performance when normalise with the overall device component. Nanotubide solutions has been previously exploited to both purify and cross-link SWCNT aerogels.[10, 11] This thesis establishes the first example of SWCNT buckypaper produced via this reductive chemistry approach. Maximising SWCNT dispersion whilst maintaining a relatively high packing density is a challenge, here carefully controlled by varying charging ratios of carbon to sodium (C:Na) and/or degree of charge. The electrochemical characteristic of nanotubide buckypapers were studied using three-electrode system while the two-electrode system was employed to study the full cell performance.

Apart from developing the electrode morphology, electrolyte and separator also carefully chose here to optimise the cell performance. The aqueous and ionic liquid electrolyte were used to study the as-fabricated cell performance in aqueous and non-aqueous systems. The development of BC nanopaper as a rigid and ultrathin separator also explored here to maximises volumetric performance in a configured full cell device. Adding covalent cross-links is shown to promote the electrochemical performance especially specific power, by promoting more uniform pore size distributions due to cross-linker molecules fix the SWCNTs position in the network which improve ion diffusion. The molar ratio of cross-linker and reductive charging agent is a key factor to achieve successful network formation. To further enhance the energy density, tensile strength and stretchability, the cross-linked nanotubide buckypaper was then electrodeposited with polypyrrole via one step electropolymerisation. The optimal performance is expected to derive from a uniform coating throughout the nanotubide buckypaper, whilst maintaining open porosity for ion transport. By adjusting electrodeposition electrolyte, electrodeposition time and pulse sequence, systematically, a rational approach to electrofabrication was established. The advantages of these as-synthesised hybrid buckypapers are illustrated for use as free-standing electrode for the multifunctional structural energy storage application that can simultaneously carry mechanical loads whilst storing excellent electrical energy.

1.1 Aims and Objectives

The aim of this Thesis is to produce highly dispersed SWCNT based buckypapers for multifunctional structural supercapacitors. The work is divided into various parts which include: optimisation of reductive charging approaches, improvement of cross-linking agent and the hybridisation of conducting polymer, with the aim to exploit and enhance the electrochemical performances, tensile strength and stretchability of as-fabricated supercapacitors.

The specific objectives are outlined as follows:

1. Prepare nanotubide buckypaper EDLC electrodes via reductive chemistry
    - Adapt a known SWCNT reductive functionalisation procedure (“nanotubide” route) to remove the impurities from SWCNT powder.

- Optimise the synthesis process by varying SWCNTs/DMAc concentration ([C]) and intermediate charging ratios of carbon to sodium by mol (C:Na) to achieve the optimum structure and density for electrochemical double layer capacitance
- Illustrate the potential of the nanotubide buckypaper to improve electrical conductivity and electrochemical performance compared with other synthesis approaches such as sonication.
- Fabricate symmetric supercapacitors from nanotubide buckypaper in both aqueous and ionic liquid electrolytes using bacterial nanocellulose as separator for high volumetric performance.

2. Investigate the effects of covalent cross-linking on nanotubide buckypaper structure and performance.
   - Optimise the difunctional, cross-linking agent concentration to improve the structure of the buckypaper.
   - Investigate the effects on ion transport, power density and gravimetric energy density of cross-linked nanotubide buckypaper.
   - Investigate the effect of reductive charging and cross-linker concentration on the indivdualisation, density, electrical conductivity and mechanical properties for different types of SWCNTs.
   - Scale up the thickness and density of the free-standing electrode by increasing mass loading of SWCNT, to maximise the overall supercapacitor performance
3. Increase energy density of the nanotubide buckypapers, by electrodepositing polypyrrole (PPy).
   - Study the effect on the physical and electrochemical properties of PPy synthesised via different approaches: chronoamperometry and pulse polymerisation.
   - Optimise the quantity and quality of PPy on the substrate by varying the electrodeposition potential, electrodeposition time and pulse sequence to improve electrochemical performance.
   - Establish whether the addition of electroactive polymer can improve tensile strength and stretchability of the nanotubide buckypapers, as well as the electrochemical energy density.

- Fabricate the asymmetric supercapacitors of PPy//cross-linked nanotubide buckypaper by balancing the mass loading of positive and negative electrodes.

1.2 Structure of the Thesis

This Thesis is divided into seven chapters including the following contents.

Chapter 1 includes an introduction and the objectives of the thesis.

Chapter 2 provides a background review of the current literature which support the study in this Thesis. The chapter presents the fundamental knowledge of SWCNT materials including synthesis, purification, electrical properties, mechanical properties and applications. It pays specific attention to the use of reductive chemistry approaches on SWCNT materials. There is an introduction to supercapacitors in general, and SWCNT-based supercapacitor in particular, including attempts to introduce pseudocapacitve hybrid components.

Chapter3 describes the characterisation techniques employed in this research. Material characterisation (including 4 point conductivity measurement, Raman spectroscopy, X-ray photoelectron spectroscopy (XPS), thermogravimetric analysis (TGA), fourier-transform infrared spectroscopy (FTIR) and scanning electron microscopy (SEM) are described here as well as fundamental electrochemical measurements such as cyclic voltammetry, electrochemical impedance spectroscopy, galvanostatic charge discharge, chronoamperometry and pulse potentiostatic deposition. This chapter also includes tensile measurements to investigate mechanical properties.

Chapter 4 is the first results chapter, focused on the reductive dissolution of nanotubide to form buckypapers. Carbon concentration and molar ratio between carbon and sodium were investigated to understand the degree of functionalisation and effect of charging ratio toward the buckypaper structure, conductivity and electrochemical performance. The as-fabricated supercapacitors using free standing nanotubide buckypaper in both aqueous and ionic liquid electrolyte and the effect of using different type of separator are also reported.

Chapter 5 is the second result chapter. This chapter focuses on the improvement of electrochemical performance via adding a cross-linker molecule and the effect on physical, mechanical and electrochemical performance using alternative SWCNT sources. The effect of

scaling thickness and density of SWCNT on the electrochemical and mechanical performance is also investigated here.

Chapter 6 contains the optimisation of hybridised nanotubide buckypaper with polypyrrole via electrodeposition approach. Tensile strength measurements compare the mechanical performance before and after hybridising polypyrrole. The electrochemical performance of as-fabricated asymmetric supercapacitor is also evaluated.

Lastly, Chapter 7 provides an overall summary and conclusion. Further work is proposed to improve electrochemical performance by using alternative cross-linking agent, modifying nanotubide structure and hybridising nanotubide buckypapers with other transition metal oxides and other conducting polymers. Additionally, the idea for developing the new cell configuration to optimise the energy density also propose here.

2. Literature review

This chapter provides the fundamental knowledge of supercapacitors and an overview of carbon nanomaterials, especially SWCNTs. The synthesis routes, the purification, and physical properties of SWCNTs are reported in detail. The different aspects of electrochemical research on SWCNTs materials (especially pertaining to capacitive energy storage) will be described in detail, including capacitance theory and the hybridisation of SWCNT with conducting polymer such as polypyrrole. The recent advanced structure designs of SWCNT based supercapacitors are also discussed here.

2.1 Introduction to supercapacitors

Electronic devices have become essential devices for our daily life, especially mobile phones, laptops, and electrical vehicles. Thus, the development for increasing the efficiency and energy storage capacity in devices is explored by many researchers. The energy storages so called supercapacitors or electrochemical capacitors have become an innovative and interesting technology. A supercapacitor has higher surface area at electrode and shorter space between two electrodes when compared with the electrochemical capacitor.[12] Supercapacitors have high power and long cycle life however, the lack of real capacitance compared with theoretical capacitance and the low energy density of the supercapacitors is a main problem that limits those applications.[13] Therefore, this Thesis is focused on developing the dispersion/individualisation of SWCNT networks, as well as the hybridisation of SWCNT composites to improve both the energy density and the efficiency of SWCNT based supercapacitors.

2.1.1 Type of supercapacitors classified by mechanism for storing charge

2.1.1.1 Electrochemical double-layer capacitors (EDLCs)

EDLCs or non-Faradaic supercapacitors store charges by accumulating ions from the electrolyte on the electrode surface.[14] Ions in the electrolyte solution diffuse through the separator, then go through the pores/surface of the electrode that has an opposite charge. Therefore, double-layer of charges is formed at each electrode (Figure 2.1a). The capacitance (C) of EDLC can be expressed via the following equation 2.1:

$$C = \varepsilon_0 \varepsilon_r \frac{S}{d}$$ Equation 2.1

Where ε_0 is the vacuum permittivity (F/m), ε_r is the dielectric constant of the electrolyte, S is the surface area of the electrode (m^2) and d is the distance of the ion to the surface of electrode (m).

The accumulation of charge (Q) on electrode surface is related to the applied potential (ΔV) by the capacitance.

$$Q = C\Delta V$$ Equation 2.2

EDLCs do not have chemical or composition changes related to Faradaic processes; thus, charge storage in EDLC is highly reversible, which makes them achieve high power density and high capacity retention when compared with pseudocapacitors and batteries. The main requirements to increase the capacitance in EDLCs are surface area, electrical conductivity, and electrochemical stability. The limitation of voltage range comes from the reduction or oxidation of electrolyte polarisation, electrode and the corrosion of current electrode. For improving the capacitance and enlarging operating voltage, controlling the pore size distribution to the size of electrolyte ions will be the interesting way. Previously, mesopores are highly desirable for EDLC electrodes due to their unique structure of mesopore network, which is more favourable for fast ionic transport than the pore networks in disordered microporous carbons.[15] It also has been recently reported that the specific capacitance can be increased by matching the sizes of pores and desolvated ions. The optimal average pore size depends on the current load due to the distortion of cations or intercalation behaviour.[16] Another route is functionalising the EDLC electrode with redox active materials to contribute to the capacitance via redox reactions, which is also called pseudo capacitive behaviour.

2.1.1.2 Pseudocapacitors

In contrast to EDLC storing charges non-Faradaically, pseudocapacitors store the charges through the redox reactions between electrodes and electrolytes (Figure 2.1b). The mechanism consists of electrosorption, reduction-oxidation reactions and intercalation processes which allows pseudocapacitors achieving greater energy densities than EDLCs. In general, pseudocapacitors have lower power density when compared with EDLCs because the

redox reaction has slower kinetics than electrostatic storage. There are two classes of pseudocapacitive materials, which are conducting polymers (polypyrrole (PPy), polyaniline (PANi) and polythiophene (PTh)) and metal oxides/hydroxides (MnO_2, $Ni(OH)_2$, RuO_2 and Co_3O_4). The mechanism of pseudocapacitor consists of charge collection via electrosorption of ions through redox reactions (capacitive faradaic process); some materials such as $Ni(OH)_2$ present the mechanism like battery store energy in the form of chemical reactants (non-capacitive faradaic process). Non-capacitive faradaic process will present peak-shaped CVs and non-linear GCDs related to electrode potential reaching equilibrium potential while capacitive potential will present most likely linear shape for GCD.[17]

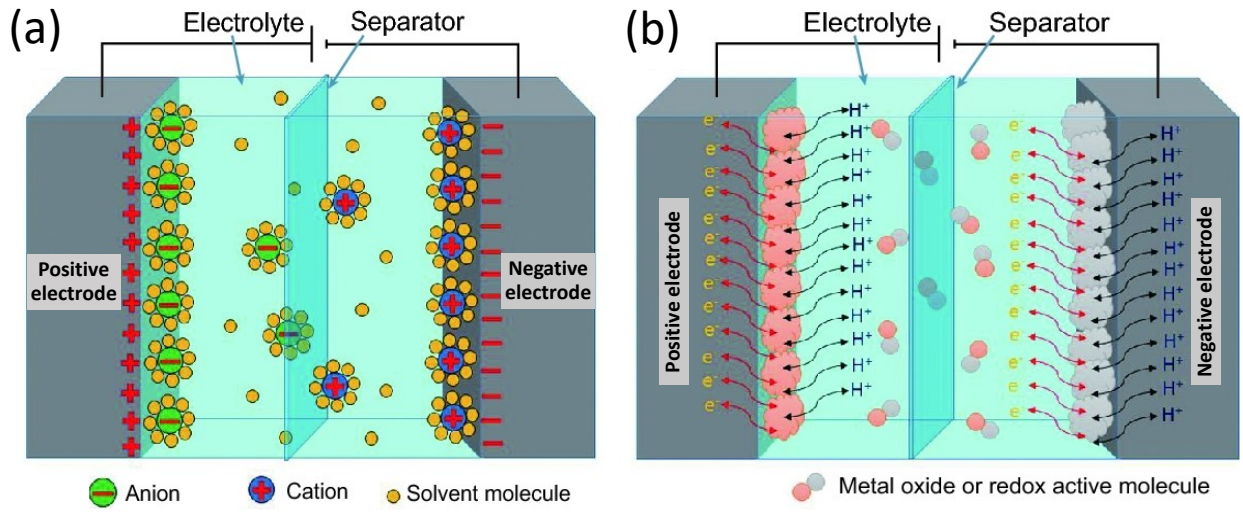

Figure 2.1 Schematic of two different charge storage mechanisms via (a) carbon based (EDLC) and (b) redox reaction-based pseudocapacitor. Adapted from Chen *et al*., 2017.[18]

2.1.1.3 Hybrid capacitor

Hybrid capacitors aim to combine the advantages from both EDLC and pseudocapacitor to have a greater performance. The materials used in this kind of devices will be able to store the charge through both Faradaic and non-Faradaic processes. The performance of hybrid capacitor devices is often dependent on their structure and is a trade-off between EDLC materials and redox active materials. The type of hybrid capacitors can be distinguished by their electrode configuration, which are composite, asymmetric and battery-type.[19] Composite supercapacitors are constructed from carbon based electrodes with pseudo capacitive materials in single electrodes. The carbon based will provide high surface area and

enhance the contact between pseudocapacitive materials and electrolyte to further improve the energy density.[20] Redox active materials, which provide faradaic capacity, should be well dispersed throughout the surface. If the redox active materials agglomerate, they will impede electrolyte ions diffusion, leading to low energy densities and higher resistances. Additionally, the agglomeration of pseudocapacitive materials will result in lower efficiency of redox reaction owning to only the material at the outer surface can collect charges. Asymmetric supercapacitors couple EDLC material as negative electrode and pseudo capacitive material as positive electrode. The asymmetric supercapacitors are able to enlarge applied voltage resulting in higher energy density. Battery-type hybrids or supercapattery are coupling supercapacitor electrode with battery electrode. The mechanism to store charge of supercapattery expects to perform like a rechargeable battery but with higher capability and longer cycle life durability.[17]

2.1.2 Type of supercapacitor classified by active materials on positive and negative electrodes.

2.1.2.1 Symmetric Supercapacitors

Symmetric supercapacitors comprise with the same kind of material on both positive and negative electrodes which can derive the capacitance only in the same range of the working potentials.

2.1.2.2 Asymmetric Supercapacitors

Asymmetric supercapacitors are fabricated from positive and negative electrodes using different kinds of materials. Asymmetric supercapacitors can provide a wider working potential by combining the different range of working potential between negative and positive electrodes and they allow to be used in the electronic devices requiring higher voltage compared with symmetric device.

2.1.3 Type of liquid electrolytes

2.1.3.1 Aqueous electrolytes

Acid-based (e.g. H_2SO_4) and alkali based (e.g. KOH) electrolytes are commonly used in aqueous supercapacitors because they are cheap and have good conductivity (about 0.8 S/m for H_2SO_4, 0.6 S/m for KOH). The nature of acid electrolyte such as H_2SO_4 has a strong influence on pseudocapacitive materials because protons from H_2SO_4 can be involved in the redox process.[21] Additionally, H_2SO_4 electrolyte can introduce oxygen functional groups on carbon materials surface resulting in the collection of charges through both pseudo capacitance and EDL capacitance. In alkaline electrolytes, small ions such as K^+ and Na^+ can benefit in intercalation-based charge storage mechanism of metal oxide (e.g. NiO_x, CoO_x and MnO_2) and metal hydroxide (e.g. $NiOH_2$, $Co(OH)_2$) because their small ionic radius allow them to intercalate/deintercalate easily into the layer of materials.[22] Unfortunately, the operating voltage is limited by the thermodynamic decomposition of pure water at 1.23 V leading to low energy density, structure transformation of active materials and lower power density than organic electrolytes.[23]

2.1.3.2 Organic electrolytes

Organic electrolytes can be charged and discharged at voltage higher than 2 V, which depends on the purity of the electrolyte. The higher operating voltage allows the device to achieve higher energy density than using aqueous electrolyte. For example, tetraethyl ammonium salts ($(C_2H_5)_4BF_4$) can be dissolved in non-aqueous solutions and has good conductivity. Tetraethylammonium tetrafluoroborate (Et_4NBF_4) in adiponitrile can provide high operating potential up to 3.75 V and displays also good stability.[24] The most commonly used organic electrolytes for EDLC are acetronitrile (ACN) and propylene carbonate (PC) due to their high conductivity, low ESR and high power performance at low temperature.[22] Although organic electrolyte is widely used in industry, they have 20-50 times higher resistance than aqueous electrolyte. Additionally, they are flammable, poisonous and expensive.

2.1.3.3 Ionic-liquid electrolytes

Ionic-liquid electrolytes (ILs) are composed of organic cations and organic anions. Generally, the type of ILs for energy storage devices is aprotic, which normally use imidazolium, pyrrolidinium, ammonium as cations with tetrafluoroborate (BF_4^-) or hexafluorophosphate (PF_6^-) as anions. ILs have numerous advantages owing to high thermal stability, non-flammability, low toxicity, good conductivity and be able to operate applied voltage higher than 3 V depending on the structure of cations and anions of ILs.[25] Nevertheless, ILs are still not appropriate to apply in a large-scale production owing to their expensive cost and low ionic conductivity. The low ionic conductivity of 1-ethyl-3-methylimidazolium tetrafluoroborate ([EMIM][BF_4]) and 1-butyl-3-methylimidazolium tetrafluoroborate ([BMIM][BF_4]) are 41 cp and 219 cp respectively, which can cause an increased resistance in the device owing to limiting the rate and power performance even when the cell voltage are increased.[26]

Table 2.1 The properties of electrolytes[27]

Electrolyte	V_{max} (V)	Resistivity (Ω·cm)	Density (g/cm^2)
H_2SO_4	1.23	1.35	1.2
KOH	1.23	1.9	1.29
Acetonitrile	2.5-3.0	18	0.78
Propylene carbonate	2.5-3.0	52	1.2
Ionic liquids (ILs)	4.0 3.25	125 (25 ˚C) 28 (100 ˚C)	1.3-1.5

2.2 Carbon nanomaterials

In recent years, carbon nanomaterials have received huge interest for supercapacitor applications due to their exceptional properties and large surface area/volume ratio at the nanoscale. sp^2 carbon can form various structures such as 0D fullerenes, 1D carbon nanotubes (CNTs), 2D graphene and 3D graphite (Figure 2.2).[28] Currently, activated carbon is most often used in commercial supercapacitors due to the moderate cost and high surface area (2500-3000 m^2/g).[29] Its conductivity and specific surface area depend on the activation method and type of carbon precursors.[7] However, the specific capacitance of activated carbon electrodes

is usually lower (< 200 F/g in aqueous electrolyte) than the theoretical capacitance (300-500 F/g). This lowered efficiency is attributed to the complex pore structure of activated carbon, containing mostly micropores.[30] Electrolyte ions (especially organic electrolytes) struggle to diffuse through this micropore sizes (< 2nm), leading to low power density, as the pores are too small and unable to collect the charges.[31]

Graphene is a carbon allotrope, which is a two-dimensional carbon sheet with honeycomb crystalline lattice. Since its isolation, it has attracted much attention as an active material electrode for energy storage devices, owing to high specific surface area (theoretically 2600 m^2/g) and good flexibility.[32] Unfortunately, the synthesis of graphene is expensive and hard to scaling. Therefore, graphene oxide (GO) and reduced graphene oxide (rGO) are favorable to use as graphene's derivatives where they are easier to synthesis and scale up.[33] GO is considered as the oxidised form of graphene which contains hydroxyl, carbonyl, alkoxyl, carboxylic acid and other oxygen functional groups. These oxygenated groups lead resulted in GO has lower conductivity compared to graphene however they also provide many advantages over graphene, including higher solubility and the possibility for surface functionalisation which is suitable to produce nanocomposite materials. [34] The oxygen functional groups of GO can be reduced with various techniques then obtain as rGO. rGO has higher conductivity than GO as the oxygen containing has been reduced however, rGO still cannot achieve the pristine graphene structure as it still contains residual oxygen and structural defects originated in the chemical oxidation synthesis of GO.[35]

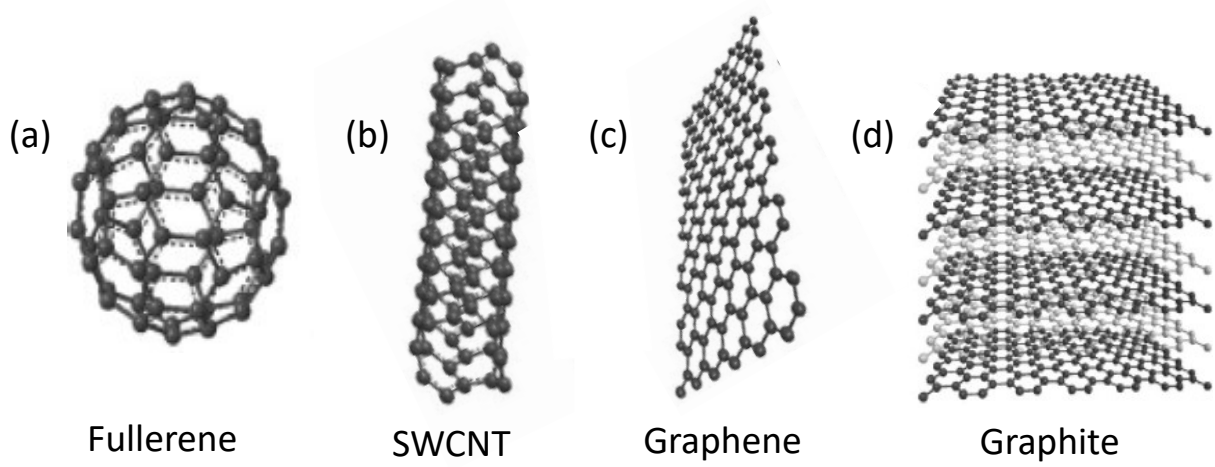

Figure 2.2 Form of sp^2-bonded carbon. (a) Fullerene (0D), (b) single-walled carbon nanotube (1D), (c) graphene (2D) and (d) graphite (3D). Adapted from Basu *et al.,* 2012[36]

Nevertheless, graphene and its derivatives have numerous problems as the active materials for energy storage devices, including both poor packing density (<0.5 g/cm^3) and restacking due to strong $\pi - \pi$ interactions, resulting in lower active surface area and lower mechanical performance. To limit restacking graphene and its derivatives have been assembled into 3D forms, such as aerogels, hydrogels or vertical sheets.[37] For example, vertically-aligned reduced graphene oxide (VArGO) with high packing density (1.18 g/cm^3) provides higher volumetric electrochemical performance (171 F/cm^3) when compared with planar reduced graphene oxide (rGO) (62 F/cm^3). This improvement is attributed the limited ion access in the restacked planar architecture, while VArGO with opened edge structure provides larger gaps between sheets leading to improve ion accessibility.[38, 39]

For 0D structures of carbon nanomaterials, the discovery of nanometre-sized molecules consisting entirely of 60 carbon atoms (C_{60}) so called "Buckminsterfullerene" promoted the discovery of other fullerenes such as C_{70} and C_{80}.[40] Carbon nanotubes (CNTs) are one dimensional structures owing to their high length to diameter ratio. CNTs can be classified into two types which are single-walled carbon nanotubes (SWCNTs) and multi-walled carbon nanotubes (MWCNTs) (Figure 2.3). CNTs have excellent physical and chemical stability, low gravimetric density and excellent electronic conductivity which can be universal to design composite electrodes for supercapacitors.[41] In addition, CNTs can provide reaction sites for functionalisation which can further benefit the electrochemical performance.[42]

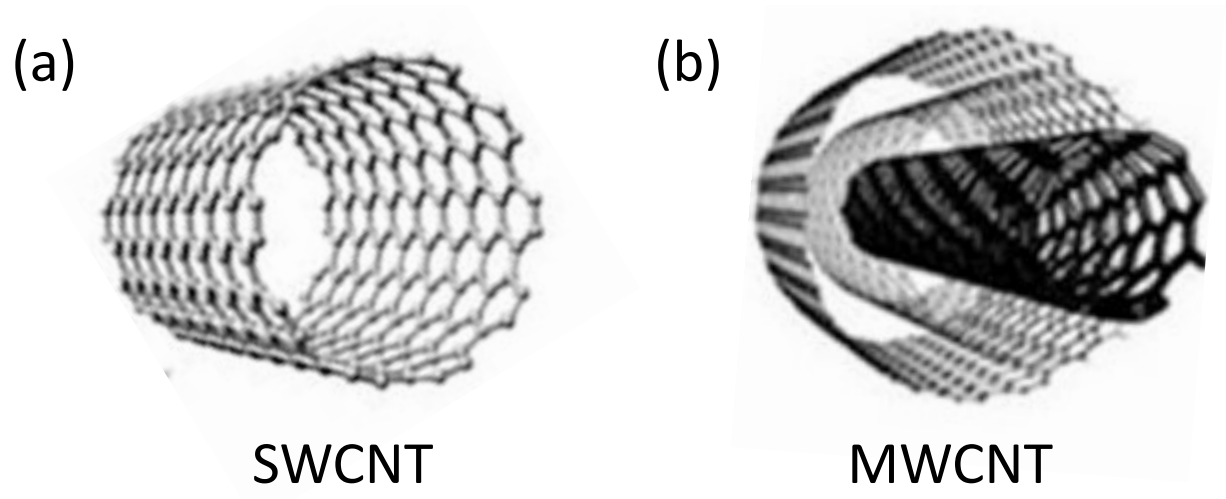

Figure 2.3 Schematic of (a) single wall carbon nanotube (SWCNT) and (b) multi-wall carbon nanotube (MWCNT) structures. Adapted from Vidu *et al.*, 2014.[43]

2.3 Single-walled carbon nanotubes (SWCNTs)

A single-walled carbon nanotube (SWCNT) consists of a graphene sheet rolled up into tubular shape with a length of up to centimetres. SWCNTs structure can be classified into three types which are zig-zag ($n \neq 0$, $m = 0$, $\theta = 0°$), armchair ($n = m$, $\theta = 30°$) and chiral nanotubes ($0° < \theta < 30°$, $n \neq m$), depending on the graphene sheet orientation.[44] The chiral vector (n.m), where n and m are chiral indices, is used to specify the types of SWCNTs. [45]

2.3.1 Synthesis of SWCNTs

In general, the main step for SWCNTs synthesis is the preferential growth and the most common SWCNT growth route is chemical vapor deposition (CVD), which provides many distinct advantages, such as low-cost, wafer-scale, and repeated growth.[46] For the CVD method used for synthesising SWCNTs, metal-based nanoparticles (usually iron or an iron alloy) serve as catalysts in both assisting carbon feedstock cracking and facilitating the nucleation of nanotubes. The composition and morphology of the catalyst nanoparticles are critical in determining the structure, length, and yield of SWCNTs.[47] Carbon dissolves in the catalyst until saturation, at which subsequent precipitation occurs and SWCNTs are formed.[48] The synthesis variables of CVD can be adjusted to control the diameter, length, purities and alignment of SWCNTs. In general, SWCNTs are produced after synthesis by removing the substrate and then processing the solution or the SWCNTs forest can be produced directly. Often, the material is treated after the initial CVD synthesis by the company to produce a purified material, by example acid washing to remove metal particles, or oxidative treatments to remove unwanted carbons. Typical commercial starting materials used for research include HiPco, Supergrowth™ , Tuball™ and CoMoCAT SWCNTs. The manufacture of HiPco SWCNTs uses a high-pressure process, which provides the SWCNTs with ca. 1 µm and have low carbonaceous impurities.[49] Supergrowth™ SWCNTs synthesised via CVD with the additional of water vapour during synthesis which allows SWCNTs to grow up to the millimetre scale.[50] Tuball™ SWCNTs use a low temperature plasma vortex of a catalyst metal source, combined with a more conventional CVD growth regime.[51, 52]

2.3.2 Electrical properties

SWCNTs are either metallic or semiconducting along their tubular axis. The electrical characteristics of SWCNTs rely on the properties variation across nanotube types. As the notation of nanotube are given as (n,m), a chiral SWNTs can be metallic (finite electron density at the Fermi level) or semiconducting (band gap varying inversely with the tube diameter), with n – m = 3q as condition for metallicity.[44, 53] Single SWCNT is found to provide very high electrical conductivity up to 4×10^5 S/cm.[54] For SWCNT network, the electrical conductivity is dependent on multiple factors such as length, diameter, chirality and deformation of the SWCNTs as well as tube interactions, tube contact angle, packing density and orientation of the network.[55] In reality, the SWCNT-SWCNT contact occurs at the nanoscale. The contact region is composed of several atoms and has very limited extension in the directions perpendicular to the incident electron flow. Furthermore, the distance between two contacting SWCNTs is less than the Fermi wavelength and the momentum relaxation length. Under these circumstances, the electron is considered to be in a ballistic transport state and can be reasonably assumed to be confined to one dimensional channels.[56, 57] In the literature, the theoretical electrical conductivity of SWCNT buckypaper is much higher than the measurement and the conductivity of buckypaper is much lower than single SWCNT owing to contact resistance between SWCNTs in the buckypaper.[58] Additionally, the synthesis procedure of buckypapers also influences the conductivity of SWCNT buckypaper prepared with different methods where the electrical conductivity of SWCNT buckypaper ranges from 10 to 1000 S/cm.[58-60] The electrical conductivity of the SWCNT buckypaper can be improved by enhancing the packing density and organizing good inter-tube contact which facilitates electron transfer.[61] Note, the contact resistance of SWCNT buckypaper is inversely proportional to the diameter where SWCNT network with small diameters has high electrical conductivity.[62, 63] Additionally, the increasing of SWCNTs or its bundle length can also enhance the electrical conductivity as the long bundles can reduce interbundle contact resistance.[64] However, the increase of defects on SWCNT buckypaper or its bundle will decrease the electrical conductivity due to scattering on lattice defects.[65, 66]

2.3.3 Mechanical properties

Carbon nanotubes have excellent stiffness and elastic modulus among nanomaterials. This stiffness results from the covalent sp^2 bonds formed between the individual carbon atoms. Mechanical properties of SWCNTs are firmly dependent on defect sites due to SWCNT structure is only 1 atom thick. SWCNTs exhibit plastic rearrangement along the length when under load, leading to stretching with failure occurring at a defect site after rearrangement.[67] The mechanical properties of SWCNTs are considered superior to MWCNTs at the single element level due to their greater perfection, and the avoidance of internal shear failures. [68] Additionally, the drastically higher diameters of MWCNTs leads to lower aspect ratios than SWCNTs despite their larger lengths which further limiting their application to composites compared to SWCNTs. SWCNTs have reported to achieve high-strength composites and structural materials due to their impressive mechanical properties (tensile strength ~52 GPa; Young's modulus ~320 to 1470 GPa) [69] which higher than conventional materials such as graphene (in plane, tensile strength ~2.5 GPa; Young's modulus ~350 GPa)[70] and carbon fibre (tensile strength ~3.8 GPa; Young's modulus ~240 GPa)[71]. Note, the values which mentioned here are taken from the literature where they provide the theoretical value. The mechanical properties in the nanoscale do not essentially follow this value and expect to achieve lower value when the materials scaled up, included defect and environmental considerations. SWCNT bundles, which caused by van der Waals force, are reported to have lower mechanical strength (6.77 GPa) than individual nanotubes.[72] Additionally, the mechanical properties of SWCNTs also decrease with the increase of defectiveness, which create during SWCNT synthesis process. The defects have shown to impact mechanical properties differently with sp^3 sites which reducing strength and vacancies within the sidewall reduce both strength and stiffness.[73]

2.3.4 SWCNT buckypapers

SWCNT buckypapers are entangled assemblies of SWCNT films with 2D paper-like structure attached to each other via van der Waals forces at the tube–tube junctions.[74] Macroscopic SWCNT buckypapers are usually reported to have an attractive balance of multi-functional properties, including high electrical and thermal conductivities, flexibility, mechanical stability, and electrochemical activity.[75] SWCNT buckypapers are known to have

lower contact resistance, higher packing density and higher conductivity when compared with SWCNT composites and/or SWCNT aerogels, due to their less voids formed in the structure.[76] In the literature, supercapacitor performance is frequently reported normalised only to the mass of the active electrode material however, whilst these data fairly highlight the exceptional intrinsic performance of materials only. For example, ultrathin films (<1 μm) deliver negligible active mass compared to the parasitic mass of the remainder of the cells which are misleading when it comes to practical application.[77] Another example is SWCNT aerogels which appear to offer a remarkable (gravimetric) performance, as the high aspect ratio of SWCNTs can enable 3D network aerogel structures with exceptionally high surface area and large open porosity, which can enhance the ion transportation in energy storage devices.[78] SWCNT aerogels have ultralow packing densities, typically consisting of >99% pore volume; in a real device, this volume must be filled with dense electrolyte, dramatically increasing the effective electrode mass. At the same time, the low density implies a poor electrochemical volumetric performance, which is important in many practical applications such as compact electronic devices and power management in electric vehicles.[3, 4] For example, [79] a low density SWCNT aerogel (0.013 g/cm^3) shows particularly high gravimetric specific energy at ~40 Wh/kg while its volumetric energy density is only ~0.52 mWh/cm^3. A thick aerogel electrode also implies high equivalent series resistance (ESR) which decreases the performance further. Reducing thickness of SWCNTs aerogel via solvent-induced collapse or mechanical compression causes bundling or restacking. [80] These processes reduce surface area and can disrupt ion transport, leading to a huge increase in charge transfer resistance. For real applications, the SWCNT electrode architecture must be designed to maximise volumetric performance, electrical conductivity and ion transport, at high mass loadings.[9] From these reasons, SWCNT buckypapers have been explored as free-standing electrodes, exploiting the excellent intrinsic properties of SWCNTs as electrochemical electrodes, whilst saving weight by obviating metallic current collectors. Buckypapers have higher packing density and higher conductivity when compared with SWCNT aerogels. The gravimetric capacitances reported for SWCNT buckypaper can be very high (up to 300 F/g in three-electrode system) compared to more conventional carbons. [81-83] For example, drop cast SWCNT films can reach 280 F**/**g in acetonitrile as electrolyte**.**[81] SWCNT film prepared by dc-arc discharge reported to have 180 F**/**g in a KOH aqueous electrolyte**.** On the other hand, a smaller capacitance was shown for SWCNT buckypaper prepared by floating chemical vapor

deposition method at 35 F/g in $LiClO_4$ electrolyte.[82] This inconsistency depends on the SWCNT type, electrode structure, and electrolyte. The strong $\pi - \pi$ interaction between SWCNTs is also another main factor which can cause the reduction the electrochemical capacitance due to the reduction in the active surface area through bundling. Buckypapers are usually prepared by vacuum-filtration of SWCNT dispersions produced by sonication in a suitable dispersant.[84] The dispersants will promote debundling and maintain SWCNTs at a stable (kinetic) suspension where ionic surfactants such as such as sodium dodecyl sulfate, sodium dodecyl benzenesulfonate, dodecyl trimethylammonium bromide and hexadecyltrimethylammonium bromide are generally used.[85] Note, some non-ionic surfactants (such as octyl phenol ethoxylate)[86], polymers[87] or DNA[88] are also reported to be used as well. The individualisation, packing density and specific surface area of SWCNT buckypapers are affected by the dispersion method; therefore, the process has to be controlled carefully.

2.3.5 SWCNT dispersion and purification approaches.

To maximise electrochemical performance, SWCNTs require individualisation/dispersion before their use in applications. Numerous studies have focused on trying to disperse SWCNTs down to the level of individual nanotubes in liquid-phase systems including intense sonication, reductive chemistry or other methods of mechanical shear.[8] SWCNTs have been dispersed with the aid of acids, macromolecules, and surfactants as well as through covalent functionalisation strategies.[89, 90]

2.3.5.1 Ultrasonication

The most universal SWCNT dispersion method is ultrasonication. The strong shear force comes from the implosion of cavitation process, growth and collapse, resulting in high energy to produce individual nanoparticles or small agglomerates.[91] The sonication process depends on various factors including solvents type, surface tension, vapor pressure and solubility. Note, sonication is more successful in less viscous solvents which match the surface energies of the SWCNTs, or with a suitable surfactant.[92] Intense probe sonication is needed to individualise SWCNTs but also induces defects or even scission at longer process times.[93] Aggressive sonication can cause serious framework damage, degrading intrinsic properties

and generating defects on the side wall.[94] Although this effect can be useful for shortening CNTs deliberately, the loss of electrical and mechanical properties remains. Raman spectroscopy is often used to monitor CNT (see Section 3.2.6); the increase of the intensity of the defect or D band compared to the corresponding graphitic or G band intensity is used to assess tube damage.[95] SWCNTs can be dispersed in water with the aid of amphiphilic surfactants or macromolecules. To date, the best solvents to stabilise sonicated SWCNTs without the need of a third phase dispersant are amides, particularly N,N-dimethylformamide (DMF) and N-methylpyrrolidone (NMP).[96] However, the suspensions can be contaminated with small particulates (<10 nm) of sonochemically degraded solvent; these particles can be undesirable and may also indicate a chemical grafting process.[97] Alternative methods, such as calendering, ball milling, shear mixing and extrusion methods, are more commonly employed in the manufacturing of polymer composites.

2.3.5.2 Oxidative treatment

Oxidative treatments are known to remove both amorphous carbon and metal particles from SWCNTs and introduce the oxygenated functional groups, especially carboxylic acids on the surface.[98] There are two commons methods which are liquid phase oxidation involving nitric acid (HNO_3), potassium permanganate ($KMnO_4$), hydrochloric acid (HCl), sulphuric acid (H_2SO_4) and gaseous phase oxidation involving O_2, H_2 or air. The most common acid treatment uses mixed HNO_3/H_2SO_4 to cut the highly bundled long ropes of SWCNTs into short, open ended pipes, and thus created many carboxylic acid groups at the open ends.[99] Acid oxidation processes generally give high yields and dissolve any metal/metal oxide impurities. However, they also introduce additional impurities and cause huge damage to the SWCNT structure. One alternative uses hydrogen peroxide (H_2O_2) which reacts with residual iron to form gently oxidising hydroxyl radicals through Fenton chemistry.[100] These radicals can remove the high curvature carbons in a less damaging approach than oxidising acids, allowing HCl, which is also shown, to dissolve the newly exposed catalysts.[101]

2.3.5.3 Superacid dissolution

SWCNT bundles dissolve spontaneously in superacid such as oleum (H_2SO_4+SO_3) and chlorosulfonic acid (CSA).[102] Superacids reversibly protonates the surface of the SWCNTs with a delocalised positive charge then this charge induces a repulsive force between nanotubes

and promotes dispersion by counteracting van der Waals attraction.[103]The dissolution of SWCNTs mostly depends on acid type that employed and defect concentration on the SWCNT surface. SWCNTs at high concentration have been shown to form liquid crystal phases with transition from isotropic to nematic phase possible both in neutral systems and charged species in superacids.[104] However, the dissolution process in this type of environment are limited by the aggressive nature of the superacids, which destroy many of the materials potentially employed for sidewall derivatisation.

2.3.5.4 Reductive dissolution of SWCNTs

Reduction dissolution of SWCNTs introduces Coulombic repulsions then utilises the charge on the nanotube to overcome the van der Waals interactions, without damaging the SWCNT structure.[105] Reductive chemistry dissolves/functionalises SWCNTs via charging with an alkali metal (commonly Na, K or a Na-K alloy) to form negatively-charged SWCNT ("nanotubide") solution.[106] The negatively charged SWCNT solutions (nanotubide) show significantly improved solubilities and exfoliations, affording thermodynamically stable solutions of individual, undamaged species at high concentrations.[105] Nanotubide solvents are usually the same with those using in sonication process including N,N-dimethylformamide (DMF), N-methylpyrrolidone (NMP) , N-cyclohexyl-2-pyrrolidone (CHP), and tetrahydrofuran (THF). There are various reductive charging methodologies, which have been developed during these years. For example, reductive alkylation of SWCNTs using alkyl halides and lithium in liquid ammonia was introduced by Birch-reduction type reactions.[107] This approach was then developed by charging SWCNTs with lithium to form SWCNTs polycarbanions under the catalytic effect of di-tert-butyl-biphenyl (DTBP). Then, charged SWCNTs were dissolved in THF to increase the dispersibility of side-wall functionalised-SWCNTs.[108] To avoid the contamination problem in the individualisation process, liquid ammonia is also used as the charging solvent since the ammonia can be easily removed by evaporation. Liquid ammonia is an excellent medium for creating alkali metal nanotubide salts without adding any charge transfer species through the intrinsic electron-solvating power of the ammonia. The reductive charging SWCNTs using liquid ammonia has found to scale consistently to the 100 mg level which shows a intrinsically scalable method for SWCNT dispersion, separation and purification.[109]Another interesting approach is reductive charging of SWCNTs via

electrochemistry. Cyclic voltammetry (CV) can charge nano-ions reversibly, and can be associated to the complex electronic density of states of SWCNTs.[110] The efficiency of electrochemical charging approach relies on the electrolyte stability and low ionic concentrations to minimise electrostatic screening. This electrochemical method offers the high purity output of individualised SWCNTs without the damaging processes; however, scalability remains limited.[101] Recently, the one-pot reduction of SWCNTs (Figure 2.4), in N,N-dimethylacetamide **(**DMAc**)** using an organic charge transfer agent **(**sodium naphthalide, NaNp**)**, has attracted attention due to its simplicity and scalability. Since DMAc is a stable solvent for NaNp and reduced SWCNTs, providing a potentially large-scale source of individualised SWCNTs.[10]

The raised Fermi level of reduced SWCNTs can be applied to access a host of nanotube functionalisation reactions. The mechanism of nanotubide reaction with an electrophile can simply be described as a single electron transfer (SET) in which SWCNTs can be attacked by radical anion in form of $[R–X]^{\cdot -}$ which decomposes to an anionic leaving group, X^-, and the radical $R^{\cdot}$, which reacts with the sidewalls of SWCNTs.[5, 6, 10] However, more detailed analysis indicated that a bound transition state is involved.

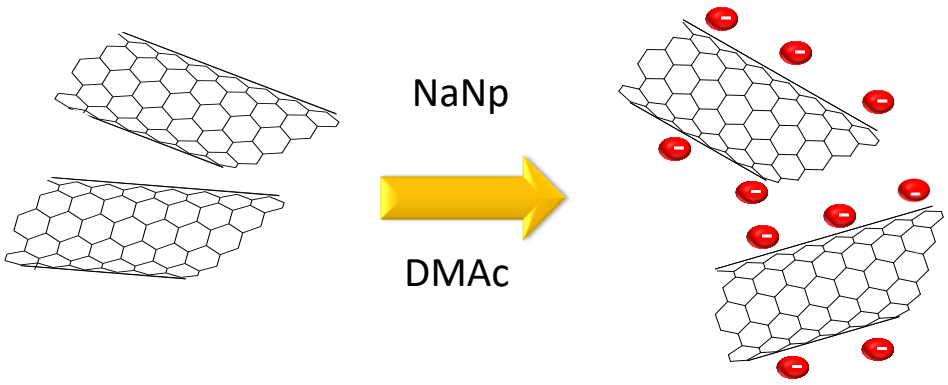

Figure 2.4 Schematic reductive charging of SWCNT powder and NaNp solution in DMAc forming a nanotubide solution.

2.3.6 Cross-linked single-walled carbon nanotube networks

The individual SWCNTs exhibit outstanding properties for energy storage, sensors, catalysts and various other applications. However, the potential performance is only partially reflected in the assembled macrostructure due to intrinsic difficulties in SWCNT processing particularly including the challenge of debundling without damaging the carbon framework.

Additionally, even once individualised, a method is needed to prevent rebundling. Therefore, cross-linked reaction becomes essential to solve this issue by fixing the carbon units in place and held a system of cohesive forces using physical and/or chemical crosslinking. Additionally, since a high power density is required at the high applied current in the energy storage application, a higher uniformity of pore size distribution and pore sized control are required; therefore, the presence of a cross-linker can give a benefit in this field. This literature section will highlight the general overview of the type of cross-linking and recent development of cross-linked SWCNT networks; then, Chapter 5 of this Thesis will highlight the improvement of using a cross-linker in nanotubide buckypaper network for energy storage applications.

2.3.6.1 Physical cross-linked method

Physical cross-linking methods are based on the cross-linking through the physical bonds taking advantage of electrostatic interactions, which are non-covalent intermolecular interactions: Van der Waals forces, hydrophobic and π-π interactions. This type of cross-linking can take place from SWCNTs on their own and/or with the additional cross-linker. In this particular case, Van der Waals forces between SWCNTs can create a self-assembled SWCNT network. Previously, SWCNTs suspensions at high concentration stabilised with sodium dodecyl sulphate (SDS) were reported to form a network from a free flowing solution state to a viscoelastic regime because the nanotubes form physical bonds with each other.[111] This results provided an excellent model system where intertube bonding contributed substantially to network elasticity, which originated from bending or stretching of individual filament.[112] An investigation of SWCNT gel network formation in aqueous dispersions is reported from rheological studies. This study showed that the cross-linking probability was confined to a finite volume, that yields the dependence of the number of contacts on the density, length, and diameter of the constituent SWCNT rods.[113] The other alternative route for non-covalent cross-linking is adding an organogelator with or without a surfactant to the SWCNTs solution.[114] Most common organogelators are long chain elastomers or molecules such as polydimethylsiloxane (PDMS) and polyvinyl alcohol (PVA) which will further benefit the stretchability properties of the organogel. Additionally, the shape and size of organogelators will also have advantages on shape and size tunability for the SWCNT network as well as the cost effectiveness and less brittle when compared with the physical gelation without organogelators.[115] The most important advantages of physical cross-linked methods

is the ease formation of coherent network with low damage on SWCNT structure throughout the process; however, the addition of organogelators can also decrease the electrical conductivity in overall SWCNT network due to the insulating properties of the organogelator itself.[116]

2.3.6.2 Chemical cross-linking method

Cross-linked SWCNT networks via chemical crosslinking methods are based of linked SWCNTs via covalent functionalisation to the SWCNT sidewalls. They are suitable for large scale production, due to the broad variety of reactions and reagents allows a wide versatility of this method. Generally, the chemical crosslinking approach requires the functional group, being most likely containing halogen functionalities, to form a covalent bond on the SWCNT surface first for direct attachment with the cross-linker molecule and then to form the covalent bonds with another adjacent nanotube. For example, assemblies of single-walled carbon nanotubes generated by covalent cross-linked iodobenzene with 1,4-diethynylbenzene and 4,4'-diethynylbiphenyl exhibit an increase in the surface area with respect to pristine SWCNTs and the porosity of the SWCNT network depends on the length of the linker.[117] p-Diiodobenzene (p-DIB) was selected as a cross-linker to produce cross-linked SWCNT aerogels via the reductive cross-linking approach due to its soluble, rigid, potentially conjugated, dielectrophilic character, thus creating an open, porous structure with high surface area (766 m^2/g) and conductivity (9.4 S/m).[11] The carboxylic acid functionalised SWCNTs cross-linked with amine polymers is also reported to produce new mechanically strong composites via using small amount of cross-linkers compared to the general approaches to improve the mechanical properties of SWCNT, which require a large amount of polymer, thus diminishing the electrical and thermal conductivities of SWCNT network. Another route to chemically cross-linking SWCNT is reported by using sidewall functionalisation.[118] This cross-linking is achievable via reactions with reactive species such as nitrenes, carbenes and radicals.[119] The simplest example for this type of reaction is obtained by using polyethylene glycol (PEG) as linker molecule which can be covalently attached to the nanotube sidewalls (Figure 2.5).[120] Note, the chemical modification of SWCNT into higher order construct SWCNT network is still challenging; therefore, a compromise between the mechanical and electrical properties of chemically cross-linked SWCNT network may be

necessary as the optimal cross-linking degree should be determined according to the desired final properties and application.

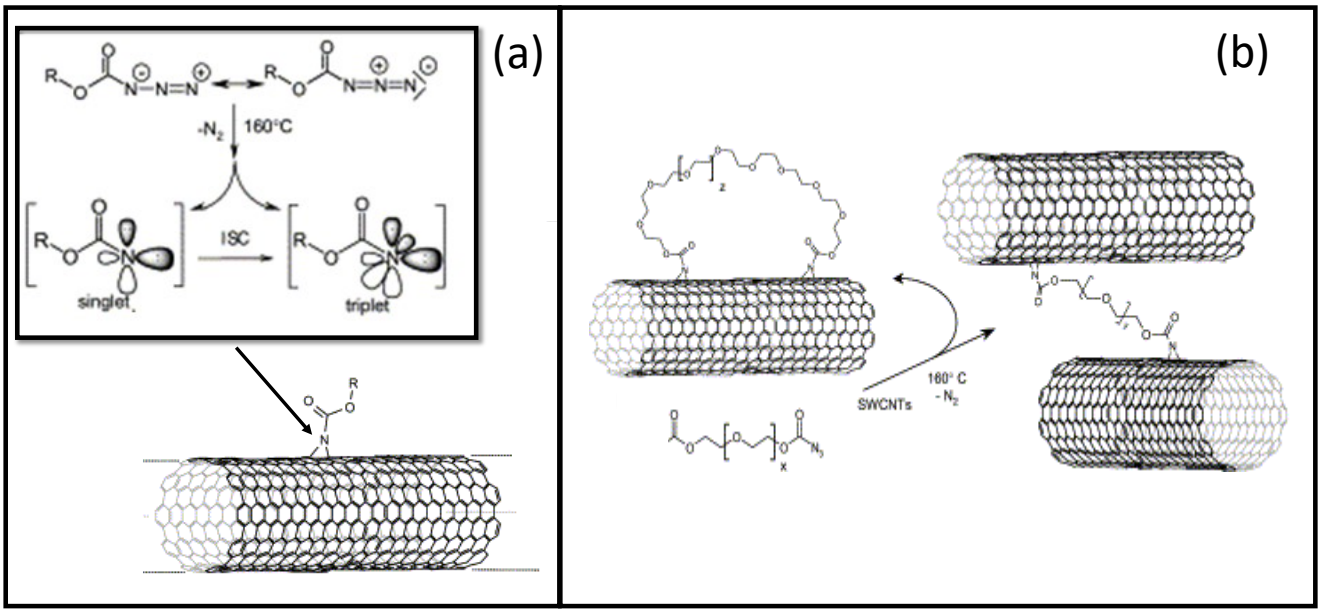

Figure 2.5 (a) Schematic presentation of the reaction of nitrenes with the nanotube sidewall. (b) Reaction of di-nitrenes with the nanotubes using di-azidocarbonate polyglycolesters as precursors. Adapted from Holzinger *et.al.,* 2004.[120]

2.3.7 SWCNT-based supercapacitors

SWCNTs are widely used as electrochemical double layer capacitive electrodes (surface physisorption) owing to their excellent electron transport, high conductivity, and electrochemical stability. On a practical level, SWCNT electrode as the active material suffer from π-π interactions caused by strong rebundling of SWCNTs leading to a reduction in the active surface area, and associated capacitance**.** The high internal resistance affects the overall device performance, reducing the specific capacitance when compared with the theoretical values (550 F/g).[121] Literature values for the intrinsic gravimetric double layer capacitance of SWCNT electrodes range from 20 to 300 F**/**g, relative to the mass of the active carbon in a half-cell electrode**.** [81-83] To address this problem of poor interconnectivity, 3D aerogels which are covalently functionalised whilst still retaining low densities which have highly porous structures are also proposed.[122] The individual components or combination(s) of these constituents in a highly porous network may have further benefits for applications. A porous network, also referred to as an aerogel, would have benefits as an electrode in

energy storage as pathways required for electrolysis can be maintained.[123, 124] However, aerogels are deformed easily under compressive load, which leads to collapsing of the microstructure (damage) and reduction in the interconnected constituents reducing surface area and interconnected pore volume.[125] Low mechanical strength and poor thermal stability of 3D structures lead to a limitation in energy storage applications.[126] In a bid to improve carbon aerogels mechanical performance and to make the structure more robust, the linear elastic region can be improved via cross-linking the nanoform elements either through chemical functionalisation or via annealing/graphitisation. Hybridisation of graphene and CNTs can lead to super elastic structures to prevent fatigue.[126] Additionally, chemical crosslinking can reduce the spaces between intertube and interbundle of CNTs leading to the enhancement in the mechanical properties.[127] Lately, cross-linked single-walled carbon nanotubes (SWCNTs) aerogels with open porous structure were prepared by using sodium naphthalide in dimethylacetamide (DMAc) with p-diiodobenzene (p-DIB) as a crosslinking agent. The charging of nanotubes leads to electrostatic repulsion, which can individualise SWCNTs without shortening them or introducing framework damage. The results have shown that this synthesis method can derive high surface area (766 m^2/g) and high conductivity (9.4 S/m) which are essential properties in electrodes for supercapacitors with high rate capability and cycling efficiency.[11] In order to enhance high capacitance, SWCNTs are favourable to use as an electrode material/substrate for hybridising with wide varieties of redox active materials.

2.3.8 SWCNT-based hybrid materials for supercapacitors

Even though, SWCNTs can exhibit high power density however, low energy density leads to the limitation in commercial use. Many researchers introduced the pseudocapacitive materials on SWCNT surface via various methods on accounts of their reversible redox reaction. The most common materials are conducting polymers and transition metal oxides which have fast reversible redox reaction. For example, PANI were successfully hybridised with SWCNTs via using m-cresol camphorsulfonic acid (CSA) as a doping agent.[128] The energy density is reported 3 times higher than pristine PANI due to CSA can form highly order interface layer on SWCNTs and π-π interaction between PANI and SWCNTs induces the conductive network, which give a benefit for ion transportation and fast redox reaction between electrode/electrolyte. MnO_2 was electrodeposited on SWCNT paper at room

temperature and exhibits higher energy density and good cyclic stability when compared with the control MnO_2 electrode.[129] $Ni(OH)_2$/SWCNT xerogel is reported to increase the electrochemical performance compared with $Ni(OH)_2$/SWCNT hydrogel due to the stronger interface bonding. Additionally, SWCNT 3D structure help to improve the conductivity and accommodate the volume change of $Ni(OH)_2$ lead to the enhancement in cyclic stability when compared with the control $Ni(OH)_2$ electrode[130]. Polypyrrole(Ppy)/SWCNT composited electrode reported to be able to improve the active sites on polypyrrole chain lead to higher specific capacitance than pure Ppy and as-grown SWCNTs electrode.[20] Recently, hybridising carbon based materials with small organic molecules such as quinones have arisen. The small aromatic molecules such as amino and hydroxyl also provide pseudocapacitance via –OH and $–NH_2$ groups instead of polymer particle which is hard to control the thickness and the agglomeration which lead to the poor conductivity[131]. Previously, 4,4'-oxydianiline were functionalised on N-doped graphene (NG) can approve that –OH groups show a stronger adsorption affinity to NG sheets compared to the one which comprised only-NH_2 group. In addition, the hybridisation between polytriazine-imide (PTI)[132] and SWCNTs will be interesting since PTI components which contain nitrogen atoms is the enhancement of the redox reaction and an increase in the ionic conductivity and thus the mass transportation. [133, 134]

2.4 Conducting polymers

To build up the multifunctional structural electrode for energy storage device, the electrode materials properties should be able to carry mechanical loads as well as to store electrochemical energy, thus substituting the traditional static load-bearing components for mass and volume savings of the whole system.[135] Among pseudo-capacitive materials, conducting polymers are considered to be promising candidates due to high theoretical capacitance, high electrical conductivity, stretchability and processibility compared to many metal oxides and the other main class of pseudocapacitive materials.[136] This is because conducting polymers contribute to pseudocapacitive behaviour by doping and de-doping charges to polymer backbone during charging and discharging processes leading to electrolyte ion intercalation and de-intercalation in polymer structure with high reversibility.[137] Additionally, conducting polymers also have benefit on mechanical stability and high conductivity imparted by their conjugated backbones which allow to delocalise π-

electrons over the entirety of the polymer chain.[138, 139] These advantages can give the potential to develop novel technologies such as wearable electronics or devices which require to obtain a mechanical loading while used. Polyaniline (PANI), poly(3,4-ethylenedioxythiophene) (PEDOT), and polypyrrole (PPy) are well-known extensively studied conducting polymers for supercapacitor electrodes. The choice of using each type of conducting polymer depends on the application of the device. For example, PANI has the highest specific capacitance, high thermal stability and is environment friendly; however, they have poor cyclic stability and low conductivity compared to PPy and PEDOT. On the other hand, PEDOT exhibits high conductivity and good cyclic stability; however, they provide lower specific capacitance and smaller specific power.[140] In general, PPy films prepared by electrochemical polymerisation with inorganic anions usually have higher mechanical properties than those of the films doped with bulky organic anions. The tensile strength of PPy films vary from 8 to 100 MPa; the elongation at break is within 2% ± 8%; the Young's modulus, 0.4 ± 4 GPa when using different dopants. The elongation at break can be increased up to 70% when PPy is synthesised at low temperatures.[141 142] Compared to those PANI and PEDOT, PPy is denser and exhibits higher volumetric specific capacitance (400–500 F/cm^3) with higher chemical, thermal stability and excellent mechanical flexibility[143] which is suitable for multifunctional applications.

2.4.1 Synthesis of polypyrrole

PPy is one of the most favourable conducting polymer for energy storage electrodes due to the facile synthesis approach, high conductivity, high energy density and is mechanical robust, which allows it to be moulded into desirable shapes without reducing electrochemical performance.[142] However, there is a limitation in PPy electrodes as PPy is a p-dopable conducting polymer which can be used as positive electrodes only. Its most crucial feature is its high mass density and hence dopant ions cannot properly reach the interior of the polymer, thus decreasing gravimetric capacitance.[142, 144, 145] The electrochemical performance of PPy varies depending on the electrode preparation. For example, PPy/carbon aerogel electrode prepared via ultrasound irradiation is reported to achieve 433 F/g in 6M KOH.[146] On the other hand, PPy/graphene aerogel electrode prepared via pulse polymerisation exhibits 625 F/g in 1 M KCl.[147] The different synthesis approaches, surfactants, medium or substrate not only derive different electrochemical behaviour but also electrical conductivity as well as

mechanical properties. The most common synthesis strategies of PPy can be classified into two categories which are chemical oxidative polymerisation and electrochemical polymerisation.[148, 149]

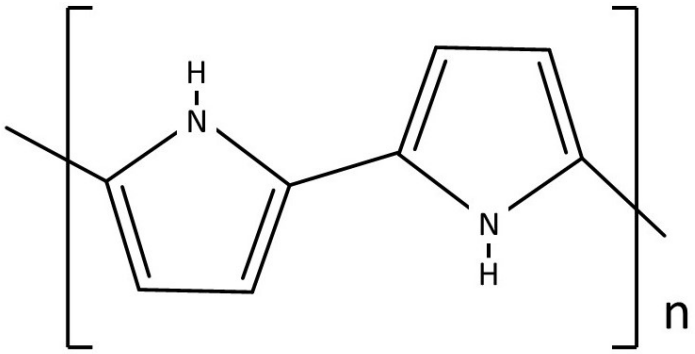

Figure 2.6 Chemical structure of polypyrrole.

2.4.1.1 Chemical oxidative polymerisation

Chemical oxidative polymerisation is a fast and facile approach to produce PPy via using monomers, oxidant (such as $FeCl_3$ and APS) and dopant with aqueous or organic solution such as benzene, acetonitrile, alcohol and chloroform or chemical vapour deposition.[143] The mechanism to produce PPy is described in Figure 2.7. In the first step, pyrrole monomers are oxidised and form a radical cation, which is then deprotonated to form bipyrrole. Following the same steps, bipyrroles get oxidised then, deprotonated and form oligomers which finally become PPy.[150] The properties of PPy from this chemically synthesis approach depend on the type of solvent, concentration, temperature, time of polymerisation and the oxidising agent. The chemical polymerisation tends to be a useful approach for preparing PPy in huge quantities; however, there is limitation of range of PPy that can be produced due to the limited number of counterion and also by-product from excess surfactant which can contaminate or produce side effects on the PPy.

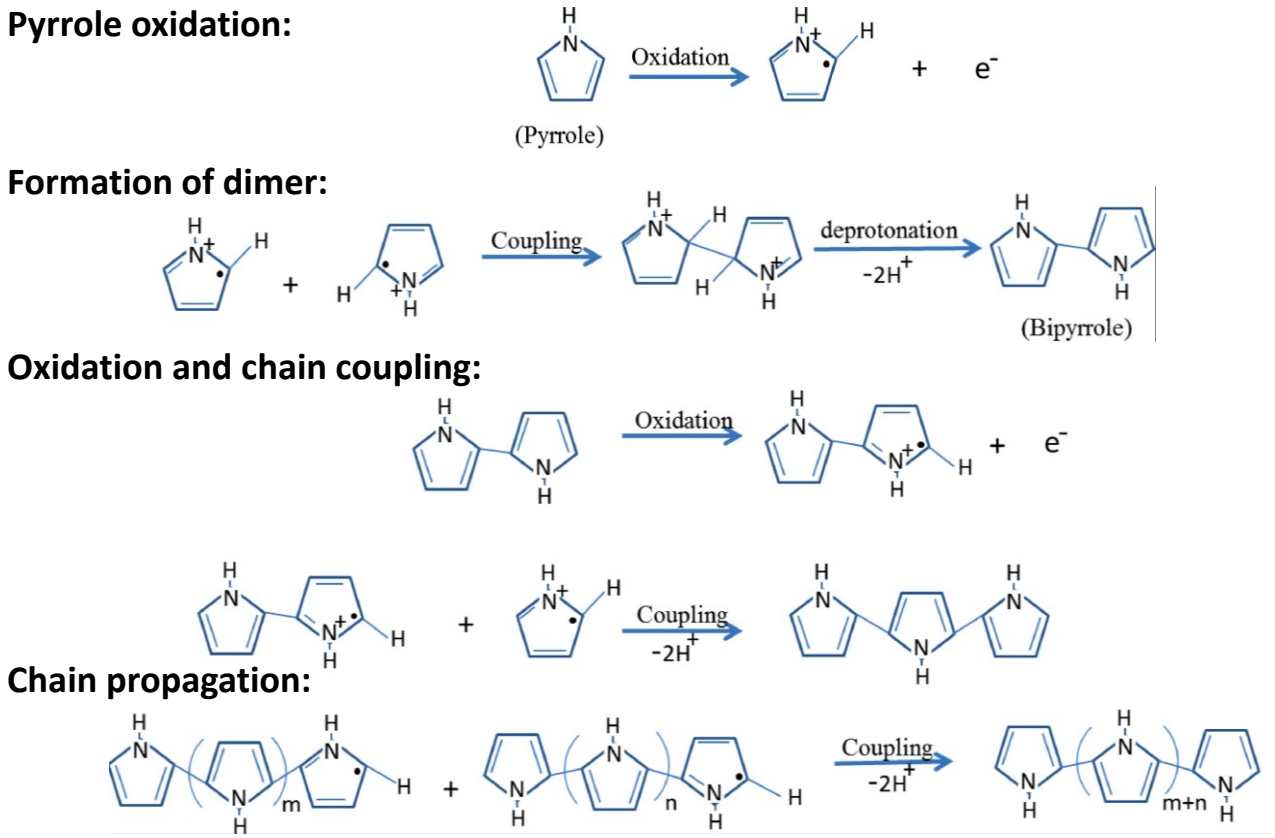

Figure 2.7 Mechanism of chemical oxidative polymerisation of PPy. Adapted from Tan *et.al.,* 2013 and Choudhary et.al, 2020.[143, 150]

2.4.1.2 Electrochemical polymerisation of PPy

Electrochemical polymerisation route is one step, facile and reproducible approach which allow to modify the structure, quantities and properties of PPy by altering electrolyte type, solvent concentration, type of applied potential regime and electrodeposited time.[151, 152] Therefore, it is an effective technique to produce PPy film on substrate without any binder.[153] During electrochemical deposition, pyrrole monomers are dissolved in the solvent which contained anodic doping salt, then pyrrole is oxidised on the surface of working electrode at anodic potential (oxidation potential). The process of polymerisation is as follows: pyrrole monomers are oxidised to form dipyrrole, then the oxidation, coupling, and deprotonation repeatedly carries on to form PPy.[143] The dopants are linked to the polymer chains by counterbalancing the charges on the stoichiometric levels. The dopant types can be the main influence on morphology, electrical conductivity and electrochemical performance of the resulting polymers.[154] There are various electropolymerisation methods for synthesising PPy which can be categorised into 3 types: cyclic voltammetry (CV), galvanostatic (GS), and

potentiostatic (PS) deposition. In direct current electrodeposition, GS and PS, the continuous deposition from using constant potential or current leads to the growth of existing nuclei instead of producing new nucleation sites leading to polymeric aggregation and high electrode resistances because of poor interconnection between conducting structures and accessible polymer, often blocking electrolyte channels at the outer surface and not forming a conformal coating of polymer. Additionally, the hydrogen evolution reaction (HER) is also reported to compete along with the deposition which influences the current efficiency and electrodeposited film properties. Compared with GS and PS deposition approaches, pulse polymerisation can be adjusted by electrodeposition period and resting period, applied current, potential and pulse cycles to make pyrrole monomers continually polymerised into PPy on new active sites, and meanwhile allow newly-formed PPy chain experiencing structural rearrangement to improve its structural stability and electrochemical activity.[147, 155] Note, the electrodeposition period and resting period need to be optimised as electrodeposition period relates to the polymerisation rate and the density of defects resulting in the effect in specific capacitance; too short resting period may lead to the agglomeration of existed nuclei polymer. [156, 157]

2.4.2 Hybridised PPy/CNT composite for supercapacitors

Due to their ability of forming stable, highly conductive, chemical stability, CNTs have attracted interest to be used as support and substrates for PPy supercapacitors. In recent years, various reports have shown the increase in the electrochemical performance of PPy by hybridisation with CNTs. For example, PPy/SWCNT electrode was synthesised and reported a promising capacitance at 265 F/g which gives rise to an increase of the specific capacitance and reducing the internal resistance compared to pristine PPy.[158] Additionally, hybrid structures comprising PPy and CNTs also report to alleviate volume swelling/de-swelling of PPy during charging and discharging, improving the supercapacitors cyclic stability. Core-shell MWCNT/PPy with inhomogeneous structures via an in-situ interfacial polymerisation route showed more ordered chain packing and more expanded molecular conformations than pure PPy due to the composite obtained better electrical conductivity.[159] Another example is an electrodeposited PPy/CNT electrode which shows the improvement of both mechanical properties and electrochemical performance. This is because the uniformly coated PPy on the SWCNTs increased the active sites on PPy chains.[158] For comparison on the cyclic stability,

PPy/CNT composite also shows the better capacitance retention when compared with PPy based supercapacitor. All-solid-state supercapacitors assembled with the electrodes showed outstanding flexibility and long cycling life which retained 95% of the capacitance after 10,000 cycles due to the better conjugated structure of PPy chains on CNT substrate, leading to higher reversibility of redox reaction.[160] To further study the influence of CNTs length on hybridised PPy/CNT composites, short and long CNTs were chosen to hybridise with PPy with the same procedure. The electrochemical performance of PPy based electrodes was prominently improved with the addition of both types of CNTs. The long CNT integrated electrode showed considerable superior capacitive behaviour and cycling stability due to the core-shell nanostructure, porous structure and interconnect conductive nano-network on account of incorporation of abundant of long CNTs.[161] In conclusion, CNTs are an appropriate modifier for PPy based electrode in order to improve electrical conductivity, mechanical properties and electrochemical performance because combining PPy with CNTs will combine pseudocapacitive behaviour of PPy and fast charge storage ability of CNTs together. However, the distribution and amount of PPy on CNT substrate need to be optimised due to access of PPy can cause the higher internal resistance and also obstruct the ion diffusion pathway which leads to poor power density.

3. Characterisation techniques and materials

The characterisation is an important key to get insight into a material's properties and structure. In this chapter, various characterisation techniques have been applied to characterise the morphology, physical properties, mechanical properties and electrochemical properties of as-synthesised materials and the electrochemical performance of as-fabricated supercapacitors. Scanning electron microscopy (SEM), Fourier transform - infrared spectroscopy (FT-IR), thermogravimetric analysis (TGA), X-ray photoelectron spectroscopy (XPS), Brunauer-Emmett-Teller (BET) surface area analysis, Raman spectroscopy and 4 probe measurement were applied to provide the morphological and physical properties of the as-synthesised materials. While cyclic voltammetry (CV), electrochemical impedance spectroscopy (EIS) and galvanostatic charge discharge (GCD) were used for the electrochemical characterisation. The tensile measurements also employed here to investigate mechanical properties. Additionally, the nanotubide buckypaper processing and the electrodeposition technique such as chronoamperometry and pulse potentiostatic deposition were also described here in order to provide more understanding on materials synthesise process.

3.1 Nanotubide buckypaper processing

3.1.1 Centrifugation

Centrifugation is a mechanical process where a centrifugal force is applied to separate particles from a heterogeneous mixture. The correlation between their size, shape, density of the particles, the rotational speed and the medium viscosity are used to achieve separation of substances.[162] To accelerate particle sedimentation, the applied centrifugal force is much larger than the simple gravitational force to allow separation of a substance occur faster than it does naturally. The rotational speed is monitored by the angular velocity and generally expressed in revolution per minute (RPM) or acceleration expressed as g where the conversion between RPM and g depend on the radius of the centrifuge rotor. Centrifugation is a useful technique for purifying and separating SWCNTs from nanotubide solution as it removes impurities and separates SWCNT bundles according to their size and acceleration.

Centrifugation carried out in this work was performed using a Sigma 2–16K centrifuge (Sigma 12139-H rotor, fixed bucket), with the acceleration set at 10000 g for 30 mins at room temperature. The nanotubide mixture was prepared inside the glovebox by transferring the solution to fluorinated ethylene propylene (FEP) centrifuge tubes and the screw caps were additionally sealed by wrapping with polytetrafluoroethylene (PTFE) tape to maintain the inert atmosphere inside the centrifuge tubes.

3.1.2 Ultrasonication in bath

Ultrasonication in bath is usually performed by submerging the vial of sample into a water bath then applying ultrasonic vibration to agitate the particles in the sample. The ultrasonic vibration creates liquid bubbles (cavities) and generate an intense shock wave in the surrounding liquid which can affect both physical and chemical properties such as breaking chemical bonds and improving the dispersion in the solution.[163] The sonication of SWCNT solution is usually used for overcoming the Van der Waals force, individualising SWCNT bundles and inducing the rupture of the aggregates, however, the intense sonication can also damage SWCNT framework and introduce defects to the structure.[164] Therefore, the length of sonication process has to be controlled carefully. In this work, an ultrasonication bath (VWR ltd. 35W) was used for 2 h to disperse SWCNT in DMAc solution for preparing a control SWCNT buckypaper.

3.2 Morphological characterisation

3.2.1 Scanning electron microscopy (SEM)

Scanning electron microscopy produces detailed topological images of a sample by scanning the surface with a focused beam of electrons. To image a material's microstructure, the electron beam emitted from the cathode tip is accelerated and focused by the anode and magnetic lens, respectively. The electrons will penetrate and interact with sample surface then the backscattered and the secondary electrons (SE) are produced. [165] The beam is normally scanned throughout the sample in a raster scan pattern and produced a signal which is naturally processed in a detailed digital image. The signal from SE is likely to be highly localised at the point of the primary electron beam generating a resolution of below 1 nm, in the best cases. For backscattered electrons (BSE), the beam electrons are reflected from the

sample by elastic scattering. BSE have much higher energy than SEs and emerge from deeper locations within the specimen. BSE images can provide compositional information but at lower resolution than SE images. SEM image contains surface information, including topography, material, and local surface charge. These three factors significantly affect the SE emission.[166] SEM samples must fit on the specimen stage and be sufficiently electrical conductive at least on the surface to prevent the accumulation of electrostatic charge. Carbon nanomaterials, especially SWCNTs, are highly conductive and do not need coating. Therefore, SEM directly visualises the morphology and aggregation state.[166] The SEM images of the as-synthesised materials in this Thesis were collected using a Sigma 300 (Carl Zeiss AG). The samples were analysed with an InLens detector, using an accelerating voltage of 5 keV, 30 µm standard aperture and 4.5 mm working distance due to it provide the sharpest images at high definition (52 KX) for nanotubide buckypapers. SEM samples were dried at 100 °C overnight under vacuum to remove humidity and then fixed on aluminium (Al) stubs using carbon tape (Agar Scientific Ltd., Essex, UK).

3.2.2 Fourier transform - infrared spectroscopy (FT-IR)

Fourier transform - infrared spectroscopy (FT-IR) probes the vibration of molecules through the absorption, emission and scattering of infrared radiation. [167] FT instruments accelerate data collection by deducing the absorbance spectrum from an interferogram obtained from broad band illumination. [168] The FT-IR spectrum is usually reported with typical wavenumbers spanning between 400-4000 cm^{-1} and used for quick identification of the functional groups present.[169] The general regions of the infrared spectrum in various types of vibrational bands are outlined in the following Figure 3.1. The section above the dash line in blue color refers to the stretching vibrations, and the green colored band below the dash line describes the bending vibrations. The complexity of infrared spectra between 1450 and 600 cm^{-1} region is commonly called the fingerprint region because of the unique pattern is found in each material. Absorption bands in the 4000 to 1450 cm^{-1} region are generally due to the stretching vibrations of diatomic units, which are named the group frequency region.[170]

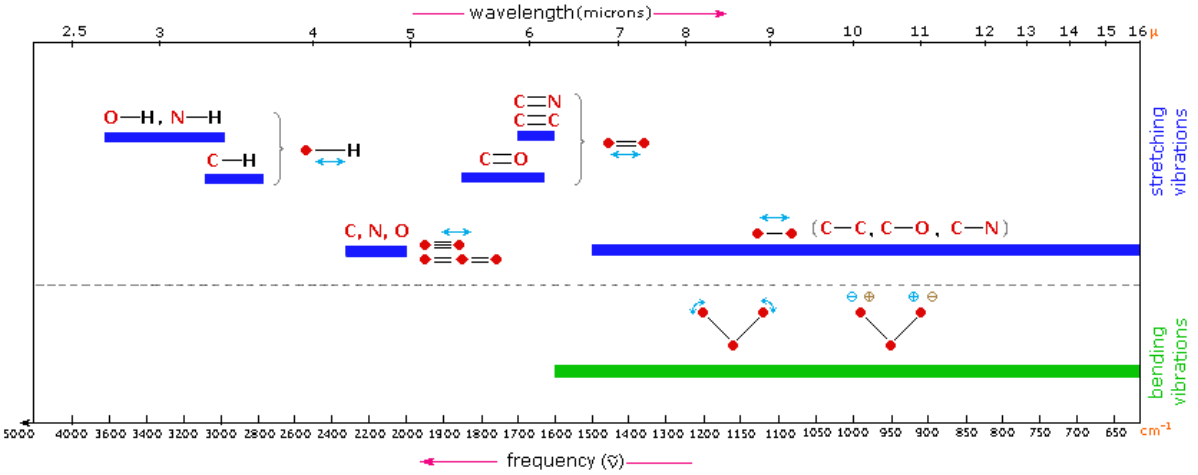

Figure 3.1 List of main IR spectroscopy bands. Reproduced from:

https://www2.chemistry.msu.edu/faculty/reusch/virttxtjml/spectrpy/infrared/infrared.htm.

3.2.3 Thermogravimetric analysis (TGA)

TGA is an analytical technique used for determining the mass change of a sample as a function of temperature, for example to assess hydration, purity, oxidation temperature, thermal decomposition and etc.[171] Typically, the specimen will be measured in air or inert atmosphere such as nitrogen, helium, or argon. Materials are inserted into a furnace chamber with a controlled heating temperature ramp and gas flow rate, although isothermal measurements are also possible. TGA is useful technique to chracterise SWCNTs as it provides the information on carbon/metal catalyst content, kinetics of decomposition, thermal stability and graphitic quality, in bulk samples without requiring special preparation.[172, 173] Thermal stability of as-received SWCNT can be investigated by heating at a constant rate under an inert atmosphere such as N_2, where no significant degradation occurs or using a temperature ramp under air, which causes the oxidation of the samples at medium-high temperatures (400-900°C). However, the mass loss due to carbon decomposition may be superimposed on the mass gain due to catalyst oxidation. The metal catalyst residue can be found in the form of oxidised derivatives (such as Fe_2O_3 for SWCNTs), from which the original metal content can be calculated.[101] In this Thesis, TGA was performed on a Mettler Toledo TGA/DSC1 with lidded 70 µL alumina pans, manually removing a premeasured background. For the measurement in this work, the samples were fixed at 1 mg for accuracy and repeatability. The samples were heated from 30 to 100°C at 45 °C/min before holding for 1 hr

at 100°C (to remove residual solvents), then ramped at 10 °C/min to 800 °C in a flow of 60 mL/min of N_2 to study the decomposition of DIB cross-linker which occur roughly around 400°C and the temperature higher than 800 °C can quantify the amount of PPy content in nanotubide buckypaper where this information will discuss further in 5.3.1 and 6.41 respectively.

3.2.4 X-ray photoelectron spectroscopy (XPS)

XPS is a technique for evaluating the surface chemistry of materials. XPS can provide the information about the elemental composition, chemical state and electrical state of the atoms that form a specific material. XPS spectra are acquired using photons to penetrate the specimen surface, which leads to atom ionisation and feature core-level photoemission effect. Every material has characteristic peaks featuring the binding energy associated with a core atomic orbital. The shape and peak position can be used for determining the chemical state of the elements forming the specimen and the peak shift may indicate a change in the oxidation state of material.[174] The excitation of sample surface in an ultrahigh vacuum (UHV, ~ $1.3x10^{-9}$ mbar) will have sufficient energy to be ionized and escape into the surrounding vacuum then its kinetic energy is analysed. The number of electrons detected is related to the sampling volume, thus the atomic percentages can be derived. The sampling depth of XPS is normally taken at 3 λ, where for Al Kα radiations is between 3 and 10 nm.[175] All XPS spectra in this study were recorded using a K-alpha$^+$ XPS spectrometer equipped with a MXR3 Al K_α monochromated X-ray source ($h\nu$ = 1486.6 eV). X-ray gun power was set to 72 W (6 mA and 12 kV). Charge compensation was achieved using the FG03 flood gun using a combination of low energy electrons and the ion flood source. Samples were etched using the standard EX06 argon ion source using 500 V accelerating voltage and 1 µA ion gun current. Survey scans were acquired using 200 eV pass energy, 1 eV step size and 100 ms (50 ms x 2 scans) dwell times. High-resolution spectra (C 1*s*, and O 1*s*) were acquired using 20 eV pass energy, 0.1 eV step size and 1 second (50ms x 20 scans = 1000 ms) dwell times. Samples were prepared by pressing the sample onto double side sticky carbon-based tape. Pressure during the measurement of XPS spectra was ≤ 1×10^{-8} mbar. Thermo Avantage software was used for data interpretation. Casa XPS software (version 2.4.16) was utilised to process the data. After subtracting the baseline using the Shirley or two point linear background type, the

quantification analysis was then carried out. All XPS spectra were charge corrected by referencing the fitted contribution of C-C graphitic like carbon in the C 1*s* signal 284.5 eV.

3.2.5 Brunauer-Emmett-Teller (BET) surface area analysis

BET is a specific surface area measurement technique. The method consists of measuring the amount of gas (usually N_2) molecules adsorbed on the material across a wide range of pressure and constant temperature using liquid nitrogen (-196 °C). [176] The process of adsorption can be physical or chemical. The physical adsorption (physisorption), which is caused by Van de Waals from adsorbate (gas), is used to measure surface area and porosity. While chemical adsorption, which is from the reaction between the solid specimen and adsorbate (gas), is used to measure the number of surface active sites which promote a specified catalytic reaction.[177] Various parameters such as temperature, pressure and characteristics of materials specimen can influence BET measurement. The BET assumes that the adsorption of gas molecules can occur randomly on materials surface. Absence of interactions between adsorbed molecules, and random probability of occupation of adsorption sites are also assumed.[178] The gas molecules are held onto the surface by gas–solid forces. While multilayer adsorption shows more than one layer of gas molecules are formed, but may not all of layers are in contact with surface layer of adsorbent. [179, 180] The general BET multi-points measurement consists of two stages which are the derivation of the monolayer capacity (n_m) from the physisorption isotherm where the BET equation is defined as follow.[180, 181]

$$\frac{P/P_0}{n(1-\frac{P}{P_0})} = \frac{1}{n_m C} + \frac{C-1}{n_m C}\left(\frac{P}{P_0}\right) \qquad \text{Equation 3.1}$$

Where n is the adsorbed amount of gas at the relative pressure P/P_0 and n_m is the monolayer capacity of the adsorbed gas. P is the pressure and P_0 is the saturation pressure of materials specimen being adsorbed at the adsorption temperature. C is an empirical constant exponentially associated to the energy of adsorbent-adsorbate interaction. From the parameter *C*, the shape of an isotherm in the BET range can be obtained. There are six different types of BET isotherms which are shown in Figure 3.2a. In general, type I isotherm is typical for microporous solids with relatively small surface area where type I(a) is for materials with micropore below 1 nm and Type I(b) is for materials with wider micropore but

not wider than 2.5 nm. Type II isotherm is typical for materials that are macro-porous or nonporous where point B on isotherm is related to the mono layer coverage. Type III is presented when the adsorbent and adsorbate have weak interaction. Type IV is the most common isotherm for mesoporous materials; Type IV isotherms show a hysteresis loop (Figure 3.2b), associated with capillary condensation while Type IV(b) is associated with smaller pores (less than 4 nm). In theory, Type IV (b) isotherms are also given by conical and tubular mesopores which are closed at the tapered end. Type V is not common and at higher relative pressure, a hysteresis loop can be detected as molecular clustering is followed by the filling of pores. Type VI isotherm is standard for multilayer adsorption of materials with highly uniform nonporous surfaces. The isotherm is in stepwise curve shape, which depends on the temperature, materials, and the gas.[177, 180, 181]

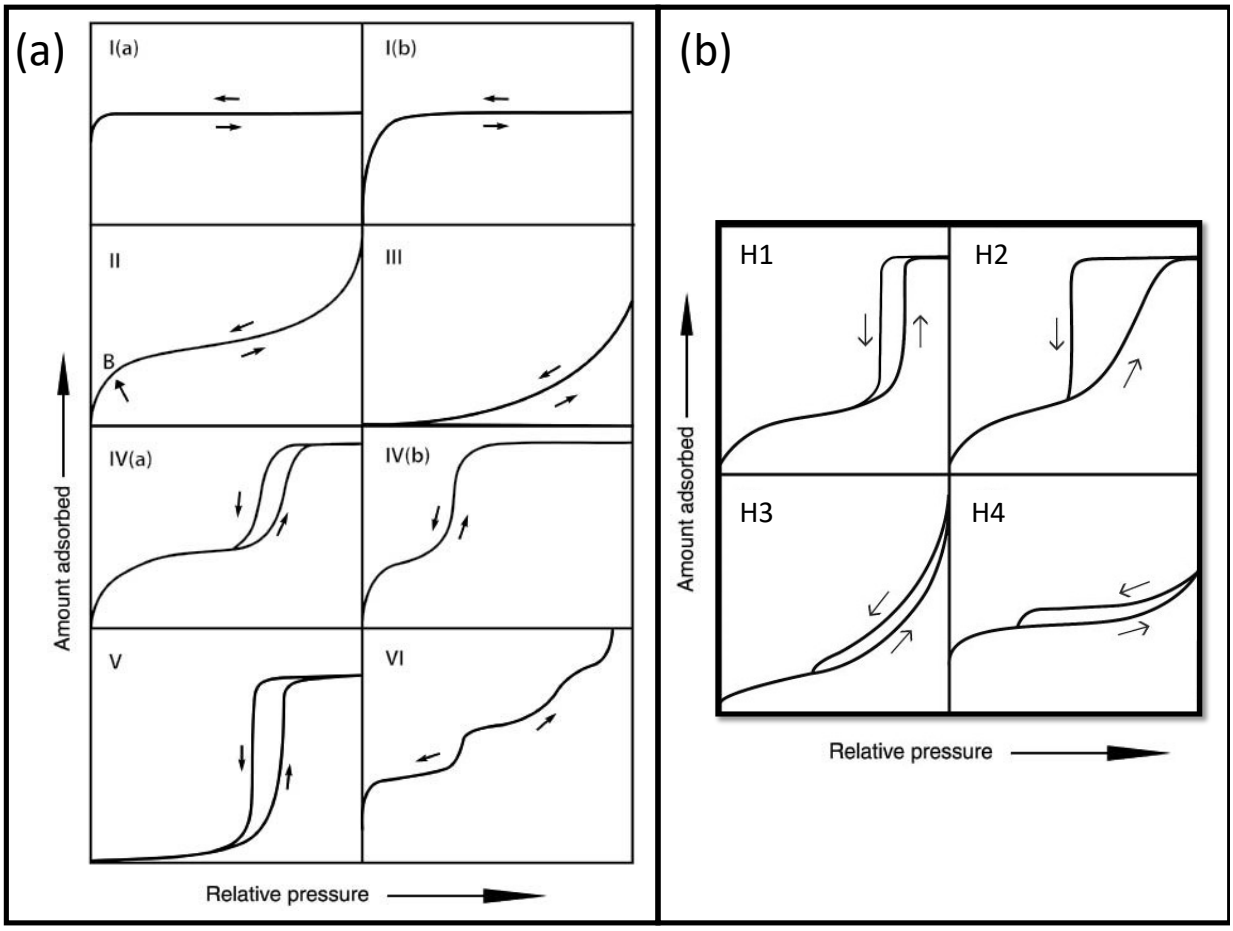

Figure 3.2 (a) Types of BET adsorption isotherms and (b) classifications of hysteresis loops occurring usually for type IV isotherms according to IUPAC classification. Adapted from Gruyter *et. al.,* 2015. [181]

To calculate the specific surface area of the sample from a BET measurement, the applicability of the fitting is limited to only some part of the isotherm and relative pressure is rarely extended above P/P_0 ~ 0.30. The correlation coefficient is acceptable when it is not lower than 0.995 for accurate measurement. The total surface can be calculated by the following equation.

$$\boldsymbol{S = \frac{n_m N_a \alpha_{ads}}{M}} \qquad \text{Equation 3.2}$$

where n_m is the monolayer capacity of the adsorbed gas and N_A is the Avogadro number. α_{ads} is the cross-sectional area of the adsorbate (0.162 nm^2 for N_2) and M is the molecular weight of the adsorbate.

In this study, the mass of BET sample was fixed at 21 mg (3 pieces of as-synthesised buckypaper) and the sample were outgassed in the BET sample tube using a SmartPrep degasser (Tristar), at 100 °C under nitrogen for 12 hours, in order to remove adsorbed atmospheric moisture, followed by quick transfer to the surface area analyser. N_2 was selected as the gas adsorption because it is sufficient to measure the total pore volume of the nanotubide buckypaper and sonicated buckypapers, which are expected to have the various pore size distribution. N_2 with 0 °C and the relative pressure range (0.02-0.3) can measure the variety of pore size including super-micropores and lower mesoporosity. Whereas CO_2, which has to measure with the higher temperature and much lower relative pressure range, can only measure the narrow microporosity.[182, 183] Additionally, we refrained from using CO_2 in the measurement is also because the oxygen functional groups from CO_2 may graft on the buckypaper surface and it can effect the sample properties if we reuse the samples for other characterisation such as electrochemical characterisation. N_2 adsorption-desorption analyses were measured using a Micromeritics Tristar 3000 analyser and calculated according to BET equation from the adsorption isotherm in P/P_0 range between 0.02 and 0.3. The pore-size distribution of the samples can be estimated from the desorption branch using the Barrett, Joyner, and Halenda (BJH) method, which is based on a modified version of the Kelvin equation.[184]

3.2.6 Raman spectroscopy

Raman spectroscopy[185] detects the vibrational and rotational modes similarly to infrared spectroscopy, but with a different excitation mode and selection rules. Raman spectroscopy relies on inelastic scattering of light which is associated in three events. Firstly, the absorption of an optical photon that excites an electron from the valence to conduction energy band. Secondly, the scattering of the excited electron through emission/adsorption of a phonon where the third one is the relaxation of the electron to the valence band via emission of a photon. [186]

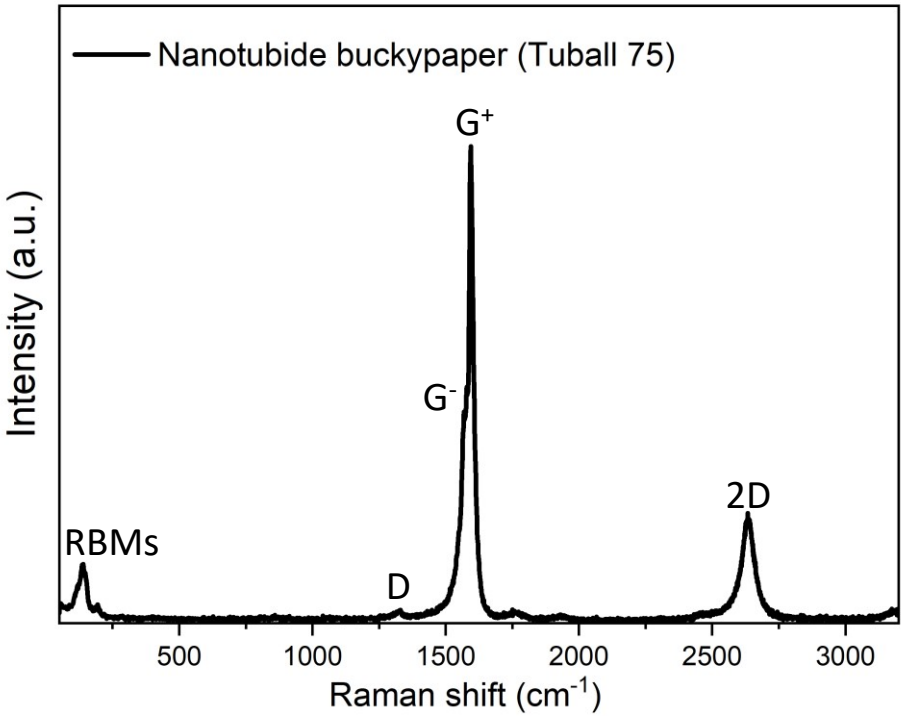

Figure 3.3 Raman spectra of nanotubide buckypaper (Tuball 75) with the characteristic peaks highlighted.

The Raman spectrum of SWCNTs (Figure 3.3) presents some characteristic features which can be defined into the Radial Breathing Modes (RBMs), the D band, 2D and two main G mode signals name G^+ and G^- which are described in detail below.

- Radial Breathing Modes (RBMs) are unique bond-stretching out of plane phonon modes which appear only in carbon nanotubes. The RBMs show the characteristic of all the carbon atoms moving coherently in the radical direction (*i.e.* the nanotubes are "breathing") in the frequency range around 100-500 cm^{-1}.[187] For SWCNTs, the

frequency of RBMs is correlated to the tube diameter intensity and chirality through the peak position. RBMs frequency is inversely proportional to the tube diameter which is expressed as the equation below.[188]

$$\omega_{RBM} = \frac{C}{d_t} + B \qquad \text{Equation 3.3}$$

where C is 248 cm^{-1} for isolated SWCNTs on SiO_2 substrate, d_t is nanotubes diameter and B is 0 for isolated SWCNTs.[189] B is approximately 10 cm^{-1} for nanotubes diameters of 1.5 ± 0.2 nm and depending on the bundling state.[188] The relation between RBM frequency and SWCNT diameter may be not accurate if the diameter is less than 1 nm since a dependence of frequency on nanotube chirality may increase from lattice distortions. The simplest way to determine SWCNT diameter can be estimate through the Kataura plot (Figure 3.4). However, an accurate position of the chirality needs to determine the effect of frequency shifting due to dielectric effects.[190]

- D mode (sp^3) is a disorder induced band at the frequency range from 1280-1600 cm^{-1}. The D band is related to the disorder of carbon nanotube lattice induced by the presence of defects on C sp^2 framework. The D band is dispersive (the phonon frequency changes from the change of excitation laser energy). The intensity of D band is commonly used to investigate the defectiveness of SWCNTs by dividing intensity of D band with the intensity of G band referred as I_D/I_G. I_D/I_G constitutes an effective parameter which can indicate the introduction of sp^3 or other defects contributes from impurities, short nanotubes, synthesis process and etc.[187] For example, I_D/I_G of SWCNT film decreases after etching the film with ethanol under high temperature due to OH radical decomposed from the ethanol.[191] The reduction in I_D/I_G along with the increase of the temperature indicating an increase in crystallinity of the films.[192]

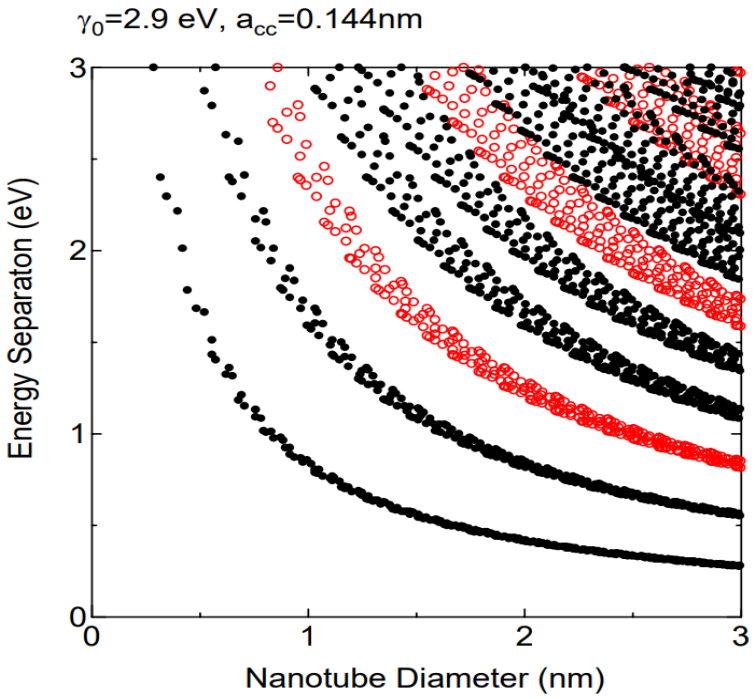

Figure 3.4 Kataura plot calculated with carbon-carbon interaction at γ_0 = 2.9 eV, bond length a_{cc} = 0.144 nm. [193]

- G mode (sp^2) is a stretching phonon mode between the two dissimilar carbon atoms A and B in the unit cell which is placed at the frequency ~ 1582 cm^{-1}. The G band is a general characteristic feature in graphitic materials and usually the largest feature of CNTs. Unlike the D band, this G band is not dispersive and can be used to probe the modification of the carbon structure and differentiate the different type of nanocarbons. For SWCNTs, G-band is composed of several peaks (up to 6) due to the phonon wave vector confinement along the SWCNTs circumferential direction and because of the symmetry-breaking effects associated with SWCNTs curvature.[187] The two main spectrum of G band are G^+ (~1590 cm^{-1})and G^- (~1570 cm^{-1}) where G^+ occurs from the vibrations of the carbon atoms longitudinally to SWCNT axis and G^- is caused by the circumferential vibrations.
- 2D (or G') is the characteristic frequency that arises at double the frequency position of the D mode. The 2D mode is dispersive, like the D mode, and strongly dependent on the perturbations of electronic structure of graphitic materials. The 2D mode can therefore be used to identify specific nanocarbons by characterised via unique

features depending on the structure of the material. For SWCNTs, the 2D band feature is correlated to the chirality of the tube due to the curvature effect.[194]

In this thesis, Raman spectra were performed using a Renishaw Invia confocal Raman spectrometer equipped with excitation laser source in a backscattered geometry, calibrated with silicon and utilising a 1800 nm grating. Statistical Raman was performed in StreamLine acquisition mode at ca. 10 µm intervals on an area of ca. 500 μm^2 with spectra between 500 - 1000 cm^{-1} using 1 % laser power, 10 s of exposure time with a laser intensity of 3.2 mW and grating 1800 l/mm. The mapping measurements were carried out over at least 3 different areas to reduce the effect of sample heterogeneity. WiRe (v4.1, build 4308) software was used to calculate I_D/I_G ratios after automatic background subtraction, for fitting the D and G^+ peaks and for plotting the ratio of D peak maximum to G^+ peak maximum. Samples mainly consisting of SWCNT buckypaper in the size of 1 cm^2 were flattened between two glass slides.

3.2.7 Electrical conductivity via 4 probe with identically space needles

Electrical conductivity (σ) is the most fundamental physical property used to classify metals, semiconductors and insulators.[195] The conductivity is important, here, as it directly influences the internal resistance, the electrochemical capacitance, capacitance retention and power density of the energy storage devices. In this Thesis, σ of the as-synthesised buckypapers are calculated from the sheet resistance (R_s) using a four probe measurement. A four probe is an instrument for measuring R_s and σ of thin films by applying current through outer probes and determining the voltage through inner probes.[196] The diameter of electrode should be four times larger than needle spacing and the thickness of the electrode had to be less than 40% of distance between probes. The Jandel four-point probes used in this project has 1 mm needle spacing with 300 µm diameter. The apparatus is connected with Keysight 34410A digital multimeter and R_s can be calculated through equation below.

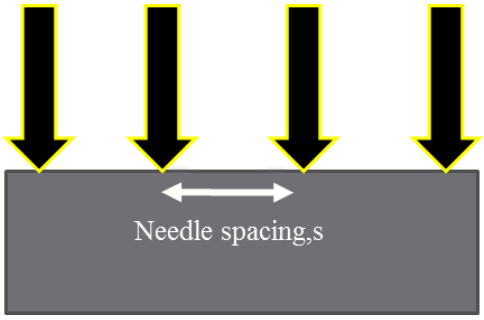

Figure 3.5 Schematic of four probe measurement.

$$R_s = \frac{\pi \cdot V}{ln2 \cdot I} \quad \text{Equation 3.4}$$

Where R_s is sheet resistance (Ω/□) and $\frac{V}{I}$ is measured resistance (Ω)

Electrical resistivity (e_r) and the conductivity (σ, S/m) can be calculated via the following equation.

$$e_r = R_s t \quad \text{Equation 3.5}$$

$$\sigma = \frac{1}{e_r} \quad \text{Equation 3.6}$$

Where t is thickness (m) and e_r is in Ω-m unit.

3.3 Electrochemical characterisation

Electrochemical analysis is a measurement of electrical quantities (current, potential and/or charges) use to study the relation between electrical and chemical properties of electrode materials. The main techniques in electrochemical analysis are potentiometry (measures potential between electrodes), voltammetry (measures current as a function of voltage) and coulometry (measures charge over time). Electrochemistry is relevant to a wide range fields such as energy storage applications, desalination, electrocatalyst, electrochemical sensors and etc.

In this section, the main emphasis particularly focuses on electrochemical measurements for understanding energy storage mechanisms using techniques such as cyclic voltammetry (CV), electrochemical impedance spectroscopy (EIS), chronoamperometry and galvanostatic charge-discharge (GCD).

3.3.1 Three-electrode measurements

Three-electrode measurements are commonly applied for basic electrochemical studies, using a working electrode, reference electrode, and counter electrode within a common electrolyte.

3.3.1.1 Working electrode (WE)

The working electrode represents the electrochemical process under study. The potential of the working electrode is compared to that of a reference electrode whilst measuring the current flowing to/from it. For electrochemical characterisation, the materials -synthesised in this Thesis were used as working electrode. Note, the as-synthesised electrodes were soaked overnight in 1 M H_2SO_4 and **[**EMIM**][**TFSI**]** for aqueous and ionic liquid before doing the electrochemical measurement to ensure that the electrolyte completes filling of the pores.

3.3.1.2 Reference electrode (RE)

The reference electrode provides a stable and well-defined electrochemical potential, against which the potential of the working electrode can be measured or controlled. It is important to fix the distance between working and reference electrodes and reduce the gap between them as much as possible, in order to control and minimise the solution resistance which represents as IR drop (potential drop). Otherwise, the IR drop may affect the intensity of the current and the position of the potential peaks. The high stability of the reference electrode potential is usually reached by employing a redox system with constant (buffered or saturated) concentrations.[197] General REs used in electrochemical measurement are silver-silver chloride electrode (Ag/AgCl), standard hydrogen electrode (SHE) and calomel electrode. The Ag/AgCl is used as reference electrode in this study because it can provide a very stable reference potential with non-toxic component and do not change over time or with temperature. The loss of KCl electrolyte, which is used as electrolyte bridge in the cell also does not change the saturated nature of the solution or the potential.

3.3.1.3 Counter electrode (CE)

The counter electrode (CE) or auxiliary electrode provides the balancing electric current to support whatever electrochemical processes occur at the WE; ideally it should not participate in the electrochemical reactions within the cell in any other way. Therefore, CE is generally made from an inert material such as platinum, gold, graphite or glassy carbon. Importantly, the total surface area of CE must be higher than the area of WE to ensure that the half-reaction occurring at the CE can occur fast enough and not limit the kinetics of electrochemical process at WE as the current is flowing between the WE and CE.[198] In this study, Pt wire is used as CE due to its inertness which can avoid the participates in redox reaction during the electrochemical measurement.

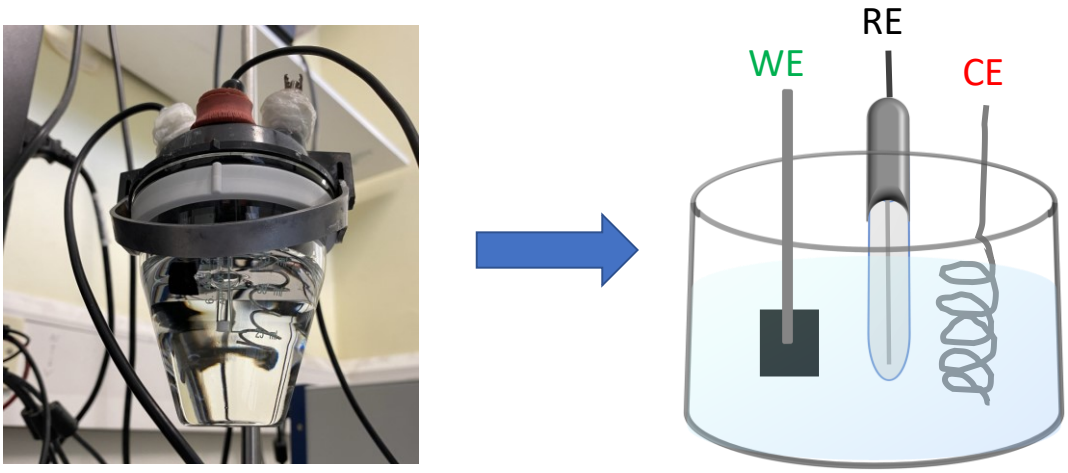

Figure 3.6 Electrochemical cell of three-electrode measurement

3.3.2 Two-electrode measurements

Although three-electrode measurements can provide important details of materials electrode such as the specific electrochemical capacitance and charge storage mechanism between electrode and electrolyte.[199] Assembling and testing a full cell are also important for understanding the potential of the tested material in a fabricated full cell which can provide a more realistic indication of its device performance and be able to compare with the commercial energy storage devices in the market. Two-electrode measurement is the simplest cell set up which is commonly used for testing energy storage devices or conversion devices such as supercapacitors, batteries, fuel cells, photovoltaic panels and etc. In this work, the as-synthesised symmetric and asymmetric devices were measured via two-electrode

measurements. The as-fabricated symmetric device was assembled by sandwiching the separator between SWCNT electrodes in Swagelok cell where Swagelok cell was closed tightly to make sure that all components are contacted to each other and prevent the electrolyte leakage. While the asymmetric devices were fabricated in the pouch cell and sealed by a vacuum sealer due to optimisation of the cell configuration. Note, the fabrication detail of as-fabricated symmetric devices and asymmetric devices will discuss further in the result Section 4.2.6 and 6.2.3 respectively. To evaluate the device performance, working electrode (WE) lead is connected to an electrode and reference (RE) and counter (CE) leads are connected to a second electrode (Figure 3.7). The applied potential is evaluated between two electrodes through the working and counter leads where the counter lead serves two functions. The counter lead can use for completing the circuit allowing charge to flow through the cell, and it can also maintain a constant interfacial potential.[197] The electrochemical evaluation for full cell devices in this work were carried via Cyclic voltammetry (CV), Electrochemical Impedance spectroscopy (EIS) and Galvanostatic charge/discharge (GCD) measurements.

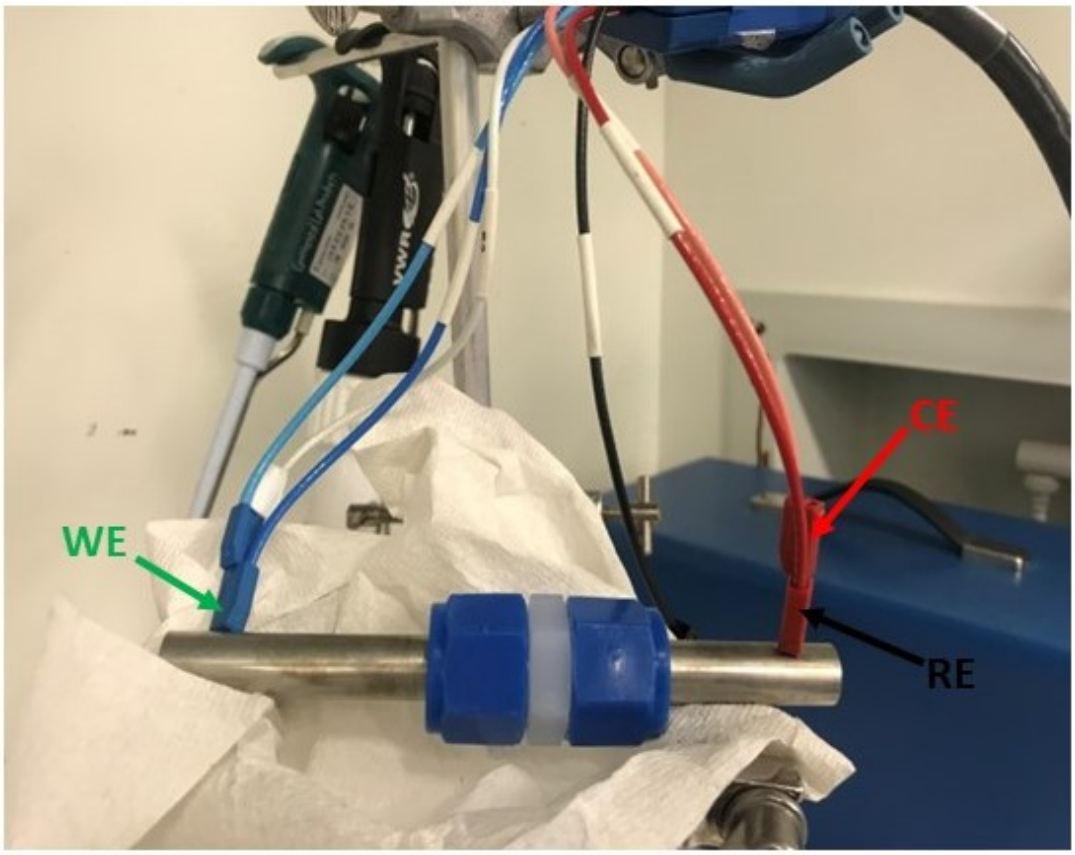

Figure 3.7 Swagelok full cell device for two-electrode measurement

3.3.3 Cyclic voltammetry (CV)

CV is a type of electrochemical measurement for studying electrolytes and materials electrochemical properties. The principle of CV is applied a potential versus time and scan the voltage in one direction and then perform the reverse cycle results in the current as a function of the sweeping voltage of the working electrode. The working electrode voltage will increase with a linear relationship when compares with time.[200] Here, in this work, the CV measurement of the as-synthesised electrodes were evaluated using Gamry Instruments Interface 1000 potentiostat /galvanostat/ZRA, run with Gamry Instruments Framework™ (v.6.24). In three-electrode measurement, Ag/AgCl and Pt rod are used as a reference electrode and a counter electrode respectively. CVs were performed at various scan rates from 10 to 500 mV/s in both 1 M H_2SO_4 and **[**EMIM**][**TFSI**]** as the electrolytes. The applied potential was performed in the stability window of both electrolytes.

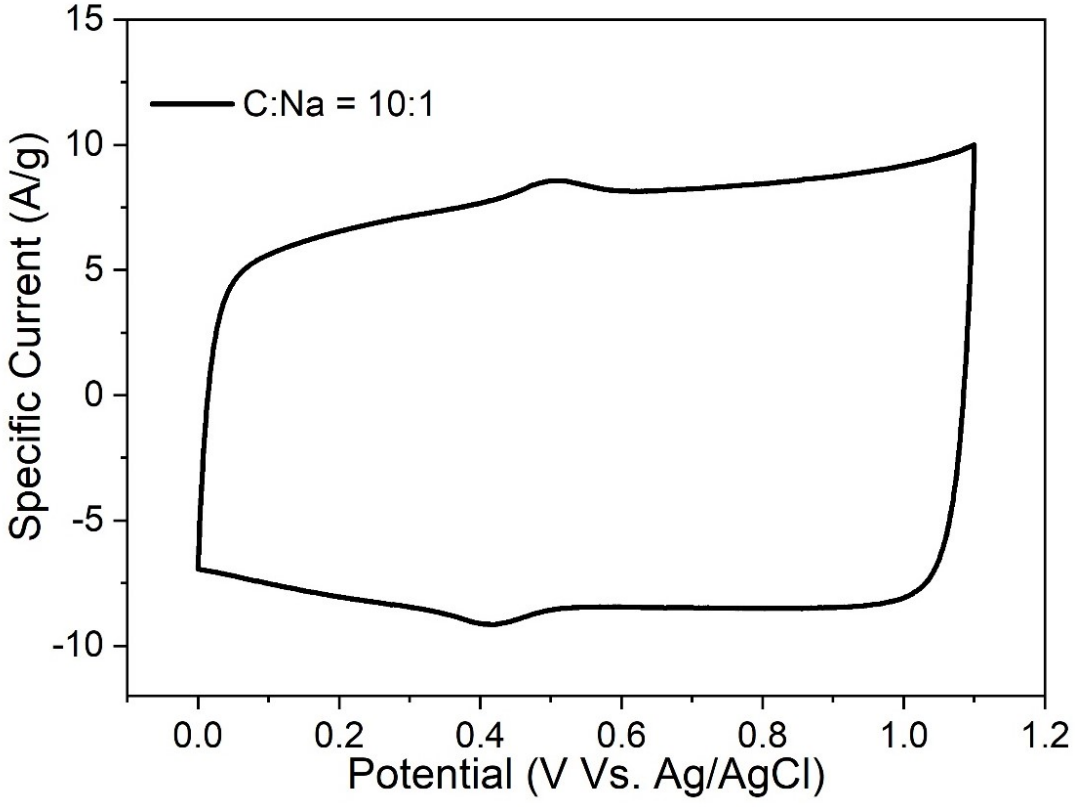

Figure 3.8 CV curve of nanotubide buckypaper in 1 M H_2SO_4

To evaluate the electrochemical performance of as-synthesised materials, the specific capacitance, which is ratio of the amount of electric charge stored in an electrode to a

difference in electric potential, is calculated from CV curves by integrating the area during the cathodic scan according to equation 3.7;

$$C_s = \frac{\int_{V1}^{V2} \mathrm{I(V)dV}}{\nu x \Delta V} \qquad \text{Equation 3.7}$$

Where C_s is specific capacitance, $\int_{V1}^{V2} \mathrm{I(V)dV}$ is area under CV curve in cathodic scan, x is the mass (g) of active materials for calculating gravimetric capacitance and is the volume (cm^3) for calculating volumetric capacitance, ΔV is working potential range(V) and **ν** is scan rate (V/s).

To evaluate the percentage of diffusion controlled and surface controlled contribution, the diffusion controlled and surface controlled contribution fraction at different scan rates can be examined from the equation below;[201, 202]

$$i = k_1 v + k_2 v^{0.5} \qquad \text{Equation 3.8}$$

k_1 and k_2 are alterable parameters determined from the slope and y-axis intercept of the plots between $i(V)$ and v, respectively. Where, $k_1 v$ represents the surface controlled contribution and $k_2 v^{0.5}$ represents the diffusion controlled contribution.

3.3.4 Electrochemical Impedance spectroscopy (EIS)

EIS is an alternative current electrochemical technique, which can be used to chracterise the charge transfer, mass transport and charge storage mechanism at the electrode-electrolyte interface by applying sinusoidal perturbation with frequency and calculating the electrical impedance (Z) response.[203] In this study, EIS here were performed in the range of frequencies from 10 mHz to 100 kHz at 0 V potential and AC amplitude at 10 mV.

$$Z(\omega) = Z' + iZ'' \qquad \text{Equation 3.9}$$

Where Z′ is the real part of impedance (Ω), Z″ is the imaginary part of impedance (Ω) and i is $\sqrt{-1}$.

Normally, the EIS data is displayed in a Nyquist plot where the real part is plotted on x-axis and the imaginary part multiplied by -1 is plotted on y-axis (Figure 3.9). The internal resistance (ESR) relates to the ionic resistance of the electrolyte, resistance of the electrode

material, and contact resistance. ESR can be calculated from the minimum intercept on the x-axis of the Nyquist plot. While the charge transfer resistance (R_{ct}) can be measured from the diameter of the semicircle in the Nyquist plot through the equivalent circuit (inset Figure 3.9). As the equivalent circuit describes and model the electrical and electrochemical properties of electrode materials and their electrochemical interface between electrode and electrolyte.[204] In this work, the Nyquist plots were fitted through Randal's equivalent circuit which comprises with ESR, R_{ct}, C_{dl} (double layer capacitance), Z_W (Warburg element with absorbing boundary condition) and C_L(specific capacitance). [205, 206]

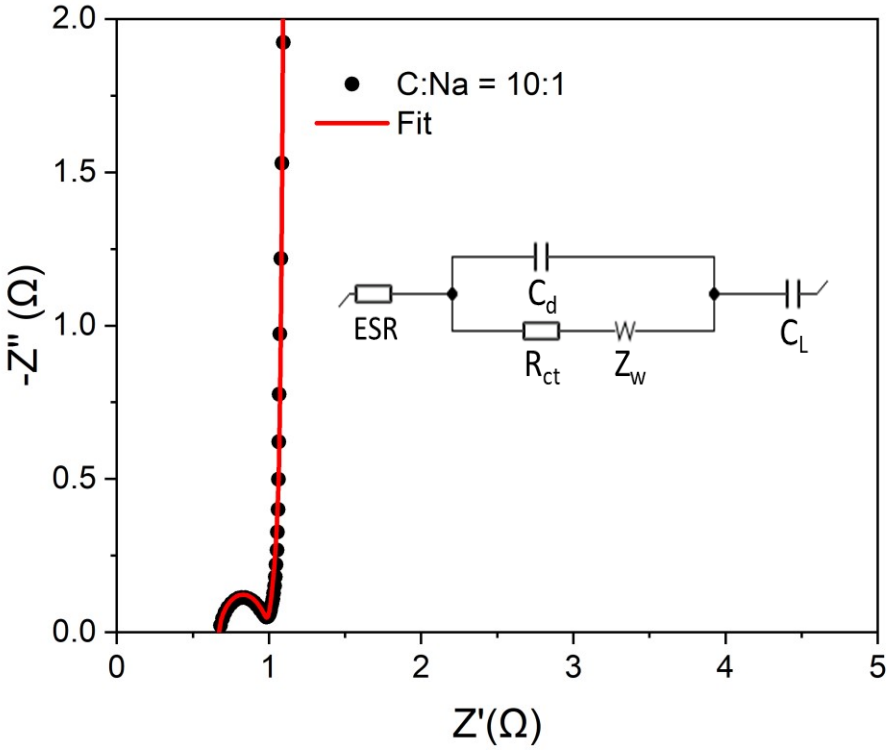

Figure 3.9 Fitted Nyquist plot of nanotubide buckypaper electrode ([C] = 1.5 mg/mL, C:Na=10:1) with inset photograph of equivalent circuit.

Additionally, EIS technique can also be used to examine the power efficiency of supercapacitor through the equation 3.10 as the response of frequency value (f_0) from Bode phase curve is associated with the relaxation time constant (τ_o).[207]

$$\tau_0 = \frac{1}{f_0} \qquad \text{Equation 3.10}$$

Where τ_o is the relaxation time (s) and f_0 is the response of frequency at the maximum point of the energy curve (Hz).

τ_o can define the boundary between the regions of capacitive and resistive behaviours for the supercapacitor. Therefore, it is well known that higher power delivery corresponds to lower (τ_o) values.[201, 208, 209]

3.3.5 Galvanostatic charge/discharge (GCD)

GCD is the standard technique used for testing the performance and cycle life of energy storage devices. In this technique, a constant current is applied between working and counter electrodes forcing the working electrode to move to a more electropositive or electronegative region, in order to force the electrochemical charging and discharging occurs. [210] The charge and discharge are conducted at constant current until a set voltage is reached and a repetitive loop of charging and discharging is called a cycle. In this work, GCD measurements were used to evaluate the as-fabricated device performance and performed at current densities varied from 1 to 100 A/g. Cyclic stability tests (1 – 50,000 cycles) of full cell supercapacitors were completed via the GCD technique applying specific current at 5 A/g.

The specific capacitance of the cell can be determined using the equation below;

$$C_{cell,s} = \frac{I_{GCD}}{x \times \left(\frac{dV}{dt}\right)} \qquad \text{Equation 3.11}$$

Where, C_s is the specific capacitance, I is discharging current (A) and Δt is discharge time (s). x is the mass (g) of whole device or active materials for calculating gravimetric capacitance and is the volume (cm^3) for calculating volumetric capacitance. ΔV is a working potential excluding *iR* drop (V) which can determine from the GCD profile (Figure 3.10).

For evaluating the energy density (E), it can be measured as a quantity per mass or per volume. The stored energy in a capacitor can be calculated by using equation 3.12 while the energy is directly proportional to its capacitance.

$$E_{cell} = i \int V dt \qquad \text{Equation 3.12}$$

The power is defined as the energy per unit time. For calculating power density, capacitors are normally presented as a circuit in series with an external “load” resistance (R). The internal components of the capacitor also contribute the resistance, which is measured by the

equivalent series resistance (ESR). The voltage during discharge is determined by these resistances. The average power density can be calculated through equation 3.13.

$$P_{av} = \frac{E}{t} \qquad \text{Equation 3.13}$$

The maximum power density can be calculated by following the equation below[211]

$$P_{max} = \frac{V_0^2}{4ESR} \qquad \text{Equation 3.14}$$

Where, V_0 is the initial applied voltage (V).

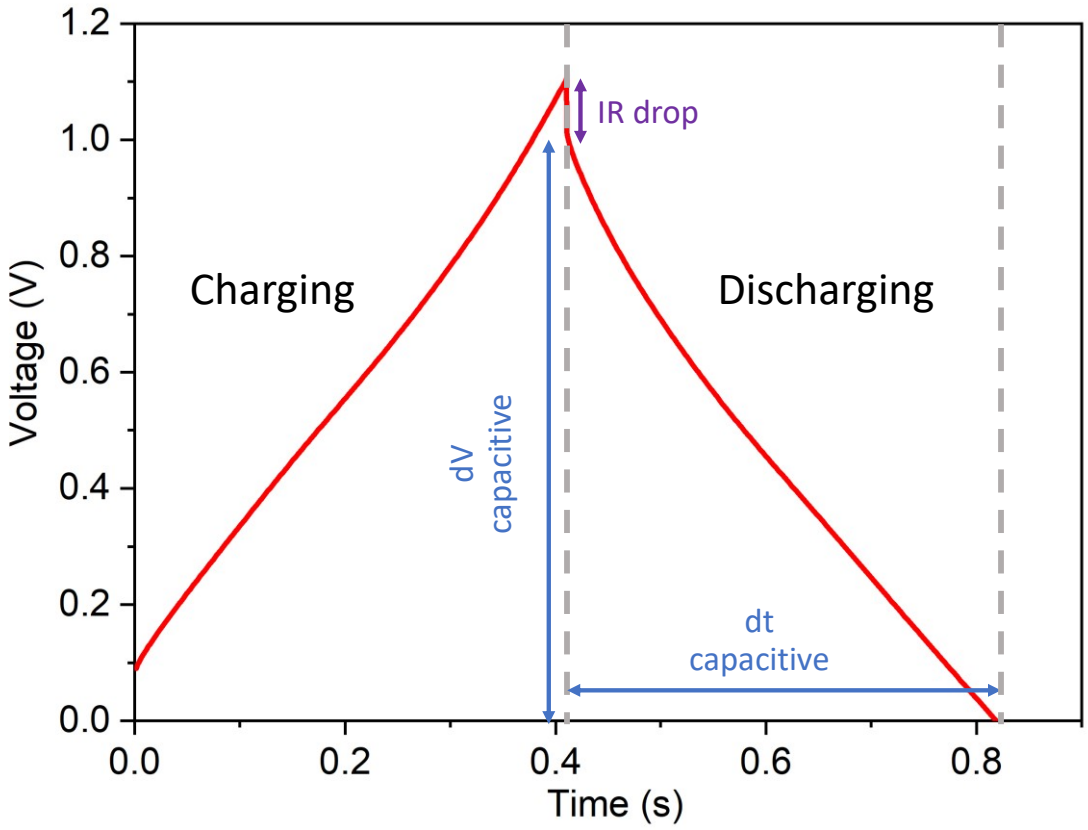

Figure 3.10 A typical galvanostatic charge/discharge profile.

3.3.6 Chronoamperometry (Direct current electrodeposition)

Chronoamperometry is a time-dependent method where a square-wave potential is applied to the working electrode. The current of the electrode, measured as a function of time, fluctuates due to the diffusion of an analyte from the bulk solution toward the sensor surface. Therefore, chronoamperometry can be used to characterise the diffusion controlled

process occurring at an electrode by measuring current–time dependence.[212] This technique can give the advancement on electrodeposition procedure by applying direct constant potential to electrodeposit/coat the desired materials on working electrode(Figure 3.11). The total electrodeposition charge (Q) can be calculated by integrating the area under the curve of the electrodeposition current versus time (Figure 3.12) which can be defined as the equation below.

$$Q = \int_0^t i(t)dt \qquad \text{Equation 3.15}$$

In this work, PPy was electrodeposited on nanotubide buckypaper by applying 0.8 V Vs. Ag/AgCl through a chronoamperometry method for 60 s using Gamry Instruments Interface 1000 potentiostat /galvanostat/ZRA. 0.1 M Pyrrole with 0.5 M H_2SO_4 as electrolyte and 0.1 M Pyrrole with 0.5 M KCl were used as the electrodeposition electrolytes.

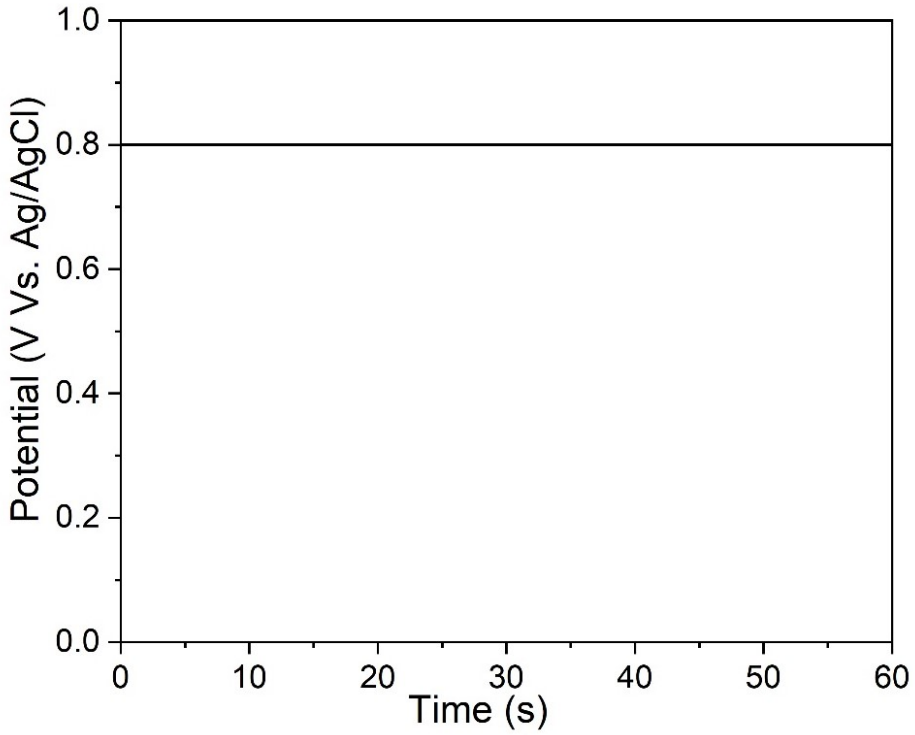

Figure 3.11 Electrodeposition of PPy via constant potential at 0.8 V

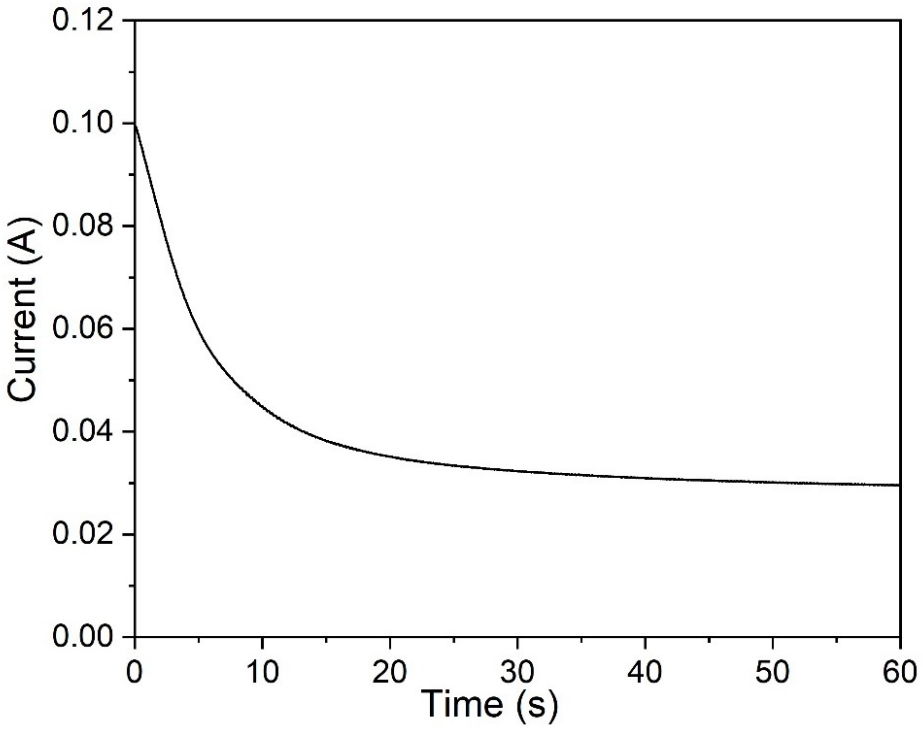

Figure 3.12 Electrodeposition current vs. time of PPy via constant potential at 0.8 V vs. Ag/AgCl.

3.3.7 Pulse potentiostatic electrodeposition

In pulse electrodeposition (PED), current/potential is applied in the form of modulated waves as shown in Figure 3.13. Compared to Chronoamperometry, PED offers additional process control variables such as the sequence of the deposition, applied potential and pulse cycle. The PED processes in this work are a double potential-step deposition where the first step is electrodeposition period (t_{on}) and the second step is resting period (t_{0V}) by applied potential at 0 V vs. Ag/AgCl. The experiments were performed using Gamry Instruments Interface 1000 potentiostat /galvanostat/ZRA. The studies of electrodeposited PPy were carried by varying the applied electrodeposition potential (0.6 to 1.2 V vs. Ag/AgCl), pulse t_{on} (0.1, 1 and 5 s), pulse t_{0V} (1, 10 and 60 s), electrodeposited electrolyte (0.1 M pyrrole 0.5 M H_2SO_4 and 0.1 M pyrrole 0.5 M KCl) and total electrodeposition time (15, 30, 45 and 60 s).

The variation in t_{on} and t_{0V} is expressed using a common parameter known as duty cycle (DC), which is defined by the equation 3.16:

$$DC = \frac{t_{on}}{t_{on}+t_{0V}} \qquad \text{Equation 3.16}$$

The average specific current (J_a) in the pulse electrodeposition is given by;

$$J_a = DC \times J_p \qquad \text{Equation 3.17}$$

Where J_p is the peak specific current.

A very simple diffusion estimate is applied to calculate the spread of pyrrole monomers through the substrate per each pulse cycle. The characteristic diffusion equation (equation 3.18) is applied by assuming the substrate thickness is uniform and consider the motion of particles along one axis only.

$$< x^2 >= 2Dt_p \qquad \text{Equation 3.18}$$

Where x is the diffusive spreading distance of pyrrole monomers in each pulse cycle and t_p is total time per each pulse cycle. D is the diffusion coefficient of pyrrole monomer in aqueous electrolyte, which is equal to 1.25×10^{-5} cm^2/s.[213]

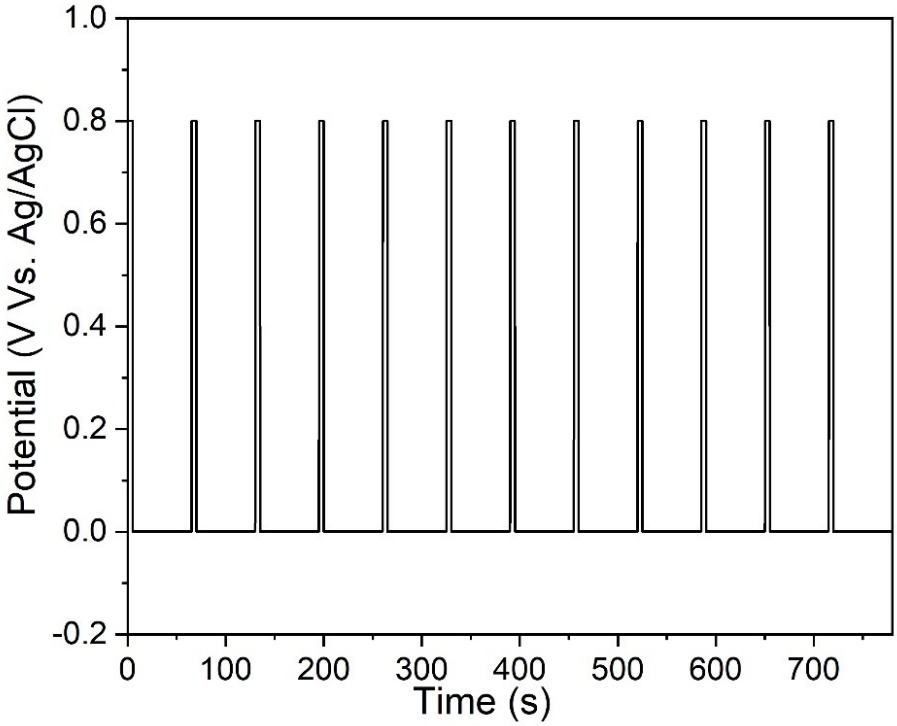

Figure 3.13 Pulse electrodeposition at 0.8 V vs. Ag/AgCl with pulse on 5 s and pulse off 60 s for 12 cycles.

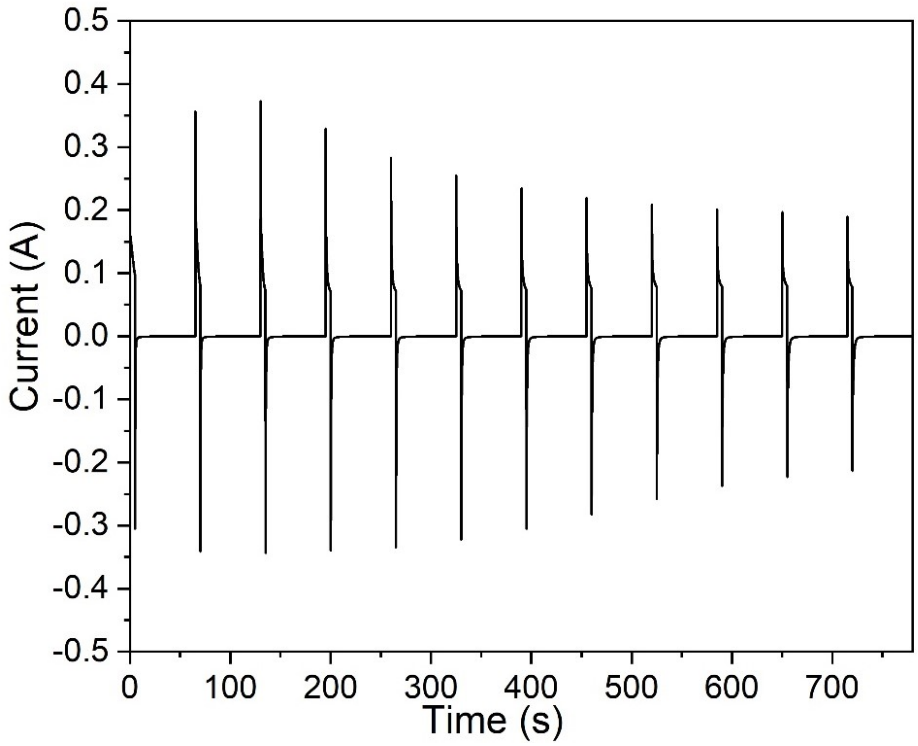

Figure 3.14 Electrodeposition current vs. time of PPy at constant potential 0.8 V with pulse on 5 s and pulse off 60 s for 12 cycles.

3.3.8 The electrochemical surface area (ECSA)

ECSA is surface area calculation technique which represents the accessible area of the electrode material which allows the electrolyte to transport and store inside the electrode. [214] The ECSA can be measured by various methods such using the Randles–Ševćik equation by focusing on the current at the anodic peak which is expected to be reaction-dependent and controlled by the diffusion of different reactant species.[215] However, there are limitation for utilising Randles–Ševćik equation in this work as the SWCNT based electrodes only have broad redox peaks and found to be deoxygenated after cyclic stability. Therefore, another method which is estimating from electrochemical double-layer capacitance (C_{dl}) by collecting CV curves in a non-Faradaic region at different scan rates is more suitable to calculated ECSA here as the capacitance of nanotubide electrodes mostly contributes from EDLC. Additionally, the ECSA is determined in the presence of electrolyte which can chracterise the kinetic reaction of electrodes resulted in the maximised utilisation of both the porous structure and heteroatoms. [216] Therefore, it is more capable to chracterise the real ion-accessible interface in electrochemical applications than BET measurement which used the gaseous

atmosphere.[216] To determine ECSA in this thesis, the currents at 0.8 V *vs.* Ag/AgCl from CV curves of as-synthesised electrodes were collected from forward scan at different scan rates. The electrochemical double layer capacitance (C_{dl}) should be equal to the slope of i_c–v plot from the linear equation 3.19 using the scan rate (v) range between 10 and 100 mV/s:

$$i_c = v \times C_{dl} \qquad \text{Equation 3.19}$$

where i_c is the capacitive current (A), and v is in V/s unit. Assuming that the capacitance obtained at 0.8 V does not have faradaic contribution. Then the ECSA can be calculated using the equation below

$$ECSA = \frac{C_{dl}}{C_s} \qquad \text{Equation 3.20}$$

where the value of the general specific capacitance (C_s) is 35 µF/cm^2 in 1 M H_2SO_4.[216, 217]

3.4 Mechanical characterisation

3.4.1 Tensile test

The ultimate tensile stress (σ_t) and strain (ε) of the buckpapers were determined using a Linkam TST350 Tensile Stress Tester with appropriate stage and computer interface (Linksys32, V. 1.9.1, Linkam Scientific Instruments Ltd. Surrey, UK). Each mechanical test sample (1.2 mm width and 20 mm long) was prepared by pressing the SWCNT buckypaper under the glass slide and cut by a razor blade, then glued to the card holder using epoxy (Araldite Rapid Adhesive, Bostik Findley Ltd., Leicester, UK). Note, the card holder is in the regtangular shape (Figure 3.15a) with the card frame has 15 mm long gap to define gauge length. The card holder is cut after clamping into the tensile test unit, such that only buckypaper properties are measured during the test (Figure 3.15b). Tests were performed at a crosshead speed of 16.7 µm/s, using a 20 N force sensor, with the load and the displacement recorded through Linkam software. Measurements followed the ASTM standard D882 for thin films less than 1 mm thick, from at least 5 specimens. The thickness of the samples is defined using the micrometer. σ_t is calculated at the maximum force (F_{max}) at the place where the sample is broken normalised by the cross-sectional area of sample (A_{CSA}) through equation 3.21. ε is calculated from the change in length of the sample from the original length to the failure length (Δx) dependent on gauge length (L) used (equation 3.22).

$$\sigma_t = \frac{F_{max}}{A_{CSA}}$$ Equation 3.21

$$\epsilon = \frac{\Delta x}{L}$$ Equation 3.22

The tensile tensile modulus of elasticity (E_t) is obtained through the slope of the linear region of the stress when plotted against strain in the range of 0.5-1% (equation 3.23).

$$E_t = \frac{\sigma}{\epsilon}$$ Equation 3.23

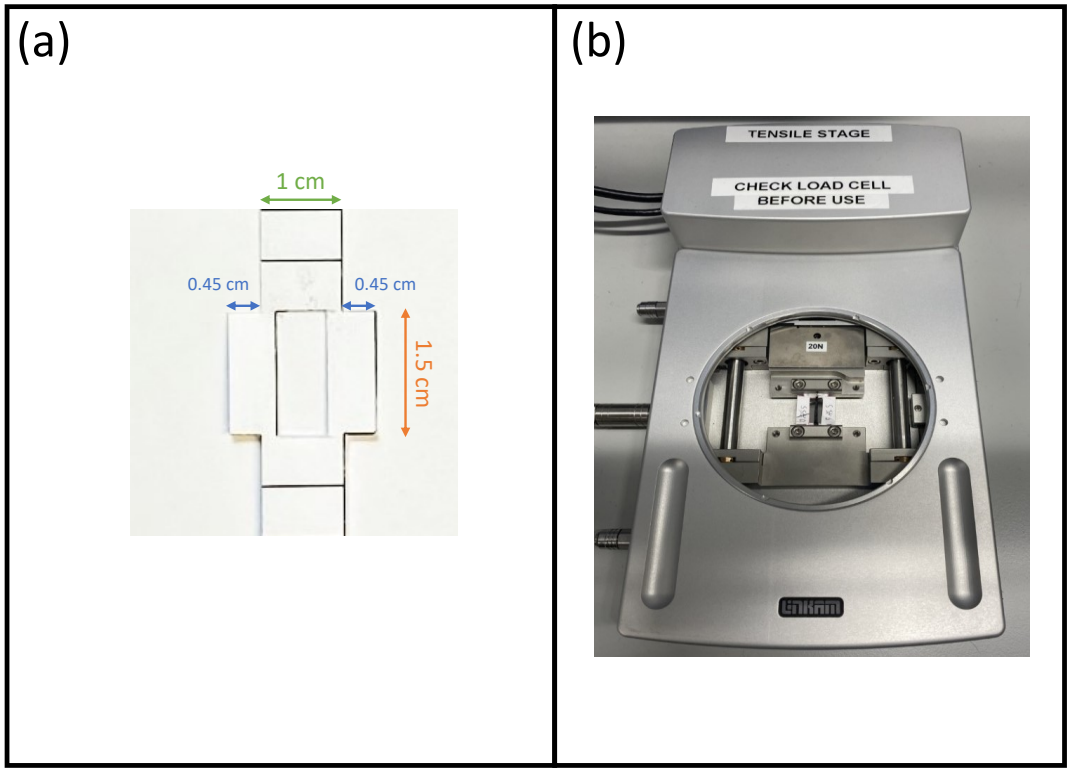

Figure 3.15 (a) the card holder template and (b) tensile stage with specimen loaded showing the cut card holder just before testing.

3.5 Materials

Tuball75 and Tuball99 single-walled carbon nanotubes powder were supplied by OCSiAl Ltd.[10] Ethyl-methyl-Imidazolium bis(trifluoromethylsulfonyl)-imide ([EMIM][TFSI], ≥98% (HPLC), ≤0.5% water), sodium (99.95%, ingot), 1,4-diiodobenzene (DIB, 98%), dimethylacetamide **(**DMAc, 99.8%**)**, dimethylformamide **(**DMF, 99.8%**)**, potassium chloride (KCl) and naphthalene (99%) were purchased from Sigma-Aldrich UK. Pyrrole monomer (99%)

was purchased from ACROS Organics™, Fisher scientific Ltd and sulphuric acid (97%) was purchased from VWR UK Ltd. DMAc was dried over 20 % volume, activated molecular sieves (3 Å) before use in the glove box. While naphthalene was dried under vacuum overnight over phosphorus pentoxide (P_2O_5) before using in the glove box. PTFE membranes were purchased from Fisher Scientific Ltd and all gases were supplied by BOC (UK).

4. Reductive dissolution of SWCNT buckypapers

4.1 Introduction

Single-walled carbon nanotubes (SWCNTs) are of particular interest to use as active materials for high power electrochemical devices due to their high electrical conductivity, chemical stability and high specific surface area.[218] Nevertheless, the major draw-back of using SWCNTs as the active material for energy storage devices is their tendency to agglomerate due to high $\pi - \pi$ interactions, leading to a reduction in the active surface area. To maximise electrochemical performance, SWCNTs require individualisation before their use in applications. Various methods have been proposed to achieve highly dispersed systems such as sonication or other mechanical shear.[8] However, these approaches are difficult to scale-up and tend to both shorten SWCNTs and degrade their intrinsic properties. To overcome van der Waals interactions without damaging the SWCNTs structure, reductive charging approaches were introduced by taking benefit of SWCNTs easily accessible electronic states to introduce Coulombic repulsions. Negatively-charged SWCNTs ("nanotubides") form thermodynamically-stable solutions of individual, undamaged species at high concentrations (Section 2.3.5.4).[10, 105] There are various methods to prepare nanotubide solutions, however one of the most scalable and simplest, is the one-pot reduction of SWCNTs in N,N-dimethylacetamide (DMAc), using sodium naphthalide (NaNp) as an organic charge transfer agent.[10] The resulting solutions are beneficial for both liquid-phase processing and subsequent reactions with a range of electrophiles.

In the literature, supercapacitor performance is usually reported normalised to the mass of the active electrode materials only. From this perspective, both porous networks and ultra-thin films can provide a remarkable (gravimetric) performance. Highly porous structures, such as SWCNT aerogels, provide a 3D network structure, with lightweight, high surface area, and efficient electron/ion transport in energy storage devices.[78] However, these data mainly highlight the excellent intrinsic performance of SWCNTs, they are misleading when it comes to practical application. Ultrathin films (<1 um) deliver negligible active mass compared to the parasitic mass of the remainder of the cells. Additionally, SWCNT aerogels are typically consisting of >99% pore volume with ultralow packing densities; in a real device, this volume

must be filled with dense electrolyte, significantly increasing the effective electrode mass. At the same time, the low density indicates a poor electrochemical volumetric performance, which is essential in many practical applications such as power management in electric vehicles and compact electronic devices.[3, 4] A thick aerogel electrode can cause a high equivalent series resistance (ESR) which decreases the performance further. Whilst it is possible to decrease the thickness of aerogels using capillary collapse or mechanical compression, the SWCNTs tend to rebundle.[80] This aggregation reduces surface area and associated EDLC, as well as interrupting ion transport path and increasing charge transfer resistance (R_{ct}). For practical application, the SWCNT electrode architecture must be developed to maximise volumetric performance, electrical conductivity and ion transportation, at high areal mass loadings.[9] SWCNT buckypapers are dried films, usually prepared by filtration. In principle, they are promising candidates for supercapacitor electrodes, however generally suffer a poor structure derived from the challenges of solvent processing. There is scope to develop improved 'buckypapers', designed to offer individualised SWCNTs, with high aspect ratio, in thick films with high bulk density. Such electrodes should provide higher conductivity, lower contact resistance, and higher volumetric performance than SWCNT aerogels.[76] In addition, the integrity and high conductivity of SWCNT buckypaper electrodes means that current collectors and conventional binders can be avoided, in principle increasing specific energy density via reducing the volume and inactive mass of overall device.[219, 220]

Whilst the nature of the active electrodes is important, the volumetric performance of a cell device also depends on the separator. The ideal separator must reduce ionic resistance whilst preventing any electronic short circuit between the two electrodes. Generally, thin highly porous membranes provide the lowest resistive losses, and maximise volumetric performance, but they must remain mechanically robust.[221] Cellulose, polypropylene, polytetra-fluorethylene (PTFE) and polyethylene membranes are well-known separators for aqueous supercapacitors. The thickness of commercial separators are roughly around 20-50 μm, including for example, 25 μm for Celgard2400 (polypropylene), 23 μm for GORE (PTFE) and 25 μm for TF4425 (cellulose) separators, respectively.[222, 223] Reducing the thickness of these established separators may have adverse effects on the mechanical strength, safety and cyclic stability.[224] Alternative membranes are needed that can offer reliable mechanical separation at lower thickness.

In this chapter, full symmetric supercapacitors, with excellent overall gravimetric and volumetric performance, are produced by optimising the nanostructure of electrodes and separator. Since individualised SWCNTs offer maximum performance, reductive charging was applied to prepare the electrode constructs. SWCNTs/DMAc concentration ([C]) and intermediate charging ratios of carbon to sodium by mol (C:Na) are known to control the level of solubilisation.[225] Therefore, conditions were optimised to maximise capacitance, using three-electrode cell measurements. To fabricate a thinner highly porous membrane, bacterial cellulose (BC) nanopaper was introduced, due to its micrometer thickness, light weight (15 g/m^2), high specific surface area (605 m^2/g) and high tensile strength.[226] The symmetric full cell devices were then fabricated using BC as a separator to maximise performance with an aqueous electrolyte. In order to enlarge applied voltage and enhance specific energy density, cells were prepared using an ionic liquid electrolyte.[227, 228]

4.2 Experimental procedure

4.2.1 SWCNT purification via NaNp/DMAc

Raw SWCNT powder were purified via reductive charging sodium napthalide approach by adapting from procedure reported elsewhere.[101] Typically, 300 mg of dried SWCNT powder (25 mmol) were introduced into a quartz tube and this was then placed into the tube furnace. The quartz tube was sealed and connected to a turbo pump (Leybold PT 70F) using a metal Swagelok joint. The quartz tube was vacuum to baseline pressure (approximately 10^{-6} mbar), and heated up to 500 ^oC with a ramp rate of 15 ^oC/min and dwelling for 20 min every 100 ^oC. The temperature was maintained at 500 °C for 10 h, before allowing the quartz tube to cool overnight under vacuum before transferring it into an mBraun glove box (nitrogen atmosphere, <0.1 ppm water, <0.1 ppm oxygen). A sodium naphthalide (NaNp) reducing stock solution was prepared by stirring equimolar amounts of sodium and naphthalene in dry N,N-dimethylacetamide (DMAc, 1 mg/mL) overnight, and normally used within 7 - 10 days from synthesis. The NaNp solution was added to a quantity of SWCNT powder in order to achieve the 1 mg/mL nanotubide concentration. The mixture was stirred for one day before being transferred to fluorinated ethylene propylene (FEP) centrifuge tubes and centrifuged at 10,000 g for 30 min outside the glovebox; to maintain the inert atmosphere inside the centrifuge tubes, the screw caps were additionally sealed by wrapping with

polytetrafluoroethylene (PTFE) tape. The supernatant containing in the nanotubide solution was then separated from the precipitate by decanting in the glove box. The sludge form of charged SWCNTs was then taken out from the glove box in a sealed glass flask with a suba-seal stopper and then quenched with dry air (N_2/O_2, 80/20) to remove the remaining charge. SWCNTs sludge was washed with DMF, water and ethanol via filtration system and then dried in vacuum oven at 110 ^{0}C for 8 h.

4.2.2 SWCNT reductive dissolution

250 mg of purified SWCNT powder were introduced into a quartz tube and then placed into the tube furnace. The quartz tube was sealed and connected to a turbo pump (Leybold PT 70F) using a metal Swagelok joint. The quartz tube was vacuum to baseline pressure (approximately 10^{-6} mbar), then heated up to 500 ^{o}C with a ramp rate of 15 ^{o}C/min and dwelling for 20 min every 100 ^{o}C. The temperature was maintained at 500 °C for 10 h, before allowing the quartz tube to cool overnight under vacuum before transferring it into an mBraun glove box (nitrogen atmosphere, <0.1 ppm water, <0.1 ppm oxygen). For preparing reductive stock solution, 50 mg of sodium and 278 mg of naphthalene were stirred in 50 mL of DMAc overnight using a glass stirring bar. NaNp was added to purify SWCNT powder. The ratio between mol C: mol Na varied between 5:1 and 15:1 (molar ratio). The nanotubide solution was stirred for 24 h.

4.2.3 Nanotubide buckypaper via reductive agent

Nanotubide buckypaper was prepared by diluting the nanotubide solution to 1-4 mg/mL with DMAc and using a syringe to dose the nanotubide solution onto a PTFE membrane (0.1 µm) placed on a filtration system inside the glove box. The volume was adjusted so that each piece of buckypaper contained 7 mg of SWCNTs. After leaving the solution to settle for 24 h, the SWCNTs buckypaper was taken out from the glove box in a sealed glass flask with a suba-seal stopper and then quenched with dry air (N_2/O_2, 80/20) to remove the remaining charge. To remove the remaining impurities, nanotubide buckypaper was washed with DMF, water and ethanol via solvent exchange. Finally, nanotubide buckypaper was vacuum dried in a vacuum oven at 110°C overnight.

4.2.4 Sonicated SWCNTs buckypaper via sonication

A control SWCNT buckypaper, used for comparison, was produced via sonication. 7 mg of raw SWCNT powder were mixed with 4.7 mL DMAc and then sonicated for 2 h using 35 W ultrasonic bath. The resulting suspension was filtered through a PTFE filter membrane (0.1 μm) and washed with DMF, water and ethanol. Finally, the sonicated SWCNT buckypaper was dried under vacuum at 110 ^{0}C overnight.

4.2.5 Fabrication of symmetric device

The BC nanopaper separator was produced from nata de coco, following a procedure reported elsewhere.[226, 229] BC nanopapers with thicknesses of 7 μm were soaked overnight in 1 M H_2SO_4 and **[**EMIM**][**TFSI**]** for aqueous and ionic liquid supercapacitors, respectively. A conventional cellulose paper (70 μm), used for comparison with BC nanopaper, was also soaked overnight in 1 M H_2SO_4. Devices were then assembled by sandwiching the separator between identical circular (10 mm diameter) SWCNT electrodes in Swagelok cell. The electrochemical properties of as-fabricated full cell devices were evaluated by CV, EIS and GCD as a two-electrode system. CV was performed at 50 mV/s and GCD was performed at specific current varied from 1 to 100 A/g. Cyclic stability tests (1 – 50,000 cycles) were completed via the GCD technique applying specific current at 5 A/g.

4.3 SWCNTs reduction and dissolution

4.3.1 Impact of SWCNT concentration to nanotubide buckypaper properties

In this chapter, a new type of buckypaper was successfully produced via reductive dissolution and subsequent filtration of charged SWCNTs (here called 'nanotubide buckypaper'). To optimise the solubilisation and functionalisation, nanotubide solutions were prepared with [C] in the range of 1 to 4 mg/mL in this section and controlled (C:Na) ratios at 10:1 which was employed from previous research study.[11] SEM images (Figure 4.1a-d) show that highly porous, uniform networks were formed by filtering nanotubide solutions with concentrations from 1 to 2.5 mg/mL. Nevertheless, evidence of agglomeration appeared (Figure 4.1e-f), consistent with the expected solubility limit of Tuball nanotubide in DMAc (above 3 mg/mL).

The electrochemical behaviour of nanotubide buckypapers prepared from different [C] was tested using CV in three-electrode configuration (Figure 4.2a). The CV curves of electrodes show a working potential range from 0 V to 1.1 V in 1 M H_2SO_4. The CV curves of every electrodes show EDLC behaviour due to the physisorption of the electrolyte ions on nanotubide buckypaper surface. [230] The pairs of broad redox peaks at 0.4 V vs. Ag/AgCl related to the redox reactions of hydroxyl and carboxylic groups on the surface of the SWCNT (Figure 4.3f). From the calculated specific capacitances, it can be seen that 1.5 mg/mL [C] electrode presents the highest volumetric and gravimetric capacitance among all the [C] range (Figure 4.2b). To study the resistance of as-synthesised electrodes, characteristic Nyquist plots (Figure 4.2c) were derived from EIS. At high-frequency, the semi-circular region denotes a significant resistive contribution where the minimum intercept on the x-axis indicates the total internal resistance (ESR) and the diameter of the semicircle relates to charge transfer resistance (R_{ct}).[231] The ESR combines resistive contributions from electrode materials, electrolyte and contact resistance.[232, 233] The high frequency semicircle was fitted with an modified Randle's equivalent circuit (Figure 3.9) to calculate R_{ct} which relates to the electrochemical interactions at the electrode surface. [234, 235] R_{ct} of nanotubide buckypapers become larger along with the increase of [C] over 2 mg/mL (Table 4.1). The increase of R_{ct} is in good agreement with SEM structure as increasing [C] gives less solubilisation leading to SWCNTs agglomeration and reducing ion transportation efficiency. Additionally, the electrical conductivity exhibits reverse trend compared with ESR of as-synthesised electrodes while increasing [C] after 1.5 mg/mL (Figure 4.2d). These results can confirm that there is a relationship between electrochemical performance, electrical conductivity and SWCNT buckypaper structure. At 1 mg/mL of [C], the electrical conductivity of nanotubide buckypaper is smaller and ESR is higher compared to 1.5 mg/mL nanotubide buckypaper electrode because high solubility of nanotubide solution creates higher buckypaper thickness.

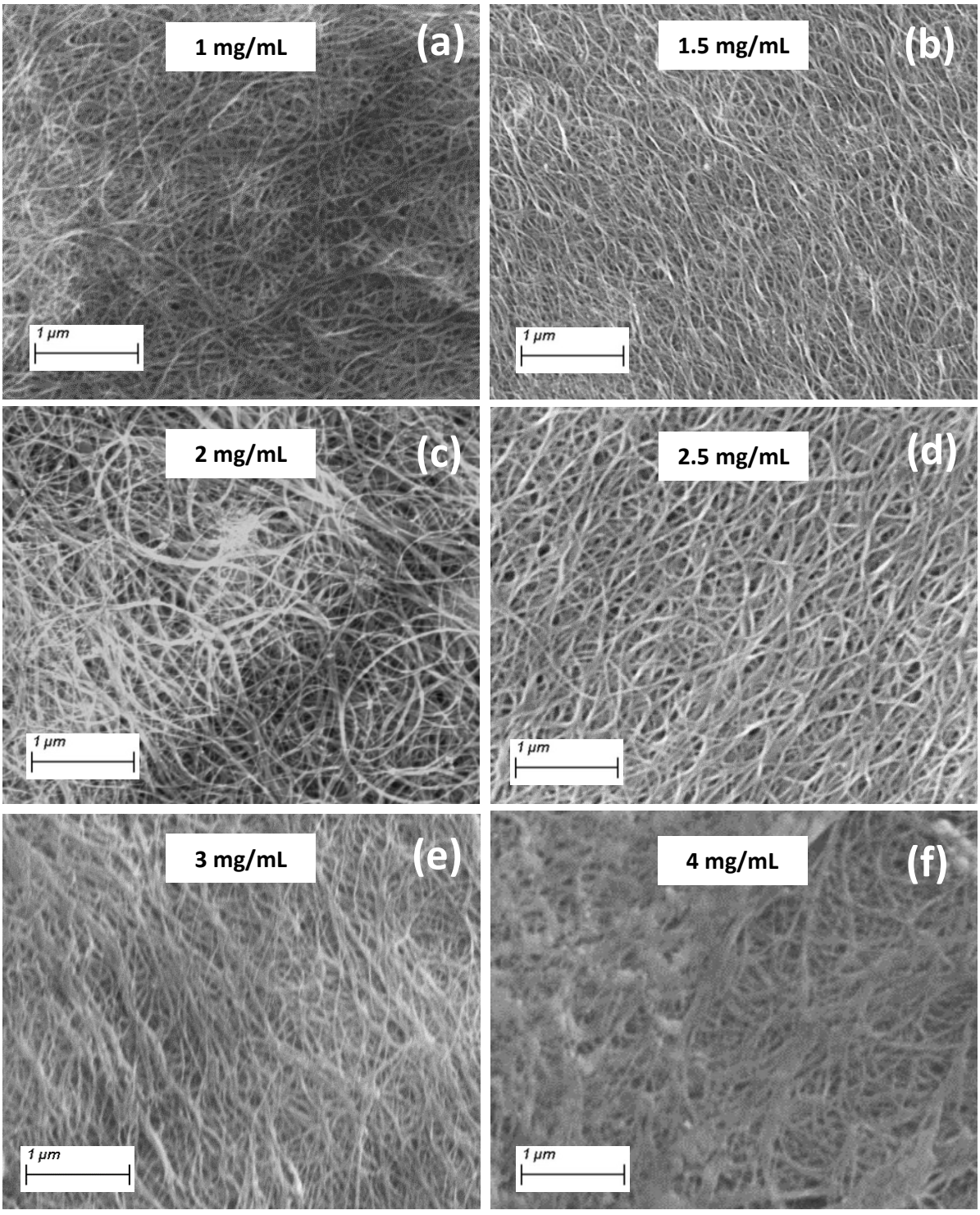

Figure 4.1 SEM images of nanotubide buckypapers with different [C] (a) 1 mg/mL, (b) 1.5 mg/mL, (c) 2 mg/mL, (d) 2.5 mg/mL, (e) 3 mg/mL and (f) 4 mg/mL.

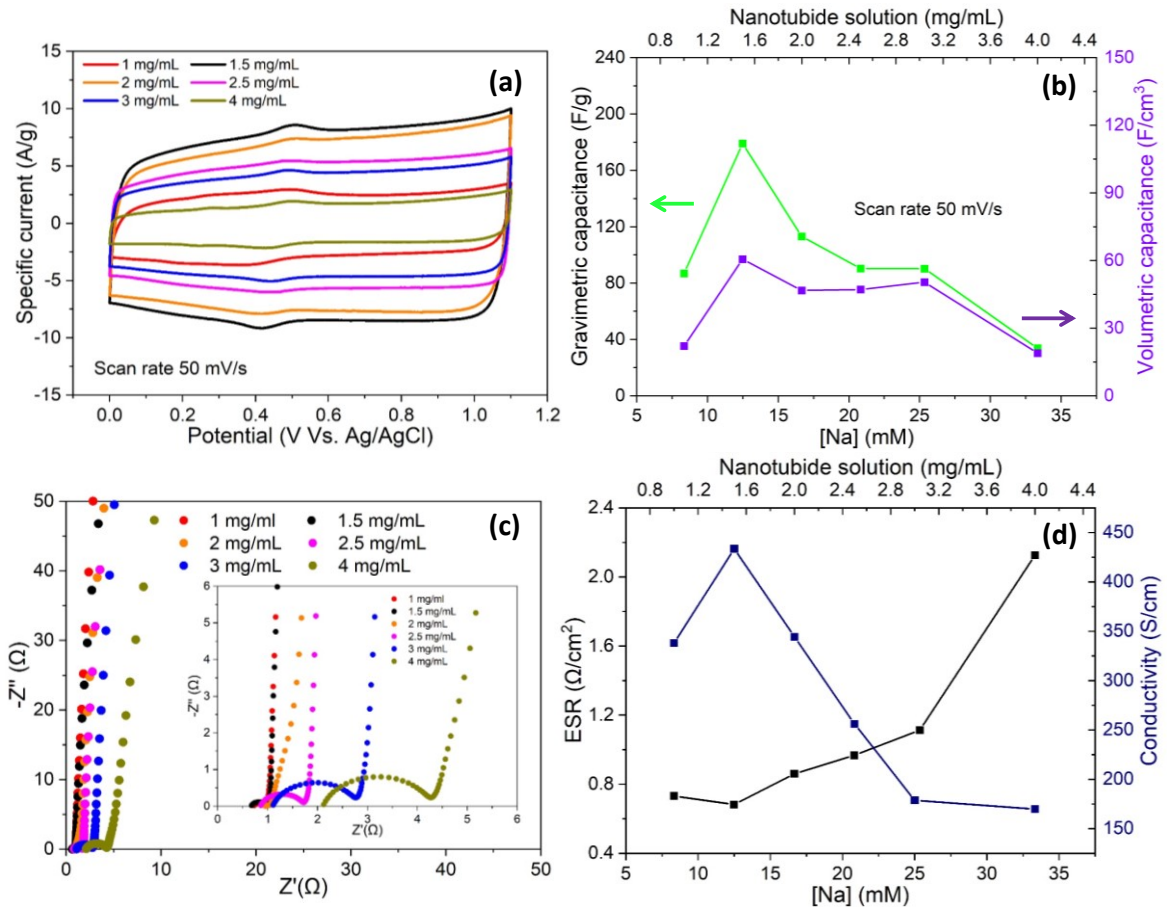

Figure 4.2 (a) CV curves at 50 mV/s and (b) gravimetric and volumetric capacitance vs. sodium concentration of nanotubide buckypapers at different carbon concentrations in three-electrode measurement. (c) Nyquist plots inset with the zoom in and (d) ESR and conductivity of nanotubide buckypapers at different absolute carbon concentrations (holding C:Na ratio constant at 10:1) in 1 M H_2SO_4.

Table 4.1 R_{ct} of nanotubide buckypaper at different [C] obtained by simulating the equivalent circuit.[205, 236]

[C] (mg/mL)	R_{ct} (Ω)
1	0.24
1.5	0.32
2	0.24
2.5	0.88
3	1.79
4	2.21

4.3.2 Impact of charging ratios of carbon to sodium (C:Na) to nanotubide buckypaper properties

Intermediate charging ratios of carbon to sodium by mol (C:Na) and/or degree of charge are known to control the level of solubilisation and dispersion.[11] To maximise the capacitance, the nanotubide solutions in this section were prepared with [C] of 1.5 mg/mL due to it provides the highest specific capacitance from previous section then C:Na ratios were varied from 5:1 to 15:1. The SEM images indicate that the quality of nanotubide dispersions decreased when C:Na increased from 5:1 to 15:1, consistent with insufficient Coulombic repulsion (Figure 4.3a-e). The O 1*s* spectra of nanotubide buckypaper (Figure 4.3f) have three peaks at 533.4, 532.4 and 531.5 eV which are assigned to C-OH, C=O and -COOH functional groups, respectively.[237, 238] Whilst oxygen may be introduced in the XPS measurement by a variety of sources, oxygen-containing functional groups may be formed during the quenching process with dry oxygen. These O groups may improve the wetting of the electrodes with aqueous electrolyte and can provide a redox contribution to the overall capacitive performance of the SWCNTs.[239, 240]

To optimise the electrochemical performance, buckypapers were prepared from nanotubide solutions at different charging ratios (C:Na). Within the applied potential window (0 V to 1.1 V *vs.* Ag/AgCl), all electrodes displayed rectangular CVs which is the characteristic of EDLC of SWCNTs (Figure 4.4a).[230] Where the minor broad redox peaks around 0.4 V vs. Ag/AgCl related to the redox reactions of hydroxyl and carboxylic groups which noted in the XPS (Figure 4.3f). The gravimetric and volumetric capacitances were both maximised for the nanotubide electrode obtained at C:Na = 10:1 (Figure 4.4b). From Nyquist plot (Figure 4.4c), the optimal (lowest) ESR (0.69 Ω) for the nanotubide electrodes is shown at C:Na equal to 10:1. At other C:Na ratios, ESR is increased, presumably due to poorer SWCNT dispersion/individualisation, as inferred from the SEM images (Figure 4.3d-e), capacitance data (Figure 4.4b) and electrical conductivity (Figure 4.5f).

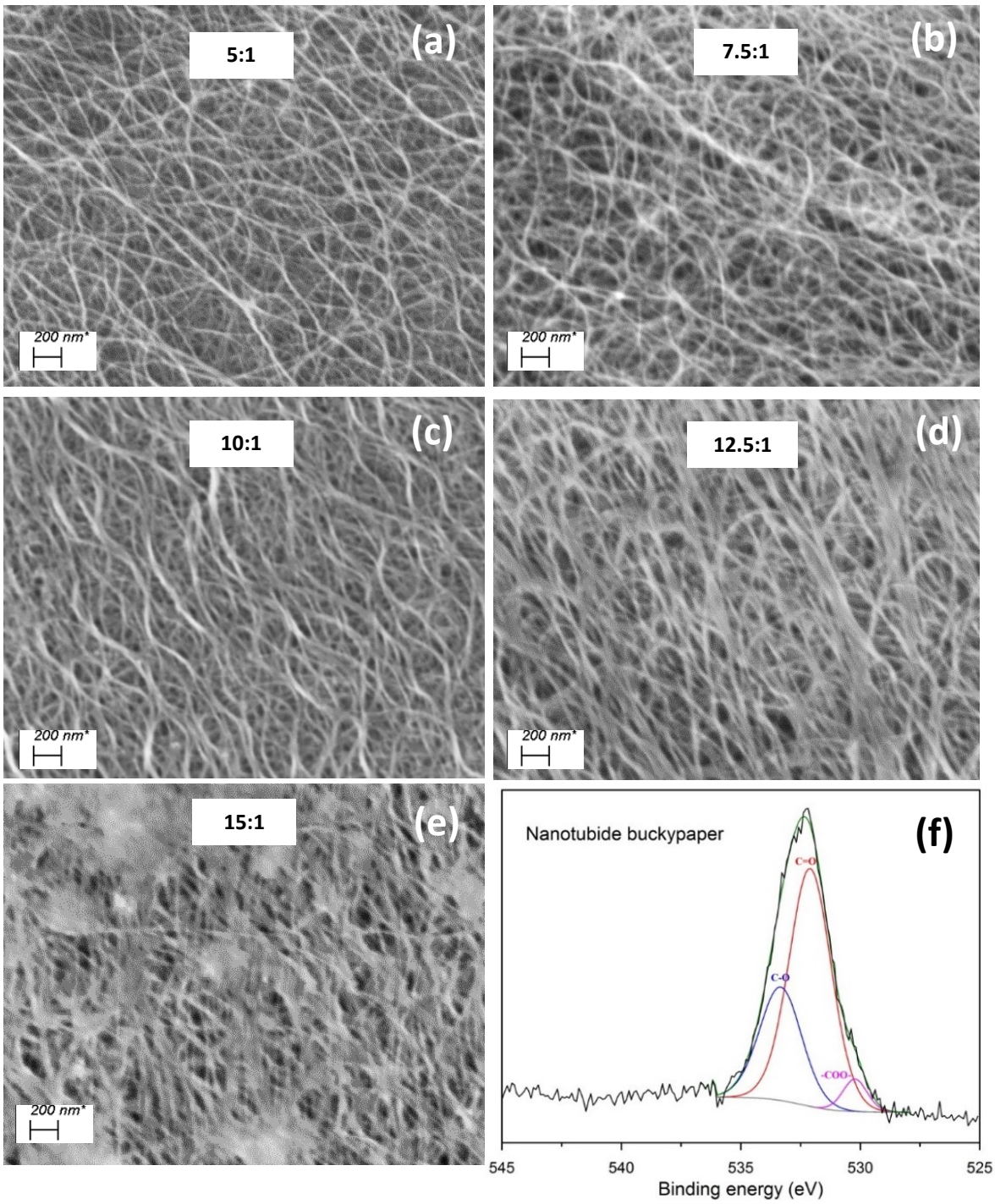

Figure 4.3 (a-e) SEM images of nanotubide buckypapers prepared at different C:Na. (f) O 1*s* of optimised nanotubide buckypaper ([C] = 1.5 mg/ mL, C:Na=10:1).

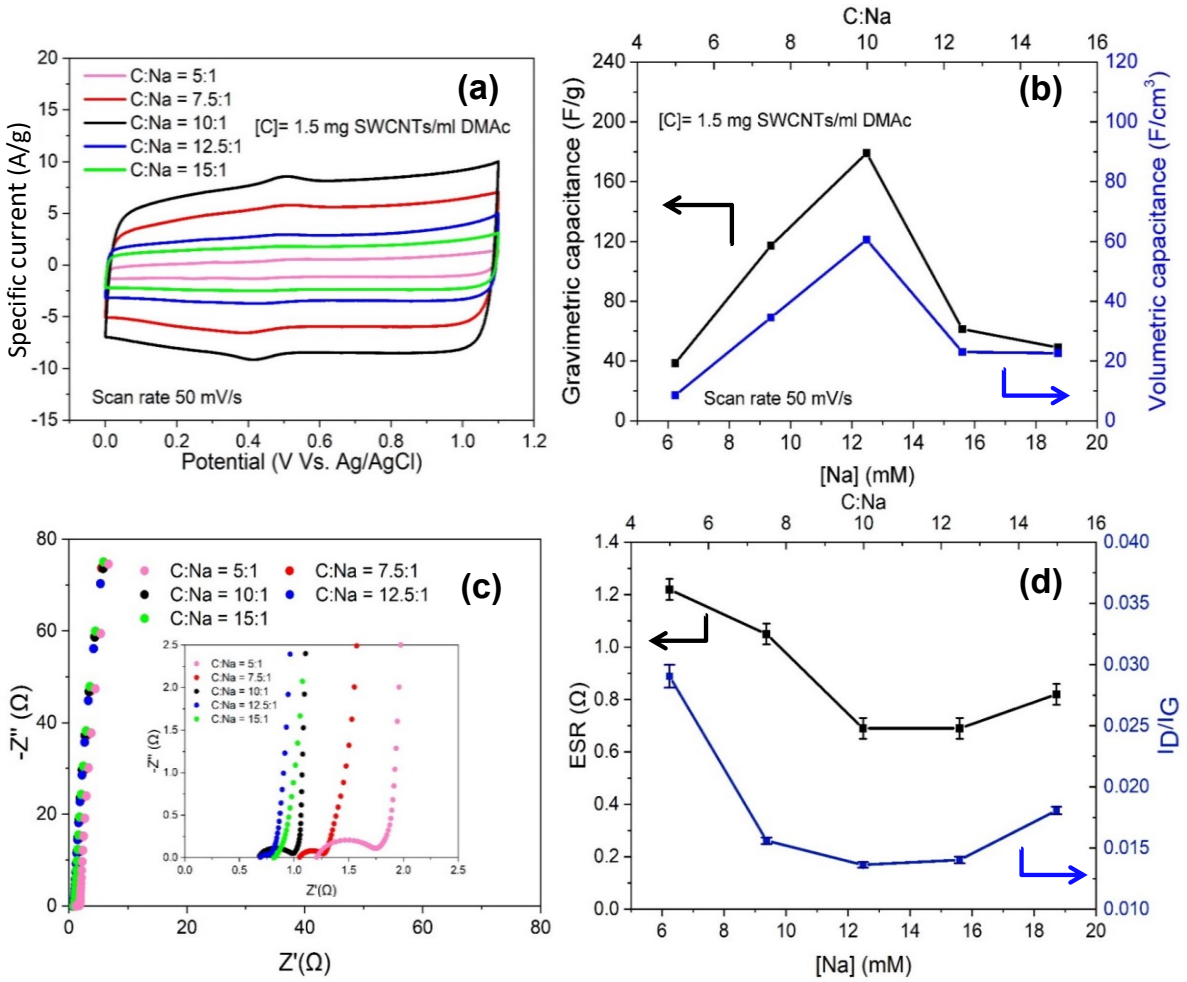

Figure 4.4 The electrochemical performance in three-electrode measurement, in 1 M H_2SO_4, of nanotubide buckypapers prepared from solutions at a given sodium concentration, or equivalent C:Na ratio: (a) CV curves at 50 mV/s; (b) variation of the gravimetric and volumetric capacitance, at 50 mV/s, with the charging ratio; (c) Nyquist plots and (d) ESR and the I_D to I_G ratio derived from Raman spectra.

As mentioned above, networks of well-dispersed SWCNTs provide high conductivity, and minimise resistive losses within bundled/agglomerated regions. The trend may be reinforced by the quality of the SWCNTs,[241] since the purification is expected to be most effective around C:Na=10:1, as confirmed here by I_D/I_G values from the Raman spectra (Figure 4.4d). R_{ct} for C:Na at 5:1 is significantly higher than the other electrodes (Figure 4.4c) and relates with a higher I_D/I_G ratio from Raman spectroscopy (Figure 4.4d). Additionally, there is an additional redox peaks at 0.25 V in nanotubide buckypaper (C:Na at 5:1, Figure 4.5a) when compared with nanotubide buckypaper from other condition (Figure 4.5b-e), suggesting that, in the presence of excess NaNp charging agent, the carbon framework starts to be damaged.

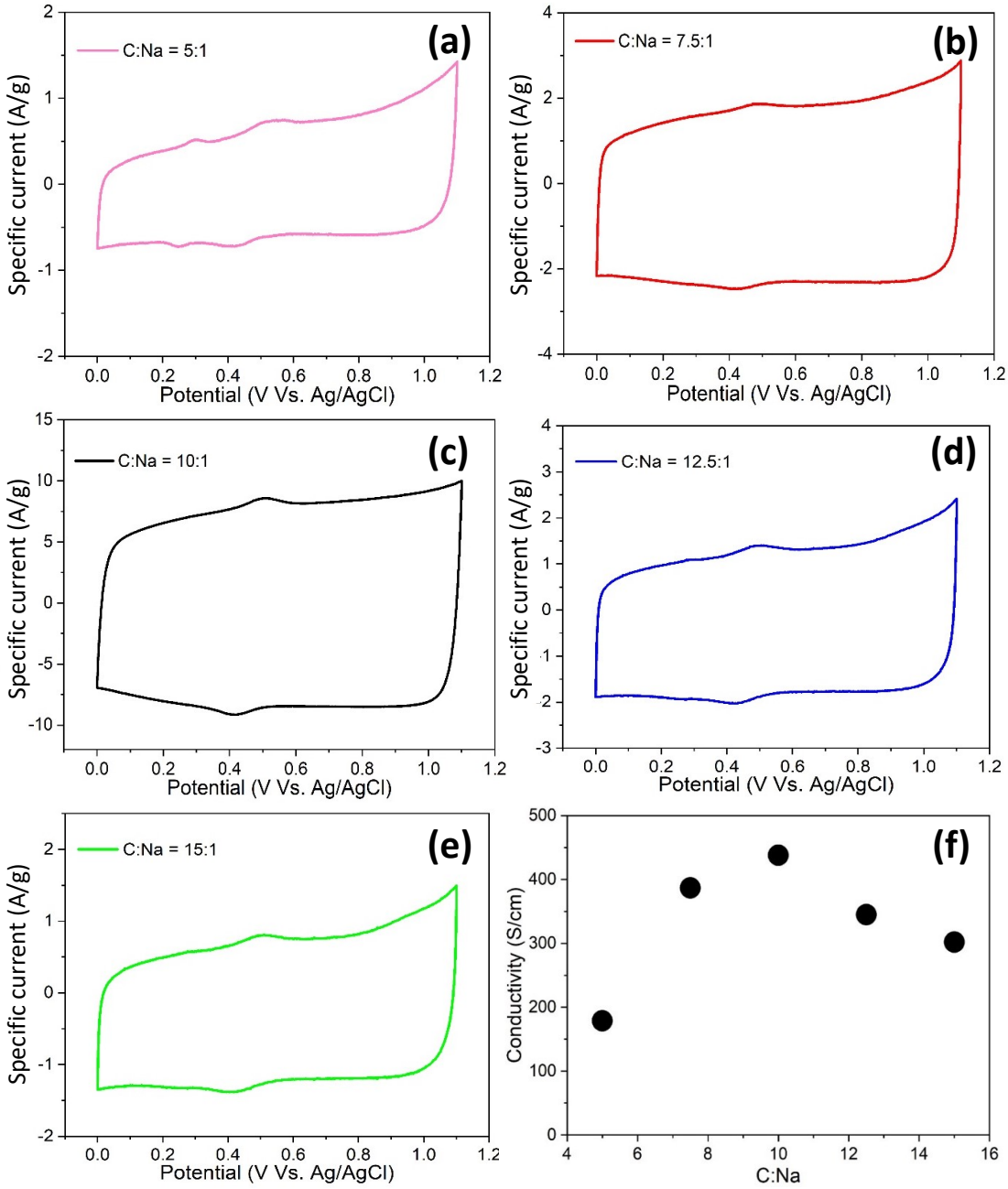

Figure 4.5 (a-e) CV curves at 50 mV/s and (f) electrical conductivity of nanotubide buckypaper ([C]=1.5 mg/mL) at different C:Na.

4.4 Alternative synthesis method for SWCNT buckypaper

4.4.1 SWCNT buckypaper via sonication

To benchmark nanotubide buckypaper against more conventional approaches, a control was produced by dispersing SWCNTs in DMAc using sonication at 1.5 mg/mL. The sonicated SWCNT buckypaper electrode was compared with the nanotubide buckypaper prepared at

the same concentration ([C]=1.5 mg/mL) and (C:Na = 10:1). SEM images of sonicated SWCNT buckypaper shows an agglomerated structure and trapped impurities on the surface (Figure 4.6a) in sharp contrast to the structure of nanotubide buckypaper which contains a network of highly dispersed SWCNTs bundles (Figure 4.6b). Nitrogen adsorption-desorption isotherms (Figure 4.6c) were used to measure the surface area and pore size distribution which are crucial to EDLC performance. Specific surface areas (SSAs) calculated through the BET model showed an improvement for the nanotubide system (412 m^2/g) compared to the sonicated control (327 m^2/g). In addition, the nanotubide buckypaper showed a narrower range of pore sizes (Figure 4.6d), predominantly mesopores between 10-50 nm. While the sonicated paper showed a broad range of micro-, meso- and macroporous structures. Ion-wall interactions slow ion transport in the micropores, in pore-diameter-dependent fashion.[242] Pore diameters larger than 10 nm are considered sufficiently large to neglect ion−wall interactions, leading to fast ion transport, at low resistance, equivalent to bulk electrolyte.[242-244] The predominance of the mesopores in the nanotubide buckypaper (maximum PSD peak at 30 nm) therefore suggests a low ionic resistance; the narrow mesopore distribution is expected to have more efficient pore utilisation.[245-247] On the other hand, in the sonicated SWCNT buckypaper, the significant fraction of micropores is expected to limit ion transport and hence power storage characteristics.[248, 249] The electrical conductivity of nanotubide paper (433 S/cm at 0.34 g/cm^3) was significantly higher than the sonicated SWCNT paper (110 S/cm at 0.33 g/cm^3) and other SWCNT buckypapers in the literature (Figure 4.6f). A higher degree of dispersion/individualisation, and the retention of longer SWCNTs, are expected to enhance the electrical conductivity.[62, 250] Notably, the electrical conductivity is the highest for the optimal dispersion conditions (Figure 4.2d and Figure 4.5f).

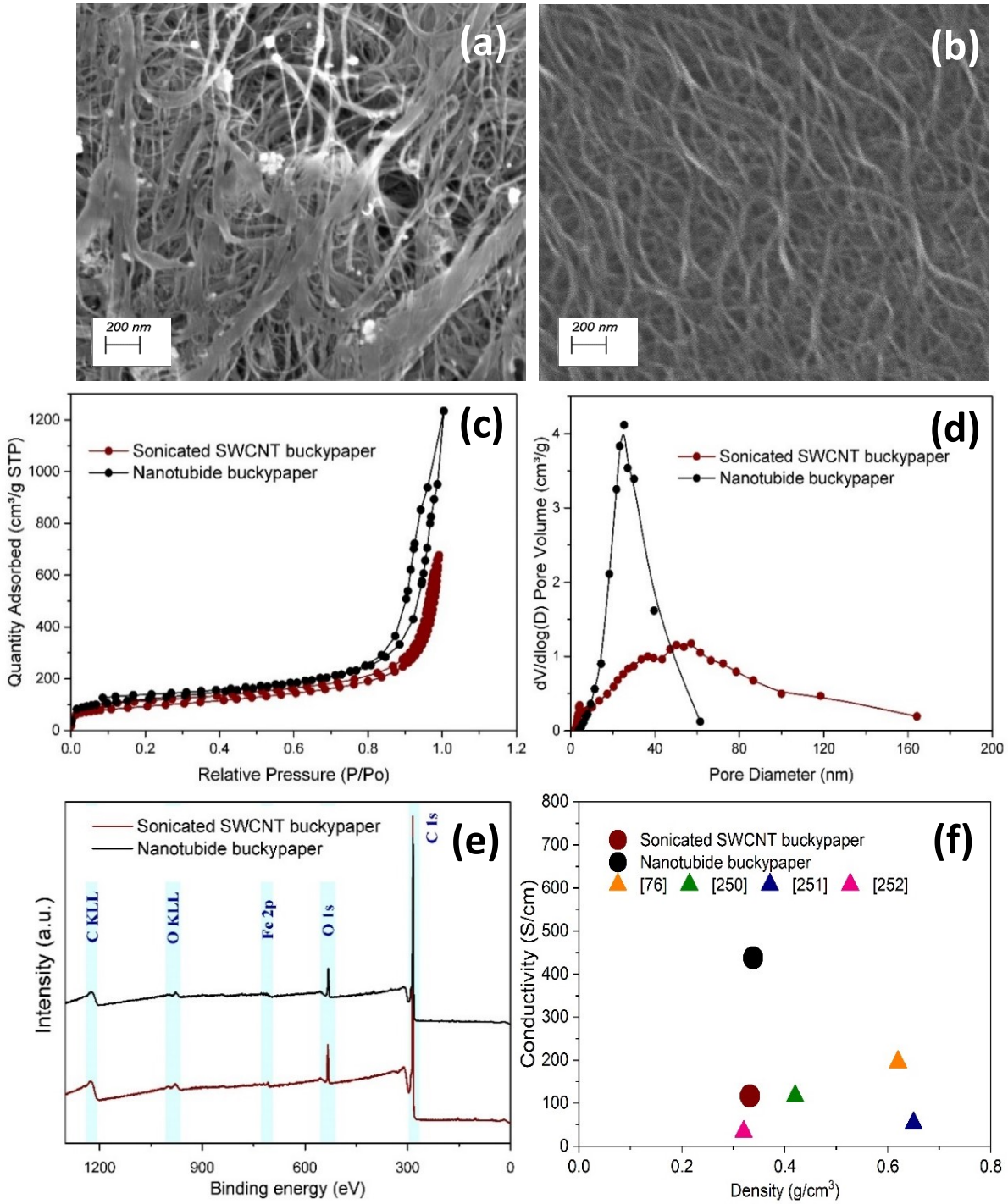

Figure 4.6 SEM images of (a) sonicated SWCNT buckypaper and (b) nanotubide buckypaper ([C] = 1.5 mg/mL, C:Na = 10:1). Comparison of sonicated SWCNT buckypaper and nanotubide buckypaper ([C] = 1.5 mg/mL, C:Na=10:1) by (c) N_2 adsorption−desorption isotherms, (d) pore size distribution (PSD) calculated by BJH technique and (e) XPS survey scans. (f) Electrical conductivity of nanotubide and sonicated SWCNT buckypapers compared to other SWCNT buckypapers in the literature.[76, 250-252]

Additionally, following reductive purification, the proportion of amorphous carbon and defective nanotubes is lowered.[10] XPS confirms the same trends (Figure 4.6e), with the metal content of the nanotubide papers (0.17 at%) lower than the sonicated ones (0.31 at%) (Table 4.2); the lower absolute values reflect the encapsulation of the residual metal catalyst within the nanocarbon structure.

Table 4.2 Element composition in buckypapers, determined by XPS

Sample	XPS		
	at% C	at% O	at% Fe
SWCNT powder (Tuball 75)	97.70	1.82	0.48
Sonicated SWCNT buckypaper	94.23	5.46	0.31
Nanotubide buckypaper ([C] = 1.5 mg/mL, C:Na = 10:1).	95.09	4.74	0.17

The optimum nanotubide ([C] = 1.5 mg/mL, C:Na = 10:1) electrode was then compared with the sonicated control, under the same conditions, in a three-electrode measurement. Both electrodes exhibited similar rectangular CV curves, typical of classic EDLC behaviour (Figure 4.7a), with only a small feature associated with redox reactions of the oxygen-groups in the surface of the SWCNTs. As the scan rate increased to 500 mV/s, , the CV curve of sonicated SWCNT buckypaper presented a more resistive shape while CV curve of nanotubide buckypaper retains a quasi-rectangular shape with more modest distortion (Figure 4.7b), highlighting the desired high power capability.[253] The much larger area under the CV curve for the nanotubide buckypaper highlights the significantly increased capacitance values, reaching 218 F/g (74 F/cm^3), as compared to 82 F/g (10 F/cm^3) for the sonicated SWCNT buckypaper (Figure 4.7c). The gravimetric performance of the nanotubide buckypaper, here, is particularly high, compared to previous studies of carbon based buckypaper electrodes (Table 4.3). The improvement is attributed to greater SWCNT dispersion providing larger

surface area with suitable mesopores for ion adsorption, within a relatively dense buckpaper, at the same time as retaining a high aspect ratio, graphiticity, and electrical conductivity. Nyquist plots (Figure 4.7d), derived from EIS data, show typical, excellent, EDLC responses. At low frequency, the Nyquist plot of nanotubide buckypaper exhibits a nearly vertical line, close to an ideal supercapacitor.[254] The ESRs of sonicated SWCNTs and nanotubide buckypapers are 1.71 and 0.69 Ω, respectively, showing a relative trend in good agreement with the electrical conductivity data (Figure 4.6f). The lower R_{ct} of nanotubide buckypaper (0.32 Ω) compared to the sonicated SWCNT electrode (1.33 Ω) is consistent with an improved pore structure.

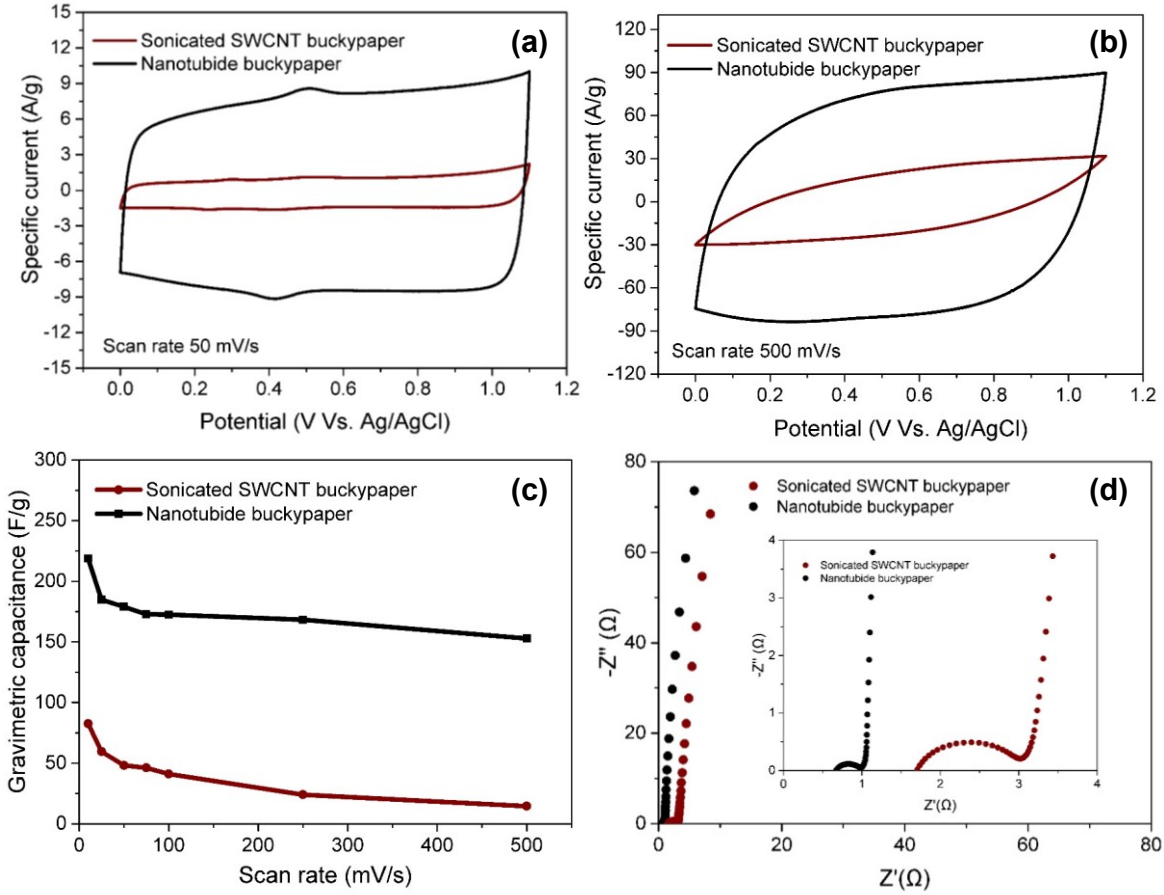

Figure 4.7 The electrochemical performance in three-electrode measurement, in 1 M H_2SO_4, comparing optimised nanotubide buckypaper to a conventionally processed control: **(**a**)** CV curves at 50 mV**/**s, **(**b**)** CV curves at 500 mV**/**s, (c) gravimetric capacitance per electrode mass as a function of scan rate and **(**d**)** Nyquist plots.

Table 4.3 Gravimetric and volumetric capacitance of carbon-based buckypaper electrodes, compared to those reported in the literature.

Note: All volumetric capacitances are calculated from total volume of electrode active materials**.**

Electrode materials	Electrolyte	C_s (F/g)	C_v (F/cm^3)	Ref.
GO/FWNT	1 M H_2SO_4	-	39 (50 mA/cm^3)	[255]
Reduced graphene (MPG)	H_2SO_4/PVA	-	18	[256]
RGO-SO_3H-MWCNT(25%)	H_2SO_4/PVA	53 (2 m V/s)	58 (2 m V/s)	[257]
rGO/poly(vinyl pyrrolidone) (PVP)	H_3PO_4/PVA	168 (1 A/g)	67 (1 A/g)	[258]
Cross-linked graphene aerogel (compressed)	1 M H_2SO_4	130 (10 mV/s)	14 (10 mV/s)	[259]
Graphene/CNT aerogel (compressed)	1 M Na_2SO_4	40 (1 A/g)	5 (1 A/g)	[80]
Holey graphene film	EMITFSI	45 (3 A/g)	54 (3 A/g)	[260]
MWCNT buckypaper	1 M Na_2SO_4	180 (10 mV/s) 85 (100 mV/s)	75 (10 mV/s) 37 (100 mV/s)	[261]
V-Aligned SWCNT buckypaper	Et_4NBF_4/propylene carbonate	80	45.6	[262]
Sonicated SWCNT buckypaper	**1 M H_2SO_4**	**82 (10 mV/s)** **41 (100 mV/s)**	**10 (10 mV/s)** **5 (100 mV/s)**	**This work**
Nanotubide buckypaper	**1 M H_2SO_4**	**218 (10 mV/s)** **172 (100 mV/s)**	**74 (10 mV/s)** **58 (100 mV/s)**	**This work**

4.5 Nanotubide buckypaper for symmetric supercapacitors

4.5.1 Bacterial cellulose nano paper as separator

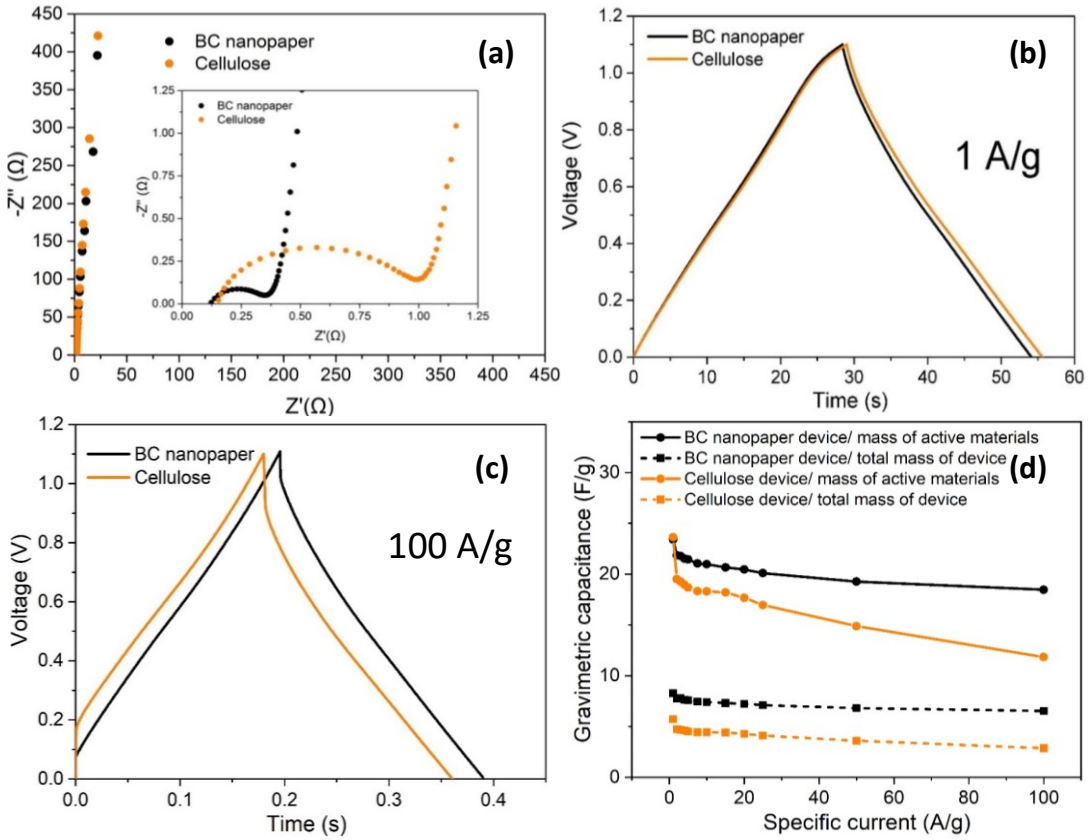

Figure 4.8 Full-cell electrochemical performance of aqueous symmetric supercapacitors using nanotubide buckypaper electrodes sandwiched with BC nanopaper (black) and cellulose (orange) as separators: (a) Nyquist plots, (b) GCD curves at 1 A/g, (c) GCD curves at 100 A/g and (d) the calculated gravimetric capacitance normalised by both active material (solid line) and total mass of device (dash line).

Having optimised the electrode material, using three-electrode measurements, symmetric full cell devices were assembled in a Swagelok system, using two nanotubide electrodes. Two separators were compared: a bacterial cellulose (BC) nanopaper[226] (7µm thick) and a conventional cellulose paper (70 µm thick). The full cell EIS showed a classic high frequency semi-circle and capacitive response at low frequency (Figure 4.8a). The exceptionally thin BC separator, provided a significant reduction in both ESR and R_{ct} of the symmetric device, attributed to a shorter ion diffusion distance through the BC separator, despite a more modest porosity. For the GCD curves at 1 A/g (Figure 4.8b), the curves of both

full cell devices with BC nanopaper and cellulose show an approximately triangular shape typical of EDLC behaviour[263] with negligible IR drop (around 0.001 V for BC nanopaper and 0.002 V for cellulose, respectively), correlating with a high Coulombic efficiency (>93%, Figure 4.8d). At high specific current (100 A/g), the IR drop is naturally much more obvious, for the devices with both BC (0.07 V) and cellulose (0.14 V) separators (Figure 4.8c). Interestingly, using BC nanopaper as separator significantly reduced the IR drop and associated losses. Many studies calculate the gravimetric capacitance of full cell devices normalised to the total mass of the two active electrodes, even though the use of this normalisation can be confusing. The calculation can provide a comparative indication of the intrinsic performance of the active material, where three-electrode measurements are not available. In line with the earlier three-electrode measurements, the performance of the nanotubide buckypaper device remains similar/better than examples in the literature, when compared on a 2-electrode basis (Figure 4.13a-b). However, the data (Figure 4.8d) again show that the type of separator has a significant effect, especially at higher discharge rates. The intrinsic specific capacitance for electrode materials is best derived from three-electrode measurements involving the reference and counter electrodes. However, it is useful to compare the performance of active materials in the 2-electrode full cell system with the three-electrode system, in order to establish how much of the intrinsic material performance has been realised. From this perspective, the maximum symmetric cell capacitance should be one quarter that of the half-cell gravimetric performance, where both are normalised to active electrode mass (the multiplier of 4 accounts for the series capacitance of the two electrodes and their combined mass).[264] In fact, the full cell capacitance from a two-electrode measurement will be lower due to differential polarisation at the positive and negative electrodes, and other effects such as the higher resistance associated with a separator and limited electrolyte access due to the presence of solid current collectors and a separator. [199, 265] Here, the full cell performance is around half of the maximum indicated by the three-electrode value (Figure 4.7c and Figure 4.9a), as is typical, but highlighting scope for further improvement in the full cell performance, for example, by adjusting positive/negative electrode masses, and/or the electrolyte.[266, 267] A more relevant approach to evaluation for practical application, is to normalise the electrochemical performance to the full mass and volume of the cell, as an estimate of the anticipated energy/power density of future devices. The present device is still a lab test cell, but its performance was normalised by the total mass and volume of device. A more

developed device would still require current collectors and encapsulation, but these components represent a relatively small additional contribution; in any case, given the high conductivity of the buckypapers, it might be possible to avoid separator current collectors in certain device geometries. By this measure, the performance of the BC separator device is very encouraging, as summarised by the gravimetric (Figure 4.9b) and volumetric (Figure 4.9c) Ragone plots, reaching an energy density of 1.2 mWh/cm^3 (1.4 Wh/kg) at a power density of 174 mW/cm^3 (194 W/kg). The energy density only drops by 25% at 100 A/g maintaining 0.9 mWh/cm^3 (1 Wh/kg) at a power density of 16.4 W/cm^3 (18.2 kW/kg). Note that the power density, here, is derived from the energy density over the discharge time (E/t), which is a more practical measure than the (much larger) theoretical maximum power that can be estimated from $V^2/(4*ESR)$; these two measures should be carefully distinguished, although not all literature does so. To illustrate this difference, the maximum power here, calculated from $V^2/(4*ESR)$, reaches as high as 303 kW/kg when normalised by mass of active materials and 107 kW/kg normalised by total mass of the device.

Using the more modest, but representative E/t measure, the Ragone plots (Figure 4.9b-c) nevertheless again highlight the advantage of the BC separator over the conventional cellulose, in good agreement with the decreased R_{ct} and IR drop (Figure 4.8a-c). The high overall rate capability of the device is attributed to the good ion transport in both the nanotubide buckypaper and the BC separator.

In addition to enhancing transport, the thin separator minimises the parasitic mass and volume associated with the separator and the electrolyte that fills it. To evaluate long-term electrochemical stability of the device based on nanotubide buckypaper, a cyclability GCD test was performed over 50,000 cycles at 5 A/g (Figure 4.10a). The Columbic efficiency in the first cycle approached 100% and remained above 98% after 50,000 cycles, demonstrating a high electrochemical reversibility and structural stability of electrode materials.[268, 269] The imbalance of the charges between charging and discharging process after cycling stability test is likely due to the iR drop effect. Surprisingly, the absolute capacitance continued to increase, reaching 112% of the initial value after 50,000 cycles (Figure 4.10a). One possible explanation is that electrolyte (electro)wetting of increasingly debundled SWCNTs improves ionic access into the electrode pores.[270] However, in the current system, a stronger effect seems to derive from a redox contribution.

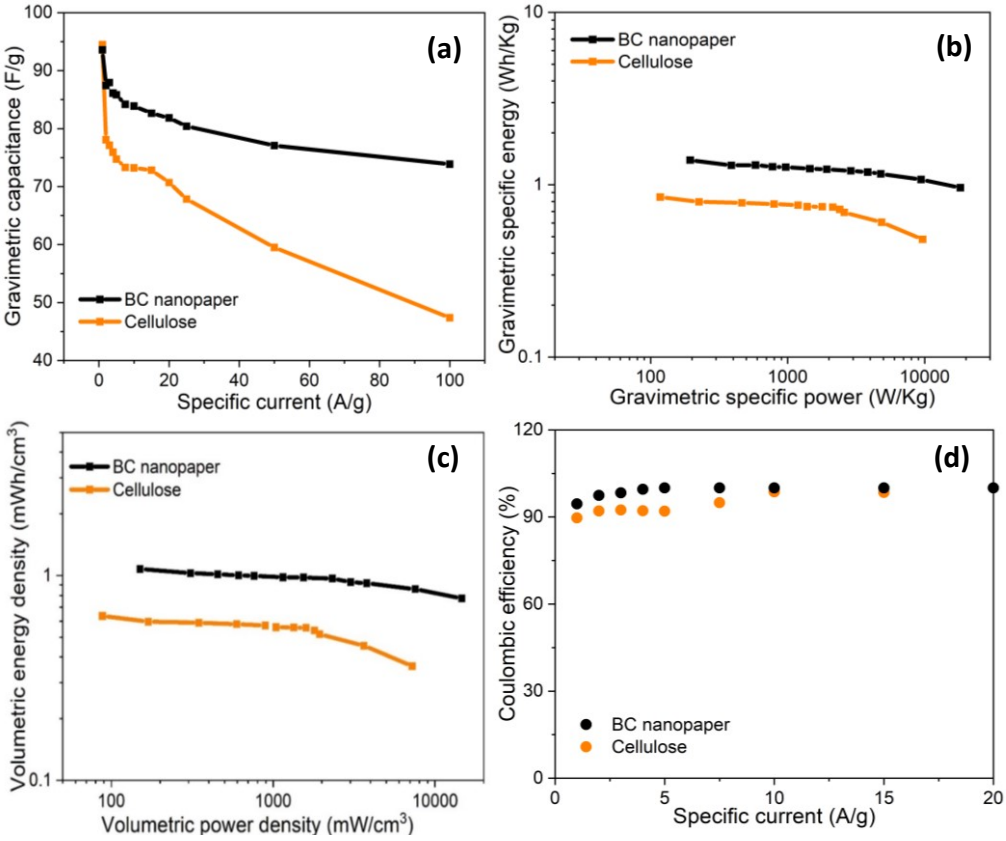

Figure 4.9 Nanotubide buckypaper symmetric supercapacitors using BC nanopaper (black) and cellulose (orange) as a separator with 1 M H_2SO_4: (a) the calculated cell gravimetric capacitance at specific current from 1 to 100 A/g and multiplied by 4 in order to compare the capacitance with three-electrode measurement, (b) cell gravimetric Ragone plots, (c) cell volumetric Ragone plots and (d) Coulombic efficiency vs. specific current.

Comparison of CV curves before and after cyclic stability testing shows a decrease of the small redox peaks around 0.4 V due to deoxygenation during cyclic testing (Figure 4.10b).[231, 271] Interestingly, redox peaks close to 0 V were observed in the CV curve after 50,000 GCD cycles. To explore the origins of these peaks, the washed and dried positive and negative electrodes were studied with XPS and Raman spectroscopy after the cyclic stability test. The XPS surveys (Figure 4.10c) show presence of two peaks at 164 and 229 eV attributed to sulphur (S2p and S2s, respectively), detected on both positive and negative electrodes due to possible adsorption of HSO^-_4 and SO_4^{2-} from the electrolyte. [231, 272] The I_D/I_G of both positive (0.048) and negative (0.023) electrodes increased slightly after cycling compared to the initial value before electrochemical test (0.014), which may be related to sulphate functional groups grafting on the electrode surface (Figure 4.10d). In addition, to the increased effective

area,due to sulphate intercalation, grafted sulphate functional groups may increase the capacitance by contributing pseudocapacitive behaviour.[273, 274]

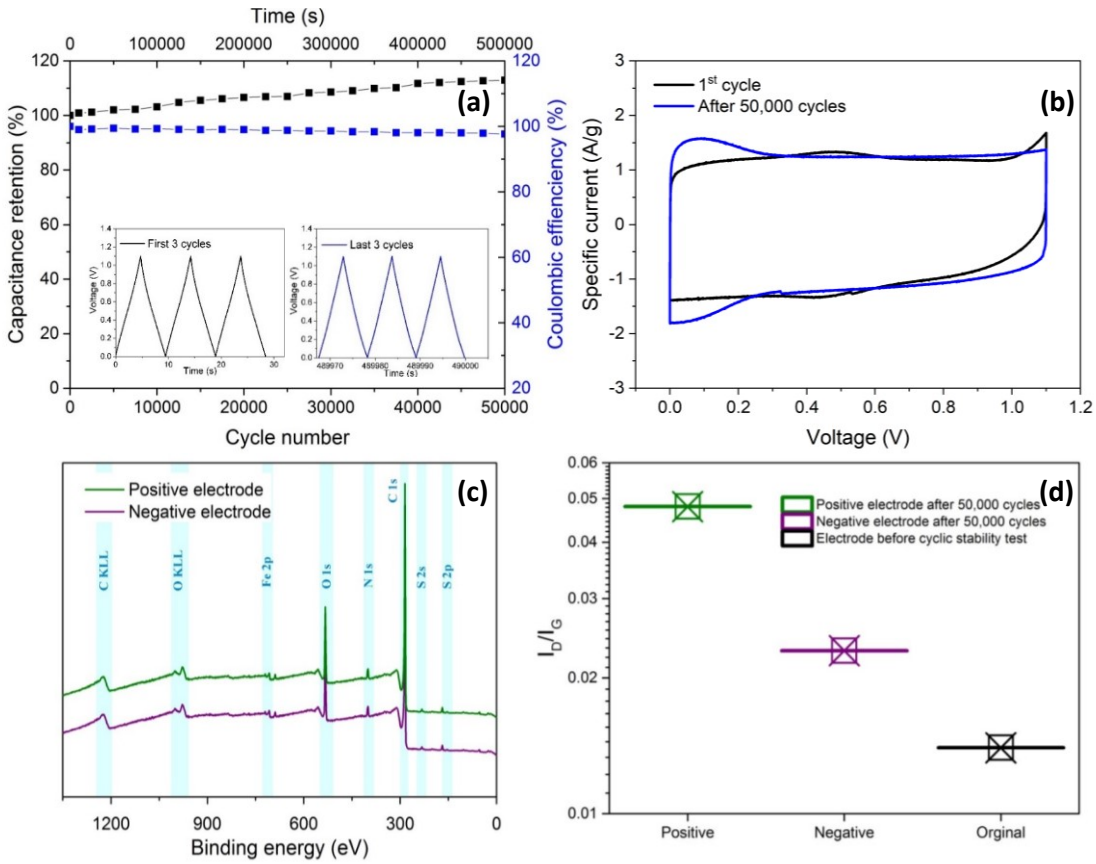

Figure 4.10 Cycling electrochemical performance of aqueous symmetric supercapacitors using nanotubide buckypaper electrodes sandwiched with BC nanopaper: (a) Capacitance retention and Coulombic efficiency during GCD cycling at 5 A/g. (b) CV curves at 50 mV/s before and after the cyclic stability test. (c) XPS and (d) Raman spectra of the as-fabricated nanotubide buckypaper device before and after cyclic stability testing in 1 M H_2SO_4.

4.6 Enlarging applied potential via using ionic liquid as electrolyte

4.6.1 Nanotubide buckypaper with ionic liquid electrolyte

Given the excellent performance in aqueous electrolyte, the nanotubide buckypaper electrode at the optimum condition ([C] = 1.5 mg/mL, C:Na = 10:1) was further investigated in [EMIM][TFSI] ionic liquid electrolyte. The use of ionic liquid was expected to improve the wetting of the SWCNT electrodes, while enhancing electrochemical potential leading to enhancing the energy density for full cell device.[275] [276] The CV curves of nanotubide buckypaper in three-electrode set up show a working potential window at 2.6 V range from

-1.0 V to 1.6 V vs. Ag in [EMIM][TFSI] (Figure 4.11a). The CV curves exhibit the unique butterfly shape in every scan rates. Similar behaviour has been previously reported for SWCNT-based materials with the explanation that the electrochemical doping of semiconducting properties of CNTs attributed to quantum capacitance contributions: the capacitance follows the density of states (DOS) near the Fermi level which manifests in dependence of capacitance on voltage.[277-279] However, this explanation is arguable because the butterfly shape only presents in ionic liquid system but does not show in aqueous system. if this behaviour is resulting from quantum capacitance, it should have been seen in every electrolytes. Therefore, another plausible explanation is the polarisation driven ingression of cation at negative potentials, and anions at positive potentials.[280] The electrochemical capacitance and the rate capability at high scan rate of nanotubide buckypapers in [EMIM][TFSI] (Figure 4.11b) are lower than the capacitance in 1 M H_2SO_4 (Figure 4.7c). This is due to the higher applied potential and lower ionic conductivity of [EMIM][TFSI] electrolyte.

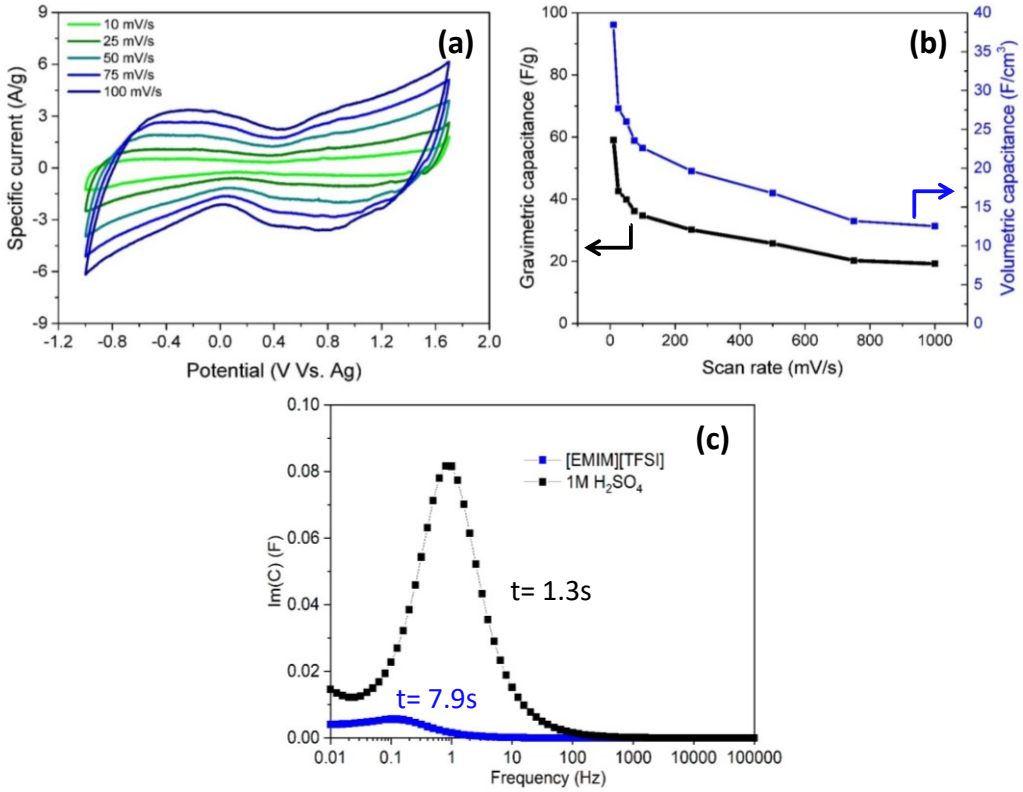

Figure 4.11 The electrochemical performance in three-electrode measurement, in [EMIM][TFSI] of optimised nanotubide buckypaper ([C] = 1.5 mg/mL, C:Na = 10:1): (a) CV curves from 10 to 50 mV/s and (b) gravimetric capacitance per electrode as a function of scan rate. (c) Imaginary capacitance against frequency of nanotubide buckypapers in [EMIM][TFSI] and 1 M H_2SO_4.

In addition, the relaxation time (τ_0), which is the minimum time required for discharging the stored energy in the electrode, was calculated, for which, it was observed that the smaller the relaxation time represents the higher power density of the electrode and electrolyte. [201, 208, 209] Hence, the response of frequency (f_0), corresponding to the maximum point of the energy curve, was estimated and represented at 0.77 and 0.12 Hz for aqueous and ionic liquid electrolytes respectively (Figure 4.11c). The relaxation time of nanotubide buckypaper in ionic liquid (7.9 s) is longer than the nanotubide buckypaper in aqueous electrolyte (1.3 s). These values present that aqueous system provide quicker access to the discharging process due to lower mobility in the ionic liquid which also relates to the lower rate capability from CV measurement in ionic liquid electrolyte.

4.6.2 Symmetric supercapacitor of nanotubide buckypaper with ionic liquid electrolyte

The symmetric device based on nanotubide buckypaper and BC nanopaper separator was tested further, in [EMIM][TFSI] ionic liquid electrolyte. The Nyquist plot (Figure 4.12a) gives ESR and R_{ct} of 3.9 and 3.6 Ω, respectively, confirming good conductivity and ion transport in the nanotubide buckypaper, although with some decrease in performance relative to the aqueous system, as expected due to lower mobility in the ionic liquid.[281, 282] The CV curves for the as-fabricated device have a stable butterfly shape (Figure 4.12b) and the GCD curves show a complex response (Figure 4.12c) attributed to quantum capacitance contributions. The effect is more obvious in the broader voltage range available in ionic liquid. The calculated electrochemical performance from GCDs (Figure 4.12e), normalised by the total volume and total mass of full device reaches 2.2 mWh/cm^3 (2.6 Wh/kg) of maximum energy density and 8.3 W/cm^3 (10.2 kW/kg) of maximum power density. As-fabricated, the symmetric ionic liquid device has twice the volumetric energy density of the aqueous device, due to the enhanced electrochemical window (Figure 4.9c and Figure 4.12e). Additionally, the electrochemical performance normalised by the mass and volume of the active material remains higher than other reported in literature (Figure 4.13a and b), with specific energy of 8.8 Wh/Kg (2.3 mWh/cm^3) and specific power of 34 kW/kg (9.1 W/cm^3). The cyclic stability of symmetric ionic liquid device was good, retaining 81% capacitance after 50,000 cycles (Figure 4.12f). However, the stability is lower than the aqueous system due to greater voltage range, combined with

the tendency for electrolyte decomposition or other side reactions after long term cycling.[25, 283] The increase after the first 3000 cycles may again relate to electrochemically driven swelling[284] or grafting of redox active species [228, 273, 274].

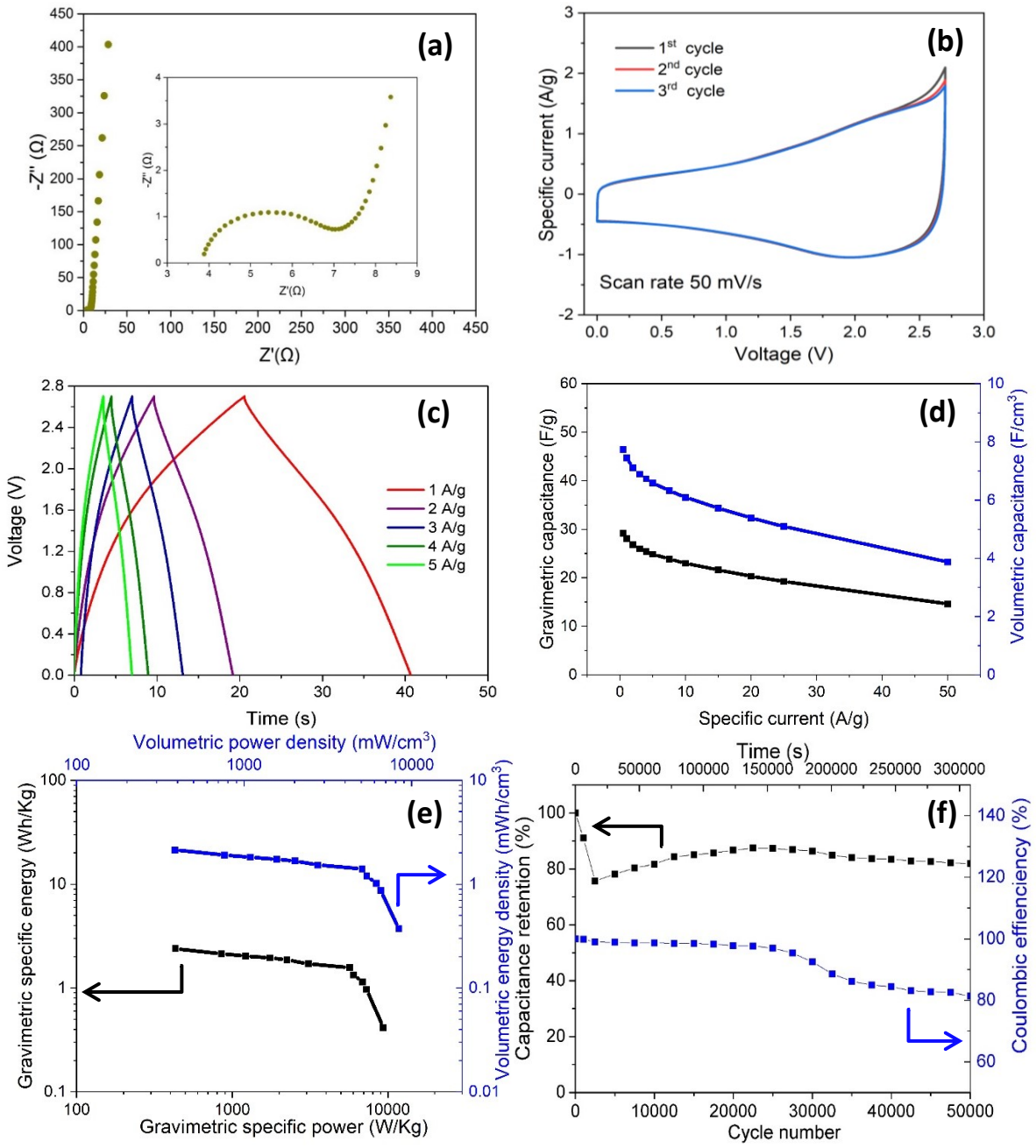

Figure 4.12 Nanotubide buckypaper symmetric supercapacitors using BC nanopaper as separator and [EMIM][TFSI] as electrolyte; (a) Nyquist plot, (b) CV curves at 50 mV/s , (c) GCD curves from 1 to 5 A/g, (d) gravimetric and volumetric capacitance, (e) Ragone plots and (f) capacitance retention and Coulombic efficiency.

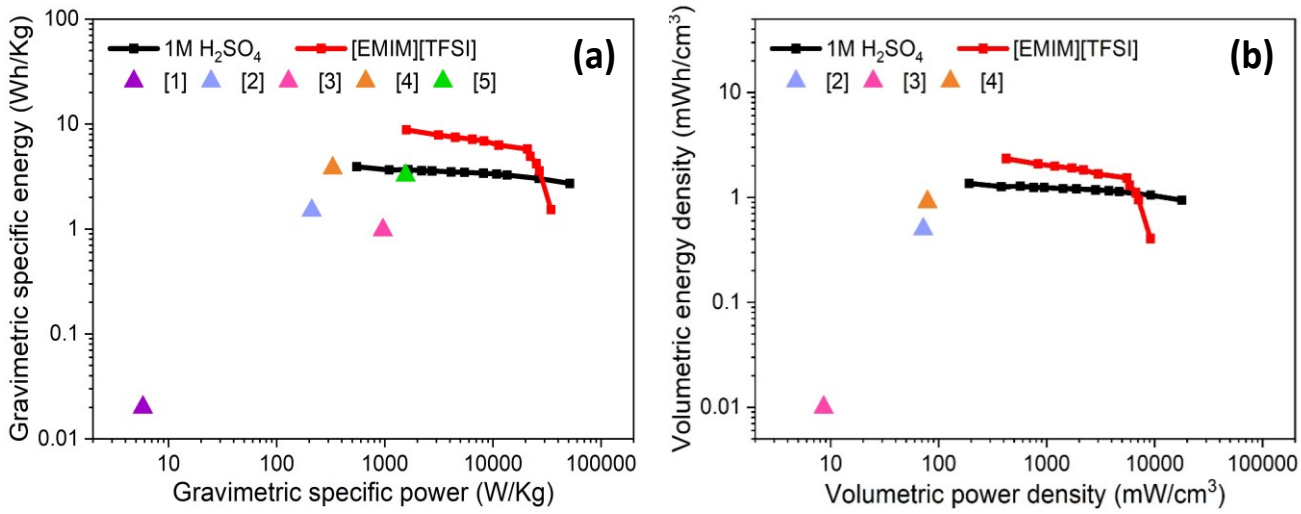

Figure 4.13 (a) Gravimetric and (b) volumetric Ragone plots for full devices of CNT based film symmetric supercapacitors from ref: 1) M. Kaempgen *et al.,* 2007 [285] 2) D. K. Kim *et al.,* 2018 [286] 3) Z. Niu *et al.,* 2013[287] 4) C. Yu *et al.,* 2009[288] 5) X. Li *et al.,* 2012 [289]. Note, full-cell symmetric supercapacitors of nanotubide buckypapers sandwiched with BC nanopaper using 1 M H_2SO_4 and [EMIM][TFSI] as electrolytes are presented in black and red lines respectively.

4.7 Conclusions

In summary, SWCNT buckypapers were successfully synthesised via reductive charging with sodium naphthalide. This method improves the dispersion of SWCNTs without damaging their structure, while contributing additional purification. The carbon and sodium concentrations in the precursor mixture play major role in the dissolution process and hence the resulting buckypaper structure and electrochemical performance. The optimised concentrations of carbon and sodium were 0.125 M and 12.5 mM, respectively, similar to optimums identified for chemical modification. These intermediate values likely reflect the balance of Coulombic repulsion and charge condensation effects, known in more conventional polyelectrolytes.[105] The optimised nanotubide buckypaper provided a specific surface area of 412 m^2/g, good electrical conductivity of 433 S/cm and significantly better electrochemical performance, compared to previous studies of carbon-based buckypaper electrodes. In combination with its intrinsic scalability, avoiding ultrasonication, reductive processing is a promising candidate for energy storage applications. The development of BC nanopaper provides a new, simple and thinner separator which decreases resistive

loses and maximises volumetric performance in a configured full cell device. The BC separator also readily prevents short circuits between the two electrodes and provides a high device efficiency with long cycle life. BC is widely available as a starting material (the raw material is typically consumed as a foodstuff). BC papers are, therefore, promising electrochemical separators for use in practical applications, in a wide range of devices.

The symmetric nanotubide buckypaper supercapacitors in both aqueous and ionic liquid electrolytes achieve high gravimetric and volumetric performances compared to other symmetric devices based on CNT buckypapers, in the literature (Figure 4.13a and b). Therefore, the reductive charging strategy is a promising approach for high-performance energy storage devices with simple paper electrodes. Further optimisation of electrode thickness, electrolyte, and cell balance will improve performance further. In addition, the wide range of nanotubide chemistry will provide a convenient route to produce hybrid redox-active SWCNT electrodes in the future, for supercabatteries,[17] with enhanced energy density, as explored further in Chapter 6.

5. Improving nanotubide buckypapers: exploring alternative feedstocks and covalent cross-linking reactions

5.1 Introduction

As shown in Chapter 4, reductively-processed nanotubide buckpapers have attractive properties, particularly high gravimetric (218 F/g at 10 mV/s) and volumetric (74 F/cm^3 at 10 mV/s) capacitance. However, the electrochemical rate capability was not high as expected; for example, the capacitance dropped 21% after increasing the scan rate from 10 to 100 mV/s even at the optimum condition ([C] = 1.5 mg/mL, NaC_{10}) with a good electrical conductivity of 433 S/cm. Supercapacitors are typically used for their power density, hence it is important to maintain high rate capability while increasing the specific current and/or scan rate. If the relatively poor rate performance is attributed to slow ion transport, due to the packing / rebundling of the SWCNTs, one solution would be to trap a more open network, though cross-linking reactions. Nanotubides are highly reductive species which can react spontaneously with suitable electrophilic functionalities such as alkyl halides, epoxies and diazonium salts.[11] The mechanism can be most simply described as a single electron transfer from the SWCNT to the reagent, which generates a radical anion that subsequently covalently binds to the sidewalls ; in fact, the detailed mechanism likely involves the formation of a complex intermediate, as elucidated by electrochemical measurements performed during this PhD program and reported elsewhere.[5, 6] This reaction can promote SWCNT network formation though cross-linking with a difunctional electrophile.[11] A cross-linked nanotubide network is expected to enhance uniformity of the pore sizes by fixing the SWCNTs position in the nanotubide gel network, and inhibiting rebundling during drying.[290, 291] Additionally, the cross-linking via reductive charging process could give the possibility to scale up the as-synthesised nanotubide buckypaper without damaging SWCNT structure and be able to maintain the good electrical and electrochemical properties.

In this chapter, cross-linked nanotubide buckypapers were formed using diiodobenzene (DIB) as a cross-linker. DIB was selected as a cross-linking agent because it is a rigid, soluble,

potentially conjugated and dielectrophilic molecule which can be used to bridge adjacent negatively charged SWCNTs to produce a closely-connected SWCNT network.[11] The first part of this chapter explores the effect of this cross-linking chemistry on electrochemical performance; DIB:Na stoichiomtry, SWCNT type, and filtration method were investigated to maximise the extent of nanotubide debundling. The optimum carbon concentration and charging ratio of nanotubide solution were maintained from the previous chapter. The effects of thickness and density on the electrochemical performance were then further studied by scaling up the mass loading of cross-linked nanotubide per unit area. In addition, since cross-linking is also expected to modulate load transfer, mechanical performance was determined to explore opportunities for multifunctional applications.

5.2 Experimental procedure

5.2.1 Cross-linked nanotubide buckypaper via gravimetric filtration

As-received Tuball75 and Tuball99 SWCNT powders were purified then introduced into the glovebox following the procedure described in Sections 4.2.1 and 4.2.3. For preparing reductive stock solution, 50 mg of sodium and 278 mg of naphthalene were stirred in 50 mL of DMAc at the room temperature overnight using a glass stirring bar. The sodium naphthalide (NaNp) was added to 75 mg of purified SWCNT powder. The ratio between mol C: mol Na and carbon concentration were fixed at the optimum condition from chapter 4 ([C] = 1.5 mg/mL, NaC_{10}). The nanotubide solution stock was stirred for 24 hrs. Then, 4.67 mL of nanotubide solution (7 mg of SWCNTs) was deposited onto PTFE membrane placed on a filtration system inside the glove box followed by the addition of 1,4-diiodobenzene (DIB) solution to initiate the cross-linking reaction. The concentration of DIB was varied from 0.5-1.25 eq relative to sodium to further study the effect of cross-linker on the buckypaper performance. After leaving a cross-linked buckypaper for functionalisation overnight inside the glovebox, the cross-linked nanotubide buckypaper was taken out from the glove box in a sealed glass flask with a suba-seal stopper and then quenched with dry air (N_2/O_2, 80/20) to remove the remaining charge. To remove the remaining impurities, and salt by-products, the quenched cross-linked nanotubide buckypaper was washed with DMF, water and ethanol via solvent exchange. Finally, cross-linked nanotubide buckypaper was dried in a vacuum oven at 110°C overnight.

5.2.2 Cross-linked nanotubide buckypaper via vacuum filtration

For preparing cross-linked nanotubide buckypapers via vacuum filtration, the nanotubide solution was prepared as described in Section 4.2.3 and followed by adding cross-linker similar to Section 5.2.1. However, the procedure of filtration was changed from filtering via gravimetric force overnight to manual vacuum filtration (Figure 5.1). Due to the inconvenience of using a vacuum pump in the glove box, vacuum was applied using a syringe. A syringe was attached to the glass connector of the filtering flask (250 mL) using flexible tubing with internal diameter 1.2 cm. The syringe was then withdrawn and held to apply vacuum; this procedure was repeated another 5 times. The as-prepared buckypapers were then taken out of the glove box in a sealed glass flask with a suba-seal stopper and quenched with dry air (N_2/O_2, 80/20), followed by solvent exchange to remove impurities with similar procedure as 5.2.1. In the final step, the buckypapers were dried at 60°C in a vacuum oven overnight. In order to studying the effect of mass loading of SWCNT per unit area on the conductivity, mechanical properties and electrochemical performance, the mass loadings of SWCNTs per buckypaper were varied from 1.4 to 3.2 mg/cm^2 at the condition of [C] = 1.5 mg/mL, C:Na = 10:1 and DIB:Na = 7.5:1 by mole.

Figure 5.1 Manual vacuum filtration set-up.

5.3 Cross-linked nanotubide buckypaper via gravimetric filtration

5.3.1 Influence of cross-linker concentration on SWCNT buckypaper properties

In the first part of this chapter, the diiodobenzene (DIB) was added into the nanotubide solution to form cross-linked nanotubide buckypapers via gravimetric filtration (Section 5.2.1). The stoichiometry between DIB and Na was varied from 0 to 1.25 to optimise the solubilisation of DIB in nanotubide solution, network structure and the electrochemical performance of the as-synthesised electrodes. The structure of as-synthesised cross-linked nanotubide buckypapers with molar ratio of DIB:Na from 0.5 to 1 (Figure 5.2a-c) show highly porous SWCNT network with larger uniform pore size and more dispersed structures compared with the uncross-linked control (Figure 4.6b). However, when the molar ratio of DIB and Na exceeds 1, SEM images show evidence of impurities which may be caused by self-condensation of DIB, leading to organic deposits on buckypaper surface (Figure 5.2d). These impurities may lead to poorer ion transport by blocking electrolyte access through buckypaper.

The electrical conductivity of cross-linked nanotubide buckypapers (Figure 5.3a) decreases with increasing concentration of DIB, both due to the intrinsically low conductivity of DIB and the reduced packing efficiency of SWCNTs in the films (Figure 5.3a). On the other hand, the cross-linked nanotubide buckypaper also has a more dispersed network which has been reported to improve inter-tube (bundle) electrical contacts and increase conductivity.[292 62] From TGA curves in N_2, The DIB reaction products decomposed and were removed around 400 ^{o}C (Figure 5.3b); the weight loss increased with DIB concentration, consistent with deposition of self-condensation products, when exceeding the stoichiometry able to react with the nanotubide directly.

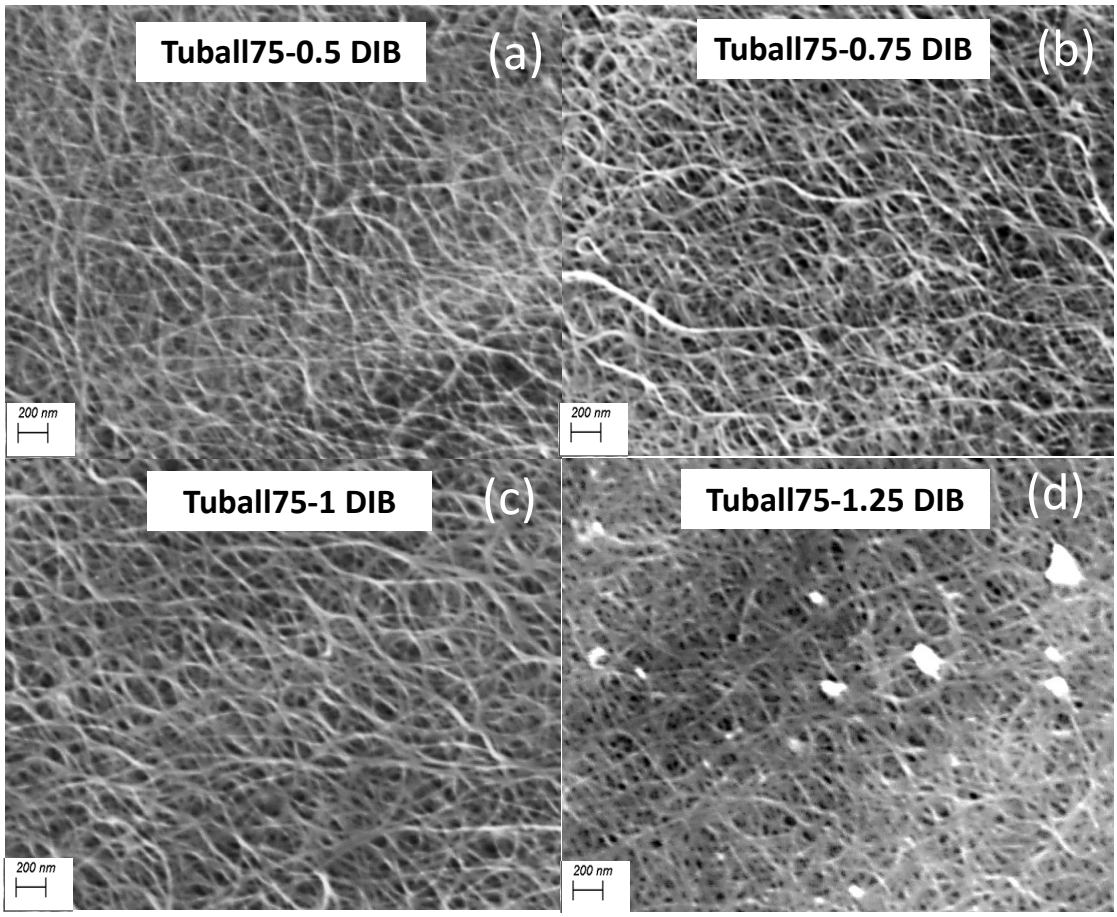

Figure 5.2 SEM images of cross-linked nanotubide buckypapers (top surface) via gravimetric filtration at different molar ratios of DIB:Na ; (a) 0.5:1, (b) 0.75:1, (c) 1:1 and (d) 1.25:1. Note, the carbon concentration and C to Na ratio of every samples are controlled at 1.5 mg/mL and 10:1 respectively.

In general, the iodine associated the metathesis reaction is removed from buckypaper as NaI during washing. However, where only one of the iodides on DIB can react, either due to the stoichiometry of the sodium available or the steric constraints on the grafting aryl group, some iodine will remain in the form of phenyl iodide grafted to the SWCNT network. [11] XPS (Figure 5.3c) shows the presence of C 1*s* and O 1*s* peaks at 284.9 and 533.2 eV respectively, in the SWCNT starting material, nanotubide buckypaper and cross-linked nanotubide buckypaper. Iron (Fe 2p), associated with the SWCNT synthesis catalyst, is also observed in all cases. However, the atomic percentages of Fe in both nanotubide buckypapers are lower than the starting material (Table 5.1), indicating that the reductive chemistry can provide a degree of purification, as reported previously.[10] The O 1s spectra of cross-linked nanotubide buckypapers (Figure 5.3d) have three peaks at 533.4, 532.4 and 531.5 eV which are assigned

to C-OH, C=O and -COOH functional groups, respectively.[237, 238] The oxygen content in cross-linked nanotubide buckypaper (3.97 at%) is higher than the starting material (1.82%, Table 5.1). This increase may be due to the formation of hydroxyl groups during quenching dry process and/or hydrolysis of the grafted phenyl iodide groups. Iodine (I 3d peak) was detected on cross-linked nanotubide buckypaper, attributed to grafted phenyl iodide associated with mono-reacted DIB linker; the concentration may be lowered by adventitious hydrolysis of the sample by atmospheric water.

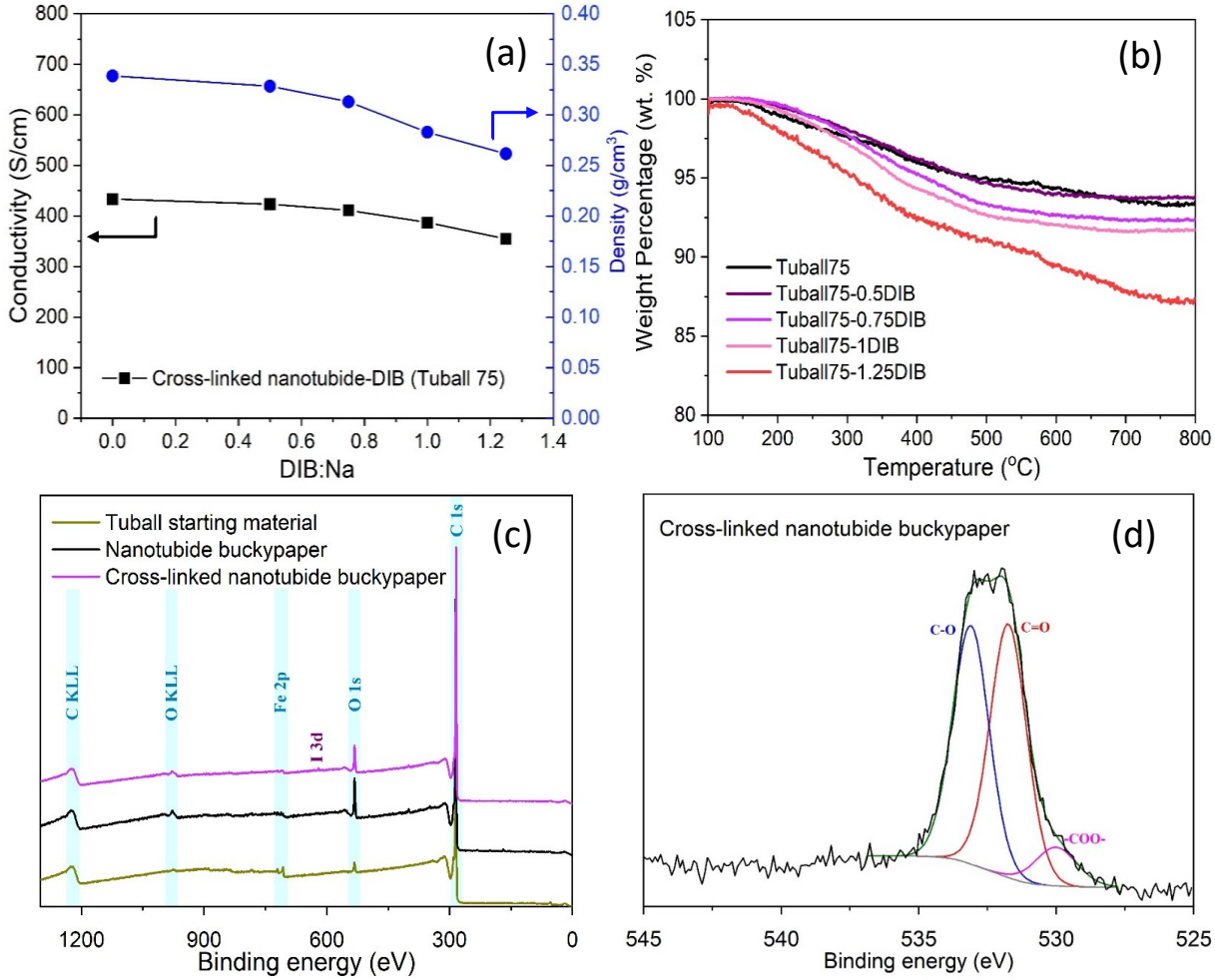

Figure 5.3 (a) Electrical conductivity- film density and (b) TGA curves under N_2 of cross-linked nanotubide buckypaper at different DIB:Na. (c) XPS survey scans of starting materials and as-synthesised buckypaper. (d) O 1*s* of cross-linked nanotubide buckypaper at molar ratio of DIB : Na 0.75:1.

Table 5.1 XPS-derived compositions of SWCNT powder, nanotubide buckypaper and cross-linked nanotubide buckypaper.

Sample	at% element			
	at% C	at% O	at% Fe	at% I
SWCNT powder (Tuball75)	97.70	1.82	0.48	0.00
Nanotubide buckypaper ([C] = 1.5 mg/mL, NaC_{10})	95.09	4.74	0.17	0.00
Cross-linked nanotubide buckypaper ([C] = 1.5 mg/mL, NaC_{10}, DIB:Na =0.75:1)	95.88	3.97	0.09	0.06

The nanotubide buckypapers cross-linked at different molar ratio of DIB:Na were studied in three-electrode measurement with 1 M H_2SO_4 as an electrolyte. In all cases, the CV curves at 50 mV/s exhibited similar rectangular shapes characteristic of EDLC behaviour. The presence of the small redox peaks on CV curves of cross-linked nanotubide buckypapers are associated with oxygen-groups (Figure 5.4a), contributing to the pseudocapacitive behaviour, as observed for nanotubide buckypapers in Section 4.3. As the scan rate increased to 500 mV/s (Figure 5.4b), the CV of uncrosslinked nanotubide buckypaper begins to distort while the cross-linked samples better retain their near rectangular shape, as well as a larger area under the curve. This result is consistent with a more open network structure leading to better ion transportation and higher electrochemical performance. The optimum cross-linking (DIB: Na = 0.75:1) maintained the electrochemical rate capability up to 92% after increasing the scan rate from 10 to 100 mV/s and increased gravimetric capacitance (20%) compared to the nanotubide buckypaper control, at 100 mV/s. However, when the molar ratio of DIB:Na exceeded 1:1, the gravimetric capacitance decreased by 27% relative to the control (Figure 5.4c). This loss of performance can be attributed to occlusion of the SWCNT network with self-condensed DIB, as observed in the SEM images (Figure 5.2d). At low scan rates, the

volumetric capacitance (Figure 5.4d) of the optimum cross-linked nanotubide buckypaper (71 F/cm^3 at 10 mV/s) was similar to the control nanotubide buckypaper (74 F/cm^3 at 10 mV/s). In this case, the improved gravimetric capacitance is counter-balanced by the lower density of the cross-linked system (Figure 5.3a), resulting in lower volumetric capacitance.

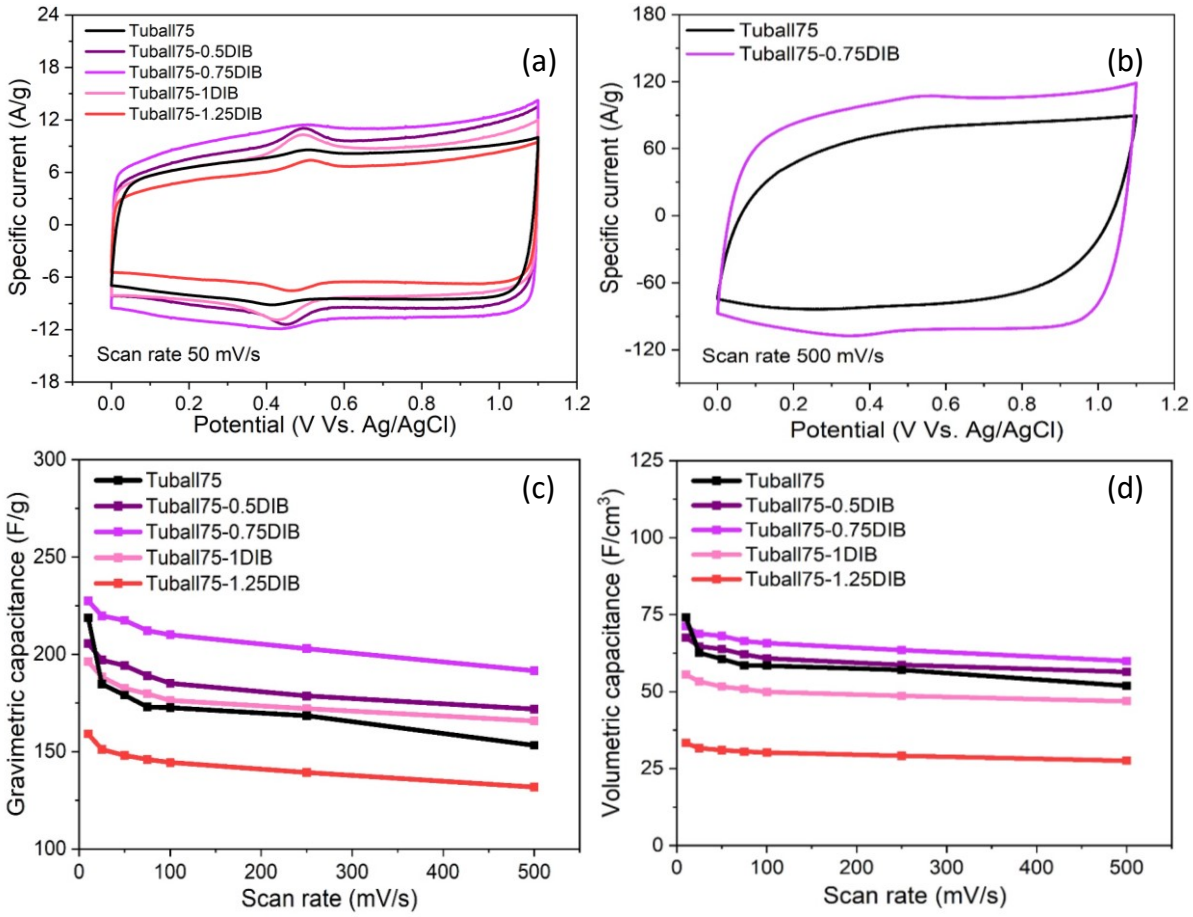

Figure 5.4 Electrochemical performance of cross-linked nanotubide buckypapers via gravimetric filtration in three-electrode system at different molar ratio of DIB:Na: **(**a**)** CV curves at 50 mV**/**s, **(**b**)** CV curves at 500 mV**/**s, (c) gravimetric and (d) volumetric capacitance as a function of scan rate in 1 M H_2SO_4.

The effect of DIB concentration on buckypaper structure can be related to electrochemical performance, by considering the accessible surface area. Conventional adsorption measurements can provide an independent measurement of textural characteristics, but unfortunately, due to COVID-restrictions, no suitable BET instrument was available. Instead, in this chapter, a more directly relevant estimate of the ECSA is used to quantify the active surface area of the electrode. The ECSA of carbon-based electrodes is commonly calculated from the double layer capacitance (C_{dl}) of the CV curve in a range with no Faradaic reaction.[214]

However, the CV curves of the nanotubide and cross-linked nanotubide buckypapers (Figure 5.5a and c) show broad redox peaks at every scan rate, due to the redox activity from oxygen functional groups. Given that the CV curves show the similar rectangular shapes with apparently small redox features, the diffusion-controlled contribution may be negligible. However, to validate this assumption more quantitatively, the total capacitance of an electrode can be divided into two parts: the capacitive and diffusion-controlled processes. The pure surface controlled process is, in principle, independent of the specific current or the scan rate, whereas the contribution related to ion diffusion (whether within the electrolyte or the electrode material) is expected to be proportional to the square root of scan rate.[293, 294] The surface controlled contribution at different scan rates can be examined by following equation 3.8 where a constant scan rate is applied. The contribution of the diffusion controlled processes was confirmed to be very small (less than 10% of the total capacitance) for both the nanotubide control (Figure 5.5b) and cross-linked nanotubide buckypaper (DIB:Na =0.75:1 , Figure 5.5d); as expected, the surface controlled contribution increases with the scan rate. Therefore, the diffusion controlled contribution may be taken as negligible and the C_{dl} can be estimated from the slope of these CV curves. The ECSA of nanotubide and cross-linked nanotubide buckypapers were calculated simply by analysing the scan of CV curves from 10 to 100 mV/s. To minimise the contribution from pseudocapacitive behaviour, the anodic current was measured at 0.8 V, far from the redox peak position; then equations 3.19 and 3.20 were applied. The highest ECSA of the cross-linked nanotubide buckypapers (627 m^2/g), achieved at 0.75 DIB:Na, is 25% higher than the nanotubide buckypaper control (474 m^2/g). The result confirms that cross-linking improves the dispersion of SWCNTs within network (Figure 5.5e). However, the ECSA reduced at higher DIB:Na ratios (Table 5.2), consistent with the occlusion discussed above.

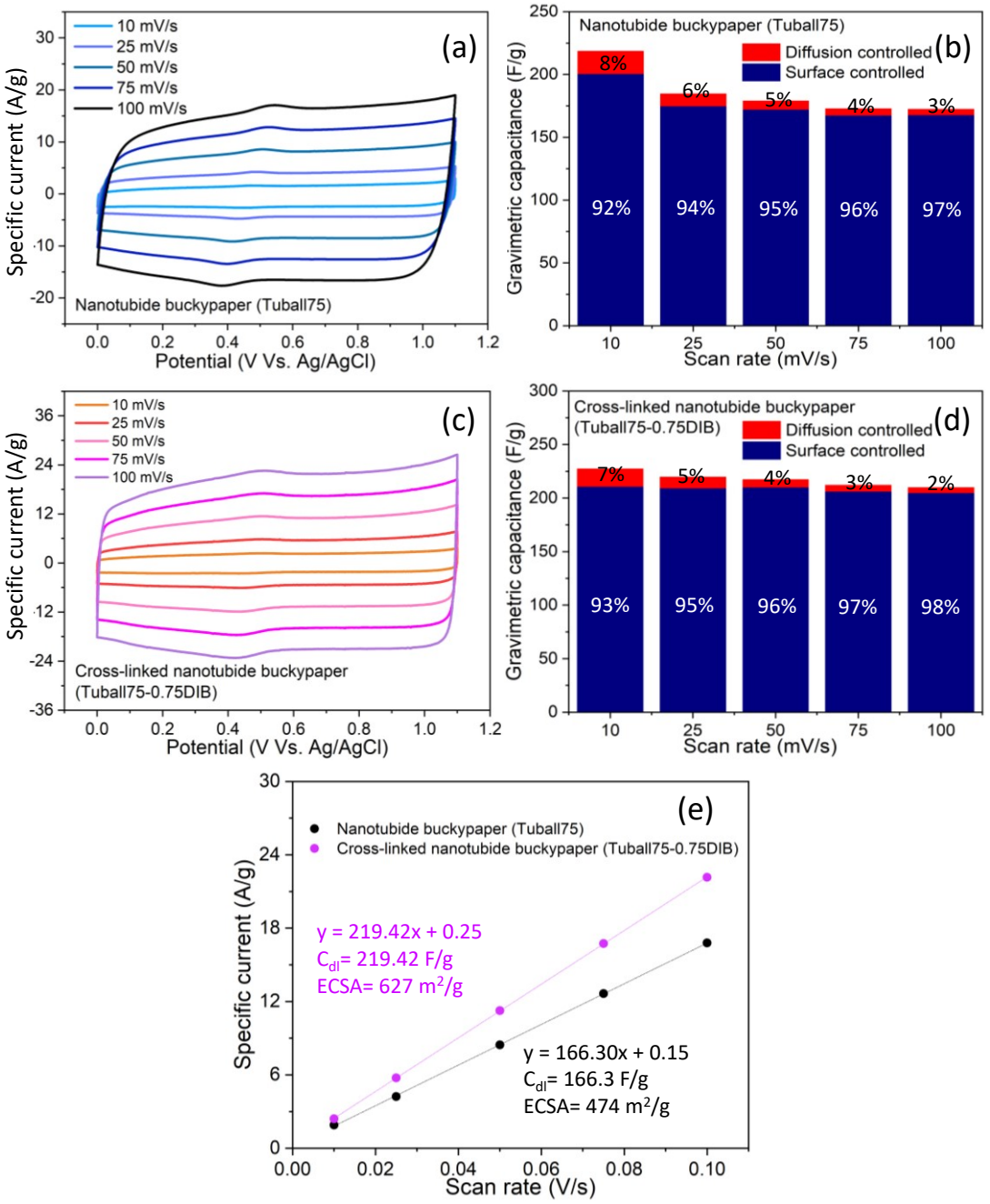

Figure 5.5 (a) CV curves at various scan rates from 10 to 100 mV/s and (b) relative contributions of the capacitive and diffusion-controlled charge at various scan rates of nanotubide buckypaper in three-electrode measurements using 1 M H_2SO_4 as an electrolyte. (c) CV curves at various scan rates from 10 to 100 mV/s and (d) relative contributions of the surface cotrolled and diffusion-controlled capacitance at various scan rates of cross-linked nanotubide buckypaper in three-electrode measurements using 1 M H_2SO_4 as an electrolyte. (e) Corresponding anodic charging current densities of cross-linked nanotubide and nanotubide buckypapers measured at 0.8 V vs. Ag/AgCl, plotted as a function of scan rate.

To study the relation of ECSA and BET of as-synthesised materials to the electrochemical performance, the ECSA (Figure 5.6a) and specific surface area from BET measurement (Figure 5.6b) of nanotubide buckypapers were benchmarked then compared with other carbon-based materials which reported in the literature.[216, 295-301] Although BETs of the full sample set were not available, the ECSA values can be benchmarked against BET obtained for the pure Tuball 75 buckypaper and the optimised cross-linked version. These values can be plotted on general literature trends. In principle, BET surface area might be expected to relate to ECSA, however, the ECSA may be proportionately lower if the larger electrolyte ions cannot fully access those areas probed by nitrogen adsoprtion. For example, activated carbon has very high specific surface area (1000-3500 m^2/g) but its specific capacitance is usually lower than 200 F/g in aqueous electrolyte; the activated carbon is mostly comprised with micropores which the electrolyte ions can hardly access. [30] While the nanotubide buckypaper has lower specific surface area at 412 m^2/g, it can nevertheless achieve 218 F/g. In general, SWCNT networks have a high ECSA for their BET because they have an open network, no slit pores, and space to accommodate a double layer.[79] The ECSA of cross-linked nanotubide buckypaper (Tuball75-0.75DIB) and Tuball75 buckypaper are considered to be in the high range when compared with other carbon materials (Figure 5.6a). These results have a same trend as the gravimetric and volumetric capacitance of the carbon-based materials where the Tuball75 buckypaper and cross-linked nanotubide buckypaper (Tuball75-0.75DIB) have shown to be in the high range value (Table 4.2). ECSA measurements is reliable technique to study the relationship between surface area and electrochemical performance as it can identify the real ion-accessible interface in electrochemical applications resulted in the maximised utilisation of both the porous structure and heteroatoms. [216]

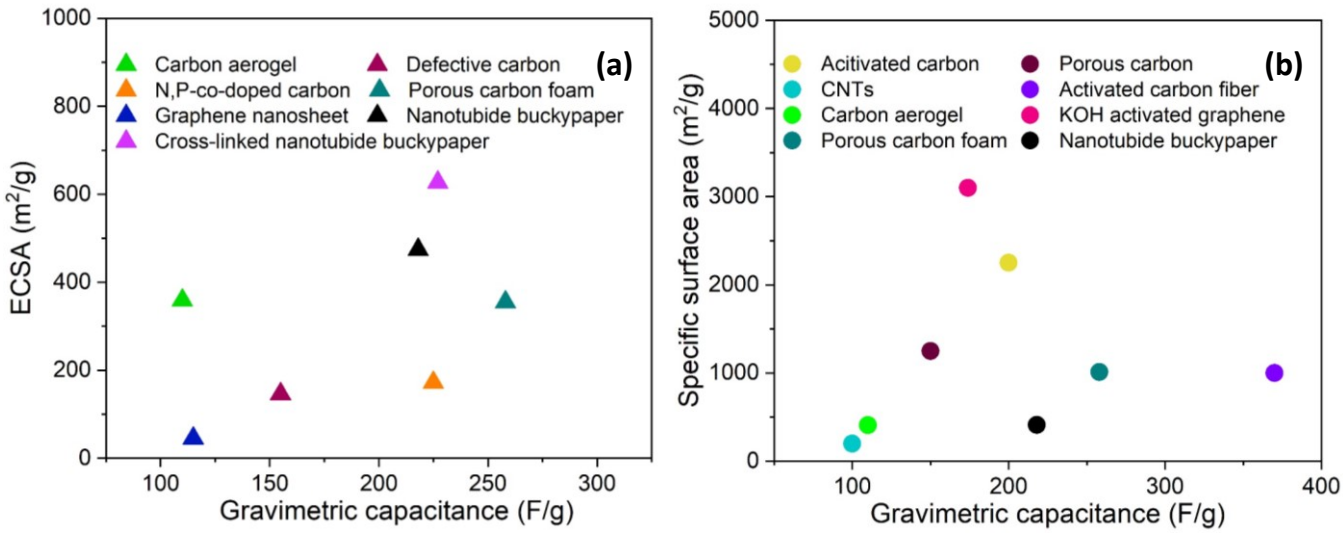

Figure 5.6 (a) ECSA vs. gravimetric capacitance of nanotubide and cross-linked nanotubide buckypaper compared to other carbon-based materials in the literature. (b) Specific surface area from BET measurement of nanotubide buckypaper compared with other carbon-based materials. [296, 300-302] Note, the ECSA and gravimetric capacitance of all carbon based materials in (a) and (b) were calculated from CV curves measured in aqueous electrolytes.

Further information about the response of the cross-linked nanotubide electrodes was obtained from EIS. Nyquist plots (Figure 5.7) show typical, excellent, EDLC responses for all electrodes due to the high intrinsic conductivity of SWCNT materials. The ESRs of cross-linked nanotubide buckypapers increase when the DIB concentration increases, showing a similar response to the electrical conductivity data (Figure 5.3a) due to increasing thickness and hence decreasing density. The R_{ct} of cross-linked nanotubide buckypaper also increases with the DIB concentration which possibly due to the occlusion of the pores. However, at the highest DIB to Na ratio (1.25:1), the R_{ct} was reduced, possibly due to the impurities deposited on top of the surface blocking pore access (Table 5.2). Note R_{ct}, gravimetric capacitance, ECSA all peak at intermediate DIB-concentrations, presumably due to the transition from DIB-crosslinking to self-condensation/coating with organic by-products.

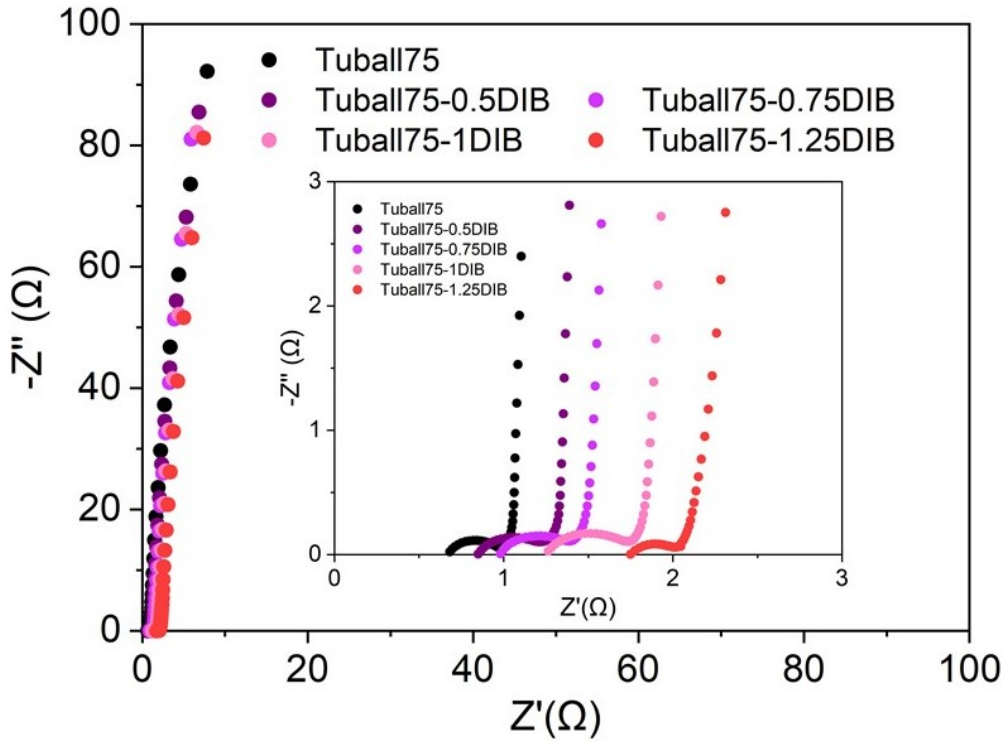

Figure 5.7 Nyquist plot of cross-linked nanotubide buckypaper at different molar ratio of DIB: Na. Where [C] = 1.5 mg/mL and C:Na=10:1 are controlled for every buckypapers.

Table 5.2 ESR, R_{ct}, thickness, density, ECSA and tensile modulus at 0.5-1% strain of nanotubide and cross-linked nanotubide buckypapers (Tuball75) at different ratios of DIB:Na.

mol DIB : mol Na	ESR(Ω)	R_{ct}(Ω)	Thickness (µm)	Density (g/cm^3)	ECSA (m^2/g)	Tensile modulus of elasticity (MPa)
0	0.69	0.32	38.4±0.5	0.34±0.01	474	300±20
0.5	0.85	0.42	40.6±0.5	0.32±0.01	558	118±27
0.75	0.98	0.45	42.6±0.5	0.31±0.01	627	84±13
1	1.26	0.51	44.2±0.4	0.28±0.01	492	79±15
1.25	1.75	0.28	47.8±0.3	0.26±0.01	389	63±12

The mechanical properties of the nanotubide and cross-linked nanotubide buckypapers (Tuball75) produced via gravimetric filtration were measured using a conventional tensile test

(as described in section 3.4.1). Note, the set of 5 specimens were prepared via cutting 1 buckypaper into 5 pieces. The scatter of the results in stress/strain curves may be associated with the difference in thickness between each speciemens caused by the variations in nanotubide deposition on the filter leading to thicker films closed to the edge of the filter.

The nanotubide buckypaper control has a tensile modulus and ultimate strength of 300±13 and 13±1 MPa, respectively. The stress-strain curve (Figure 5.8a) shows a plastic yielding behaviour, with a strain to failure of around 10%. The response is typical conventional buckypapers prepared by filtration of surfactant stabilised dispersions [strength ~10 MPa].[76] Various attempts have been made, in the literature, to improve the mechanical performance of buckypapers, including for example wet pressing and cross-linking[303], stretching and pressing[304], and embedding in resin[305, 306]. The cross-linked nanotubide buckypapers show a different stress strain response to the control (Figure 5.8b-e). There is no yielding, instead a linear elastic behaviour to brittle failure, or even a strain-stiffening effect. The absolute strength and modulus gradually decrease with the proportion of cross-linker (Figure 5.8f). One key factor is the density of the films; higher density is expected to lead to higher strength and stiffness. Indeed, the modulus does follow density in these samples (Table 5.2). However, the dramatically high modulus and different character of the control from the cross-linked samples indicates a more fundamental difference in load transfer mechanism. Stress transfer in the control nanotubide buckypaper is expected to derive from van der Waals interactions and nanotube entanglement.[307, 308] There is a significant degree of contact between the (re)bundled SWCNTs generating an effective stress transfer and relatively high stiffness at low loads, but little to prevent inter-tube sliding, leading to softening and plasticity. In contrast, the more dispersed cross-linked samples have less direct contact between the SWCNTs, reducing the initial load transfer and hence stiffness. However, the covalent cross-links do not permit sliding, generating a linear elastic response, or even strain hardening as the network locks.[309, 310] The change in mechanical behaviour is good evidence for chemical modification of the SWCNTs which mediates load transfer.

Although the cross-linked samples have lower strength, they have higher strain to failure (Figure 5.8b-e). This inverse relationship is often observed; here the lower density samples can presumably deform further due to elastic deformation of the network, particularly where node sliding is prevented.[311, 312]

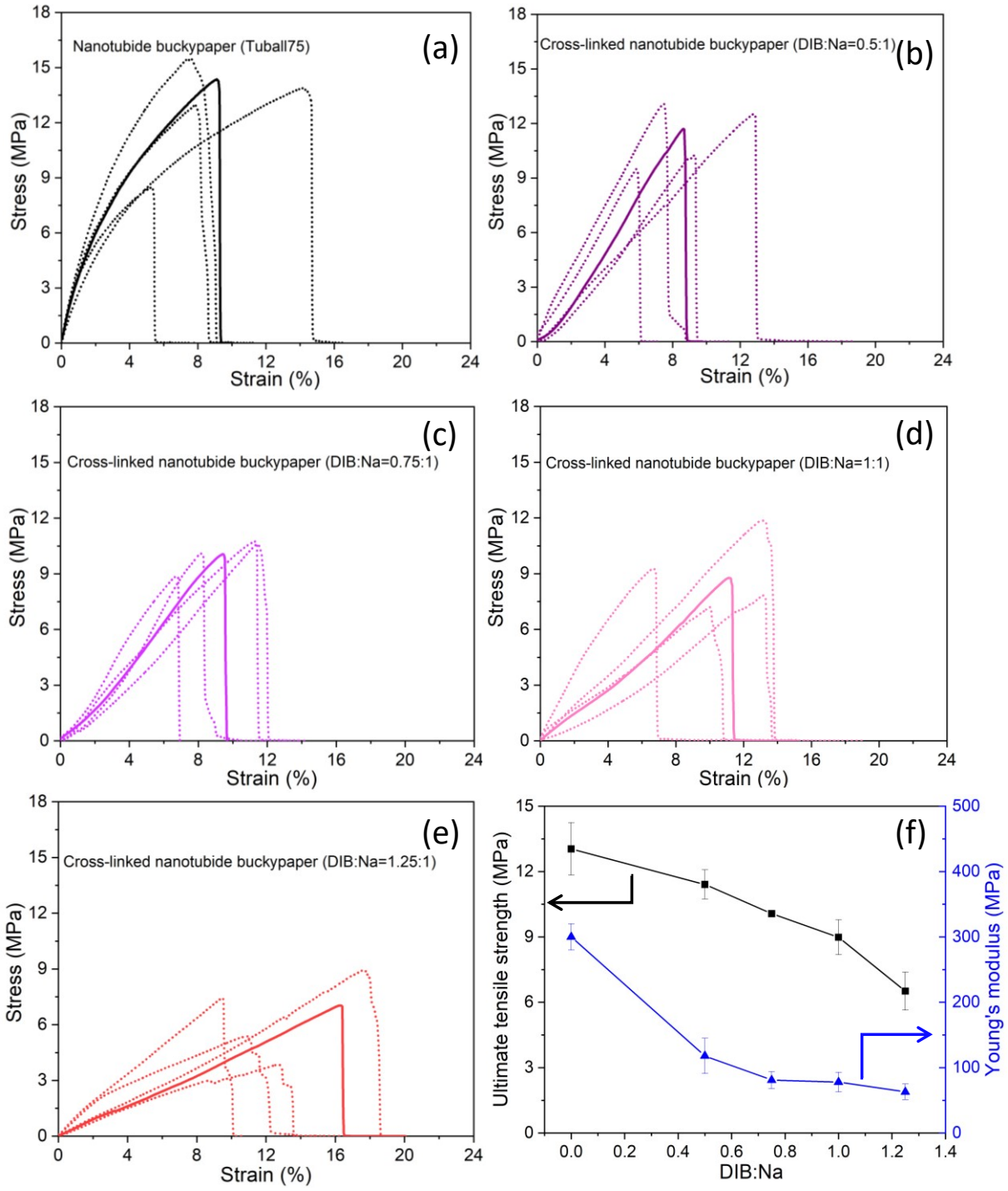

Figure 5.8 Stress–strain curves of (a) nanotubide (Tuball75) and cross-linked nanotubide (Tuball75) buckypapers at different DIB: Na ratios: (b) 0.5:1, (c) 0.75:1, (d) 1:1, (e) 1.25:1. (f) Ultimate tensile strength and tensile modulus at 0.5-1% strain of nanotubide and cross-linked nanotubide buckypapers (Tuball75). The solid line is a 'typical' sample in the middle of the data range; the dashed lines are the responses of other four samples tested at the same condition.

5.3.2 Influence of SWCNT type on nanotubide buckypaper properties

Up to this point, the results in this thesis have used Tuball75 as the SWCNT feedstock, due to its low cost, availability, and high graphitic quality. However, as implied by the name it contains a minimum of only 75% SWCNTs, with the balance consisting mostly of catalytic iron. During the course of the thesis, the manufacturer, OCSiAl, released a new purified grade Tuball99, with almost all of the iron removed via an acid treatment. Since, the carbon encapsulated iron is expected at best to be electrochemically inactive, and only acts as parasitic mass in this system, it was interesting to compare the performance of buckypapers developed using Tuball99. Control and cross-linked nanotubide buckypapers were produced from Tuball99 with the same process described in 5.3.1, using the optimum carbon concentration and charging ratio ([C]=1.5 mg/mL, C:Na= 10:1) found for Tuball75. The SEM image of the nanotubide buckypaper from Tuball99 at low magnification shows locally aligned domains, reminiscent of liquid crystal domains, and relatively large bundles which may potentially due to rebundling of this pure material (Figure 5.9a). At high magnification, the pore size of Tuball99 nanotubide buckypaper (Figure 5.9c) is smaller than Tuball75 nanotubide buckypaper (Figure 5.9e) which may be because Tuball75 buckypaper contains impurities which can disrupt the rebundling.

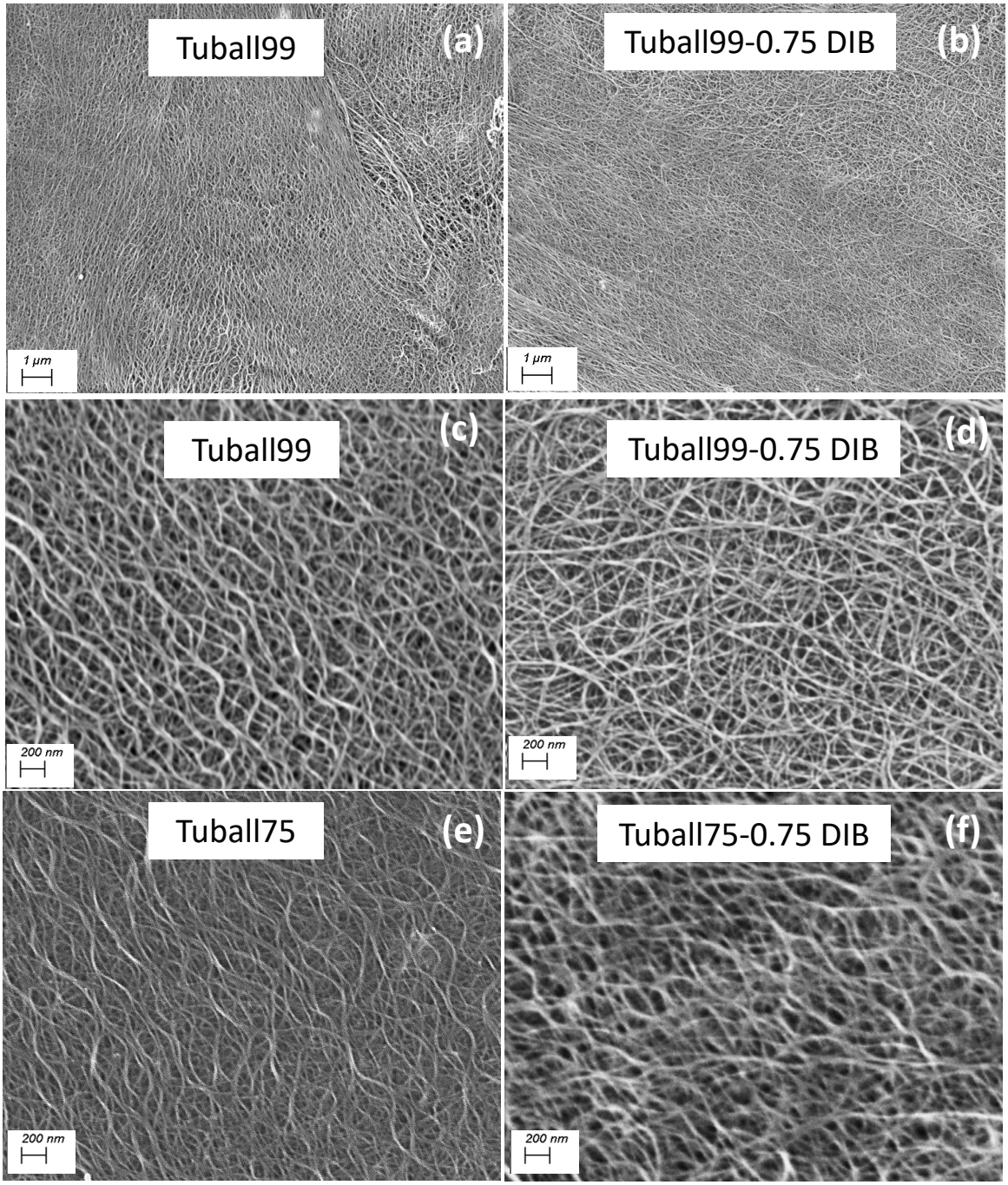

Figure 5.9 (a-b) High magnification and (c-d) low magnification SEM images of nanotubide and cross-linked nanotubide buckypapers using Tuball99 as the starting material. SEM of (e) nanotubide buckypaper and (f) cross-linked nanotubide buckypapers (Tuball75-0.75DIB).

Raman spectroscopy was used to characterise the intrinsic properties of Tuball75 and Tuball99 following the procedure which described in Section 3.2.6. The I_D/I_G of nanotubide buckypaper from Tuball99 (0.034) is higher than Tuball75 (0.014) due to the increasing of defect from purification procedure since the synthesis of raw materials.[313] [314]After

functionalisation, the I_D/I_G intensity in both cross-linked nanotubide buckypaper from Tuball75 (0.093) and Tuball99 (0.391) increases when compared with the uncross-linked buckypaper due to the attachment of functional groups, creating in plane defects(Figure 5.10a).[315] The presence of RBM in all samples confirms the presence of SWCNTs (Figure 5.10b) and the average nanotube diameter of SWCNT was estimated from the relation between RBM frequency (ω_{RBM}) and nanotube diameter using equation 3.3. The RBM vibration of Tuball75 and Tuball99 includes mainly two peaks at 132 cm^{-1} and 192 cm^{-1}, corresponding to SWCNTs diameters of 1.55 and 1.25 nm respectively.[188, 316] The lower RBM band of Tuball75 (peak 1) has higher intensity than Tuball99 whereas the RBM peak of Tuball99 at higher frequency (peak 2) has a higher intensity, suggesting that Tuball99 contains smaller diameter SWCNTs.[317]

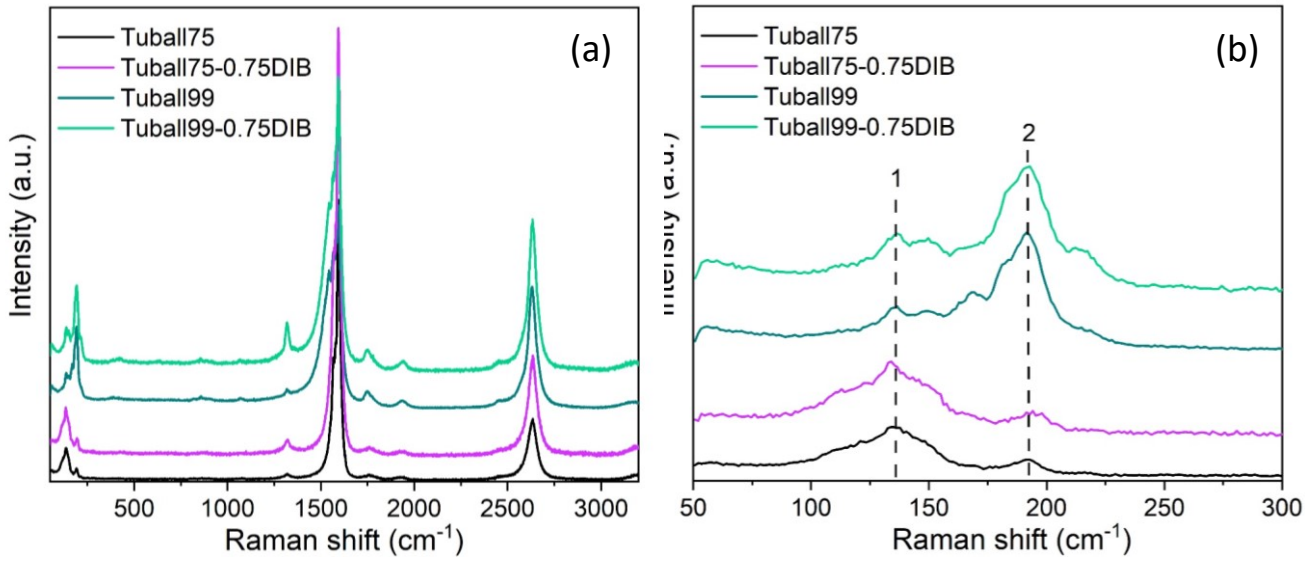

Figure 5.10 (a) Raman spectra and (b) RBM region and of of nanotubide and cross-linked nanotubide buckypapers from Tuball75 and Tuball99.

Adding the DIB cross-linker to Tuball99 nanotubide solutions provides larger uniform pore sizes and a well dispersed network structure compared to the control Tuball99 nanotubide buckypaper (Figure 5.9b and d). The better packed bundle structure in Tuball99 nanotubide buckypaper leads to a higher packing density and a reduced thickness when compared with Tuball75 nanotubide buckypaper (Table 5.3). In addition, the DIB linker has a much greater effect on the dispersion, thickness and density of cross-linked nanotubide buckypaper for Tuball99 compared to Tuball75. For example, the thickness of cross-linked nanotubide Tuball99 buckypaper (DIB:Na = 0.75:1) increased by 46% compared to the uncrosslinked

Tuball99 control, while the thickness of cross-linked Tuball75 buckypaper (DIB:Na = 0.75:1) only increased by 10% compared to the Tuball75 control. This contrasting response is likely because the Tuball75 buckpaper already has a larger pore size and a more open network without using the DIB linker, due to the presence of impurities particles that limit SWCNT packing. In the Tuball99 system, the DIB has a much greater effect on the rebundling process.

The effect DIB:Na ratio on the electrochemical performance of Tuball99 buckpapers was examined using 1 M H_2SO_4 as an electrolyte. CV curves of all electrodes (Figure 5.11a) show rectangular shapes with a couple broad redox peaks, similar to Tuball75 (Figure 5.4a). The gravimetric capacitance of cross-linked Tuball99 buckypaper shows a similar trend to Tuball75 with increasing DIB concentration (Figure 5.11c). The optimum condition is equivalent DIB:Na 0.75 but the capacitance starts to drop once DIB:Na > 1. At low scan rate, the Tuball99 control buckypaper shows a higher volumetric capacitance (83 F/cm^3 at 10 mV/s) than the cross-linked samples due to the high density and low thickness. However, at high scan rate, the Tuball99 control buckypaper has a huge capacitance drop, achieving only 58% of the original capacitance at 500mV/s (Fig. 5.10d). This drop is also assigned to the dense packing that leads to a lower ion diffusion efficiency, as can be recognised through the clear distortion of the CV shape at 500 mV/s (Figure 5.11b). Even though the gravimetric capacitance is superior, the volumetric capacitance of cross-linked Tuball99 buckypaper at optimum conditions (DIB:Na = 0.75:1) has a lower performance than the Tuball99 control buckypaper, due to the 46% larger thickness. All the Tuball99 buckypapers (Figure 5.11d) have higher volumetric performance at low scan rate when compared with Tuball75 electrodes, due to the much thinner film at the same electrode area size (Table 5.2 and Table 5.3). However, Tuball99 electrodes have poorer rate capability and lower gravimetric performance due to the less open network structure when compared with Tuball75 buckypapers (Figure 5.4d).

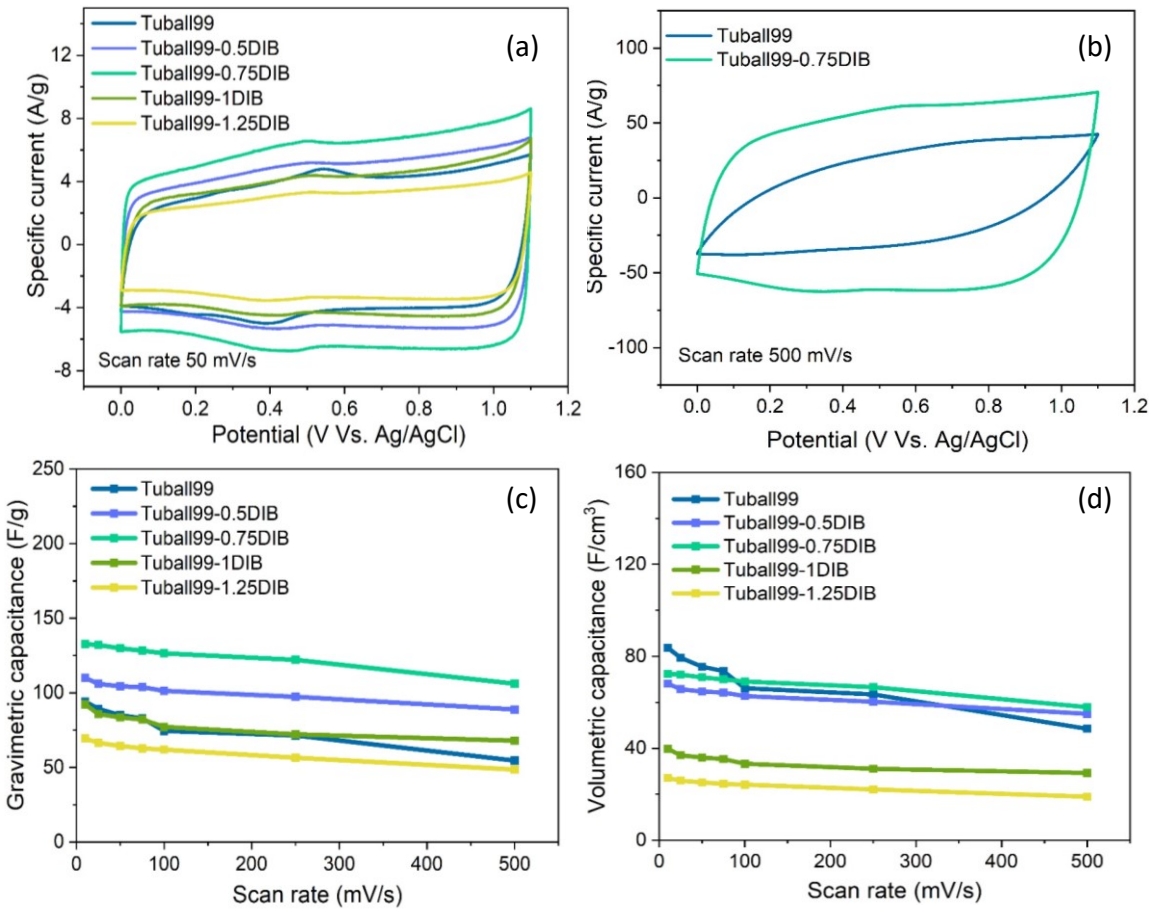

Figure 5.11 The electrochemical performance of cross-linked nanotubide buckypaper from Tuball99 at different molar ratio of DIB:Na : (a) CV curves at 50 mV/s, (b) CV curves at 500 mV/s, (c) gravimetric and (d) volumetric capacitance as a function of scan rate in 1 M H_2SO_4.

Nyquist plots of cross-linked Tuball99 buckypapers (Figure 5.12) show that both ESR and R_{ct} increase with DIB concentration, as the linker insulates the SWCNTs (increasing resistivity), and increases the thickness of electrode limiting both ion and electron transport (Table 5.3). As observed in CV, EIS shows that Tuball99 has lower gravimetric capacitance than Tuball75 papers, due to a lower ECSA (Table 5.2 and 5.3). At the optimum ratio of DIB to Na (0.75:1), the ECSA of cross-linked Tuball99 buckypaper is increased by 71% relative to the control Tuball99 buckypaper, indicating that the DIB linker successfully prevents re-bundling. The DIB-linker affects the ECSA of Tuball99 buckypaper more dramatically that the equivalent Tuball75 papers, as observed in the CV responses discussed above. Despite these consistent conclusions, it is worth noting that the optimum carbon concentration and charging ratio between carbon and sodium may, in principle, not be the same for Tuball99 as Tuball75, and further improvement of Tuball99 buckpapers may be possible.

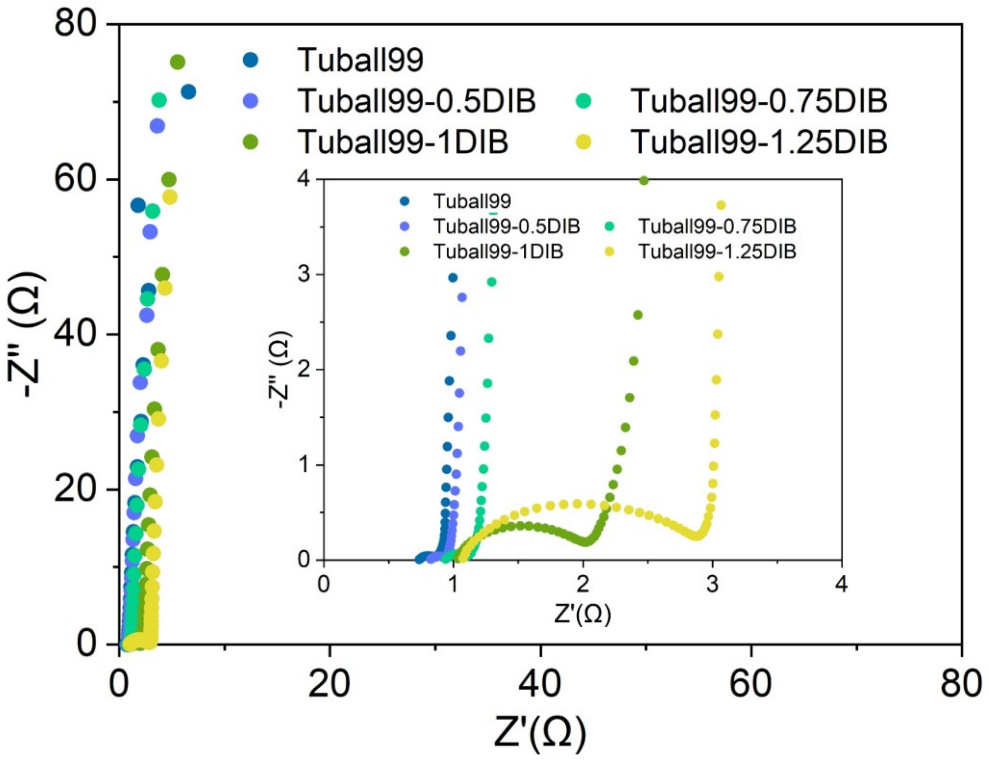

Figure 5.12 Nyquist plot of cross-linked Tuball99 nanotubide buckypaper at different molar ratios of DIB:Na.

Table 5.3 ESR, R_{ct}, thickness, density, ECSA and tensile modulus at 0.5-1% strain of nanotubide and cross-linked nanotubide buckypapers (Tuball99) at different ratios of DIB:Na.

mol DIB : mol Na	ESR(Ω)	R_{ct}(Ω)	Thickness (µm)	Density (g/cm^3)	ECSA (m^2/g)	Tensile modulus of elasticity (MPa)
0	0.73	0.15	16.8±0.3	0.98±0.03	241	783±86
0.5	0.83	0.17	22.6±0.5	0.62±0.01	299	-
0.75	0.96	0.20	24.6±0.2	0.54±0.01	414	179±27
1	1.09	1.01	29.0±0.5	0.41±0.01	259	-
1.25	1.16	1.76	32.0±0.1	0.31±0.01	195	-

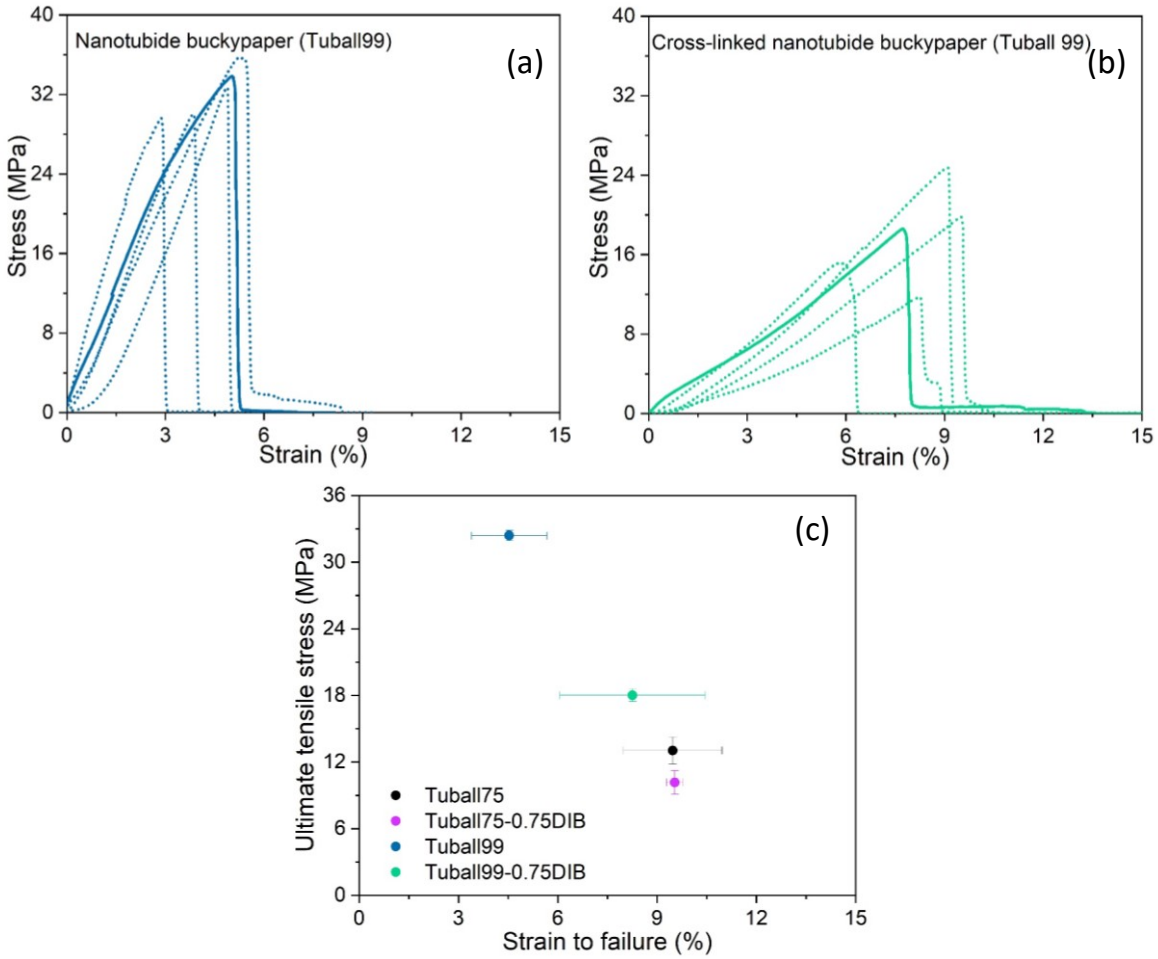

Figure 5.13 Stress–strain curves of (a) nanotubide buckypapers (Tuball99) and (b) cross-linked nanotubide buckypapers (Tuball99; DIB:Na=0.75:1). (c) average stress and strain of nanotubide and cross-linked nanotubide buckypapers from Tuball75 and Tuball99. Note, the straight line is the sample which present in the middle range of data and the dash line is other four samples which tested at the same condition.

The mechanical properties of the Tuball99 buckypapers are improved relative to the Tuball75 samples (Figure 5.13a and b), consistent with the density trends (Table 5.3). The uncrosslinked Tuball99 buckypaper has significantly higher ultimate tensile stress (32 MPa) than all the other samples (Figure 5.13c); the dense bundled structure is expected to provide better load transfer than the highly dispersed network.[308] Similarly, the tensile modulus of nanotubide buckypaper (Tuball99, 783±86 MPa) is 2.6 times higher than of nanotubide buckypaper (Tuball75, 300±13 MPa).

5.4 Cross-linked nanotubide buckypaper via vacuum filtration method

5.4.1 Effect of filtration procedure

Originally, the nanotubide buckypapers were formed by gravimetric filtration of the nanotubide solution through a PTFE membrane overnight. However, this procedure likely results in some DMAc solvent evaporating into the glovebox atmosphere and accumulating in the solvent trap, damaging the glovebox filter. Vacuum filtration was tested to speed up the process and protect the glovebox. A syringe was used to reduce the pressure in the filtration flask, accelerating the process to last only 30 minutes (see Section 5.2.2). However, changing from gravimetric to vacuum filtration reduced thickness and increased density (Table 5.4), with associated changes in electrochemical performance. In three-electrode measurements at 50 mV/s (Figure 5.14a), the areas under the CV curves of the vacuum filtered samples are reduced and the gravimetric capacitance decreases (Figure 5.14c), as might be expected for a more densely packed structure, consistent with a reduced estimated ECSA (around 23% lower, Table 5.4).

More surprisingly, at high scan rate, 500 mV/s (Figure 5.14b), the CV curves for the vacuum filtered electrodes remain rectangular, indicating a better rate performance than the gravity-filtered electrodes. Although the packing density may have increased, the reduced electrode thickness may be the dominant effect, as highlighted by the improved volumetric capacitance of the vacuum-filtered samples (Figure 5.14d).

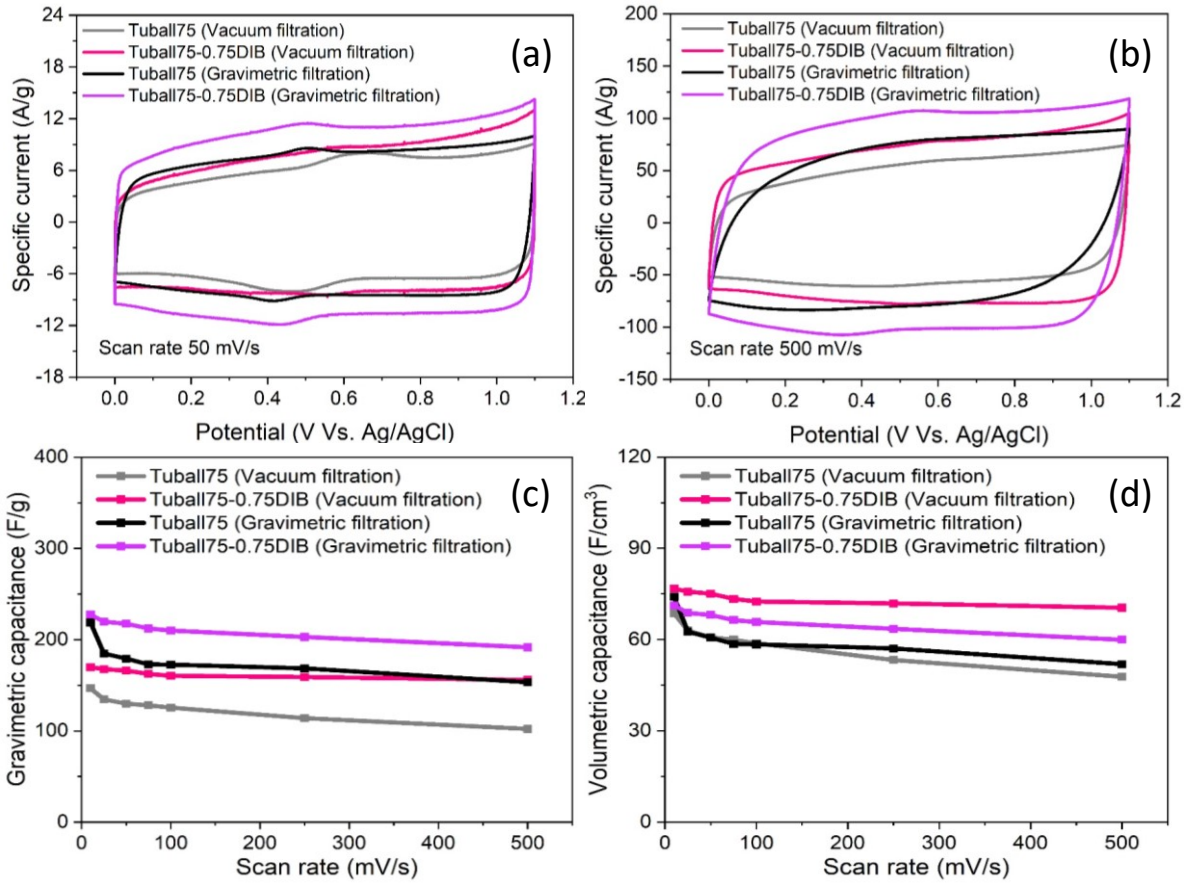

Figure 5.14 Electrochemical performance of cross-linked nanotubide buckypapers and nanotubide buckypapers (Tuball75) via different filtration methods in three-electrode measurement: (a) CV curves at 50 mV/s, (b) CV curves at 500 mV/s, (c) gravimetric and (d) volumetric capacitance as a function of scan rate in 1 M H_2SO_4.

In the Nyquist plots (Figure 5.15), all electrodes exhibit a nearly vertical line at low frequency, close to an ideal supercapacitor, with a low ESR (Table 5.4). The R_{ct} is lowered for the vacuum-filtered electrodes than the gravity-filtered electrodes consistent with a more dominant affect of the reduction in the thickness, giving the better rate capability observed by CV (Figure 5.14c and d). The vacuum-filtered, cross-linked buckypaper (Tuball75) has the best volumetric capacitance (77 F/cm^3 at 10 mV/s) and the best rate performance, retaining 94% of the low frequency capacitance at 500mV/s.

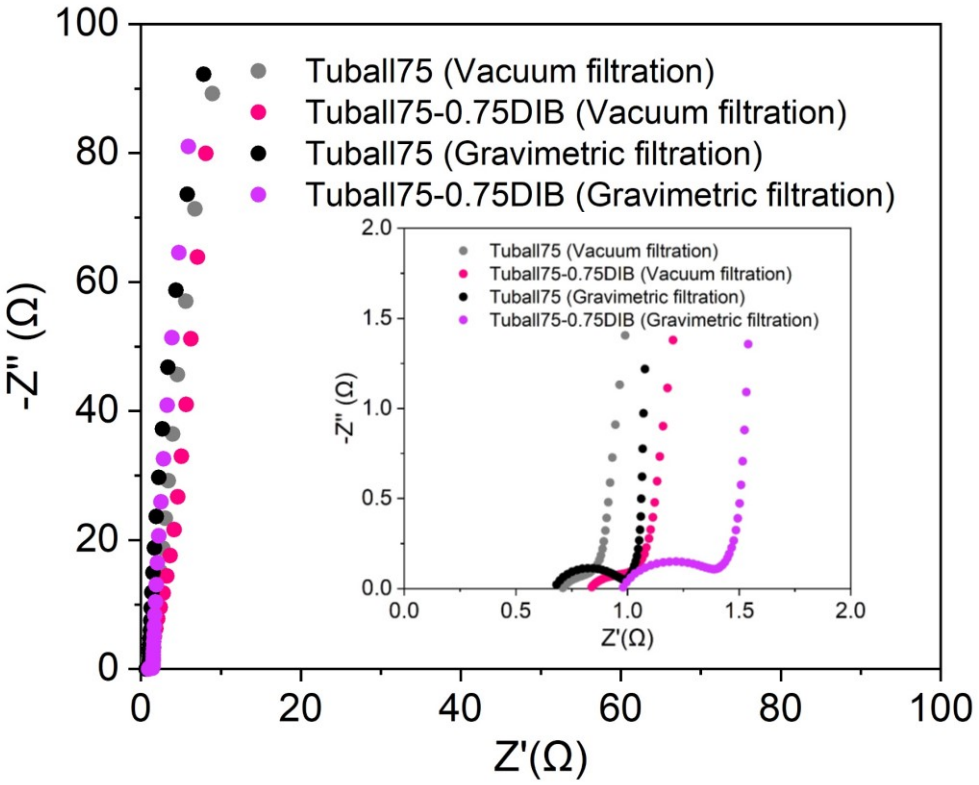

Figure 5.15 Nyquist plot of cross-linked and uncross-linked Tuball75 buckypapers via gravimetric and vacuum filtration.

Table 5.4 ESR, R_{ct}, thickness, density and ECSA of nanotubide and cross-linked nanotubide buckypapers (Tuball75) via gravimetric and vacuum filtration.

Electrode	ESR(Ω)	R_{ct} (Ω)	Thickness (μm)	Density (g/cm^3)	ECSA (m^2/g)
Tuball75 (Gravimetric filtration)	0.69	0.32	38.4±0.5	0.34±0.01	474
Tuball75-0.75DIB (Gravimetric filtration)	0.98	0.45	42.6±0.5	0.31±0.01	627
Tuball75 (Vacuum filtration)	0.73	0.15	27.2±0.4	0.46±0.01	363
Tuball75-0.75 DIB (Vacuum filtration)	0.83	0.37	32.4±0.4	0.42±0.01	465

5.4.2 Effect of electrode mass loading

The search for the most successful cross-linked nanotubide electrode was then extended by varying the electrode thickness, to find the optimum balance between maximising the active material and its rate performance. The mass loading of SWCNT starting material was increased from 1.4 to 3.2 mg/cm^2 while maintaining the optimum conditions found to give the best volumetric capacitance and rate performance in the previous section (charging ratio (C:Na), carbon concentration [C] and DIB:Na ratio held at 10:1, 1.5 mg SWCNT/mL DMAc and 7.5DIB:1Na, respectively). To avoid the problem of DMAc solvent evaporating into the glovebox atmosphere and damage the glovebox filter, all buckypapers in this section were prepared via vacuum filtration. Buckypapers were successfully produced at a range of increasing SWCNT loadings, however, the density gradually increased (Table 5.5), likely due to more freedom to organise within the film during drying. In aqueous three-electrode measurements at 50 mV/s, the CV curves of the electrodes at SWCNT mass loading of 1.4, 1.8 and 2.2 mg/cm^2 show the classic near-rectangular shape; however, the CV curves show increasing distortion above 2.8 mg/cm^2 (Figure 5.16a). This behaviour is even more obvious at higher scan rates. At 500 mV/s (Figure 5.16b), only electrodes with mass loading lower than 2.2 mg/cm^2 can maintain the rectangular shape while others show heavily distorted shapes which implies poor electrochemical rate capability. The volumetric performance (Figure 5.16d) drops less than gravimetric performance (Figure 5.16c) due to the volume of buckypapers not increasing proportionally to the mass loading (Table 5.5).

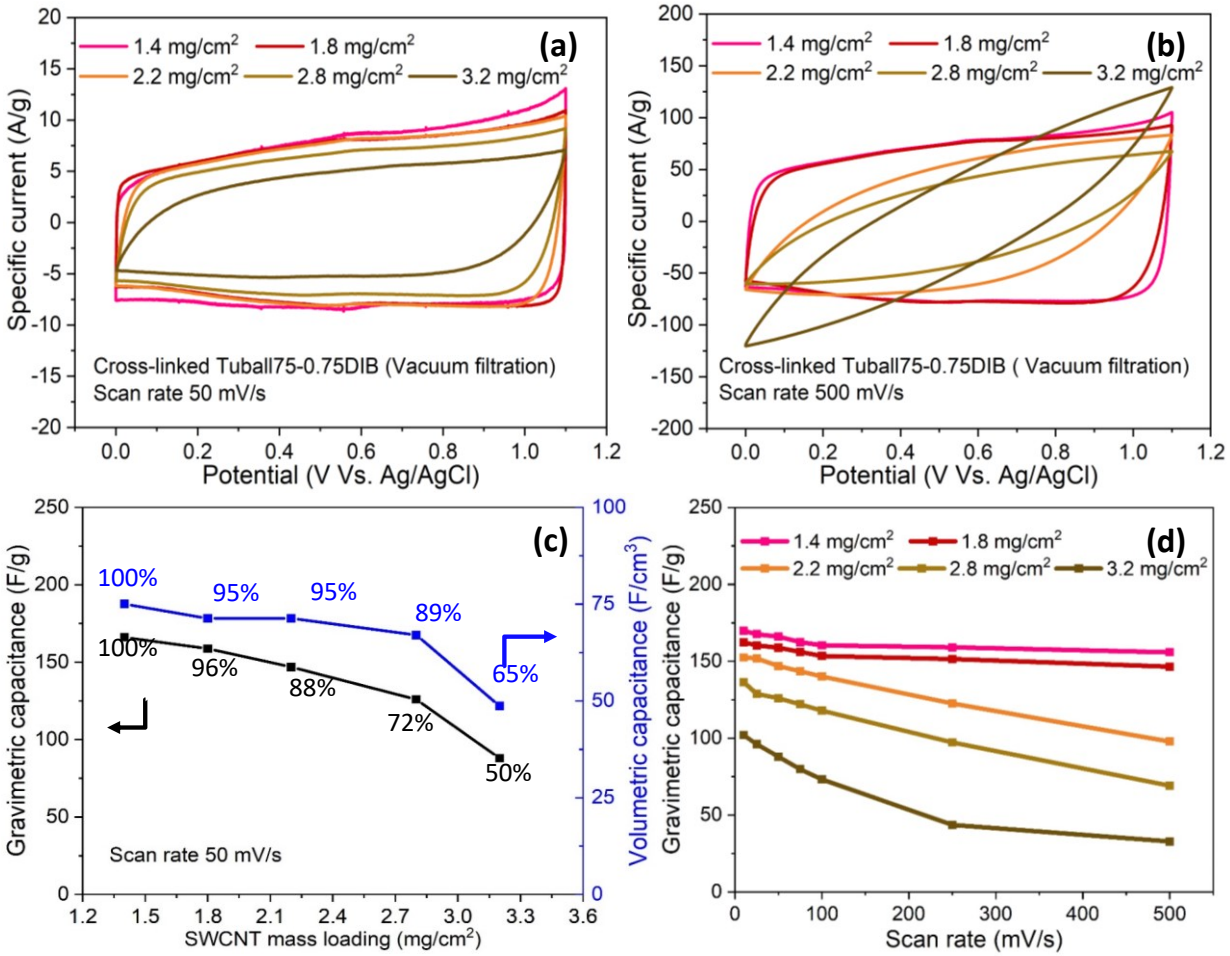

Figure 5.16 Electrochemical performance of cross-linked nanotubide buckypapers (Tuball75, DIB:Na 0.75:1) at different SWCNT mass loading per area: (a) CV curves at 50 mV/s, (b) CV curves at 500 mV/s, (c) gravimetric and volumetric capacitance vs. SWCNT mass loading, at 50 mV/s, and (d) gravimetric capacitance as a function of scan rate in 1 M H_2SO_4, at varying mass loadings.

The Nyquist plots show good capacitive responses, with increasing R_{ct} as the mass loading increases, with a dramatic jump at the highest loading; the increasing thickness and increasing density presumably combine to limit ionic access and transport through the electrode (Figure 5.17).[318, 319] This result is in good agreement with the obvious resistive CV shapes (Figure 5.16b) and the significant capacitance drop at high scan rates when increasing the SWCNT mass loading (Figure 5.16d).

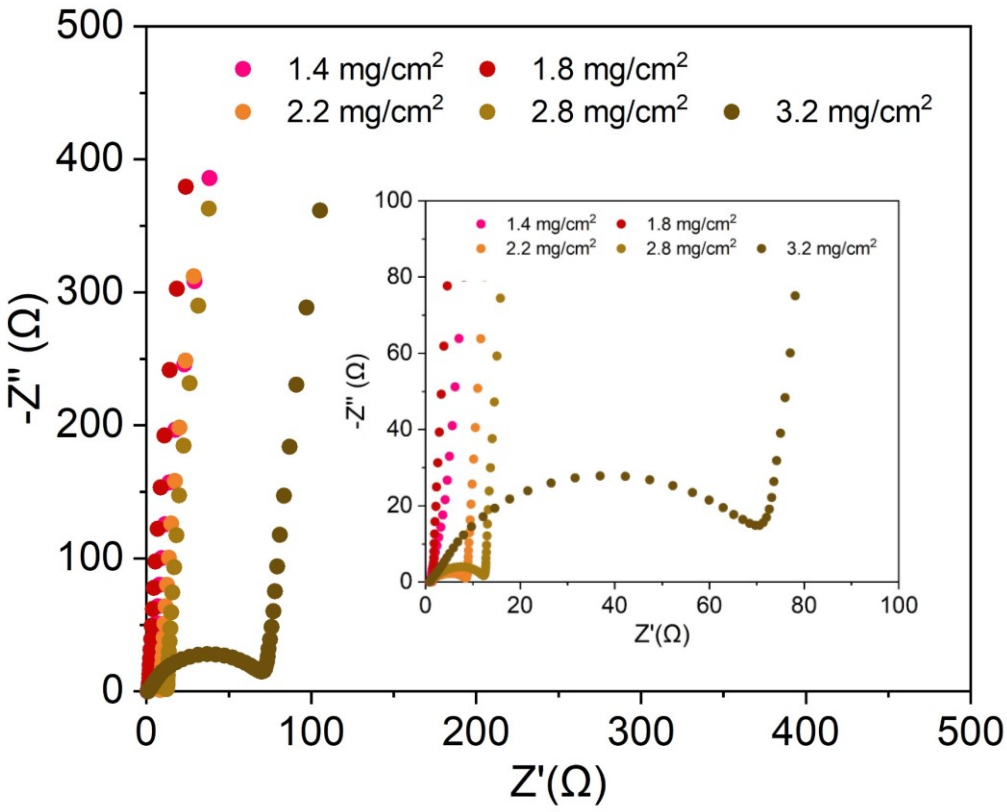

Figure 5.17 Nyquist plots of cross-linked nanotubide buckypapers (Tuball75, DIB:Na 0.75:1) at different SWCNT mass loading**.**

Mechanically, the vacuum-filtered cross-linked buckypapers (Figure 5.18a) show much higher strength and stiffness than the gravity-filtered cross-linked buckpapers (Figure 5.8c), by 18 MPa and 10 MPa of strength respectively for the standard SWCNT areal loading, due to more contact between SWCNT-SWCNT in the denser film at the same mass loading results the improvement in sharing the load. However, the strain to failure is reduced because the vacuum filtration method provide the thinner film. Increasing SWCNT mass loading leads to a huge increment in strain to failure and a decrease in the average Young moduli of the electrodes (Figure 5.18e and Table 5.5). The reason for these trends is less clear, given that the average density is increasing; it may be that increasing inhomogeneity within the film thickness affects the mechanical response.

Table 5.5 ESR, R_{ct}, thickness, density, ECSA and tensile modulus at 0.5-1% strain of cross-linked nanotubide buckypapers (Tuball75, DIB:Na 0.75:1) via volumetric filtration at different mass loading.

Mass- loading (mg/cm^2)	ESR(Ω)	R_{ct}(Ω)	Thickness (µm)	Density (g/cm^3)	ECSA (m^2/g)	Tensile modulus of elasticity (MPa)
1.4	0.83	0.37	32.4±0.4	0.42±0.01	465	345±61
1.8	0.96	0.50	39.8±0.7	0.45±0.01	457	148±24
2.2	1.13	7.87	46.8±0.5	0.47±0.01	448	-*
2.8	1.00	11.80	54.6±0.5	0.53±0.01	388	108±12
3.2	0.91	78.10	60.2±0.6	0.55±0.01	174	105±22

*There is no data for 2.2 mg/cm^2 due to sample failure during the test.

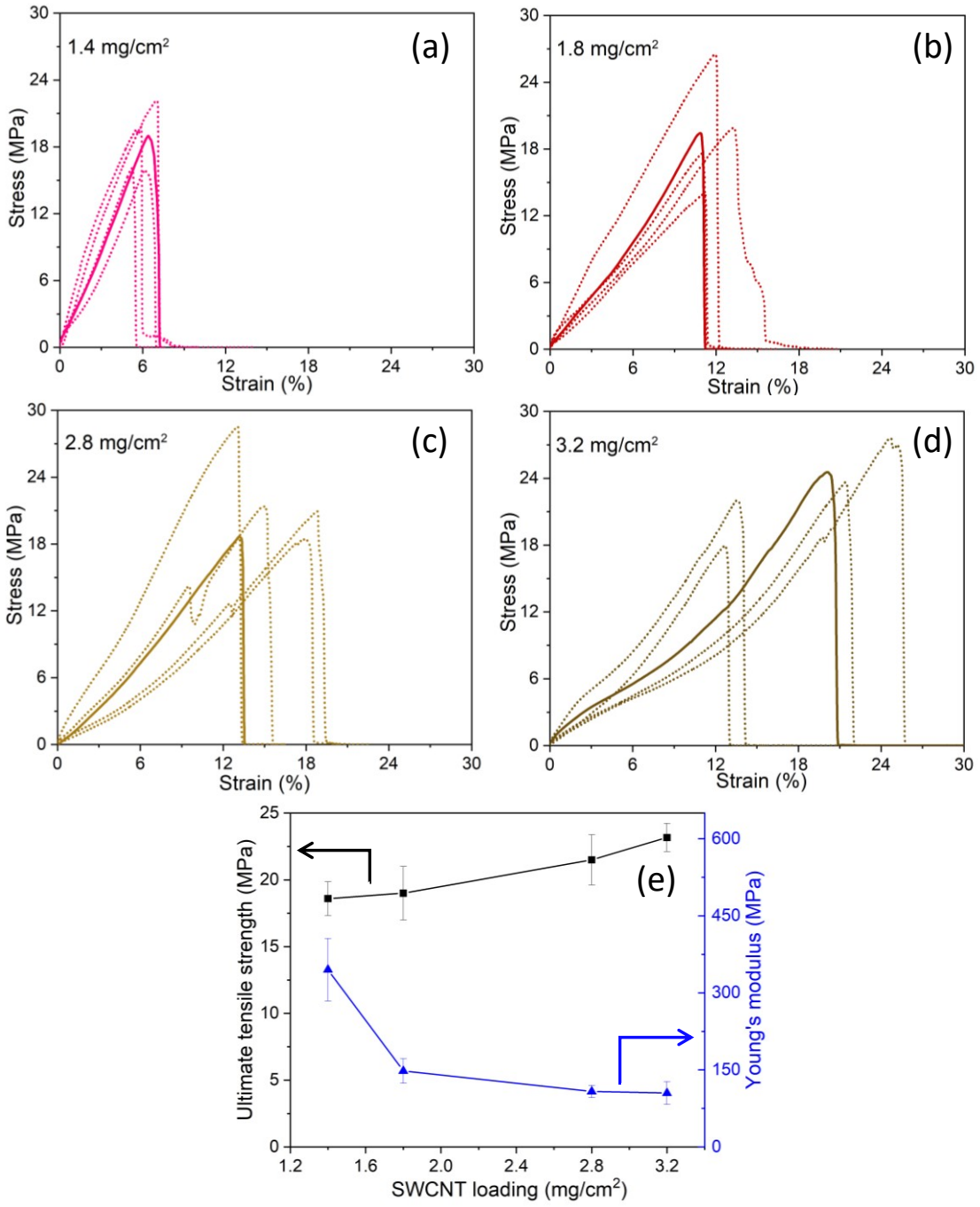

Figure 5.18 Stress–strain curves of cross-linked nanotubide (Tuball75; 0.75 DIB: 1 Na) buckypapers from vacuum filtration at different SWCNT mass loading: (a) 1.4 mg/cm^2, (b) 1.8 mg/cm^2, (c) 2.8 mg/cm^2 and (d) 3.2 mg/cm^2. (e) Average tensile strength and tensile modulus at strain 0.5-1% of cross-linked nanotubide buckypapers (Tuball75; 0.75 DIB: 1 Na) from vacuum filtration at different SWCNT mass loading. Note, the straight line is a sample in the middle range of data (the median sample) and the dash lines are the other four samples tested at the same condition.

5.5 Conclusion

This chapter details the improvement and optimisation of the electrochemical performance of as-synthesised buckypapers, using reductive functionalisation combined with a covalent cross-linking reaction. Although, the use of DIB as the cross-linker for nanotubide aerogel has been reported previously[11], the use of reductive functionalisation to produce compact buckypapers with high volumetric performance had not been studied. The dielectrophile DIB manifested a high reactivity for sodium nanotubide salt and effectively formed gel networks. The molar ratio between DIB and sodium has been found to be a crucial factor that affects the dispersion, electrode density, electrical conductivity, and electrochemical and mechanical performance. The initial SWCNT concentration (0.125M), 0.75 equivalent of DIB, and 12.5 mM of sodium concentration were found to be the optimums to balance the requirements to charge the nanotubes, maximise coulombic repulsion, avoid screening, and effectively cross-link results in maximise the electrochemical performance of the cross-linked nanotubide buckypaper (227 F/g at 10 mV/s for Tuball75). In the optimised case (Tuball75), the cross-linked electrode, has an enhanced capacitance, especially gravimetrically, and a higher rate capability (maintaining up to 89% of low frequency capacitance at 500 mV/s, compared to 70% for the uncross-linked buckpaper). Higher than 0.75 equivalents of DIB were found to reduce both gravimetric and volumetric capacitance due to the deposition of insulating organic material.

The effect of different purity SWCNT source starting materials was also explored here. Tuball99, which has a much lower iron catalyst content than Tuball75, provided a higher packing density for as-synthesised nanotubide buckypaper at the same carbon concentration, reductive charging ratio and equivalent cross-linking ratio as Tuball75. The capacitance trend of Tuball99 with increasing DIB concentration was similar to Tuball75 which confirms that a unique optimum sodium concentration led to the best outcome of the reaction (both in term of resulting properties of the material and cross-linking). The benefit of the cross-linking has shown to provide effective debundling of the as-received SWCNTs which aggregate, facilitate grafting reactions then result in a cross-linked network with enhanced electrochemical surface area. The Tuball99 buckypapers can be suitable for use in the supercapacitors which

require significant mechanical loading, as they have a superior Young's modulus (783 MPa) to the Tuball75 buckypapers (300 MPa).

Both Tuball75 and Tuball99 buckypapers show that adding DIB cross-linker at the optimal condition generally improves the gravimetric performance and enhances rate capability. The ratio between cross-linker and available charge (DIB:Na) plays an important role in adjusting structure and its electrochemical performance. Despite a consistent reductive dispersion process, the method and rate of assembly also affects structure and performance. Vacuum filtration provides a faster productive rate, a higher packing density and reduced film thickness than simple gravimetric methods. The vacuum-filtered electrodes also provided higher volumetric capacitance, greater electrochemical rate capability and higher mechanical strength, through a higher packing density and thinner film at the same mass loading. The performance of the most successful cross-linked nanotubide electrodes was then extended by scaling up the electrode thickness, to find the optimum balance between maximising the active material and its rate performance; ionic transport limitations were found to dominate at SWCNT loadings above 2.8 mg/cm^2 (film thicknesses greater than 55 microns).

6. Hybridising nanotubide buckypapers with PPy for high volumetric performance supercapacitors

6.1 Introduction

The nanotubide buckypaper supercapacitors developed in Chapters 4 and 5 offer excellent performance, but their energy densities are ultimately limited by the double layer capacitance. Hybridising the cross-linked nanotubide buckypaper (CNB) with pseudocapacitive materials can introduce additional Faradaic mechanisms to increase electrochemical energy storage. Conducting polymers are particularly promising redox active components as they are easily deposited in situ, offer excellent specific performance, and can be produced sustainably.[136] Using CNB as a substrate could potentially support the conducting polymer particularly efficiently, combining an open network structure with a high electrical conductivity. Carbon nanotubes are particularly noted for their combination of mechanical and electrochemical performance, that has already been exploited in structural energy storage devices (Section 2.3). For multifunctional applications requiring a balance between electrochemical and mechanical performance, conducting polymers are also promising candidates due to relatively their high electrical conductivity, stretchability and processibility. [136]

In this chapter, a redox active polymer, polypyrrole (PPy) was chosen to hybridise with CNB due to its high theoretical capacitance (620 F/g)[320], good mechanical performance (tensile strength 40-85 MPa and Young's modulus 400-800 MPa)[321] and high reversibility compared to other pseudocapacitive materials as mentioned in Section 2.4.1. [140] Even though PPy has been successfully combined with carbon-based substrates in previous research studies in numerous configurations (see Section 2.4.2), further improvement of the quantity, structure and distribution of PPy within an optimised carbon framework are possible. The ideal microstructure provides a highly connected, highly electrical conductive carbon (nanotube) network, with sufficient pore volume to accommodate a significant proportion of polymer, whilst retaining sufficient pore volume for electrolyte access (low ionic resistance). The polymer coating within the porous electrode must be thin enough that ion diffusion is not limited, and that volume changes associated with intercalation can be readily accommodated.

Any external polymer overcoating should be avoided, to minimise pore blockage since any obstruction of the ion diffusion pathway leads to poor power density and lower energy density at high applied specific current.[155] Carbon nanotubes are particularly effective network formers, offering high conductivity at low volume fractions. Suitable deposition of PPy within the network should offer high volumetric and gravimetric energy whilst providing the superior power. Electrochemical deposition was selected as the best approach to modulate the microstructure of the PPy, since electrodeposition potential, electrolyte, time and pulse sequence can all be conveniently manipulated. Full cells were fabricated as asymmetric supercapacitors using the hybridised PPy-cross-linked nanotubide buckypaper (PPy-CNB) as positive electrode and CNB as negative electrode. The hybrid PPy-CNB electrodes were optimised in acid electrolyte to exploit the fast charge transfer and the smaller hydration sphere radius of H^+ compared to other cations.[283] To balance full cells, and obtain the best specific performance, the capacitances of the positive and negative electrodes should be matched. Given the capacitance ratios of the optimised EDLC CNB and PPY-CNB electrodes, a new design of asymmetric supercapacitor was developed by sandwiching one positive hybrid electrode (PPy-CNB) between two negative electrodes (CNBs). The BC nanopapers were used as separators between these three-electrodes exploiting the ultrathin thickness (7 µm) to minimise the resistive loss, reduce the overall volume of the whole device and maintain cell lifetime (see Section 4.5.1). Throughout this chapter, the effects of introducing PPy into the CNB electrodes on the mechanical performance were evaluated, to evaluate the system for potential application in multifunctional structural energy storage devices.

6.2 Experimental procedure

6.2.1 Hybrid PPy-CNB via electrodeposition method.

Cross-linked nanotubide buckypapers (Tuball75, CNBs) prepared via the optimised vacuum filtration method ([C] = 1.5 mg/mL, C:Na = 10:1, DIB:Na = 7.5:1 and SWCNT mass loading 1.4 mg/cm^2, see Section 5.2.2) were dried and used as substrates. Hybrid PPy-CNBs were synthesised via electrochemical polymerisation in a three-electrode cell (Figure 6.1a), using Ag/AgCl and Pt wire as a reference and counter electrodes, respectively. Initially, two different electrodeposition electrolytes were prepared, 0.1 M pyrrole in 0.5 M KCl and 0.1 M

pyrrole in 0.5 M H_2SO_4, to explore the effect of electrolyte type on the PPy properties. Firstly, the electrodeposition of PPy on CNB was performed at 0.8 V with pulse sequence in the 'on' pulse (5 sec), and applied potential at 0 V vs. Ag/AgCl during the 'resting' time (denoted (t_{on}_t_{0V} equal to 5s_60s) for 12 cycles to select the best electrolyte. In the set of pulsed experiments, PPy was synthesised with pulse sequence 5s_60s for 12 cycles, at a range of applied potentials from 0.6 V to 1.2 V. Once the applied potential and the electrolyte were defined, the t_{on}_t_{0V} sequence was optimised using the set of 0.1s_10s, 0.1s_60s,1s_1s,1s_10s,1S_60s, 5s_10s and 5s_60s, with the total accumulated pulse on time (t_{on}) held constant at 30 s. The amount of PPy deposited was then optimised by varying the total pulse cycle from 15 to 60 cycles following by varying the applied potential between 0.6 V and 1.2 V vs. Ag/AgCl using the optimum pulse sequence 1s_60s for 30 cycles. After polymerisation, the PPy-CNBs were washed with ethanol and DI water several times to remove the residue of monomers and electrolyte then dried at 60°C in vacuum oven overnight.

6.2.2 Fabrication of asymmetric devices

The asymmetric devices in this section were assembled using the PPy-CNB at the optimum condition (0.8 V, pulse sequence 1s_60s, 30 cycles) as positive electrode and CNBs ([C] = 1.5 mg/mL, C:Na=10:1, DIB: Na=0.75:1 and SWCNT mass loading 1.8 mg/cm^2) as negative electrode in a pouch cell made of vacuum bag (Polybags LTD., ACLITE11).

The new architecture of the asymmetric device (Figure 6.1c) was developed by sandwiching one positive electrode (hybrid PPy-CNB) between two negative electrodes (CNBs) using platinum plate as current collector. The conventional design (Figure 6.1b), with one positive and one negative electrode, was also fabricated here. The BC nanopaper separator used in the nanotubide buckypaper symmetric supercapacitor (Chapter 4) was also used here as a separator. The BC nanopaper was soaked overnight in 1 M H_2SO_4 before use and the pouch cell was sealed using a vacuum sealer (Buffalo CD969, pressure -0.8 bar, 50s, 7 cycles). The electrochemical properties of as-fabricated full cell devices were evaluated by CV, EIS and GCD as a two-electrode system. CVs were performed between 1 and 500 mV/s in the voltage range from 0 to 1.1 V to identify the electrochemical characteristics of the different cell architectures. EIS was performed by applying the range of frequencies from 10 mHz to 100 kHz at 0 V potential and AC

amplitude at 10 mV. GCD was performed at current densities varying from 1 to 50 A/g in the voltage range from 0 to 1.1 V and cyclic stability tests (50,000 cycles) were completed via the GCD technique a at 5 A/g.

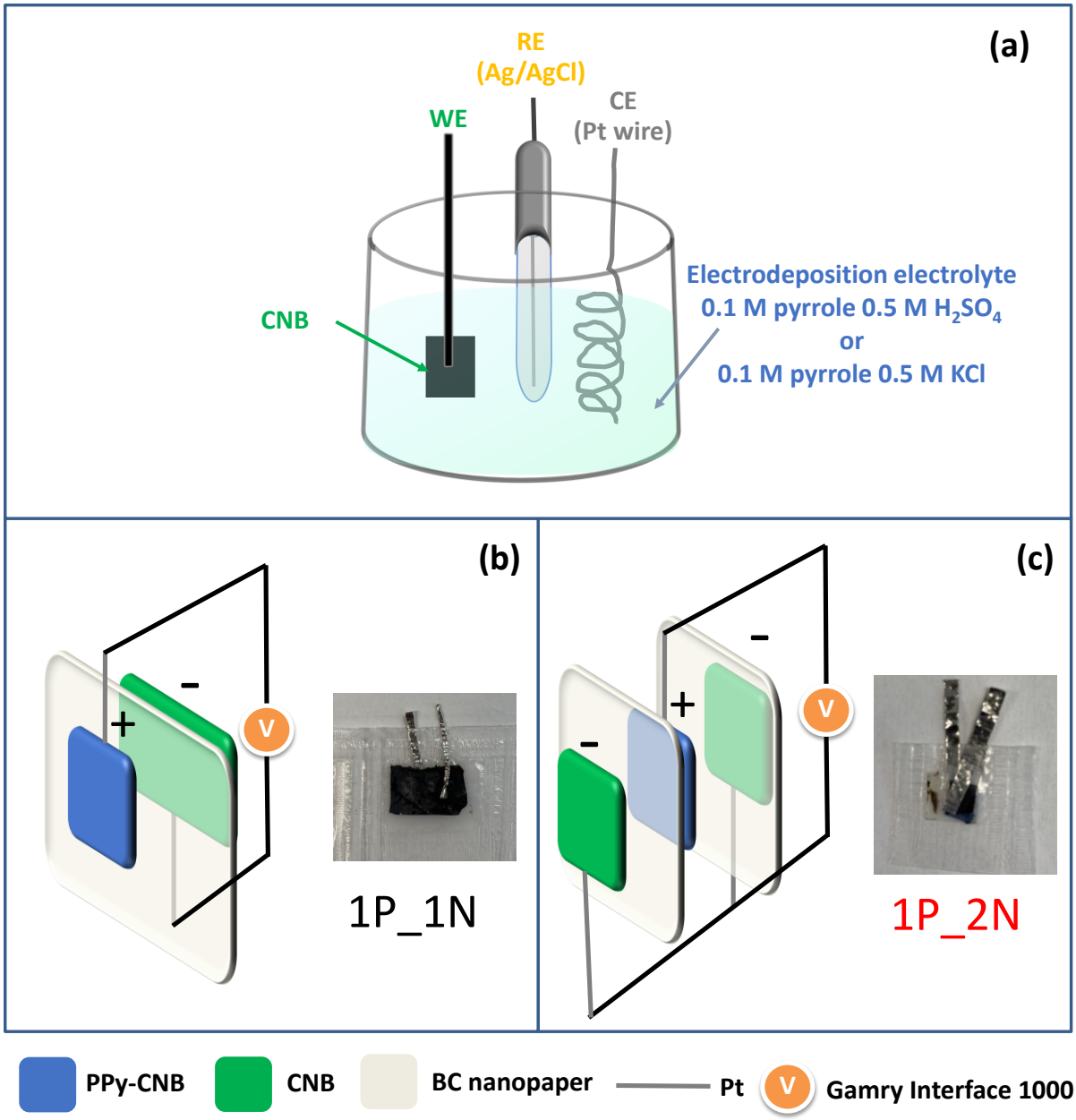

Figure 6.1 (a) Electrochemical polymerisation of PPy in three-electrode system. The configuration of PPy-CNB//CNB asymmetric supercapacitor with 1 M H_2SO_4: (b) common design with one positive and one negative electrode and (c) new design with one positive electrode sandwiched in the middle between two negative electrodes with the same areal size for all electrodes.

6.3 Electrodeposition of PPy on CNB

6.3.1 The effect of electrodeposition electrolyte on the electrochemical performance

The choice of electrolyte is known to influence the reaction mechanism during electropolymerisation, resulting in different properties of electrodeposited PPy.[322] KCl and H_2SO_4, are both common electrodeposition electrolytes for PPy [322-324], and were tested for their suitability with CNB electrodes. The concentration of the electrodeposition electrolytes was fixed at 0.1 M pyrrole in 0.5 M KCl and 0.1 M pyrrole in 0.5 M H_2SO_4 respectively. The pulsed electrodeposition was performed as described in Section 6.2.1, at +0.8 V, pulse sequence 5s_60s for 12 cycles. This electrodeposition potential was selected from the literature where 0.8 V is the oxidation potential of pyrrole.[150, 325] While the pulse on time at 5 s was estimated to be sufficiently short that only the pyrrole monomer already present within the pore volume of the CNB would be consumed; during the "off" period, fresh monomer diffuses into the porous of CNB to replenish the supply.[326, 327] As expected, the structure of the PPy on CNB changes when the electrodeposition occurs in different electrolytes (SEM, Figure 6.2). The PPy electropolymerised in H_2SO_4 displays a cauliflower-like structure (Figure 6.2a) while the PPy synthesised in KCl displays cylindrical structures (Figure 6.2b). H_2SO_4 provides a larger quantity of PPy than KCl when using the same pulse sequence (Table 6.1) because H_2SO_4 has a higher conductivity than neutral electrolyte.[322]

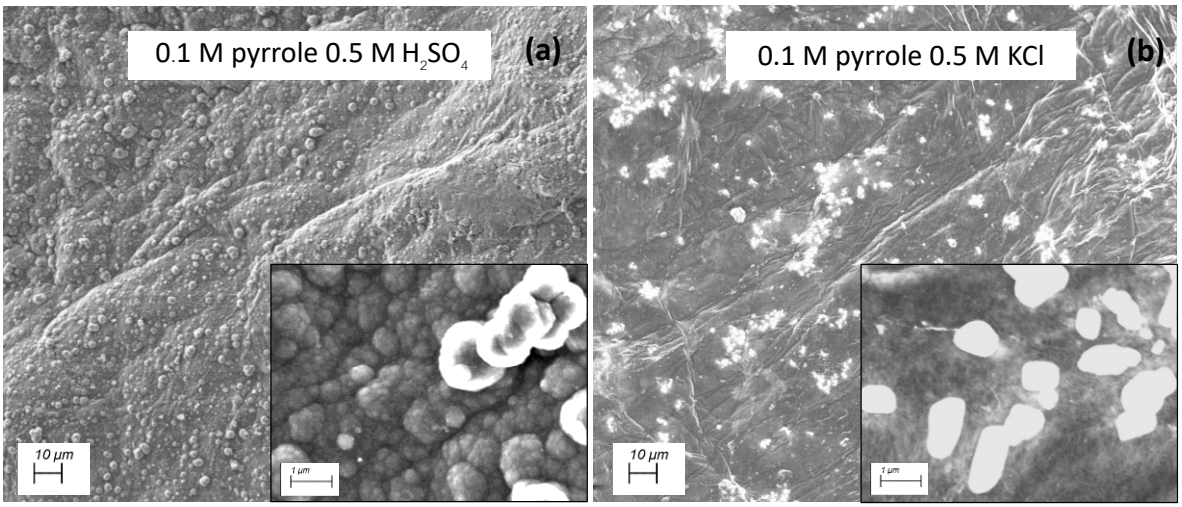

Figure 6.2 SEM images of PPy-CNB using pulse polymerisation method (0.8 V vs. Ag/AgCl, 5s_60s for 12 cycles) with different electrodeposition electrolytes: (a) 0.1 M pyrrole 0.5 M H_2SO_4 and (b) 0.1 M pyrrole 0.5 M KCl.

To further characterise their electrochemical performance, PPy-CNBs were cycled from -0.4 to 0.8 V vs. Ag/AgCl in CV measurements with 1 M H_2SO_4 as an electrolyte. The PPy-CNB synthesised in 0.5 M KCl has a narrower electrochemical operating range, as it seems to catalyse the hydrogen evolution reaction (HER, Figure 6.3a), at a less negative potential than PPy-CNB synthesised in 0.5 M H_2SO_4. At 50 mV/s, the CV curves of electrodes synthesised in 0.5 M KCl present greater distortion (Figure 6.3b) even though its PPy do not cover or obstruct the nanotubide network like the high agglomerated PPy from 0.5 M H_2SO_4 at the same monomer concentration, electrodeposition potential and electrodeposition time. The higher resistance of the deposit in KCl system is in good agreement with ESR data (Table 6.1) leading to lower electrochemical rate capability (Figure 6.3c and d). The hybrid PPy-CNB produced from 0.5 M KCl provide the highest gravimetric performance at low scan rate (Figure 6.3c). However, its volumetric capacitance (Figure 6.3d) is lower than PPy-CNB produced from 0.5 M H_2SO_4 because 0.5 M KCl system can produce PPy around 40% of 0.5 M H_2SO_4 at the same condition. While the thickness of PPY-CNBs synthesised in 0.5 M KCl and 0.5 M H_2SO_4 are increased by 37% and 46% from the substrate thickness respectively.

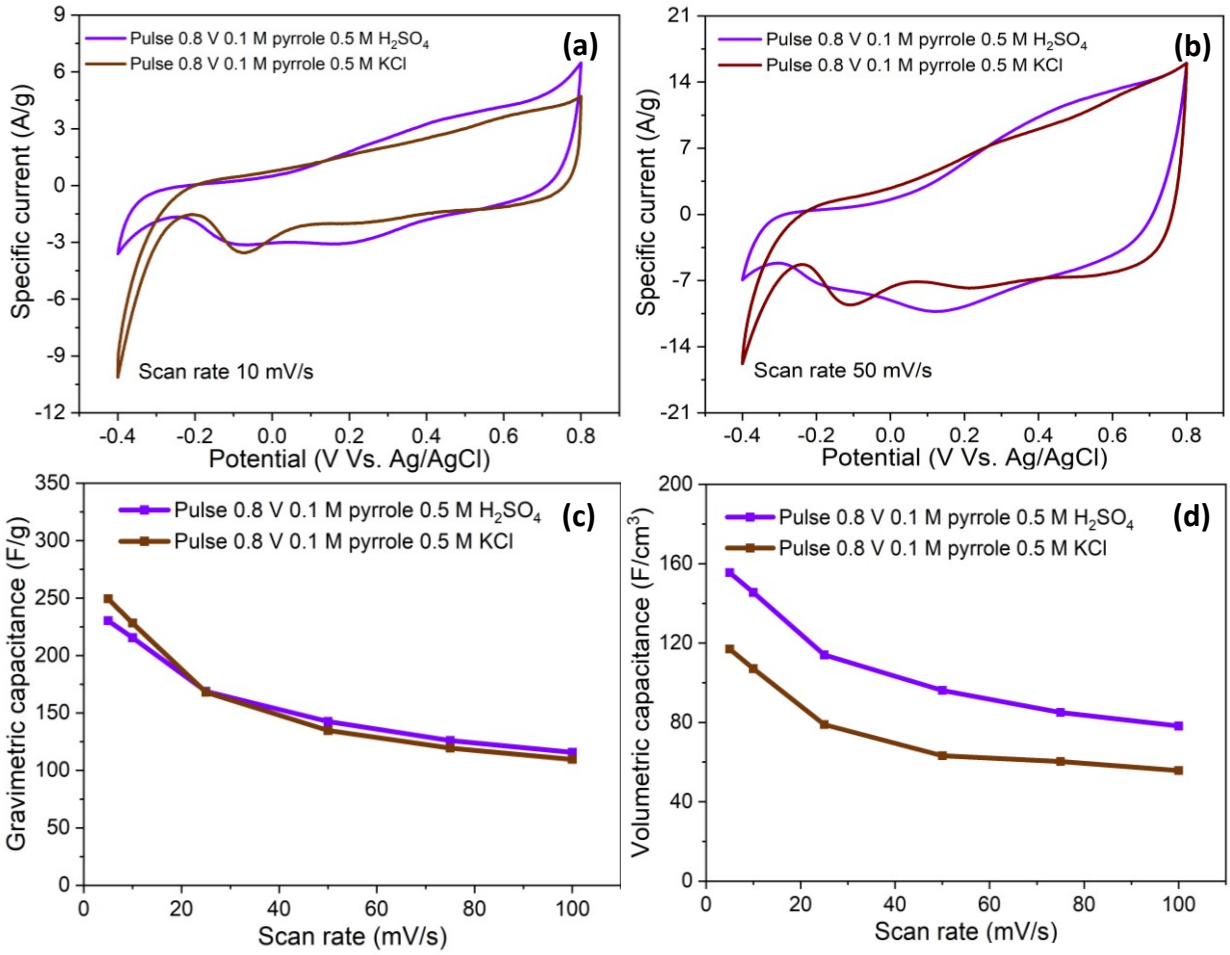

Figure 6.3 Electrochemical performance of PPy-CNB using different electrodeposition electrolytes: **(**a**)** CV curves at 10 mV**/**s, **(**b**)** CV curves at 50 mV**/**s, (c) gravimetric and (d) volumetric capacitance as a function of scan rate in 1 M H_2SO_4.

By EIS, the H_2SO_4 electrolyte produced a lower ESR, attributed to the higher intrinsic conductivity of the sulphate doped PPy. [322, 323] However, R_{ct} was larger, presumably due to the greater thickness of PPy deposited within the CNB (Figure 6.4).

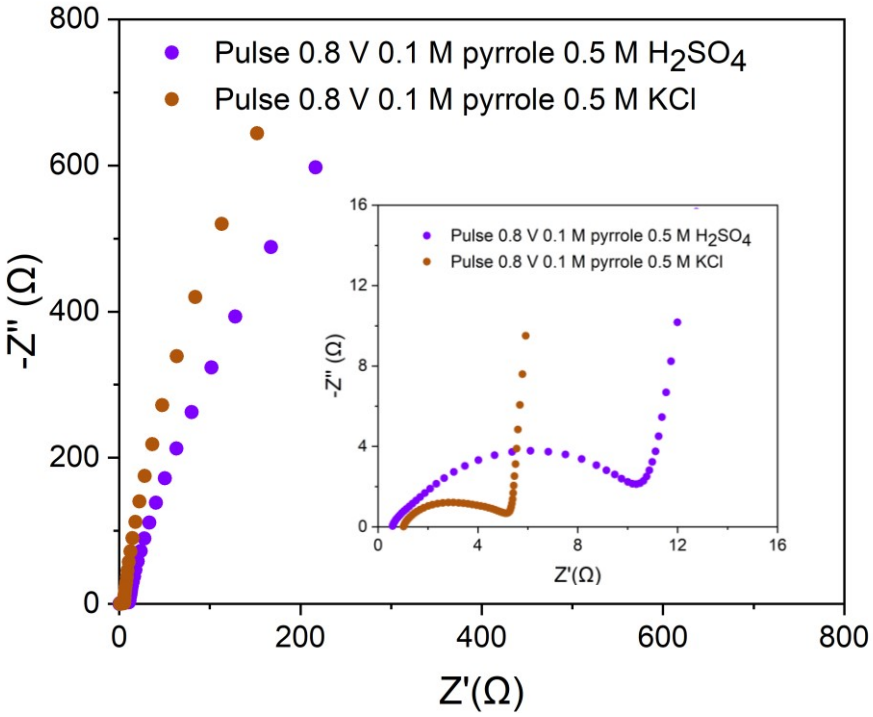

Figure 6.4 Nyquist plots of PPy-CNB with different electrodeposition electrolytes (0.1 M pyrrole 0.5 M H_2SO_4 and 0.1 M pyrrole 0.5 M KCl).

Table 6.1 ESR, R_{ct}, knee frequency, thickness, electrodeposition charge, mass loading and electrodeposition efficiency of PPy-CNBs synthesised from different electrodeposition electrolytes.

Electrode	ESR (Ω)	R_{ct} (Ω)	Knee freequency (Hz)	Thickness (μm)	Electrodeposition charge of PPy (C/cm^2)	PPy loading (mg/cm^2) and electrodeposition efficiency (%)
CNB substrate (Tuball75-0.75DIB)	0.83	0.37	158.00	32.4±0.4	-	-
0.1 M Pyrrole 0.5 M H_2SO_4	0.58	9.82	5.01	47.4±0.6	16.26	1.87 (17%)
0.1 M Pyrrole 0.5 M KCl	1.24	5.30	9.97	44.4±0.9	7.17	0.75 (15%)

6.3.2 The electrodeposition technique and electrodeposition potential

Based on the previous section, 0.1 M pyrrole with 0.5 M H_2SO_4 was used for further electrodepositions, to explore the effect of the pulse sequence and potential on the homogeneity of the PPy deposits. The electrodeposition time was fixed at 60 s for chronoamperometry and the total accumulated pulse on time was also controlled at 60 s for pulse polymerisation with t_{on} at 5 s and t_{0v} at 60 s in each cycle. From SEM images, the PPy particles exhibited the typical cauliflower-like morphology structure[328, 329] under all conditions tested (Figure 6.5b-f). The PPy covers the whole surface, obscuring the underlying nanotubes in all cases, except at the lowest pulse voltage of 0.6 V (Figure 6.5b). In the latter case, only small quantities of PPy are visible, consistent with the lowest polymerisation current and smallest total charge (Table 6.2). As the potential increased, the current, deposition charge, and mass of PPy deposited all increased, although the electrodeposition efficiency decreased (Table 6.2). These trends are also consistent with previous studies.[330 331] The amount of PPy deposited when applying a constant rather than pulsed potential (0.8 V vs. Ag/AgCl) was lower, at the same total 'on' time ; although the electrodeposition efficiency was the same, the total electrodeposition charge was lower in the continuous case, due to a lower current, presumably due to monomer supply limitations (Table 6.2). Pulsing, therefore, appears effective at increasing the monomer supply during polymerisation.

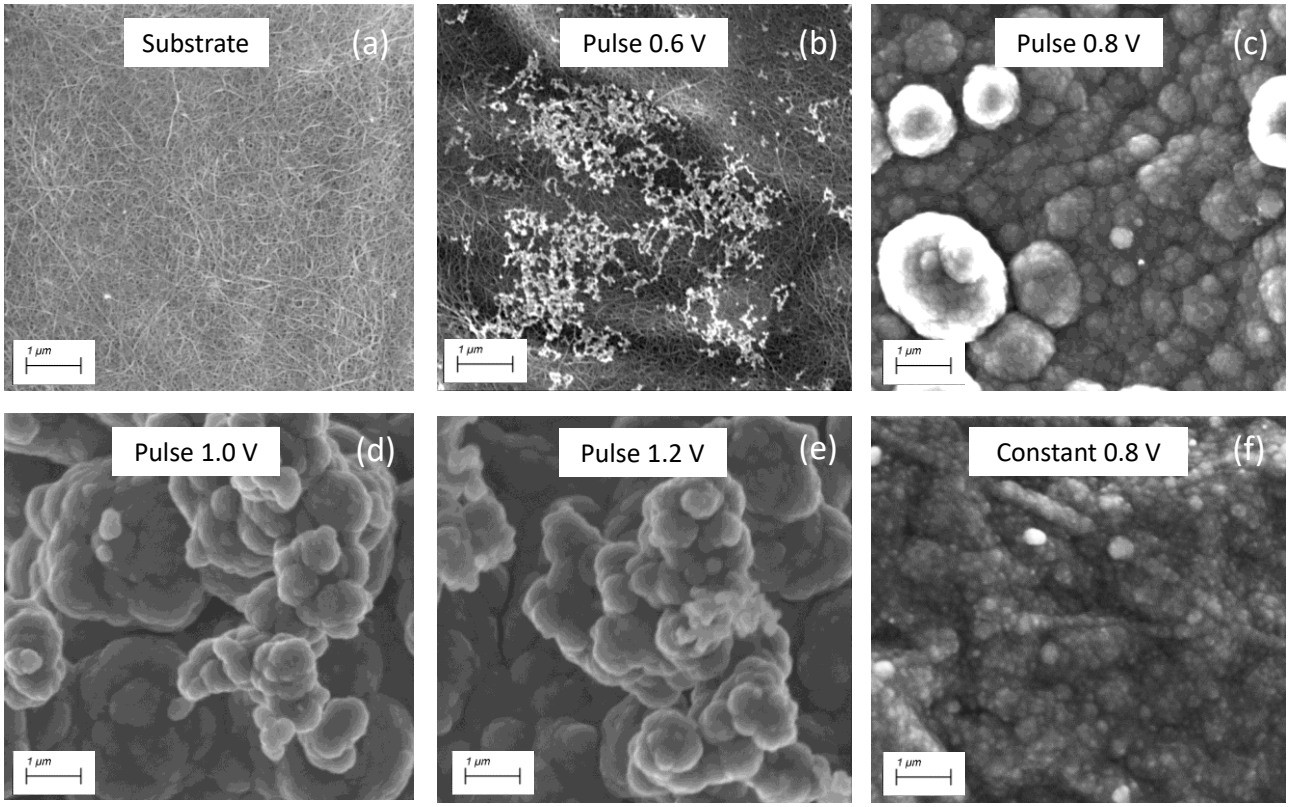

Figure 6.5 SEM images of (a) CNB and electrodeposited PPy on CNB at pulse sequence 5s_60s for 12 cycles with different applied potentials: (b) 0.6 V, (c) 0.8 V, (d) 1.0 V and (e) 1.2 V vs. Ag/AgCl. (f) SEM image of electrodeposited PPy on CNB from constant applied potential at 0.8 V vs. Ag/AgCl for 60 s.

The chronoampometry data show more detail about the growth processes (Figure 6.6). At constant applied potential (0.8 V) (Figure 6.6a), the initial current maximum at 0.6 A/cm^2 decays on a time-scale of around 10 s, reached a steady state, consistent with a diffusion limited reaction. This timescale confirms that the 5 s pulses are a reasonable choice to minimise diffusive effective. For pulse polymerisation (Figure 6.6b), the specific current curves show two opposite polarity current transients on each pulse. The positive (oxidation) current is associated with the capacitive charging of the electrochemical double layer (the capacitance is significant due to the underlying CNB substrate) combined with the oxidative polymerisation of the pyrrole; when the potential returns to zero, the negative current is associated with the discharge of the double layer.[332, 333] The positive current at the end of each pulse, where the capacitive signal has mostly decayed, indicates the polymerisation current, which remains larger for the pulse deposition than the diffusion limited constant potential deposition, at the same total deposition time.

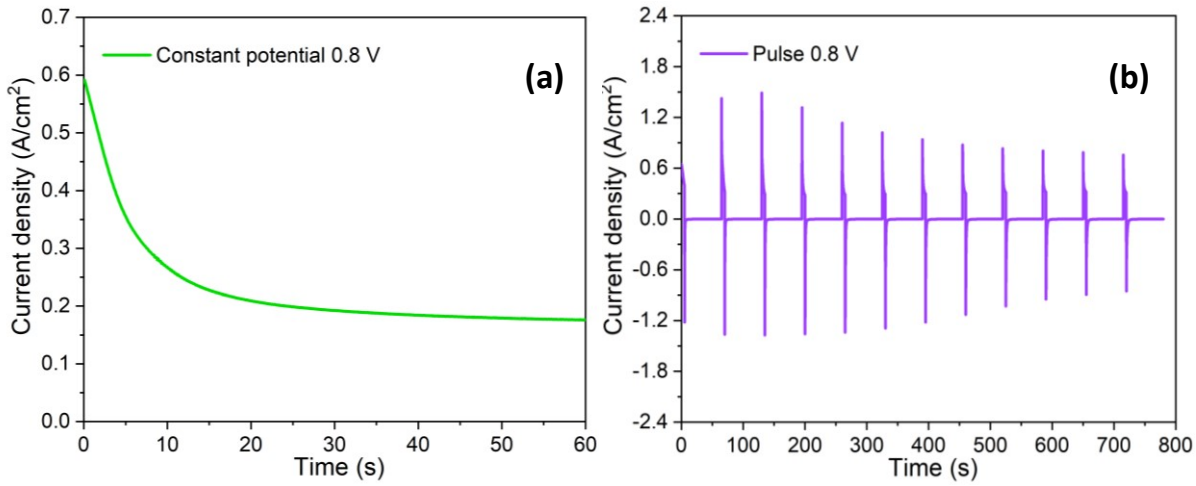

Figure 6.6 Chronoampometry of PPy polymerisation at (a) constant potential 0.8 V and (b) pulse 0.8 V at pulse sequence 5s_60s for 12 cycles. Note, both electrodes were synthesised at the same concentration 0.1 M pyrrole and 0.5 M H_2SO_4 and same total electrodeposition time at 60 s.

In the FTIR spectra (Figure 6.7), the typical characteristic of SWCNT appeared in every sample as the CNB was used as a substrate. The peak at 1980 and 2150 cm^{-1} are background artefacts and the broad peak at 1070 cm^{-1} represents the C-O-C stretching vibration. [334, 335] From every electrodeposited PPy-CNB samples, the characteristic peaks at 1545 cm^{-1} and 1446 cm^{-1} can be assigned to the pyrrole ring fundamental vibrations.[336] The broad peaks at 1274 cm^{-1} and 1025 cm^{-1} represent C-H/C-N in-plane deformation vibration and those at 1160 cm^{-1} were related to the C-N stretching vibration. The absorption bands at 960 cm^{-1} corresponds to stretching vibrations of doped polypyrrole.[337]

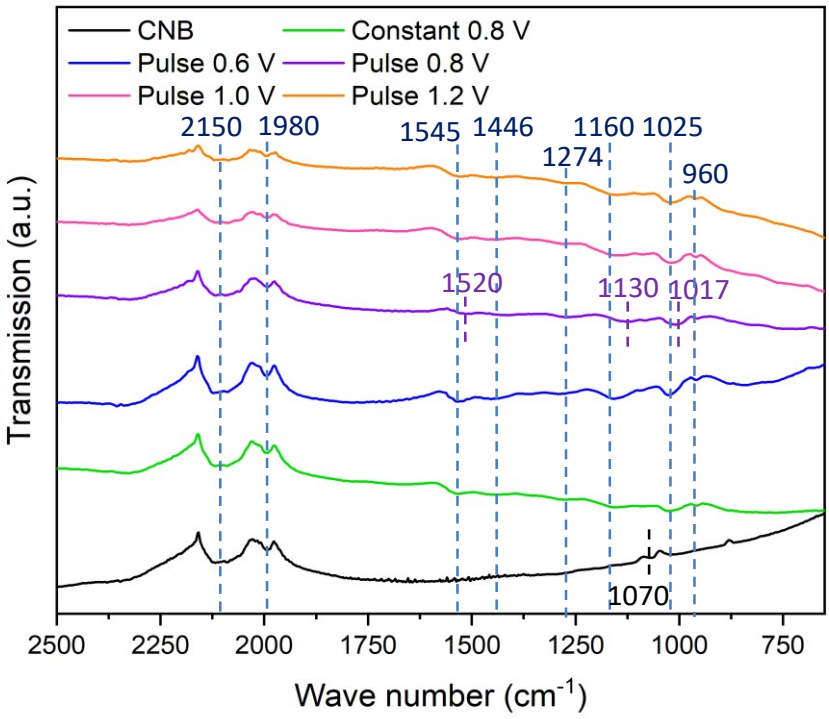

Figure 6.7 The FTIR spectra of CNB and hybrid PPy-CNBs synthesised from constant potential at 0.8 V for 60s and pulse sequence 5s_60s for 12 cycles with different applied potentials.

Table 6.2 ESR, R_{ct}, knee frequency, thickness, electrodeposition charge, mass loading and electrodeposition efficiency of PPy-CNBs synthesised from pulse sequence 5s_60s for 12 cycles and constant potential.

Electrode	ESR (Ω)	R_{ct}(Ω)	Knee Frequency (Hz)	Thickness (µm)	Electrodeposition charge of PPy (C/cm^2)	PPy loading (mg/cm^2) and electrodeposition efficiency (%)
Constant potential 0.8 V	1.43	26.15	7.97	45.6±0.5	13.57	1.64 (17%)
Pulse 0.6 V	0.51	2.09	9.97	43.8±0.4	6.80	1.21 (26%)
Pulse 0.8 V	0.58	9.82	5.01	47.4±0.6	16.26	1.87 (17%)
Pulse 1.0 V	0.57	82.12	0.50	48.8±0.7	25.93	2.00 (11%)
Pulse 1.2 V	0.71	132.40	0.32	51.0±0.8	26.50	2.17 (11%)

The electrochemical performance in this section was performed in a three-electrode system, the applied potential range of hybrid PPy-CNB is shifted to the negative range (-0.4 V to 0.8 V vs. Ag/AgCl) when compared with CNB (0 - 1.1 V vs. Ag/AgCl, Figure 5.14a) due to the pseudocapacitive characteristics of PPy. The CV curves of PPy-CNBs (Figure 6.8a and b) are not rectangular and provide obvious redox peaks confirming the existence of pseudocapacitive charge storage.[338] Note, the applied potential in this set up was found to be too large as the OER and HER appeared in all cases due to the electrolyte decomposition; nevertheless, they provide an indication of the extent of PPy redox activity. Perhaps surprisingly, the largest area under CV curve is obtained from the pulse electropolymerised electrode at 0.6 V vs. Ag/AgCl (Figure 6.8a), resulting in the highest (apparent) capacitance (Figure 6.8c and d). While the other electrodes synthesised at higher applied potential have more PPy deposited, there is less area under CV curves because the PPy coats the surface of the electrodes, blocking access to the EDLC contribution of the SWCNTs and the pseudocapacitive contribution of the internal PPy. At 50 mV/s, the CVs of PPy-CNBs (Figure 6.8b) show a clear resistive CV shape while the CV curve of the pure substrate (CNB via vacuum filtration, Figure 5.14a) shows the classic, near-rectangular shape typical of EDLCs. The distorted shape of CV curves at high scan rates is associated with the poor electrochemical rate capability, especially for the electrodes synthesised at 1.0 and 1.2 V vs. Ag/AgCl which have a highly agglomerated morphology (Figure 6.5d and e). The gravimetric capacitance (Figure 6.8c) of the sample at 0.6 V vs. Ag/AgCl achieves the highest capacitance (287 F/g at 5 mV/s), however exhibits a poorer rate capability (159 F/g at 100 mV/) when compared with CNB (171 F/g at 5 mV/, Figure 5.14c) due to the nature of pseudocapacitive materials. The other PPy-CNBs present lower gravimetric capacitance than the original substrate which again highlights the loss of access (Figure 6.8c), and the need for further optimisation. The volumetric capacitances of PPy-CNBs show higher performance compared with the substrate as the increase in volume is small compared with the increase of mass in the whole electrode, due to the PPy forming inside the pore structure (Figure 6.8d). At the electrodeposition potential (0.8 V), the pulse polymerisation provides a slightly better electrochemical performance than the constant potential deposition, presumably as more PPy is deposited within the film rather than at the surface (Figure 6.8c and d). The t_{0V} duration in pulse polymerisation allows monomers to diffuse in and polymerise inside the electrode

network while the constant potential deposition has found to have the diffusion limit and create PPy in longer chain leads to surface polymerisation.[157, 339]

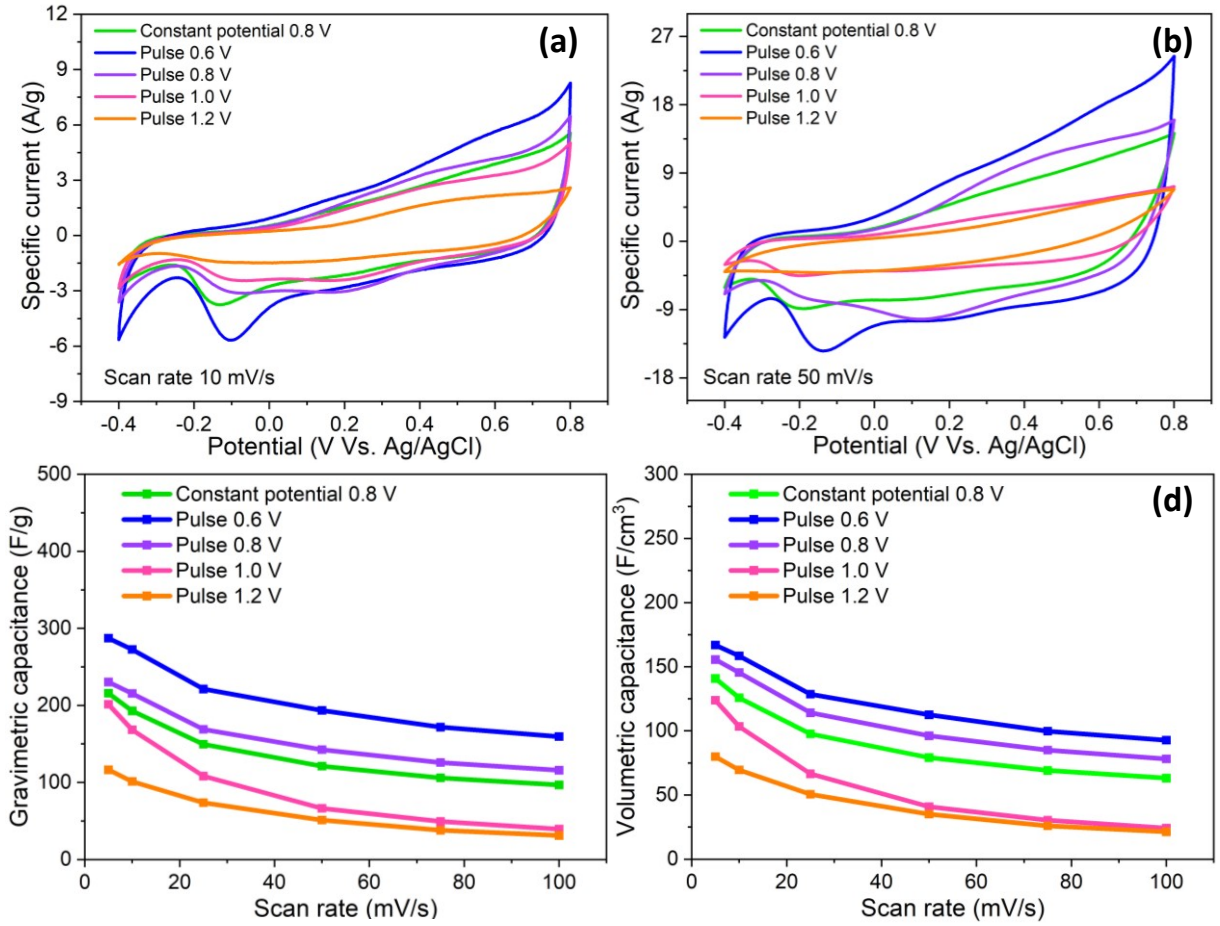

Figure 6.8 The electrochemical performance of electrodeposited PPy-CNBs synthesised from constant potential at 0.8 V for 60s and pulse sequence 5s_60s for 12 cycles with different applied potentials: (a) CV curves at 10 mV/s, (b) CV curves at 50 mV/s, (c) gravimetric and (d) volumetric capacitance as a function of scan rate in 1 M H_2SO_4.

From the Nyquist plots (Figure 6.9 and Table 6.2), ESR and R_{ct} of the PPy-CNB electrode synthesised at constant potential are higher than the pulse electropolymerised electrode at the same potential suggesting that pulse polymerisation provides better distribution of PPy within the film and better electrical conductivity. For pulse polymerisation, both the electrochemical data and the SEM images show that the total deposition time at 60s is excessive, as PPy overcoated the buckypaper surface (Figure 6.5b-e). Higher potentials deposit larger quantities of overcoated PPy (Table 6.2), increasing R_{ct}. To estimate the power of the electrode material, the knee frequencies of each electrode was defined; this characteristic maximum operating frequency can be related to the diffusion coefficient and

effective diffusion length of the active material;[340] higher knee frequency implies a higher power capability.[341] The knee frequency can be defined as the point at which the impedance of the circuit starts to be dominated by its imaginary (capacitive behaviour) or the point on the complex plane that divides the high and low frequency impedance regions.[342, 343] The highest knee frequency (Table 6.2) was observed from the electrode synthesised from pulse depostion at 0.6 V which implies that it has the fastest charge transfer reaction among these electrodes. The result is consistent with the small amount of accessible PPy deposited. The decreased knee frequency at increased electrodepostion potential mirrors the rate capability observed in the CV measurements (Figure 6.8c and d). The electrode synthesised at constant potential (0.8 V) has higher knee frequency when compared with the electrode synthesised from the pulse polymerisation (0.8 V) likely due to the smaller quantity of PPy deposited (Table 6.2). The lower knee frequency and lower rate capability following PPy overcoating the buckypaper surface is related to the reduction in electrolyte access to the inside structure and increased diffusion distance with film thickness.[344]

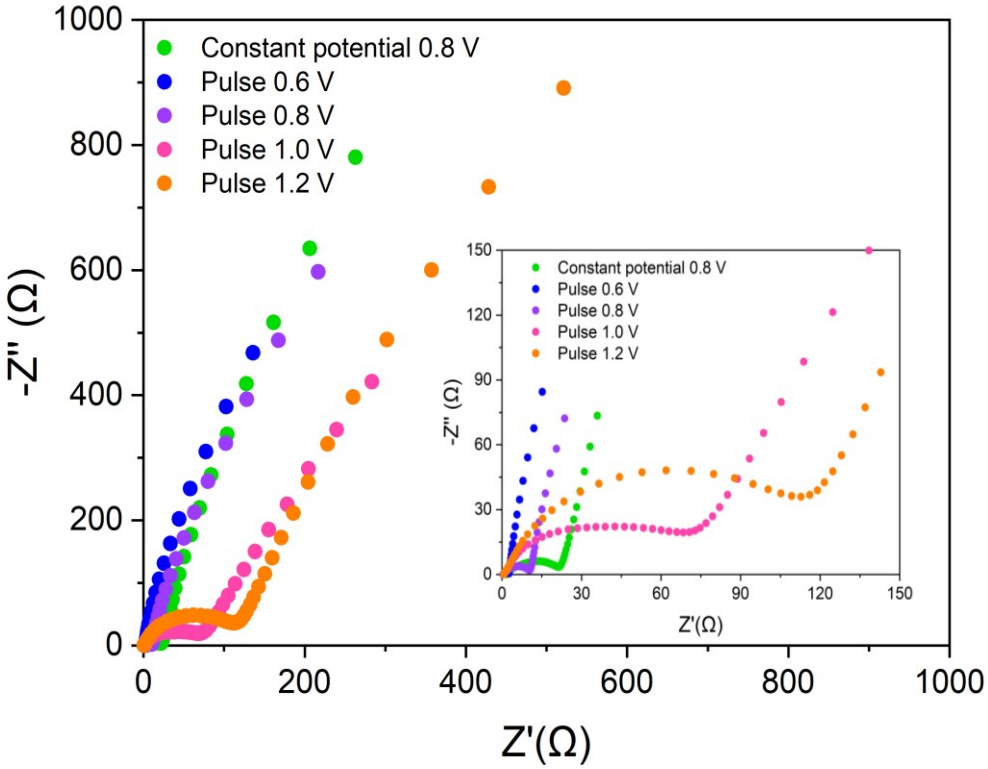

Figure 6.9 Nyquist plots of electrodeposited PPy-CNBs synthesised from constant potential at 0.8 V for 60s and pulse sequence 5s_60s for 12 cycles with different applied potentials.

6.3.3 The degradation of PPy after cycling stability

The hybridised PPy-CNBs produced using these pulse sequence in this section (5s_60s for 12 cycles) have very poor cycling stability. After 50 cycles, even the electrode with the best capacitance and rate performance (deposition at 0.6 V vs. Ag/AgCl, Figure 6.10a), only maintains 80% of its initial capacitance. The problem is likely exacerbated by the excessive potential window selected, since HER and OER reactions degrade the electrode materials through gas evolution and decompose the electrolyte.[345-347] The degradation is even worse for the electrode from electrodeposited with the 0.8 V pulsed potential (Figure 6.10b), maintained only 48% capacitance after the 50th cycle; the thicker PPy deposits are expected to tolerate cycling less effectively.[347] Therefore, the quantity and distribution of PPy on the buckypaper needs to be optimised both to enhance the specific energy density and to maintain the good cycling stability.

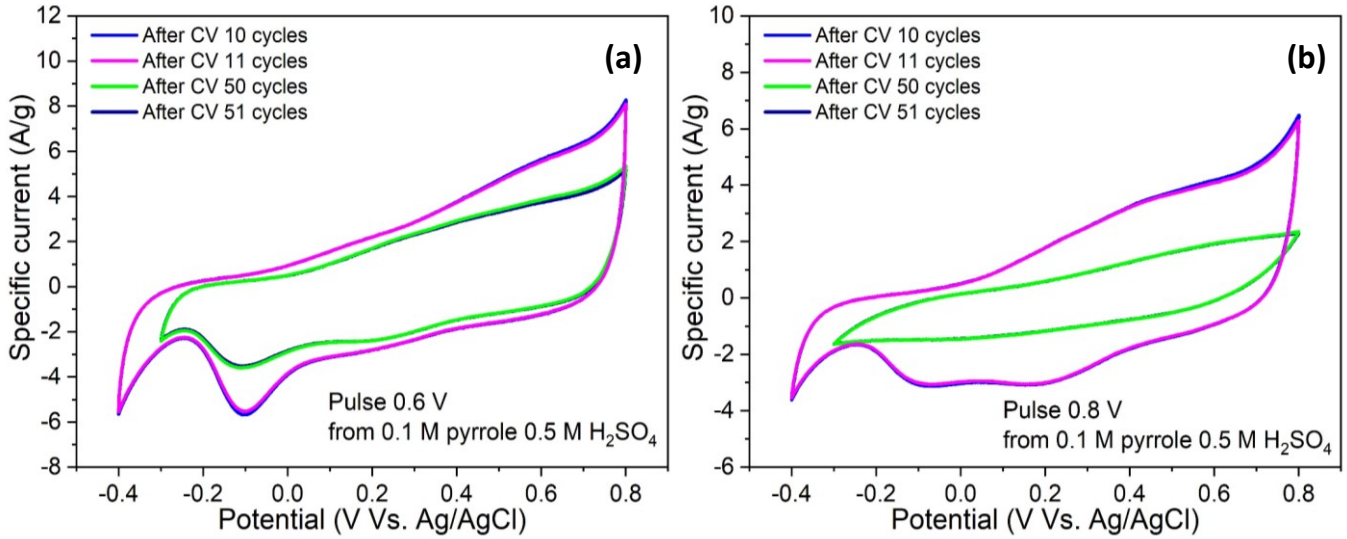

Figure 6.10 CV curves at 10 mV/s of PPy nanotubide buckypapers from pulse polymerisation method (5s_60s, 12 cycles) at different electrodeposition potential: (a) 0.6 V and (b) 0.8 V vs. Ag/AgCl.

6.4 The optimisation of pulse polymerisation method

6.4.1 Optimising pulse sequence

Preliminary studies in the previous sections identified the acidic electrolyte (Section 6.3.1) and pulsed electrodeposition technique (Section 6.3.2) as most promising for further development. However, the pulse sequence applied in previous section deposited too much PPy in too thick layer on the surface, resulting in poor ion transportation and stability. Therefore, in this section, the total deposition time is reduced and the pulse sequence developed to match the total charge in each pulse to the quantity of monomer present within the film. The aim is to avoid the concentration gradients that develop once the monomer present within the internal pores is consumed; if the pulse on time is too long, the process becomes controlled by diffusion of the monomer from the bulk, leading to deposition and overcoating at the outer surface of the electrode. Additionally, the time off period must be long enough to allow the monomer supply within the porous film to be refreshed by diffusion.[157] The ideal structure is a thin layer of PPy deposited uniformly over the CNB network but without fully filling the pores or overcoating the surface. In this case, the PPy deposits should enhance the specific energy and maintain the high specific power of SWCNT, at the same time. To produce the ideal PPy-CNB electrode, the pulse sequence, the electrodeposition time and electrodeposition potential were further optimised. Since the pulse on time are known to control size and chain defects of the PPy and the shorter pulse on time is found to improve the electrical conductivity of PPy.[157, 339, 348] In this section, the 0.1 s,1 s and 5 s were selected as pulse on time per each pulse cycle by considered that the pulse on time at 5 s is found to be sufficiently short but enough time to diffuse the pyrrole monomers into the pore volume of the CNB and successfully produced PPy. The diffusion of electrodeposited electrolyte ions is the significant transport process for electrodeposition reactions. The characteristic diffusion distance (x) of pyrrole monomers through the substrate in each pulse cycle can be estimated (equation 3.18) to ensure that the time in each pulse cycle is sufficiently long. The approach assumes that the number of electrodeposited ions transferred from the bulk electrolyte to the electrode surface can be explained by Fick's law.[349] From the calculation, x values (Table 6.4) of each pulse cycle of 0.1s_10s, 0.1s_60s, 1s_1s, 1s_10s, 1s_60s, 5s_10s and 5s_60s pulse sequence shows longer diffusion distance

than the substrate thickness (32 μm) which confirm that the time in each pulse cycle of all sequence sets are enough to let electrodeposited electrolyte ions pass through the whole substrate. When the electrodeposition reaction proceeds at an appreciable rate, there will be a decrease in the activity of the electrodeposited ions at the electrode/solution interface. If the electrodeposition is carried on continuously, the electrolyte ions will be replaced by diffusion and migration throughout electrode thickness and the electrolyte ion concentration will fall from the bulk value even though the electrodeposition potential is fixed.

From SEM images (Figure 6.11), even though the total accumulated pulse on time is fixed at the same range, the quantities and features sizes of the deposited PPy vary with pulse sequence. As the pulse on time per each cycle decreases from 5 s to 0.1 s, as well as the electrons of each pulse which can calculate from the integration of current vs. time of electrodeposition curve. Pulse sequence at 0.1s_60s for 30 cycles (Figure 6.11a) shows the least amount of PPy on top of the surface compared to other sequences because it has the least amount of electrodeposition charges (Table 6.4). The pulse t_{on} at 1 s and t_{0v} at 10 s and 60 s show similar PPy size which randomly polymerised on top of network surface (Figure 6.11c and d). While the pulse sequence at 5s_60s shows the highest amount of PPy on the surface due to having the highest electrodeposition charge and highest PPy mass loading (Table 6.4). Additionally, the PPy particles electrodeposited from 5s_60s pulse sequence shows the larger agglomerated particles on the surface (Figure 6.11f) because 5s is the longest pulse on time which contributes to the highest electrodeposition charges when considered only one pulse cycle. The longer pulse on time results in the longer polymer chains[327] resulted in some PPy particles from 5s pulse on time deposited on the surface as the particles sizes are too large to fill inside the network.

The resting period by applied 0 V vs. Ag/AgCl in pulse electropolymerisation is also effected the mechanism of the polymerisation. If pulse t_{0V} between two consequent pulses is too short, pyrrole monomers do not have time to diffuse inside the buckypaper network results in the polymerisation happen on the surface instead (Figure 6.11 b and e).

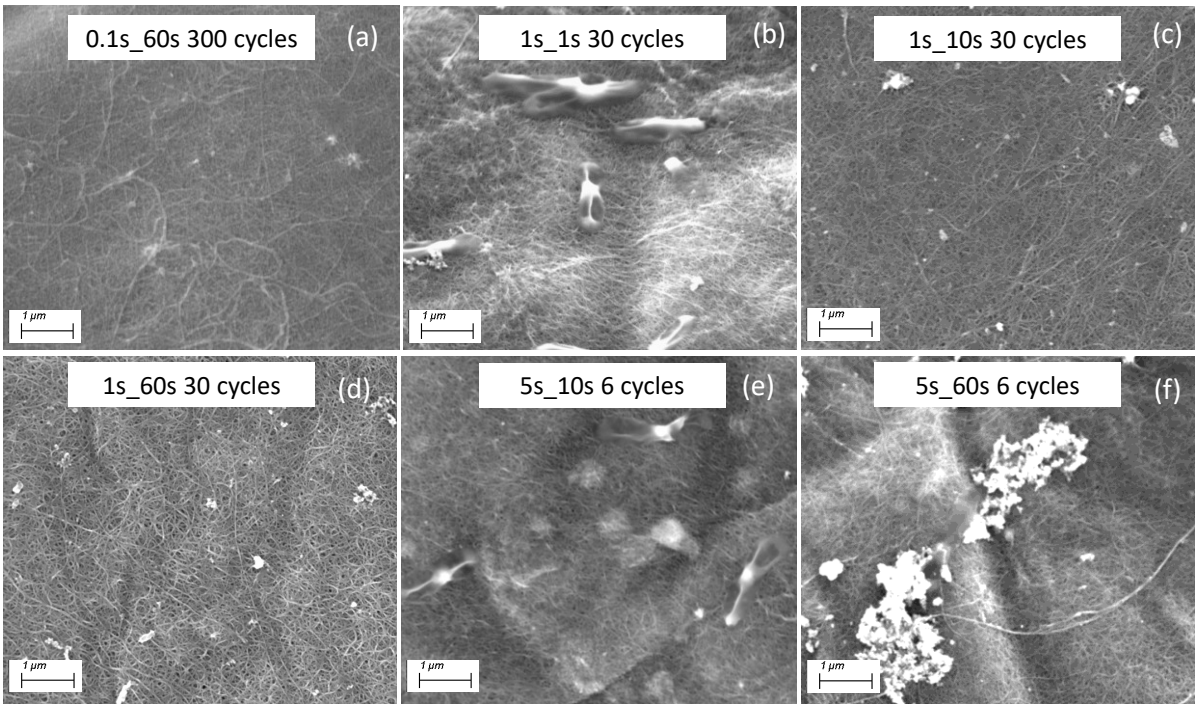

Figure 6.11 SEM images of PPy-CNBs from pulse polymerisation at 0.8 V vs. Ag/AgCl electrodeposition potential with different pulse sequence (t_{on}_t_{off}): (a) 0.1s_60s for 300 cycles, (b) 1s_1s for 30 cycles, (c) 1s_10s for 30 cycles, (d) 1s_60s for 30 cycles, (e) 5s_10s for 6 cycles and (f) 5s_60s for 6 cycles. Note, all PPy were synthesised in a three-electrode configuration using Pt wire as counter electrode, Ag/AgCl as reference electrode and 0.1 M pyrrole and 0.5 M H_2SO_4 as electrolyte.

From SEM images of the PPy-CNB (Figure 6.12a), it is clear that a significant amount of PPy polymerised inside the buckypaper network , most likely before the deposition on the external surface.[350] The FTIR spectra (Figure 6.12b) show similar PPy features as discussed above (Figure 6.7), [351 337] however, the intensity is weaker due to the shorter total deposition time, and hence lower PPy content. The stronger signal from PPy seen for the longer pulse on time 5 s can be attributed to the greater proportion of PPy deposited on the outer surface, under diffusion control, compared with the electrodes prepared from pulse on time 0.1 s and 1 s.

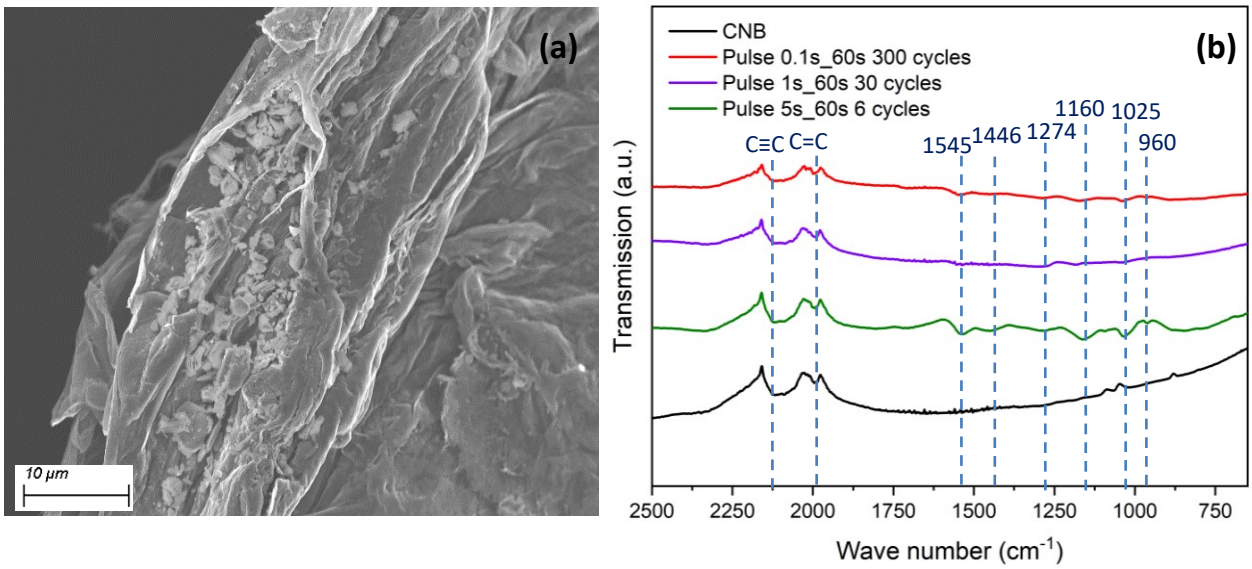

Figure 6.12 (a) Cross-sectional SEM image of PPy-CNB (0.8 V, 1s_60s, 30 cycles) and (b) FTIR of CNB and hybridised PPy-CNB electrodeposited using different pulse sequences.

The current transients during electrodeposition (Figure 6.13) show three characteristic stages depending on the pulse sequence: capacitive charging, the faradaic process for polymerisation and the capacitive discharging (Figure 6.13a). The specific current of every curves show two opposite polarity currents: the positive current combines the initial capacitive charging of the double layer associated with the high surface area network with the oxidative electropolymerisation of PPy; the negative current is associated with discharging the double layer. There could also be a contribution of pseudocapacitive charging/discharging of the deposited PPy.[332] The oxidative current tends towards a finite positive value, associated with the steady state, diffusion limited, oxidative polymerisation. For all the pulse sequences with 1 s and 5 s pulse on time (Figure 6.13c-f), the peak capacitive specific current generally increases with time as PPy is deposited, as the capacitance of the system increases. The polymerisation currents appear relatively stable after initial nucleation in the first cycle(s); at longer total polymerisation times, a lower polymerisation current would be expected (as seen in Section 6.3.2, above). The shortest pulse on time (0.1 s) shows a different dependence (Figure 6.13b); here the time is too short to complete the double layer charging to clearly see the polymerisation current. However, capacitive peak current drops during the initial deposition cycles, presumably as some double layer capacitance is switched to PPy pseudocapacitance which cannot be accessed at short timescales.

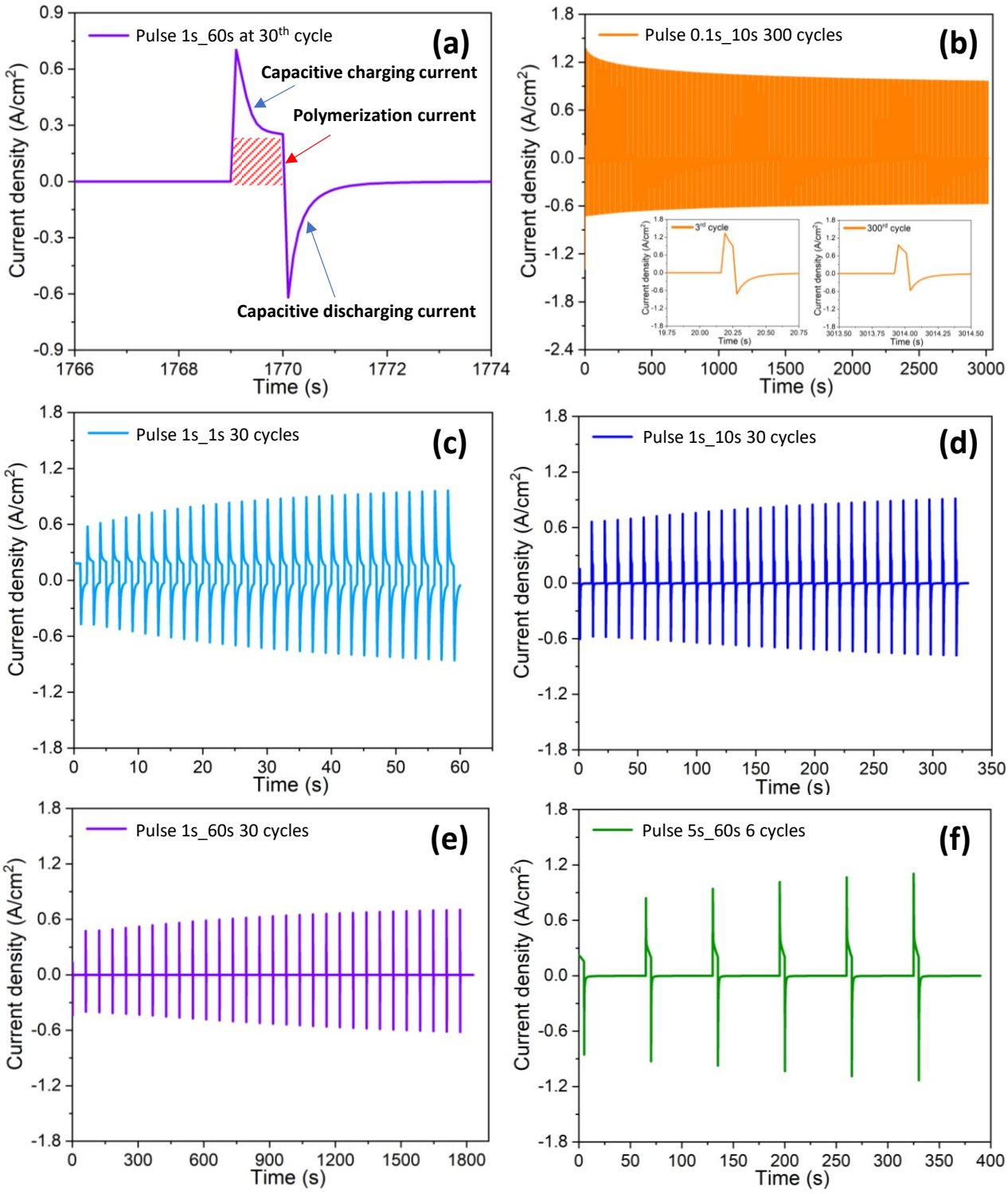

Figure 6.13 Chronoampometry of PPy electrodeposition at different pulse sequences (a) single pulse cycle of the sequence 1s_60s, with schematic assignments, (b) 0.1s_10s for 300 cycles with inset of single pulse at 3rd and 300th cycle, (c) 1s_1s for 30 cycles, (d) 1s_10s for 30 cycles, (e) 1s_60s for 30 cycles and (f) 5s_60s for 6 cycles. All electrodes were synthesised at the same electrodeposition potential 0.8 V, the same total cumulative pulse on time and the same electrodeposition electrolyte 0.1 M pyrrole 0.5 M H_2SO_4.

The TGA curves (Figure 6.14a) of as-synthesised materials were recorded by heating the samples at a temperature range of 100 to 800 °C under nitrogen atmosphere. The CNB substrate shows a one step weight loss at 400 °C which is attributed to the decomposition of the grafted phenyl cross-links formed by reaction with DIB. The PPy-CNBs show three weight loss steps at 250, 400 and over 600 °C. The first stage at around 250 °C is attributed to the initial degradation of the PPy backbone[352], the second stage at 400 °C again to the cross-link decomposition, and the final stage at over 600 °C to the pyrolysis of the remaining PPy residue.[353] The final weight losses at 800°C (indicated in Figure 6.14a) can be used to estimate the mass of PPy deposited. The higher weight loss seen at longer pulse on times (5 s compared to 1 s) is consistent with the greater PPy mass loading and electrodeposition charge, observed at the same total pulse on time (Table 6.4).

The presence of the PPy was confirmed via XPS characterisation. The survey XPS spectra (Figure 6.14b) of PPy-CNBs produced via different pulse sequences show the presence of the characteristic peak of N 1*s* (~400 eV) due to the formation of PPy in the composite.[354, 355] A clear increase in O 1*s* peaks (~532 eV) and the presence of S 2s (~229 eV) and S 2p (~164 eV) are possibly due to the adsorption of HSO^-_4 and SO_4^{2-} from the electrodeposition electrolyte. The characteristic peak C 1*s* (~285 eV) is present in both the CNB substrate and the PPy backbone. The C 1*s* spectrum of the PPy-CNB composite (taking the 1s_60s, 30 cycle sample as an example, Figure 6.14c) can be fitted to a C–C peak at 284.5 eV attributed to sp^2 carbons, and then additional peaks: C–N/C–O at 285.5 eV, C=N/C=O at 286.5 eV, –COO– at 288.9 eV and π-π* at 201 eV .[356-358] Where the C-OH, C=O and -COO- functional groups are from CNB substrate (Figure 5.3d and Figure 6.14c) and C-N and C=N functional groups are from PPy.[354, 355] The nitrogen peak, which is almost entirely absent in the CNB substrate, is characteristic of the introduction of PPy. The deconvolution of the N 1s region (Figure 6.14d) shows a major signal at ~400 eV, assigned to the neutral pyrrolylium nitrogen (–NH) group of the pyrrole unit, the C=N defects of PPy is at ~398 eV, and the polaron ($C–N^+$) structure at ~401 eV, respectively.[359]

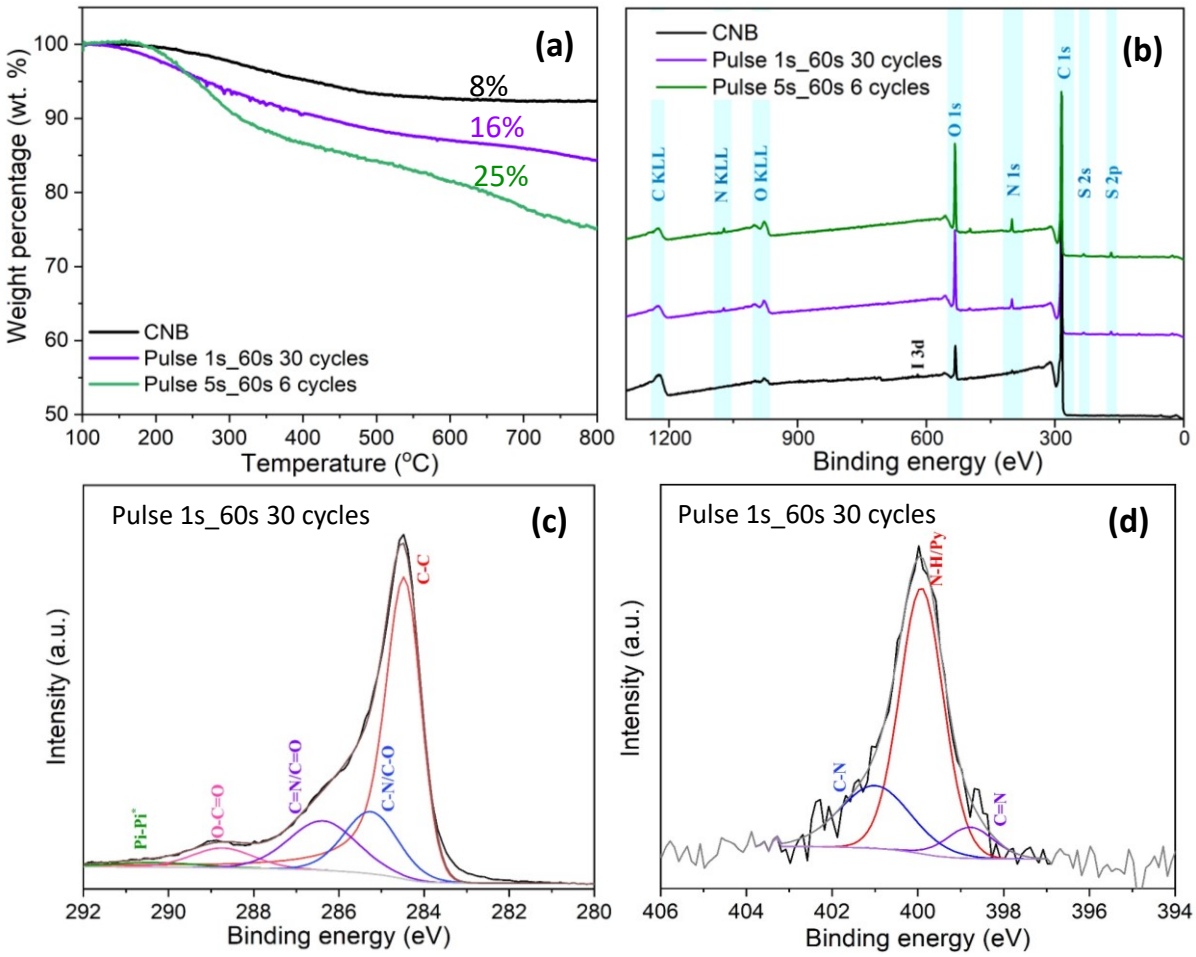

Figure 6.14 (a) TGA (N_2) curves and (b) XPS survey scans of CNB substrate and PPy-CNBs at different pulse sequence. (c) C 1*s* and (d) N 1*s* of PPy-CNB synthesised from 0.8 V vs. Ag/AgCl, 1s_60s for 30 cycles.

Table 6.3 XPS content of CNB and PPy-CNB.

Sample	%at C	%at O	%at Na	%at N
CNB substrate	93.3	5.8	0.2	0.7
PPy-CNB 1s_60s for 30 cycles	83.7	13.7	0.2	2.4
PPy-CNB 5s_60s for 6 cycles	80.1	15.8	0.2	3.9

The electrochemical performance of hybrid PPy-CNBs was investigated via CV and EIS techniques using three-electrode measurement. Pt wire, Ag/AgCl and 1 M H_2SO_4 were used

as counter electrode, reference electrode and electrolyte respectively. In Section 6.3.2, HER was identified below -0.3 V; therefore, in this section, the applied potential range was set from -0.3 to 0.8 V vs. Ag/AgCl. In all cases, the CV curves (Figure 6.15a) show a pair of redox peaks (−0.2 to 0.6 V vs. Ag/AgCl) attributed to redox behaviour of PPy.[360] The CV curve at 50 mV/s of PPy-CNB from pulse sequence 1s_60s for 30 cycles shows less distortion compared with PPy-CNBs synthesised from other pulse sequences (Figure 6.15b) suggesting a better electrochemical rate capability. This sample also shows the maximum gravimetric (Figure 6.15c) and volumetric performance (Figure 6.15d). Looking at the CV curves of the most promising sample in detail (Figure 6.15e), confirms that the relative redox peak contribution decreases with increasing the scan rate.[361] More quantitatively, the capacitive contribution fraction at different scan rates can be portioned via equation 3.8. The diffusion-controlled PPy redox reaction contribution to the overall capacitance drops from 76% at 1 mV/s to 24% at 100 mV/s due to the slow pseudo-capacitive kinetics at the electrode/electrolyte surface (Figure 6.15f).[362] [361] The overall capacitance decreases at higher scan rate due to the lack of ion insertion, as reported elsewhere in literature.[201, 363, 364] The EDLC capacitance of the PPy-CNB is lower than the capacitance of CNB (Tuball75-0.75DIB, Figure 5.14c) due to the PPy deposition which reduces the ion accessible surface area.

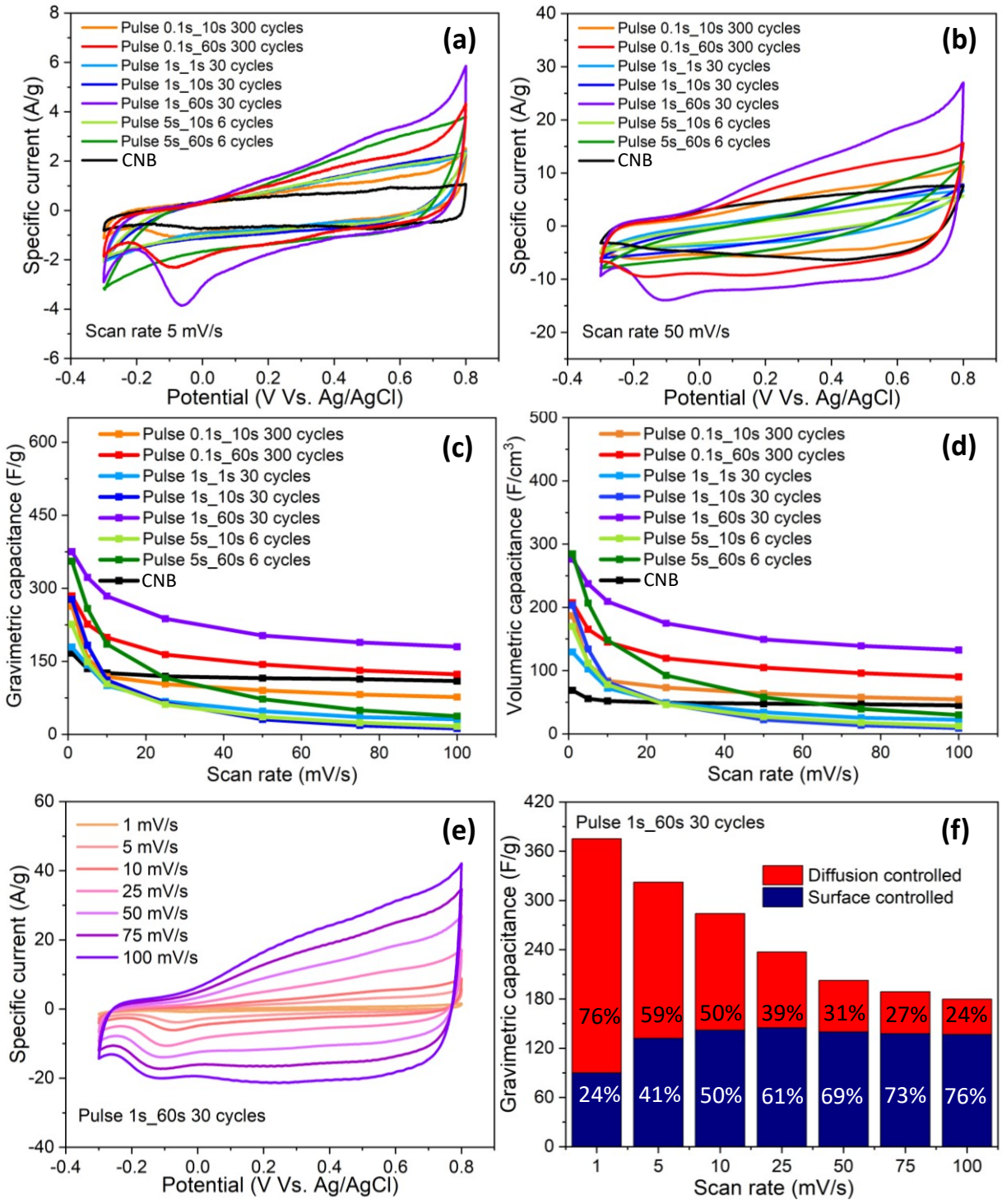

Figure 6.15 Electrochemical performance of PPy-CNBs in three-electrode measurement at different pulse sequence using 1 M H_2SO_4 as an electrolyte: (a) CV curves at 5 mV/s, (b) CV curves at 50 mV/s, (c) gravimetric and (d) volumetric capacitance as a function of scan rate n in 1 M H_2SO_4. (e) CV curves at various scan rates from 1 to 100 mV/s of electrode prepared at pulse 0.8 V on 1s_60s for 30 cycles and (f) relative contributions of the surface controlled and diffusion-controlled capacitance at various scan rates of (e).

At intermediate frequencies, the Nyquist plots (Figure 6.16a) for the PPy-CNBs are less vertical than the CNB substrate, bending towards 45°, due to slow ion diffusion. Similarly, the knee frequencies of the PPy-CNBs are much lower than the CNB substrate (Table 6.4), again indicating slow diffusive effects associated with the redox reaction of PPy.[365, 366] In addition, the knee frequency of PPy-CNBs synthesised from pulse t_{0V} at 1 s and 10 s are lower than the knee frequency of electrode synthesised from pulse t_{0V} at 60 s, presumably as the longer t_{0V} allows a more uniform redistribution of monomer and hence PPy. More uniformly deposited PPy should be thinner, less prone to pore blockage or surface overcoating, and therefore offer better rate performance. The R_{ct} of the CNB (Table 6.4) similarly also increase after hybridisation with PPy, particularly for the smaller pulse t_{0V} (1 s and 10 s).

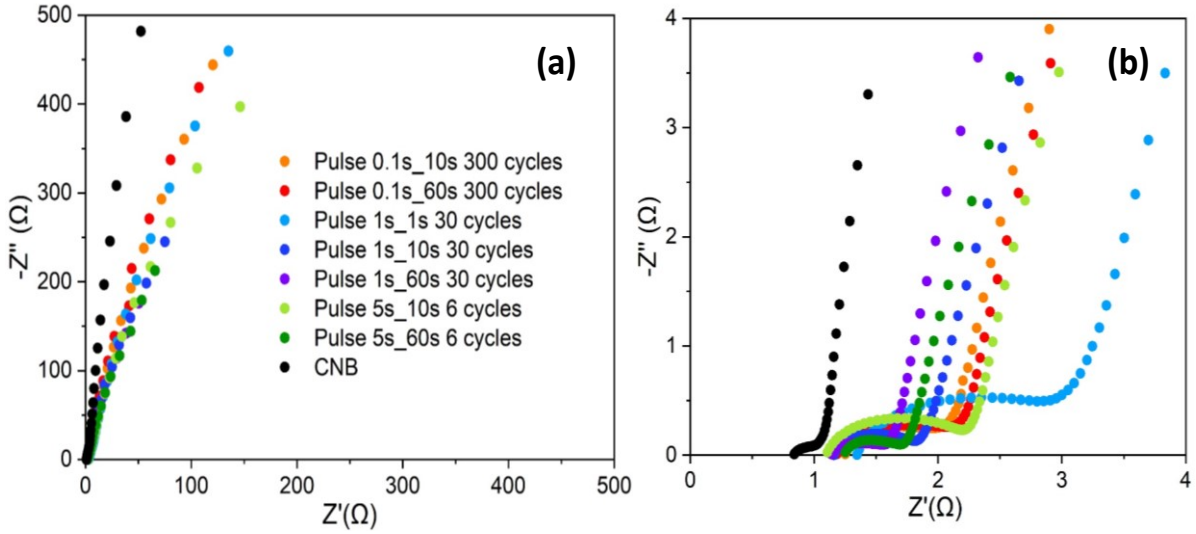

Figure 6.16 Nyquist plots of CNB and PPy-CNBs synthesised from different pulse sequences: (a) full range and (b) magnified at the low frequency range.

Overall, the pulse sequence should be designed to deposit a thin layer of PPy uniformly over the SWCNT network. The pulse resting period must be sufficiently long to allow for monomer replenishment. Longer resting periods simply extend the overall fabrication process. Around 60s off is sufficient for the CNBs used in this study, although the exact value is expected to depend on thickness (squared). The pulse on time should be sufficient to deposit a significant fraction of the monomer in the pores each cycle, but not deplete it. Too short pulse on time mean that current is lost to capacitance double layer charging, making the polymerisation inefficient. The optimum in the current sample is a pulse on time around 1 s, although it is expected to vary with monomer concentration and substrate porosity.

Table 6.4 ESR, R_{ct}, knee frequency, thickness, electrodeposition charge, the characteristic diffusion distance, mass loading and electrodeposition efficiency of PPy on CNB synthesised from different pulse sequence.

Electrode	ESR (Ω)	R_{ct} (Ω)	Knee Frequency (Hz)	Thickness (µm)	Electrodeposition charge of PPy (C/cm^2)	Distance x (µm)/cycle	PPy loading (mg/cm^2) and electrodeposition efficiency (%)
CNB substrate (Tuball75-0.75DIB)	0.83	0.37	158.00	32.4±0.4	-	-	-
0.1S_10S 300 cycles	1.25	1.05	38.42	33.6±0.4	3.53	158.9	1.05 (43%)
0.1S_60S 300 cycles	1.18	1.32	49.87	34.6±0.4	4.46	387.6	1.19 (38%)
1S_1S 30 cycles	1.34	2.06	20.03	35.2±0.5	3.25	70.7	1.21 (53%)
1S_10S 30 cycles	1.16	0.74	24.93	34.8±0.5	3.62	165.8	1.22 (48%)
1S_60S 30 cycles	1.14	0.56	63.34	35.0±0.7	3.61	390.5	1.25 (50%)
5S_10S 6 cycles	1.11	1.29	9.97	36.0±0.4	3.97	193.6	1.37 (50%)
5S_60S 6 cycles	1.25	0.55	15.63	35.2±0.5	5.83	403.1	1.48 (36%)

6.4.2 Optimising the total pulse cycle

Having established the optimum pulse polymerisation conditions in previous section (0.8 V vs. Ag/AgCl, 1s_60s), this section explores the effect of the total accumulated pulse on time (PPy content) by varying the total pulse cycle from 15 to 60 cycles. As expected, the total PPy loading increased systematically with the total pulse cycle, as the total electrodeposition charge was increased from 2.4 to 5.2 C/cm^2 while increased the total pulse cycle from 15 to 60 cycles. The total number of cycles was chosen to avoid significant overcoating – as shown by the minimal increase in film thickness observed (Table 6.5). There was surprisingly little change in the CV curves, with increasing PPy content. However, the redox peaks first increase and sharpen as more PPy is introduced, then broaden and separate especially at the higher scan rate (Figure 6.17a and b). The poor reversibility of redox reaction especially in PPy-CNB prepared from 45 and 60 pulse cycles leads to the poorer electrochemical rate capability (Figure 6.17c and d) as the buckypaper thickness increases (Table 6.5). The absolute specific capacitance of the electrodes is almost similar, suggesting that it is dominated by the PPy performance, with relatively little remaining EDLC from the SWCNTs; however, the intermediate pulse cycle (30 cycles) does offer the best performance, combining a larger amount of PPy without additional rate limitations. The specific volumetric performance (Figure 6.17d) of the electrodes also show little difference due to the small increase in the total film thickness (Table 6.5).

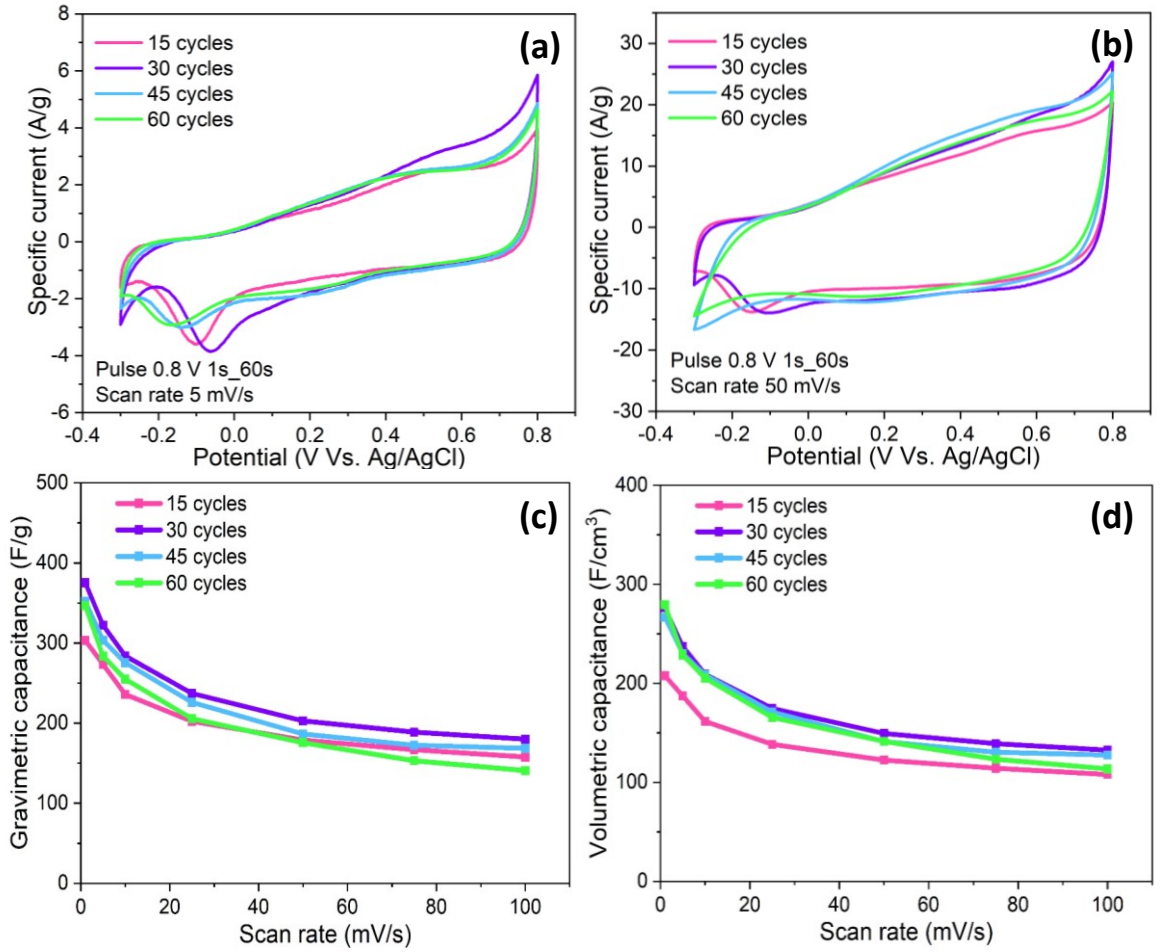

Figure 6.17 Electrochemical performance of PPy-CNBs systhesised from different total pulse cycles (mass loadings): (a) CV curves at 5 mV/s, (b) CV curves at 50 mV/s, (c) gravimetric and (d) volumetric capacitance as a function of scan rate normalised by mass and volume of active electrodes in 1 M H_2SO_4. Note, the pulse sequence which used to synthesis these PPy-CNBs were set at at 0.8 V vs. Ag/AgCl and 1s_60s.

The Nyquist plots (Figure 6.18) show a reduction in ESR when the total pulse cycle exceeds 30 cycles due to increasing density of the electrodes as PPy fills the pores within the SWCNT network (Table 6.5). However, kinetic resitrictions associated with thicker PPy deposits and overcoating causes a decrease in knee frequency and an increase of R_{ct} when the total pulse cycle exceeds 30 cycles (Table 6.5). The distortion of CV curves at 50 mV/s (Figure 6.17b) shows similar trends above 30 pulse cycles associated with slight capacitance reduction and poorer rate capability (Figure 6.17c and d).

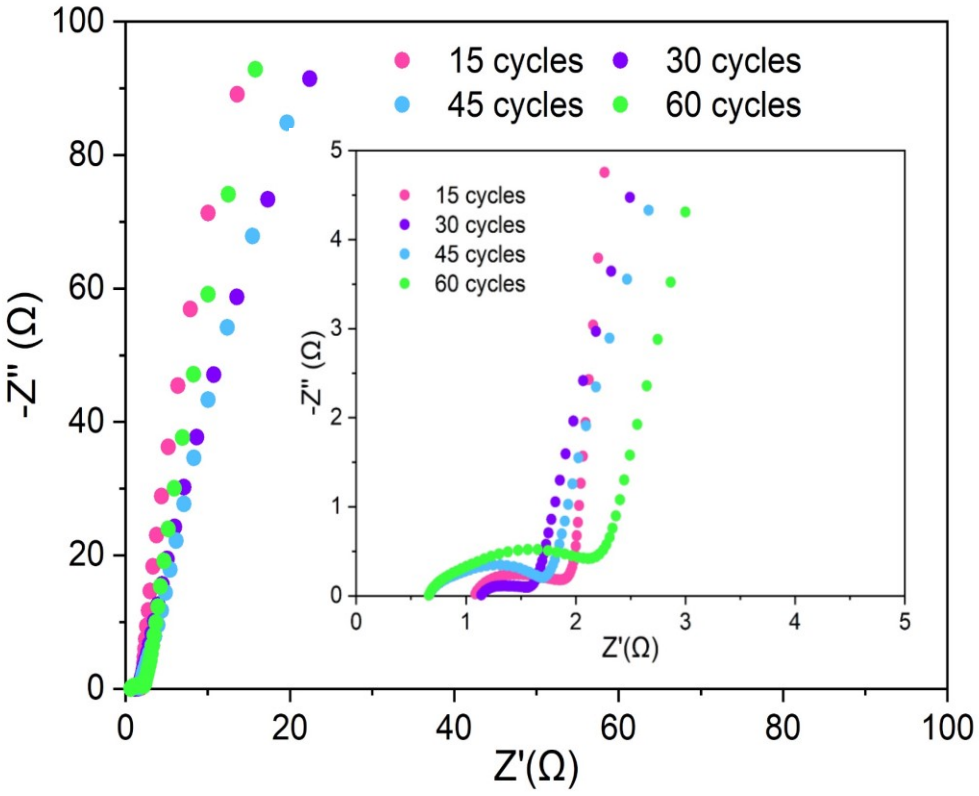

Figure 6.18 Nyquist plots of PPy-CNBs systhesised from different total pulse cycles using pulse sequence at 0.8 V vs. Ag/AgCl and 1s_60s.

Table 6.5 ESR, R_{ct}, knee frequency, thickness, density, electrodeposition charge and mass loading of PPy on CNB synthesised at different electrodeposition charges per unit area, using pulse sequence at 0.8 V vs. Ag/AgCl and 1s_60s.

Electrode	ESR(Ω)	R_{ct}(Ω)	Knee frequency (Hz)	Thickness (μm)	Density (g/cm^3)	Electrodeposition charge of PPy (C/cm^2)	PPy loading (mg/cm^2)
CNB substrate (Tuball75-0.75DIB)	0.83	0.37	158.00	32.4±0.4	0.42±0.01		-
1s_60s for 15 cycles	1.09	0.96	99.73	32.6±0.5	0.68±0.01	2.4	0.41
1s_60s for 30 cycles	1.14	0.56	63.34	35.0±0.7	0.73±0.01	3.6	1.25
1s_60s for 45 cycles	0.67	1.13	38.42	37.6±0.5	0.76±0.01	4.5	1.5
1s_60s for 60 cycles	0.66	1.79	24.93	39.8±0.5	0.81±0.01	5.2	1.8

6.4.3 Influence of electrodeposition potential

The influence of applied PPy deposition potential on electrochemical performance was explored in Section 6.3.2 using 5s_60s for 12 pulse cycles. However, this pulse sequence was found to deposit too much PPy, leading to excessive overcoating. Therefore, the effect of applied potential is reinvestigated in this section using the optimum pulse sequence from previous section (1s_60s for 30 cycles). Consistent with the mass uptake, the SEM images (Figure 6.19a to d) show the amount of PPy increases with applied potential because the electrodeposition charge also increases (Table 6.6). When the applied potential exceeded 1.0 and 1.2 V vs. Ag/AgCl, the PPy was found to fully cover the buckypaper surface (Figure 6.19c and d).

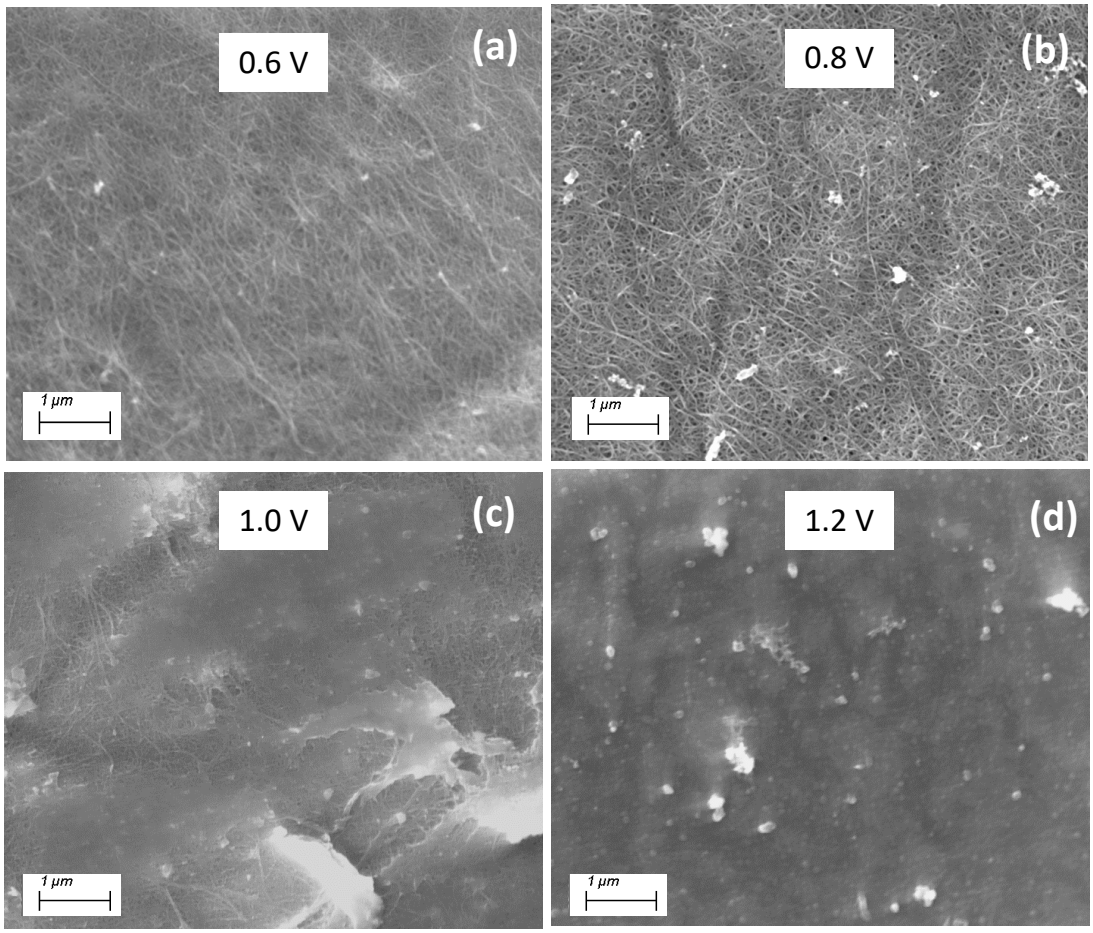

Figure 6.19 SEM images of PPy-CNBs synthesised from pulse 1s_60s for 30 cycles at different electrodeposition potential: (a) 0.6, (b) 0.8, (c) 1.0 and (d) 1.2 V vs. Ag/AgCl.

Table 6.6 ESR, R_{ct}, knee frequency, thickness, electrodeposition charge, mass loading and electrodeposition efficiency of PPy on CNB synthesised from different electrodeposition potential.

Electrode	ESR(Ω)	R_{ct}(Ω)	Knee frequency (Hz)	Thickness (µm)	Electrodeposition charge of PPy (C/cm^2)	PPy loading (mg/cm^2) and electrodeposition efficiency (%)
CNB substrate (Tuball75-0.75DIB)	0.83	0.37	158.00	32.4±0.4	-	-
0.6 V 1s_60s 30 cycles	0.66	0.84	99.73	32.6±0.6	0.42	0.41 (141%)
0.8 V 1s_60s 30 cycles	1.14	0.56	63.34	35.0±0.7	3.61	1.25 (50%)
1 V 1s_60s 30 cycles	0.66	1.04	49.87	37.6±0.5	8.73	1.5 (25%)
1.2 V 1s_60s 30 cycles	0.71	3.79	9.97	38.0±0.5	11.36	1.8 (23%)

The chronoampometry at the different electrodeposition potentials (Figure 6.20) shows the behaviour discussed in section 6.4.1, with both positive and negative current transients. The chronampometry traces at different voltages actually represent different stages of the deposition, as the higher voltages have much greater PPy content (Table 6.6). At the electrodeposition potential 0.6 V (Figure 6.20a), the specific current shows the lowest value compare with the specific current of the electrode from other applied potential results in the least amount of PPy (Table 6.6). Thus the 0.6 V shows the early stages of thin PPy deposition when the original EDLC signal is largely unchanged (Figure 6.20b). While the electrodeposition potential at 0.8 V and 1 V show the similar trend of current transients (Figure 6.20c-f) which begin to show an increase in capacitance associated with the PPy contribution (Figure 6.20 d and f). While 1.2 V highlights the pore blockage associated with excess deposition as the layer thickens and eventually overcoats, the EDLC signal is supressed (Figure 6.20g and h).

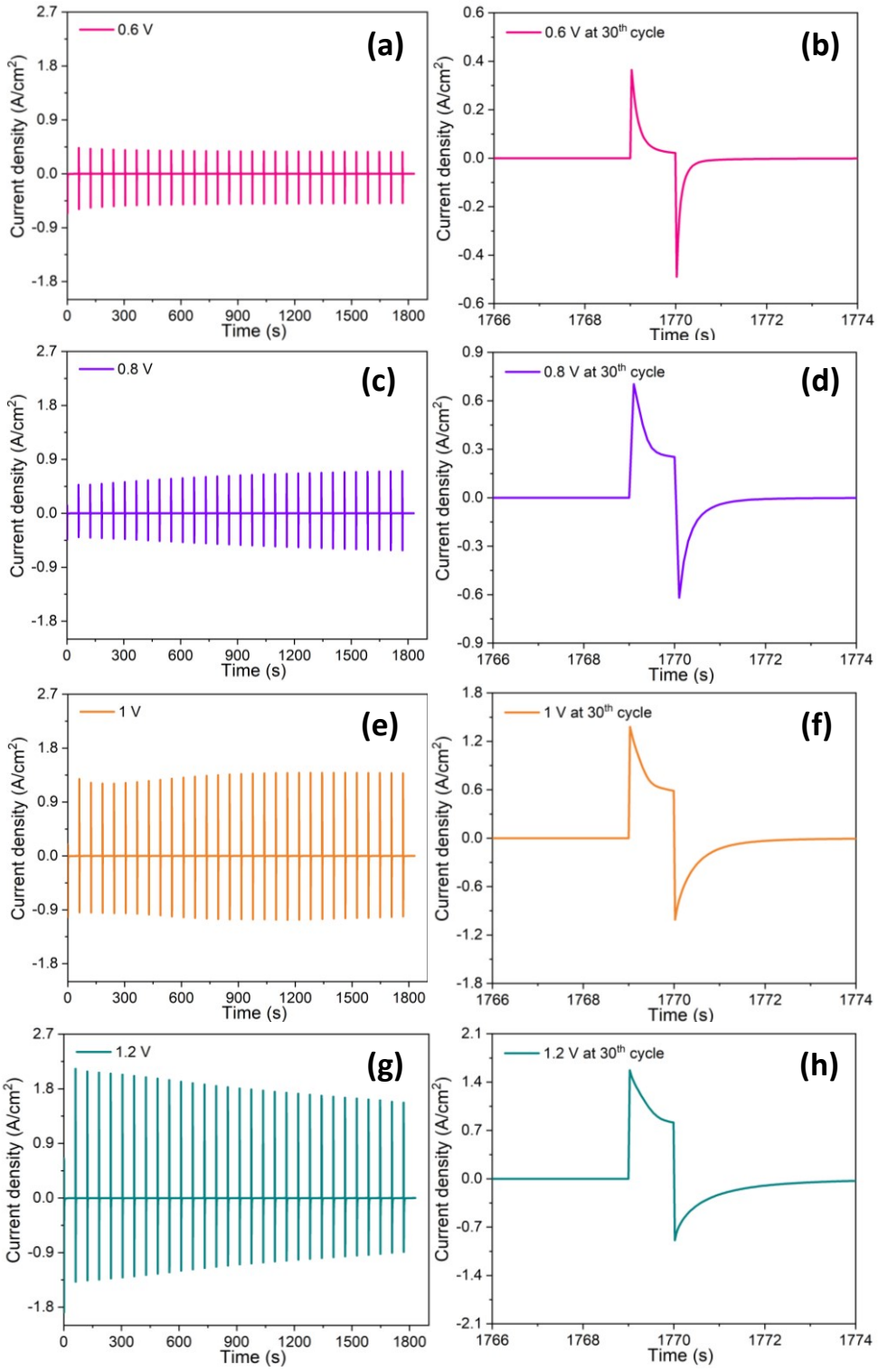

Figure 6.20 Chronoampometry of PPy electrodeposition at different applied potential (a) 0.6 V, (b) 0.8 V, (c) 1 V and (d) 1.2 V. Current as the function of time at 30th pulse cycle of PPy electrodeposition at different applied potential (b) 0.6 V, (d) 0.8 V,(f) 1.0 V and (g) 1.2 V. All were synthesised at the same concentration 0.1 M pyrrole 0.5 M H_2SO_4 and pulse sequence 1s_60s for 30 cycles.

The PPy-CNB synthesised at 0.8 V vs. Ag/AgCl showed the highest gravimetric and volumetric capacitances at both 5 mV/s (Figure 6.21a) and 50 mV/s (Figure 6.21b) and achieves the highest electrochemical rate capability compared with the electrodes synthesised at other potentials (Figure 6.21c and d). The CV curves of PPy cross-linked nanotubide buckypaper from 0.6 V vs. shows lower CV curve area compared to 0.8 V vs. Ag/AgCl and shows a response similar to pure CNB due to the low amount of PPy on the SWCNT network. The CV curves of electrodes deposited at 1.0 and 1.2 V (Figure 6.21 a and b) show a heavily resistive shape due to the dense surface overcoating with PPy which fully obstructs the pores of SWCNT network (Figure 6.19c and d).

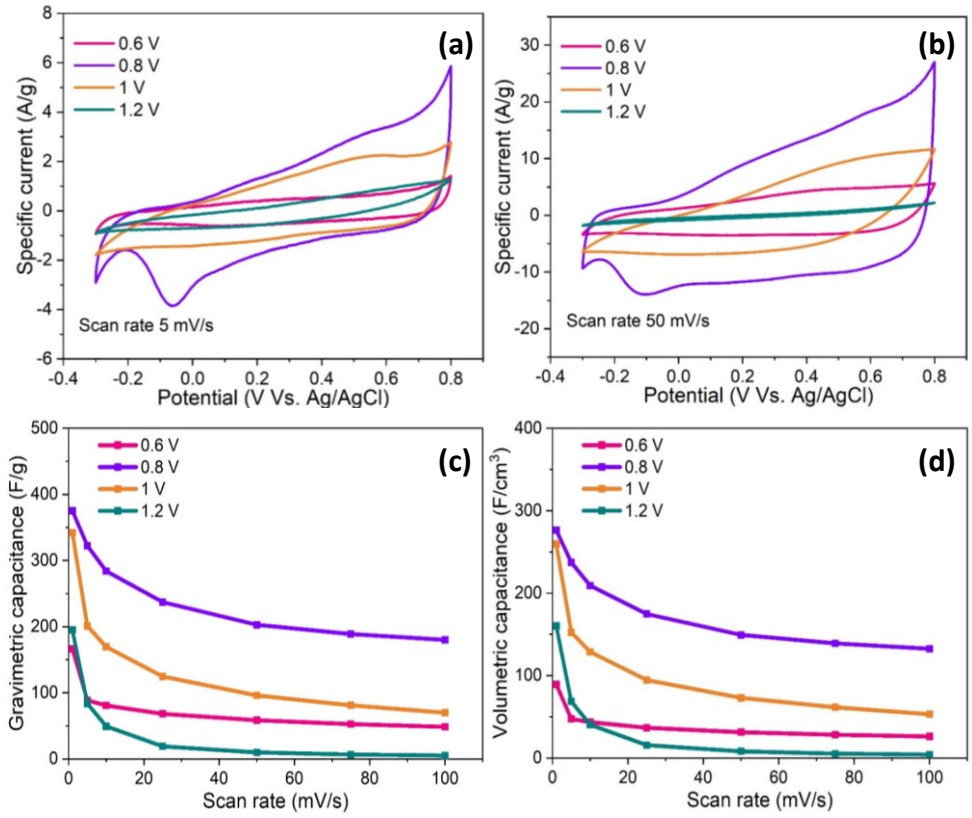

Figure 6.21 Electrochemical performance of PPy-CNBs synthesised with pulse sequence 1s_60s for 30 cycles at different applied potential: **(**a**)** CV curves at 5 mV**/**s, **(**b**)** CV curves at 50 mV**/**s, (c) gravimetric and (d) volumetric capacitance as a function of scan rate in 1 M H_2SO_4.

From the Nyquist plots (Figure 6.22), the electrodes deposited at 1.0 and 1.2 V also show higher R_{ct} values and lower the knee frequencies (Table 6.6), implying lower specific power density. These data confirm that the quantities of PPy critical control performance because excess PPy obstruct the ion pathway.

Effective multifunctional structural electrodes need strategies that might simultaneously improve electrochemical and mechanical performance. Hybridising PPy with CNB is one promising possibility, as the redox polymer is expected to not only enhance the specific energy but also improve load transfer between the CNTs. This potential synergy was explored by applying tensile tests to the optimum hybrid PPy-CNB (0.8 V vs. Ag/AgCl, 1s_60s for 30 cycles) compared to the pure CNB substrate. The introduction of PPy dramatically decreased the tensile modulus (at 0.5-1% strain) from 345±61 MPa (Table 5.5) to 110±11 MPa due to the dramatically increased in tensile strain of hybrid electrode (Figure 5.18a and Figure 6.22b). The stress-strain curves of PPy cross-linked nanotubide buckypaper (Figure 6.22b) show a plastic yielding behaviour, with an average strain to failure at 22%. The big improvement in strain of the hybrid composite may be attributed to the PPy filling in the pores within the cross-linked nanotubide network, improving load transfer and limiting the propagation of the cracks.[367] The modest enhancement in tensile strength of PPy-CNB (22±1 MPa) when compared with the pure CNB substrate (18±1 MPa, Figure 5.18a) may also be attributed to the improved load transfer and delayed failure.[368, 369]

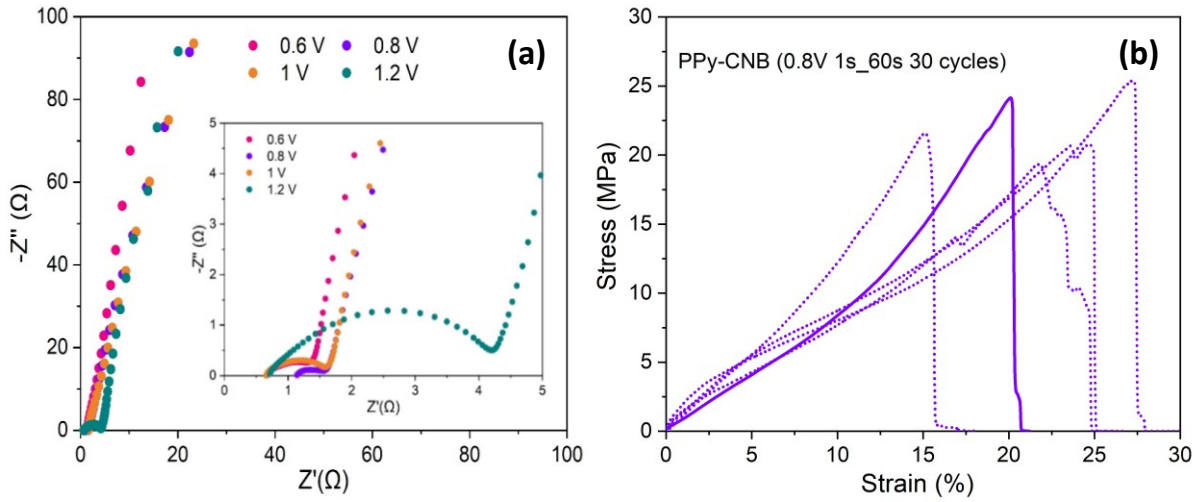

Figure 6.22 (a) Nyquist plot of PPy-CNBs synthesised from pulse sequence 1s_60s for 30 cycles with the different electrodeposition potential. (b) Stress–strain curves of PPy-CNBs synthesised from pulse 1s_60s for 30 cycles at 0.8 V vs. Ag/AgCl.

6.5 Hybrid PPy-CNB//CNB asymmetric supercapacitor

Having optimised the electrodeposition of PPy on CNB and investigated electrode properties through three-electrode measurement, full cell devices were further explored by fabricating pouch cells using PPy-CNB as the positive electrode and CNB as the negative electrode. PPy is a p-dopable conducting polymer, therefore, it can be used as positive electrode only where the dopants produce positive polarons.[370] Since the capacitance of positive and negative electrodes are not equal, the mass between positive and negative electrodes needed to be balanced to optimise the full cell performance. The mass ratio was calculated via equation 6.1, [371, 372] where C_{s+} and C_{s-} are the specific capacitance of positive and negative electrodes respectively. V_+ and V_- are the potential of positive and negative electrodes respectively.

$$\frac{m_+}{m_-} = \frac{C_{s-}V_-}{C_{s+}V_+} \qquad \text{Equation 6.1}$$

The area ratio between positive and negative electrode was calculated via equation 6.2 to optimise the size between positive and negative electrodes where ρ_{A+} and ρ_{A-} are the area density of positive and negative electrodes respectively. Note, the area density of PPy-CNB synthesised from 1s_60s for 30 cycles is 2.6 mg/cm^2.

$$\frac{A_+}{A_-} = \frac{m_+\rho_{A+}}{m_-\rho_{A-}} \qquad \text{Equation 6.2}$$

The PPy-CNB (positive electrode) in this section was synthesised from 0.8 V electrodeposition potential at pulse sequence 1s_60s for 30 cycles as it provides the maximum electrochemical performance. Using CNB at 1.4 mg/cm^2 as a negative electrode, the calculated area ratio between positive and negative electrodes is around 0.31 which implies significantly different areal sizes between negative and positive electrodes leading to a higher resistance and slower ion transportation in the cell device. Therefore, the CNB (negative electrode) in this section was synthesised using SWCNT mass loading at 1.8 mg/cm^2 instead of 1.4 mg/cm^2 to reduce the size difference between positive and negative electrode. From Section 5.4.2, it was known that the 1.8 mg/cm^2 electrode offered 95% of the electrochemical performance of the 1.4 mg/cm^2 electrode. The positive and negative electrode area ratio was recalculated from the electrochemical performance of PPy-CNB at

optimum conditions and CNB with 1.8 mg/cm^2 mass loading then, giving the area ratio at 0.41. The substrates for PPy-CNB (positive electrode) were maintained at 1.4 mg/cm^2 of SWCNT mass loading to be able to compare the electrochemical performance of the hybrid electrodes from the three-electrode measurements.

After balancing the mass and area between positive and negative electrodes, the asymmetric supercapacitor was fabricated in the general design (1P_1N) using one positive electrode sandwiched with a separator and negative electrode as described in Figure 6.1b. Where the in house BC nanopaper[226] (7 µm thick) was again used as an ultra-thin separator since it was found to improve performance in the pure EDLC configurations (see Section 4.5.1). In the 1P_1N device, the negative electrode has a bigger size to balance the increased areal capacitance of the positive electrode. The CV curve of 1P_1N at 10 mV/s (Figure 6.23a) shows small peaks from the redox reaction of PPy whilst the CV curve at 500 mV/s (Figure 6.23b) shows a distorted shape without any redox peaks, indicating poor electrochemical rate capability. The unbalanced positive and negative electrode sizes of the 1P_1N device leads to insufficient electrode utilisation and increases the resistance of the whole cell device. Therefore, to reduce the resistance of the cell device, a new architecture (1P_2N) was developed by sandwiching one positive hybrid electrode (PPy-CNB) between two negative electrodes (CNBs) with the same area size in each electrode (Figure 6.1c) to shorten the ion transportation path between electrodes. The CV curves (Figure 6.23a and b) of 1P_2N device provide the higher redox peak area at 10 mV/s and less distortion at 500 mV/s indicating the better capacitance rate capability (80%). Unfortunately, the area under the CV curves of 1P_2N device is smaller than for 1P_1N, resulting in lower electrochemical capacitance (Figure 6.23c and d). This outcome was unexpected since the new configuration (1P_2N) should provide at least higher or equal performance compared to the normal 1P_1N design. In principle, the 1P_2N device is enabled by the high conductivity of the buckypaper that can allow it to act as an integral, porous current collector, maintaining access on both sides. However, these first 1P-2N devices used Pt plates as a back-up current collector inserted centrally, so some area of positive electrode may be obstructed, leading to the lower electrochemical performance. It is also possible that the top and bottom of the films are not fully equivalent and may create other performance issues. The 1P_2N device has a higher overall thickness due to the design which stack 3 electrodes and 2 separators together. While

1P_1N device only comprise with the 2 electrodes and 1 separator. In the end, the gap between gravimetric and volumetric performance from the two devices is similar, but once optimised the 1P_2N device may offer improvements. At the same area size electrodes, 1P_2N, can shorten ion diffusion distance, therefore increasing the kinetics of ion transfer. The gravimetric capacitance ratio between capacitive and diffusion controlled of 1P_2N (Figure 6.23e) and 1P_1N (Figure 6.23f) devices were examined via equation 3.8. The diffusion controlled contribution of both devices reduced steadily with increasing scan rate as expected for hybrid devices.[363] The diffusion controlled contribution of 1P_2N device is slightly higher than 1P_1N in every scan rate; since the rate capability from 1P_2N is higher than 1P_1N, the new architecture merits further study.

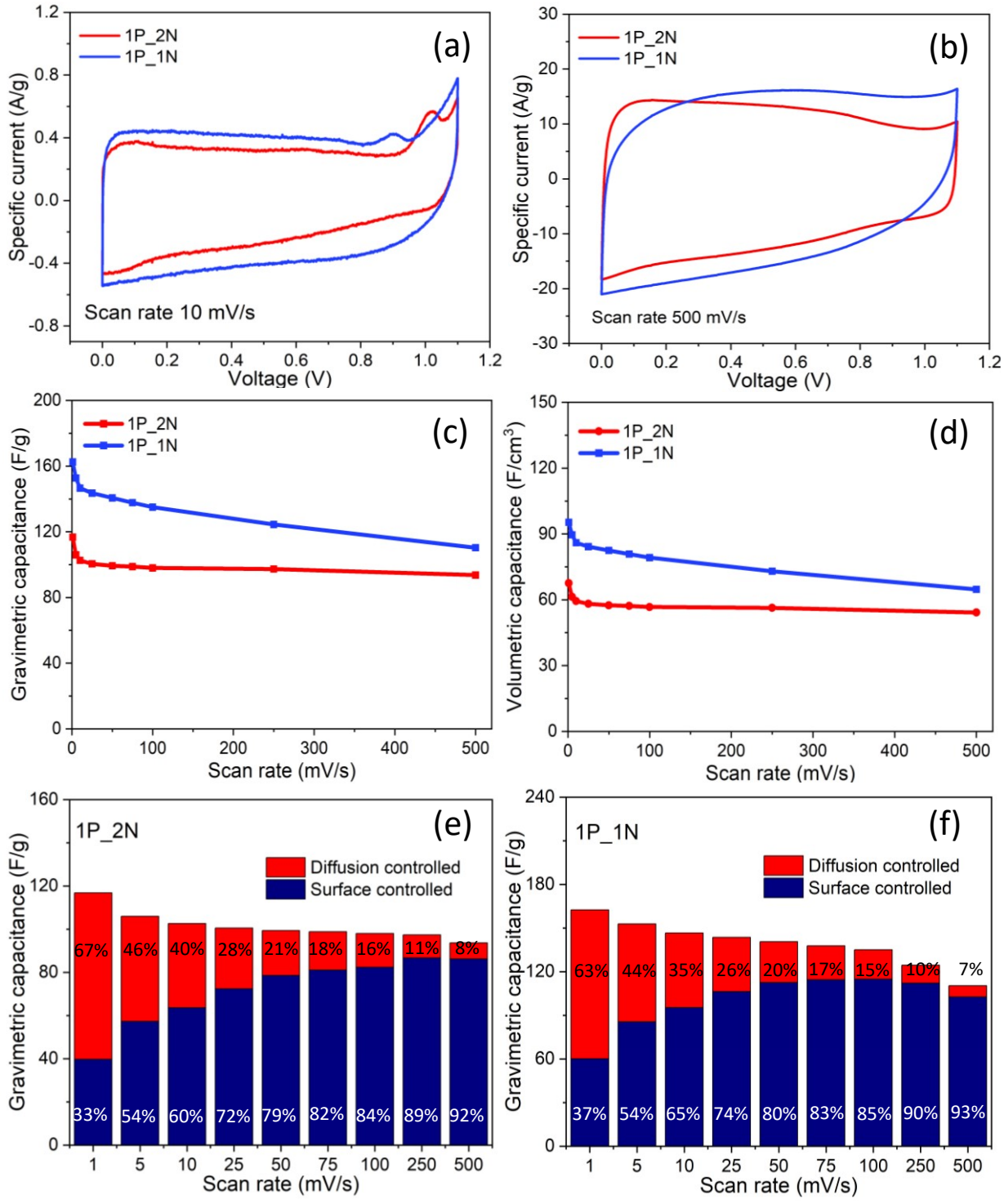

Figure 6.23 Asymmetric supercapacitors of PPy-CNB//CNB using BC nanopaper as separators and 1 M H_2SO_4 as electrolyte; (a) CV curves at 10 mV/s, (b) CV curves at 500 mV/s, (c) gravimetric capacitance and (d) volumetric capacitance normalised by the mass and volume of positive and negative electrodes. Contribution ratio between the surface controlled and diffusion controlled capacitance at various scan rates of (e) 1P_2N and (f) 1P_1N devices.

The hybrid full cell devices were compared to the aqueous full cell, symmetric pure EDLCs developed in Section 4.5.1. Nyquist plots (Figure 6.24a) highlight the exceptionally small ESR values of 0.12, 0.47 and 0.62 Ω for symmetric, 1P_2N and 1P_1N devices respectively, which reflect the high conductivity of the nanotubide buckypapers, CNB, PPy-CNB, the ultrathin BC nanopaper, and the good contact between the constituents. At low frequencies, the Nyquist plots of all three devices exhibit a nearly vertical line, close to an ideal supercapacitor implying good electrochemical capacitive behaviour with fast ion diffusion.[254] The dependence of the capacitance on frequency (Figure 6.24b) normalised by the mass of the devices, which included electrodes, electrolyte and separator, shows distinct responses. The symmetric nanotubide buckypaper supercapacitor has less sensitivity to frequency, as expected, maintaining performance to around 100 Hz.[373] The hybrid devices have a higher capacitance due to the pseudo-capacitive contribution but drop off sooner with frequency. The gravimetric capacitance of 1P_2N is lower than 1P_1N as noted in the discussion of the CV measurements (Figure 6.23c). The GCD at 1 A/g of symmetric device shows a symmetrical triangular shape typical of EDLC behaviour[263]. The hybrid devices (Figure 6.24c) display an irregular triangular shape particularly for the 1P_2N device, suggesting that the capacitance has a significant contribution from redox activity.[360] The discharging time of 1P_1N is longer than 1P_2N device due to the higher specific capacitance (Figure 6.24c) in good agreement with the result from CV and EIS measurements (Figure 6.23c and Figure 6.24b). The gravimetric (Figure 6.24d) and volumetric (Figure 6.24e) capacitance were calculated from GCD curves via equation 3.11, normalising with the mass and volume of electrodes and the device (electrodes, electrolyte and separator) in order to study the influence of electrode materials, separator and electrolyte to the electrochemical performance. The gravimetric capacitance normalised by mass of the device of 1P_2N and 1P_1N devices are increased by 32% and 69% when compared with symmetric nanotubide buckypaper device. The volumetric capacitance is even greater, 2.1 and 2.5 times higher than the symmetric device, for 1P_2N and 1P_1N devices respectively. Hybridising PPy in electrode show a larger improvement in volumetric than gravimetric region as the redox active material is mostly stored within the buckypaper paper pore network. Therefore, the increment in volume of buckypaper is much less when compared with the increment in mass of buckypaper (Table 6.6).

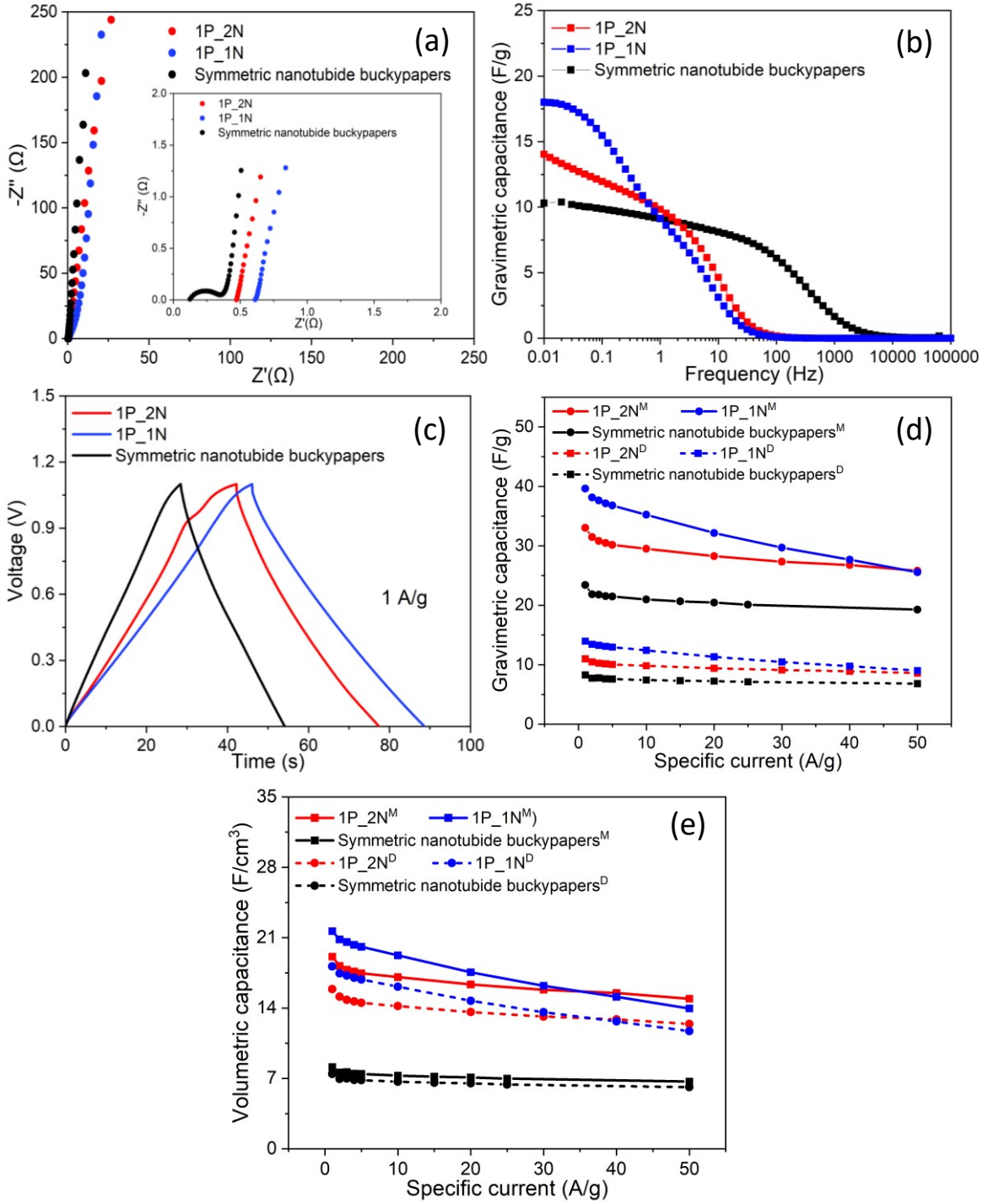

Figure 6.24 Symmetric supercapacitor of nanotubide buckypapers and asymmetric supercapacitors of PPy-CNB//CNB (1P_1N and 1P_2N) using BC nanopaper as separators with 1 M H_2SO_4 as electrolyte; (a) Nyquist plots, (b) the gravimetric capacitance of electrodes according to the frequency normalised by total mass of the device, (c) GCD curves at 1 A/g , (d) the calculated gravimetric capacitance and (e) the calculated volumetric capacitance normalised by both active material (straight line, M) and total mass of device (dash line, D).

The Ragone plot of 1P_1N shows an energy density of 3.8 mWh/cm^3 (7.2 Wh/kg) at a power density of 277 mW/cm^3 (532 W/kg). The energy density drops by 69% at 50 A/g maintaining 1.2 mWh/cm^3 (2.3 Wh/kg) at a power density of 7.7 W/cm^3 (14.7 kW/kg). While the 1P_2N device shows a slightly lower energy density of 3.0 mWh/cm^3 (5.1 Wh/kg) at a power density of 303 mW/cm^3 (524 W/kg), it achieves a smaller drop, 45%, and achieve higher power density of 10.6 mW/cm^3 (18.3 kW/kg) when compared with the 1P_1N device at 50 A/g (Figure 6.25a and b). Note, all of these data are normalised by the mass and volume of positive and negative electrodes in order to compare with the electrochemical performance from the literature. The gravimetric energy density of both fabricated asymmetric devices may be not particularly high, however, the volumetric energy density of the fabricated devices are particularly promising when compared with other asymmetric PPy-carbon based supercapacitors from literature. [374-379] Importantly, the power density of fabricated devices is exceptionally high in both gravimetric and volumetric terms when compare with those from literature. Encouragingly, and perhaps surprisingly, the power densities are also comparable with the already excellent nanotubide symmetric supercapacitors. Clearly the optimisation of the PPy nanostructure on the highly conductive SWCNT framework is effective at maintaining conductivity, with the intrinsically lower rate performance of the polymer mitigated by the structure and the polymer's higher energy density.

The stability and reversibility of an electrode material are key factors in determining applicability as in real supercapacitors. The cycling stability performance of the as-fabricated asymmetric devices were tested at 5 A/g for 50000 cycles (Figure 6.25 c and d). The columbic efficiency of both as-fabricated devices are relatively high and maintain up to 99% after 50000 cycles. In general, PPy usually sustains a poor long-term stability during cycling as the shrinking and swelling of PPy associated with intercalation may lead to degradation.[380, 381] In fact, research studies of conducting polymer composites usually report the cyclic stability tests over fewer than 20000 cycles and their capacitance retention is mostly achieved than 90% after 10000 cycles.[137, 382] In contrast, the capacitance retention of 1P_2N device is noticeably high and achieved 93% after 50000 cycles. On the other hand, the capacitance retention of 1P_1N device is only 54% showing that the electrode suffers from a relatively poor cycling stability due to the unfavourable configuration. The improved cycling stability of 1P_2N device can be attributed to the new design configuration of the cell which provides

the optimum utilisation of active materials and better ion transportation in the overall device. The increase in capacitance in the first few thousand cycles of 1P_2N may be due to the activation of PPy materials and the grafting of sulphate functional group from the sulfuric electrolyte on the electrode surface as observed in the symmetric devices (Figure 4.10a).

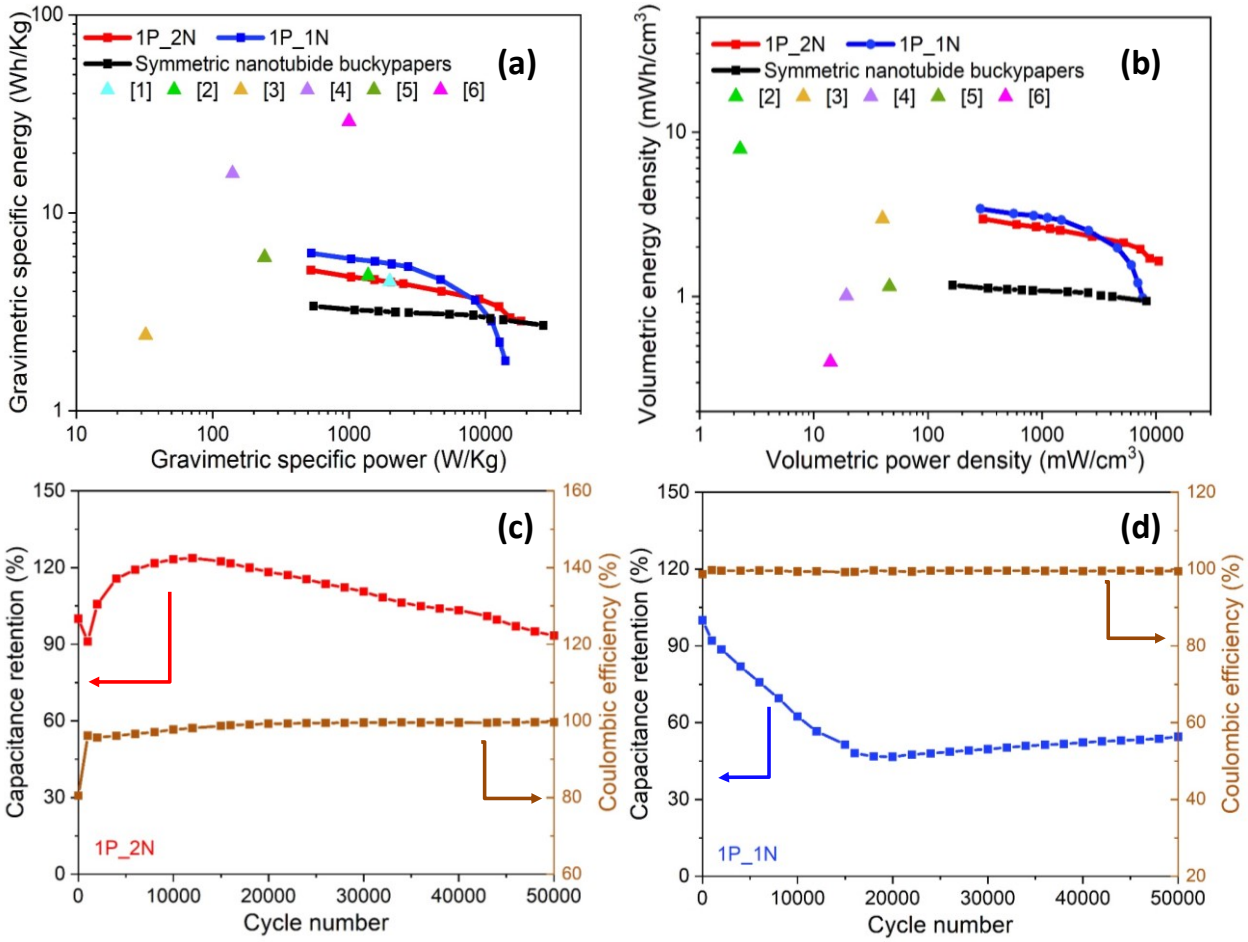

Figure 6.25 Symmetric supercapacitor of nanotubide buckypapers and asymmetric supercapacitors of PPy-CNB//CNB (1P_1N and 1P_2N) using BC nanopaper as separators with 1 M H_2SO_4 as electrolyte; (a) gravimetric Ragone plots and (b) volumetric Ragone plots normalised by mass and volume of active electrodes then compared with the literature from ref: 1) Y.Su *et al.,* 2015[374] 2) C. Ren *et al.,* 2020 [375] 3) J.Yu *et al.,* 2017[376] 4) J.Zhu *et al.,* 2017[377] 5) N.Wang *et al.,* 2020[378] 6) D.Dubal *et al.,* 2016[379]. Capacitance retention and Coulombic efficiency of (c) 1P_2N device and (d) 1P_1N device.

6.6 Conclusions

In summary, PPy were successfully electrodeposited on CNB via the pulse polymerisation and chronoamperometry techniques. The aim was to distribute the PPy uniformy within the pore buckypaper network without overcoating the surface, to achieve higher specific energy without increasing buckypaper thickness (volume). The pulse sequence, electrodeposition potential, electrodeposition charge per area and the electrodeposition electrolyte were controlled to achieve the desired structure. Increasing pulse-on time, electrodeposition potential and pulse cycle increased the quantity of PPy deposited. The electrodeposition electrolyte pH affected the quantity, structure and conductivity of the PPy deposits, even at the same monomer concentration. The use of H_2SO_4 as electrodeposition electrolyte provided a desirable, conductive, cauliflower-like structure, with higher electrochemical performance. The pulse polymerisation method shows better electrochemical performance than simple potentiostatic deposition, as more ideal microstructures can be deposited. Using the CNB with 32 µm thickness and 0.42 g/cm^3 density as a substrate, the optimum pulse sequence for electrodepositing PPy on cross-linked nanotubide buckypaper was found to be at 0.8 V vs. Ag/AgCl, 1s_60s for 30 cycles. Longer pulse on times became diffusion limited leading to undesirable surface coating; obstruction of the ion diffusion path lead to lower electrochemical performance and poorer electrochemical rate capability. Electrodeposition potential over 0.8 V vs. Ag/AgCl and longer electrodeposition cycles than 30 cycles deposited excess quantities which fully covered the surface dramatically reducing performance. In principle, the optimum quantity of PPy on each substrate material, will be different depending on the thickness, density conductivity and structure of the substrate. However, the chapter provides general design principles and numerical guidelines on pulse design sequence.

The most important point is the polymer needs to be well distributed in the SWCNT network. Overall, the pulse sequence should be designed to achieve this structure. The voltage should be selected to avoid nucleation limitations but avoid rapid uncontrolled growth. The pulse resting period must be sufficiently long to allow for monomer replenishment by diffusion. Longer resting period simply extend the overall

fabrication process. The necessary diffusion time can be estimated by simple Fick's law diffusion; more accurate calculations or simulations including tortuosity could be considered but may not be necessary. Rough scaling depending on thickness squared may be useful to consider. The pulse-on time should be sufficient to deposit a significant fraction of the monomer in the pores each cycle, but not deplete it. The time can be tuned by considering the pore volume, monomer concentration, and the deposition current (taking into account electrodeposition efficiency of the deposition process). Too short a pulse-on time may mean that current is lost to capacitance double layer charging, making the polymerisation inefficient. The total number of cycles should be selected to deposit sufficient polymer including as much redox active material as possible without blocking the ion conduction channels. The necessary number of cycles can be estimated by considering the electrodeposition charge, efficiency, and the density of the polymer deposited.

The mechanical testing of PPy-CNB shows an interesting synergy: the addition of the polymer improves both electrochemical and mechanical performance. Compared to the control pure buckpaper, tensile strength increased by 22% and strain to failure by 300%, due to improved density and load transfer. The results indicate potential applications in the growing field of structural energy storage devices.

Preliminary asymmetric full cell devices were prepared in two geometries, attempting to balance the capacities of the optimised PPy-enhanced electrodes with the optimised EDLC electrodes from Chapter 5. Even these initial devices showed considerable promise. The volumetric capacitance normalised by the volume of the device was 2-2.5 times of the symmetric nanotubide buckypaper device. The huge improvement in volumetric capacitance after hybridisation with PPy reflects not only the pseudocapacitive contribution but also the small increment in volume (8%) of buckypaper when compared with the increment in its mass (85%). In addition, the volumetric capacitance normalised by the volume of the whole cell, including electrolyte and separator is not much decreased, due to the advantages of the ultrathin BC nanopaper separator introduced in Chapter 4. Although the current devices had Pt current collector tabs for convenience, in principle, the buckypaper is sufficiently conductive to act as is own intrinsic current collector, obviating the need to add further mass and volume for this purpose. The

integrity of the buckypapers themselves provides a means of fabrication without relying on coating of metal foils as pursued in typical commercial devices. The device can therefore be prepared entirely from organic materials, at least in principle. A new "1P_2N" architecture was developed exploiting the advantages of the buckypaper electrodes; although not yet fully optimised, it shows considerable promise. The energy density normalised by volume and mass of electrodes of 1P_1N and 1P_2N devices reach up to 3.8 mWh/cm^3 (7.2 Wh/kg) and 3.0 mWh/cm^3 (5.1 Wh/kg), respectively. The new design (1P_2N) shows exceptional high-power density comparable with the nanotubide buckypaper symmetric devices and provide improvement in the electrochemical rate capability (55%) and stability (93%) compared with 1P_1N device which can only achieve 31% and 54% rate capability and stability, respectively. These results highlight that cell design is important to maximise the electrode utilisation. The lower value in energy density of 1P_2N may be resolved by improving current collection in future.

The as-fabricated asymmetric supercapacitors achieve good specific energy and exceptional high specific power especially when normalise by volume, compared to other asymmetric devices based on PPy-carbon materials, in the literature (Figure 6.25a and b). Therefore, the combination of pulse polymerisation, reductive charging strategy and the use of ultrathin BC nanopaper as a separator is a promising approach for high-performance energy storage devices with simple paper-style electrodes. In addition, the hybridisation of PPy with nanotubide buckypaper has proved that nanotubide chemistry can provide a convenient route to produce hybrid redox-active SWCNT electrodes with robustness, high energy density, excellent power density along with extraordinary stability. The use of the same materials synthesis procedure with different types or/and other electro active polymers will be suitable for hybrid supercapacitors and polymer batteries.

7. Conclusion and future studies

7.1 Conclusions

This thesis provides a versatile reductive processing route to produce nanotubide buckypapers with highly dispersed networks. The one step reductive process has shown to improve the dispersion of SWCNTs without damaging their structure, while contributing additional purification, demonstrates good versatility and ease of functionalisation. The carbon and sodium concentrations have found to influence the dispersion/individualisation, density, electrical conductivity and the electrochemical performance of nanotubide buckypaper. At the optimum condition ([C] = 1.5 mg/mL, NaC_{10}), the optimised nanotubide buckypaper provided a specific surface area of 412 m^2/g, good electrical conductivity of 433 S/cm and significantly better electrochemical performance, compared to previous studies of carbon-based buckypaper electrodes. However, the electrochemical rate capability was not high as expected; for example, the capacitance dropped 21% after increasing the scan rate from 10 to 100 mV/s.

With the addition of DIB cross-linker, the SWCNT network dispersion, ECSA, electrochemical rate capability and gravimetric capacitance of cross-linked nanotubide electrode are increased when compared with nanotubide buckypaper. The molar ratio between DIB and sodium has been found to be a crucial factor that affects the dispersion, electrode density, electrical conductivity, electrochemical and mechanical performance. The highest capacitance of both Tuball75 and Tuball 99 are from the preparation of DIB:Na at 0.75:1 confirms that a unique optimum sodium concentration led to the best outcome of the reaction (both in term of resulting properties of the material and cross-linking). The benefit of the cross-linking has shown to provide more effective debundling in Tuball99 which is more aggregated. Hence the [C] and (C:Na) of reductive charging Tuball99 need to be studied further.

Changing procedure from gravimetric to vacuum filtration, the higher pulling force via vacuum filtration causes higher packing density compared to gravimetric filtration leading to the improvement in volumetric electrochemical performance, electrochemical rate capability

and stress transfer ability. Additionally, changing filtration method has not shown any effect to the dispersion of nanotubide solution. This procedure (vacuum filtration) could be scaled up and cross-linked nanotubide buckypaper with an areal density of up to 2.8mg/cm^2 has found to maintain the superior electrochemical performance.

Hybridising PPy on cross-linked nanotubide buckypaper (CNB) enhance gravimetric and volumetric performance when compared with CNB due to the pseudocapactive behaviour of PPy. The pulse sequence, electrodeposition potential, electrodeposition charge per area and the electrodeposition electrolyte were found to control the size and quantity of electrodeposited PPy. The acidic electrodeposition electrolyte provides higher quantity and better conductivity of the PPy when compared with neutral electrolytes, even at the same monomer concentration. The pulse polymerisation method provides the hybrid PPy-CNB with better electrochemical performance than simple potentiostatic deposition, as more ideal microstructures can be deposited and the optimum pulse sequence is found to be at 0.8 V vs. Ag/AgCl, 1s_60s for 30 cycles. Too short pulse resting period results in the polymerisation happen on the surface as pyrrole monomers do not have time to diffuse inside the buckypaper network. While too short pulse on time suggests that current is lost to capacitance double layer charging, making the polymerisation inefficient. Using CNB as substrate, electrodeposition potential over 0.8 V vs. Ag/AgCl and longer electrodeposition cycles than 30 cycles have to provide excessive quantities which fully covered the surface dramatically reducing performance. Note, the optimum quantity of PPy will be different on each material substrate, depending on the substrate properties.

For the mechanical performance, the tensile strength has found to directly rely on the density of the electrode and the tensile modulus of Tuball99 shows 2.6 times higher than Tuball75. Addition of the DIB cross-linker decreases the tensile stress due to the more dispersed cross-linked samples have less direct contact between the SWCNTs, reducing the initial load transfer and hence stiffness. Hybridising PPy on CNB has found to improve load transfer and delay failure between the CNTs as its tensile strength increased by 22% and strain to failure increased by 300% when compared with nanotubide buckypaper.

The as-fabricated symmetric and asymmetric supercapacitors using nanotubide buckypaper, CNB and hybrid PPy-CNB as electrode materials achieve good specific energy and exceptional high specific power especially when normalise by volume, compared to other symmetric carbon-based device and asymmetric devices based on PPy-carbon materials respectively. The use of ultrathin BC nanopaper as a separator provided a significant reduction in both ESR and R_{ct} compares to the conventional separator, prevents short circuits with a high device efficiency which is suitable to use in a wide range of devices.

Even though the new architecture 1P_2N device exhibits poorer energy density compared with the common design 1P_1N device. 1P_2N device has shown to reduce the overall resistance of the device and provide higher power density, and rate capability especially at high specific current. These data have pointed out that 1P_2N configuration can promote the utilisation of the electrode materials and provide the high cycle life therefore, it is promising to develop and suitable for the practical applications.

7.2 Future Work

7.2.1 Optimising carbon concentration and charging ratio between carbon and sodium for the different SWCNT type

In this Thesis, the carbon concentration [C] and charging ratio (C:Na) of the nanotubide solution have found to be key factors which effect the buckypaper structure and electrochemical performances. Nanotubide solution at the optimum condition (1.5 mg/mL of [C] and 10:1 of (C:Na)) has produced nanotubide buckypaper with highly dispersed SWCNT networks from Tuball75. However, with these conditions, the structure of nanotubide buckypaper (Tuball99) has found to be not completely well-disperse and shows aligned domains with relatively large bundles results in the gravimetric capacitance and rate capability of Tuball99 are lower than Tuball75. Hence, the optimum of [C] and (C:Na) may be different depend on the SWCNT type. Where the relation between the tube size, impurity, conductivity of the starting materials and the reductive charging process need to be further studied.

7.2.2 Alternative cross-linkers

The use of DIB, which is a dielectrophilic molecule as a cross-linker has successfully improved the pore structure of cross-linked nanotubide buckypaper, leading to the improvement in electrochemical rate capability. Therefore, a further investigation on using alternative cross-linking agents would be interesting as the size of the linker can adjust the pore size of SWCNT networks. Having the electrode with the desired pore size that matches the solvated ions can provide the potential to achieve higher energy density as the electrolyte ions can fill inside the electrode sufficiently. Additionally, using the different type of cross-linking agents can also increase higher conductivity and tensile strength properties. For example, using the longer conductive linkers could impart more elasticity and robustness which will be useful for the flexible supercapacitor.

7.2.3 Optimising the 1P_2N cell configuration.

The energy density of a new architecture (1P_2N) is still not comparable with the common design 1P_1N, as it is not yet optimised. The reduction in capacitance when compared with 1P_1N device may be because the Pt plate (the current collector), which is inserted in between the separator and the positive electrode in the middle of the cell, obstruct the accessible surface area of the positive electrode. This problem can resolve by removing all Pt plates in the system and consider the positive and negative electrodes themselves as the current collectors as the CNB is conductive enough. Additionally, the symmetric nanotubide buckypaper which was fabricated in a Swagelok cell has already proved this concept that the nanotubide itself can act as current collector and be able to reduce the mass, volume and resistance of the cell configuration.

7.2.4 Hybridising other pseudocapacitive materials on CNB for energy storage application.

The result of electropolymerising PPy on CNB has proved that nanotubide chemistry can provide a convenient route to produce hybrid materials which achieve high electrochemical

and mechanical performance suitable for multifunctional application. Therefore, hybridising nanotubide buckypaper with other pseudocapacitive materials is also interesting to explore to produce hybrid materials with the different properties, following the need of the applications.

For example, hybridising PANI with CNB to further enhance the energy density as PANI has higher theoretical specific capacitance (2000 F/g)[383] than PPy (620 F/g) [320]. Additionally, the combining of PPy-CNB with other pseudocapacitive materials such as transition metal oxides could also be another promising approach to enhance the energy density while maintain the superior power density of hybrid PPy-CNB.

References

1. B. Arash, Q. Wang and V. K. Varadan, 2014, 4, 6479.
2. J. N. Coleman, U. Khan, W. J. Blau and Y. K. Gun'ko, *Carbon*, 2006, 44, 1624-1652.
3. J. Zhao, Y. Li, G. Wang, T. Wei, Z. Liu, K. Cheng, K. Ye, K. Zhu, D. Cao and Z. Fan, *Journal of Materials Chemistry A*, 2017, 5, 23085-23093.
4. Q. Wang, J. Yan and Z. Fan, *Energy & Environmental Science*, 2016, 9, 729-762.
5. J. Chattopadhyay, S. Chakraborty, A. Mukherjee, R. Wang, P. S. Engel and W. E. Billups, *The Journal of Physical Chemistry C*, 2007, 111, 17928-17932.
6. A. J. Clancy, P. Sirisinudomkit, D. B. Anthony, A. Z. Thong, Jake L. Greenfield, M. K. Salaken Singh and M. S. P. Shaffer, *Chemical Science*, 2019, 10, 3300-3306.
7. L. L. Zhang and X. S. Zhao, *Chemical Society Reviews*, 2009, 38, 2520-2531.
8. H. Yoon, M. Yamashita, S. Ata, D. N. Futaba, T. Yamada and K. Hata, *Scientific Reports*, 2014, 4, 3907.
9. S.-Y. Lin and X. Zhang, *Journal of Power Sources*, 2015, 294, 354-359.
10. A. J. Clancy, J. Melbourne and M. S. P. Shaffer, *Journal of Materials Chemistry A*, 2015, 3, 16708-16715.
11. M. De Marco, F. Markoulidis, R. Menzel, S. M. Bawaked, M. Mokhtar, S. A. Al-Thabaiti, S. N. Basahel and M. S. P. Shaffer, *Journal of Materials Chemistry A*, 2016, 4, 5385-5389.
12. Y. Wang, Z. Shi, Y. Huang, Y. Ma, C. Wang, M. Chen and Y. Chen, *The Journal of Physical Chemistry C*, 2009, 113, 13103-13107.
13. A. G. Pandolfo and A. F. Hollenkamp, *Journal of Power Sources*, 2006, 157, 11-27.
14. T. B. Patrice Simon, Frederic Favier, in *Supercapacitors Based on Carbon or Pseudocapacitive Materials*, DOI: doi:10.1002/9781119007333.ch1.
15. W. Xing, S. Z. Qiao, R. G. Ding, F. Li, G. Q. Lu, Z. F. Yan and H. M. Cheng, *Carbon*, 2006, 44, 216-224.
16. R. Mysyk, E. Raymundo-Piñero and F. Béguin, *Electrochemistry Communications*, 2009, 11, 554-556.
17. G. Z. Chen, *International Materials Reviews*, 2017, 62, 173-202.
18. X. Chen, R. Paul and L. Dai, *National Science Review*, 2017, 4, 453-489.
19. M. S. Halper, Ellenbogen, James C., *Conference Proceedings McLean, Virginia,* 2006.
20. K. H. An, K. K. Jeon, J. K. Heo, S. C. Lim, D. J. Bae and Y. H. Lee, *Journal of The Electrochemical Society*, 2002, 149, A1058-A1062.
21. G. Pognon, T. Brousse, L. Demarconnay and D. Bélanger, *Journal of Power Sources*, 2011, 196, 4117-4122.
22. C. Zhong, Y. Deng, W. Hu, J. Qiao, L. Zhang and J. Zhang, *Chemical Society Reviews*, 2015, 44, 7484-7539.
23. B. François, P. Volker, B. Andrea and F. Elzbieta, *Advanced Materials*, 2014, 26, 2219-2251.
24. A. Brandt, P. Isken, A. Lex-Balducci and A. Balducci, *Journal of Power Sources*, 2012, 204, 213-219.
25. M. P. S. Mousavi, B. E. Wilson, S. Kashefolgheta, E. L. Anderson, S. He, P. Bühlmann and A. Stein, *ACS Applied Materials & Interfaces*, 2016, 8, 3396-3406.
26. M. Armand, F. Endres, D. R. MacFarlane, H. Ohno and B. Scrosati, *Nature Materials*, 2009, 8, 621.

27. A. Burke, *Electrochimica Acta*, 2007, 53, 1083-1091.
28. A. Eatemadi, H. Daraee, H. Karimkhanloo, M. Kouhi, N. Zarghami, A. Akbarzadeh, M. Abasi, Y. Hanifehpour and S. W. Joo, *Nanoscale Res Lett*, 2014, 9, 393.
29. R. P. E., L. F. and B. F., *Advanced Materials*, 2006, 18, 1877-1882.
30. H. J. Y., L. Mengping, E. K. M. F. and K. R. B., *Advanced Functional Materials*, 2017, 27, 1605745.
31. H. Shen, E. Liu, X. Xiang, Z. Huang, Y. Tian, Y. Wu, Z. Wu and H. Xie, *Materials Research Bulletin*, 2012, 47, 662-666.
32. M. D. Stoller, S. Park, Y. Zhu, J. An and R. S. Ruoff, *Nano Letters*, 2008, 8, 3498-3502.
33. A. Raslan, L. Saenz del Burgo, J. Ciriza and J. L. Pedraz, *International Journal of Pharmaceutics*, 2020, 580, 119226.
34. A. T. Smith, A. M. LaChance, S. Zeng, B. Liu and L. Sun, *Nano Materials Science*, 2019, 1, 31-47.
35. S. Pei and H.-M. Cheng, *Carbon*, 2012, 50, 3210-3228.
36. S. Basu and P. Bhattacharyya, *Sensors and Actuators B: Chemical*, 2012, 173, 1-21.
37. M. F. El-Kady, Y. Shao and R. B. Kaner, *Nature Reviews Materials*, 2016, 1, 16033.
38. Y. Yoon, K. Lee, S. Kwon, S. Seo, H. Yoo, S. Kim, Y. Shin, Y. Park, D. Kim, J.-Y. Choi and H. Lee, *ACS Nano*, 2014, 8, 4580-4590.
39. H. W. Kroto, J. R. Heath, S. C. O'Brien, R. F. Curl and R. E. Smalley, *Nature*, 1985, 318, 162-163.
40. R. B. Mathur, B. P. Singh and S. Pande, *Carbon Nanomaterials Synthesis, Structure, Properties and Applications*, 2017.
41. X. Sun, H. Sun, H. Li and H. Peng, *Advanced Materials*, 2013, 25, 5153-5176.
42. A. Borenstein, O. Hanna, R. Attias, S. Luski, T. Brousse and D. Aurbach, *Journal of Materials Chemistry A*, 2017, 5, 12653-12672.
43. R. Vidu, M. Rahman, M. Mahmoudi, M. Enachescu, T. D. Poteca and I. Opris, *Front Syst Neurosci*, 2014, 8, 91-91.
44. R. Saito, M. Fujita, G. Dresselhaus and M. S. Dresselhaus, *Applied Physics Letters*, 1992, 60, 2204-2206.
45. A. Aqel, K. M. M. A. El-Nour, R. A. A. Ammar and A. Al-Warthan, *Arabian Journal of Chemistry*, 2012, 5, 1-23.
46. Y. Chen and J. Zhang, *Accounts of Chemical Research*, 2014, 47, 2273-2281.
47. S. Bhaviripudi, E. Mile, S. A. Steiner, A. T. Zare, M. S. Dresselhaus, A. M. Belcher and J. Kong, *Journal of the American Chemical Society*, 2007, 129, 1516-1517.
48. M. Kumar and Y. Ando, *Journal of Nanoscience and Nanotechnology*, 2010, 10, 3739-3758.
49. M. J. Bronikowski, P. A. Willis, D. T. Colbert, K. A. Smith and R. E. Smalley, *Journal of Vacuum Science & Technology A*, 2001, 19, 1800-1805.
50. K. Hata, D. N. Futaba, K. Mizuno, T. Namai, M. Yumura and S. Iijima, *Science*, 2004, 306, 1362-1364.
51. A. J. Clancy, E. R. White, H. H. Tay, H. C. Yau and M. S. Shaffer, *Carbon*, 2016, 108, 423-432.
52. M. R. Baptist, *RU 2157060*, 2012, H01J 37/30.
53. E. A. Laird, F. Kuemmeth, G. A. Steele, K. Grove-Rasmussen, J. Nygård, K. Flensberg and L. P. Kouwenhoven, *Reviews of Modern Physics*, 2015, 87, 703-764.
54. P. G. Collins and P. Avouris, *Scientific american*, 2000, 283, 62-69.
55. D. Jack, C. Yeh, Z. Liang, S. Li, J. Park and J. Fielding, *Nanotechnology*, 2010, 21, 195703.

56. W. S. Bao, S. A. Meguid, Z. H. Zhu and G. J. Weng, *Journal of Applied Physics*, 2012, 111, 093726.
57. S. Datta, in *Electronic Transport in Mesoscopic Systems*, ed. S. Datta, Cambridge University Press, Cambridge, 1995, DOI: DOI: undefined, pp. ix-xi.
58. Q. Xia, Z. Zhang, Y. Liu and J. Leng, *Composites Part B: Engineering*, 2020, 199, 108231.
59. H. Chu, Z. Zhang, Y. Liu and J. Leng, *Carbon*, 2014, 66, 154-163.
60. Q. Xia, Z. Zhang, H. Chu, Y. Liu and J. Leng, *Composites Part A: Applied Science and Manufacturing*, 2018, 113, 132-140.
61. L. Zhang, X. Wang, W. Xu, Y. Zhang, Q. Li, P. D. Bradford and Y. Zhu, *Small*, 2015, 11, 3830-3836.
62. P. E. Lyons, S. De, F. Blighe, V. Nicolosi, L. F. C. Pereira, M. S. Ferreira and J. N. Coleman, *Journal of Applied Physics*, 2008, 104, 044302.
63. W. Ma, L. Liu, R. Yang, T. Zhang, Z. Zhang, L. Song, Y. Ren, J. Shen, Z. Niu and W. Zhou, *Advanced Materials*, 2009, 21, 603-608.
64. A. Kaskela, P. Laiho, N. Fukaya, K. Mustonen, T. Susi, H. Jiang, N. Houbenov, Y. Ohno and E. I. Kauppinen, *Carbon*, 2016, 103, 228-234.
65. T. Susi, A. Kaskela, Z. Zhu, P. Ayala, R. Arenal, Y. Tian, P. Laiho, J. Mali, A. G. Nasibulin and H. Jiang, *Chemistry of Materials*, 2011, 23, 2201-2208.
66. H.-Z. Geng, K. K. Kim, K. P. So, Y. S. Lee, Y. Chang and Y. H. Lee, *Journal of the American Chemical Society*, 2007, 129, 7758-7759.
67. A. Hirsch and C. Backes, *Angewandte Chemie International Edition*, 2010, 49, 1722-1723.
68. M.-F. Yu, B. S. Files, S. Arepalli and R. S. Ruoff, *Physical Review Letters*, 2000, 84, 5552-5555.
69. Z. Shi, Y. Lian, F. H. Liao, X. Zhou, Z. Gu, Y. Zhang, S. Iijima, H. Li, K. T. Yue and S.-L. Zhang, *Journal of Physics and Chemistry of Solids*, 2000, 61, 1031-1036.
70. M. Meyyappan, *Carbon nanotubes: science and applications*, CRC press, 2004.
71. S. Ibraheem and S. Bandyopadhyay, in *Hybrid Polymer Composite Materials*, eds. V. K. Thakur, M. K. Thakur and R. K. Gupta, Woodhead Publishing, 2017, DOI: https://doi.org/10.1016/B978-0-08-100791-4.00007-0, pp. 163-191.
72. M. F. Yu, B. S. Files, S. Arepalli and R. S. Ruoff, *Phys Rev Lett*, 2000, 84, 5552-5555.
73. A. Zandiatashbar, G.-H. Lee, S. J. An, S. Lee, N. Mathew, M. Terrones, T. Hayashi, C. R. Picu, J. Hone and N. Koratkar, *Nature communications*, 2014, 5, 3186.
74. J. A. Rojas, L. A. Ardila-Rodríguez, M. F. Diniz, M. Gonçalves, B. Ribeiro and M. C. Rezende, *Heliyon*, 2019, 5, e01386-e01386.
75. A. Izadi-Najafabadi, S. Yasuda, K. Kobashi, T. Yamada, D. N. Futaba, H. Hatori, M. Yumura, S. Iijima and K. Hata, *Advanced Materials*, 2010, 22, E235-E241.
76. J. Che, P. Chen and M. B. Chan-Park, *Journal of Materials Chemistry A*, 2013, 1, 4057-4066.
77. P. Sirisinudomkit, E. Senokos, N. Rubio and M. S. P. Shaffer, *Materials Advances*, 2021, DOI: 10.1039/D0MA00898B.
78. S. Najib and E. Erdem, *Nanoscale Advances*, 2019, 1, 2817-2827.
79. K. L. Van Aken, C. R. Pérez, Y. Oh, M. Beidaghi, Y. Joo Jeong, M. F. Islam and Y. Gogotsi, *Nano Energy*, 2015, 15, 662-669.
80. E. Wilson and M. F. Islam, *ACS Applied Materials & Interfaces*, 2015, 7, 5612-5618.
81. J. Barisci, G. Wallace and R. Baughman, *Faculty of Engineering - Papers*, 2000, 147, 4580–4583.

82. Z. Niu, W. Zhou, J. Chen, G. Feng, H. Li, W. Ma, J. Li, H. Dong, Y. Ren, D. Zhao and S. Xie, *Energy & Environmental Science*, 2011, 4, 1440-1446.
83. S. Perathoner and G. Centi, in *Emerging Materials for Energy Conversion and Storage*, eds. K. Y. Cheong, G. Impellizzeri and M. A. Fraga, Elsevier, 2018, pp. 305-325.
84. A. M. Díez-Pascual, J. Guan, B. Simard and M. A. Gómez-Fatou, *Composites Part A: Applied Science and Manufacturing*, 2012, 43, 1007-1015.
85. M. F. Islam, E. Rojas, D. M. Bergey, A. T. Johnson and A. G. Yodh, *Nano Letters*, 2003, 3, 269-273.
86. R. Rastogi, R. Kaushal, S. K. Tripathi, A. L. Sharma, I. Kaur and L. M. Bharadwaj, *Journal of Colloid and Interface Science*, 2008, 328, 421-428.
87. Y. Y. Huang and E. M. Terentjev, *Polymers*, 2012, 4, 275-295.
88. M. Zheng, A. Jagota, E. D. Semke, B. A. Diner, R. S. McLean, S. R. Lustig, R. E. Richardson and N. G. Tassi, *Nat Mater*, 2003, 2, 338-342.
89. J. Zhang, L. Gao, J. Sun, Y. Liu, Y. Wang, J. Wang, H. Kajiura, Y. Li and K. Noda, *The Journal of Physical Chemistry C*, 2008, 112, 16370-16376.
90. L. Liang, W. Xie, S. Fang, F. He, B. Yin, C. Tlili, D. Wang, S. Qiu and Q. Li, *Journal of Materials Chemistry C*, 2017, 5, 11339-11368.
91. Y. T. Shah, A. Pandit and V. Moholkar, *Cavitation reaction engineering*, Springer Science & Business Media, 2012.
92. L. Dumée, K. Sears, J. Schütz, N. Finn, M. Duke and S. Gray, *Nanomaterials (Basel)*, 2013, 3, 70-85.
93. G. Pagani, M. J. Green, P. Poulin and M. Pasquali, *Proceedings of the National Academy of Sciences*, 2012, 109, 11599-11604.
94. Q. Cheng, S. Debnath, E. Gregan and H. J. Byrne, *The Journal of Physical Chemistry C*, 2010, 114, 8821-8827.
95. S. Giordani, S. D. Bergin, V. Nicolosi, S. Lebedkin, M. M. Kappes, W. J. Blau and J. N. Coleman, *The journal of physical chemistry B*, 2006, 110, 15708-15718.
96. K. D. Ausman, R. Piner, O. Lourie, R. S. Ruoff and M. Korobov, *The Journal of Physical Chemistry B*, 2000, 104, 8911-8915.
97. H. C. Yau, M. K. Bayazit, J. H. G. Steinke and M. S. P. Shaffer, *Chemical Communications*, 2015, 51, 16621-16624.
98. S. Niyogi, M. A. Hamon, H. Hu, B. Zhao, P. Bhowmik, R. Sen, M. E. Itkis and R. C. Haddon, *Accounts of Chemical Research*, 2002, 35, 1105-1113.
99. J. Liu, A. G. Rinzler, H. Dai, J. H. Hafner, R. K. Bradley, P. J. Boul, A. Lu, T. Iverson, K. Shelimov and C. B. Huffman, *Science*, 1998, 280, 1253-1256.
100. Y. Wang, H. Shan, R. H. Hauge, M. Pasquali and R. E. Smalley, *The Journal of Physical Chemistry B*, 2007, 111, 1249-1252.
101. A. J. Clancy, E. R. White, H. H. Tay, H. C. Yau and M. S. P. Shaffer, *Carbon*, 2016, 108, 423-432.
102. L. M. Ericson, H. Fan, H. Peng, V. A. Davis, W. Zhou, J. Sulpizio, Y. Wang, R. Booker, J. Vavro, C. Guthy, A. N. G. Parra-Vasquez, M. J. Kim, S. Ramesh, R. K. Saini, C. Kittrell, G. Lavin, H. Schmidt, W. W. Adams, W. E. Billups, M. Pasquali, W.-F. Hwang, R. H. Hauge, J. E. Fischer and R. E. Smalley, *Science*, 2004, 305, 1447-1450.
103. S. Ramesh, L. M. Ericson, V. A. Davis, R. K. Saini, C. Kittrell, M. Pasquali, W. E. Billups, W. W. Adams, R. H. Hauge and R. E. Smalley, *The Journal of Physical Chemistry B*, 2004, 108, 8794-8798.

104. F. Hof, S. Bosch, S. Eigler, F. Hauke and A. Hirsch, *Journal of the American Chemical Society*, 2013, 135, 18385-18395.
105. A. J. Clancy, M. K. Bayazit, S. A. Hodge, N. T. Skipper, C. A. Howard and M. S. P. Shaffer, *Chemical Reviews*, 2018, 118, 7363-7408.
106. S. A. Hodge, S. Fogden, C. A. Howard, N. T. Skipper and M. S. P. Shaffer, *ACS Nano*, 2013, 7, 1769-1778.
107. F. Liang, A. K. Sadana, A. Peera, J. Chattopadhyay, Z. Gu, R. H. Hauge and W. E. Billups, *Nano Letters*, 2004, 4, 1257-1260.
108. A. García-Gallastegui, I. Obieta, I. Bustero, G. Imbuluzqueta, J. Arbiol, J. I. Miranda and J. M. Aizpurua, *Chemistry of Materials*, 2008, 20, 4433-4438.
109. S. Fogden, C. A. Howard, R. K. Heenan, N. T. Skipper and M. S. P. Shaffer, *ACS Nano*, 2012, 6, 54-62.
110. S. A. Hodge, M. K. Bayazit, H. H. Tay and M. S. P. Shaffer, *Nature Communications*, 2013, 4, 1989.
111. L. A. Hough, M. F. Islam, P. A. Janmey and A. G. Yodh, *Physical Review Letters*, 2004, 93, 168102.
112. M. Gardel, J. H. Shin, F. MacKintosh, L. Mahadevan, P. Matsudaira and D. Weitz, *Science*, 2004, 304, 1301-1305.
113. D. T. N. Chen, K. Chen, L. A. Hough, M. F. Islam and A. G. Yodh, *Macromolecules*, 2010, 43, 2048-2053.
114. M. C. Gutiérrez, D. Carriazo, A. Tamayo, R. Jiménez, F. Picó, J. M. Rojo, M. L. Ferrer and F. del Monte, *Chemistry – A European Journal*, 2011, 17, 10533-10537.
115. K. H. Kim, M. Vural and M. F. Islam, *Advanced Materials*, 2011, 23, 2865-2869.
116. M. B. Bryning, D. E. Milkie, M. F. Islam, L. A. Hough, J. M. Kikkawa and A. G. Yodh, *Advanced Materials*, 2007, 19, 661-664.
117. R. Kumar and C. N. R. Rao, *Journal of Materials Chemistry A*, 2015, 3, 6747-6750.
118. A. Satti, A. Perret, J. E. McCarthy and Y. K. Gun'ko, *Journal of Materials Chemistry*, 2010, 20, 7941-7943.
119. M. Holzinger, O. Vostrowsky, A. Hirsch, F. Hennrich, M. Kappes, R. Weiss and F. Jellen, *Angewandte Chemie - International Edition*, 2001, 40, 4002-4005.
120. M. Holzinger, J. Steinmetz, D. Samaille, M. Glerup, M. Paillet, P. Bernier, L. Ley and R. Graupner, *Carbon*, 2004, 42, 941-947.
121. T. Chen and L. Dai, *Materials Today*, 2013, 16, 272-280.
122. G. George and G. Costas, *2D Materials*, 2017, 4, 032001.
123. Z.-Y. Sui, Y.-N. Meng, P.-W. Xiao, Z.-Q. Zhao, Z.-X. Wei and B.-H. Han, *ACS Applied Materials & Interfaces*, 2015, 7, 1431-1438.
124. J. Luo, H. D. Jang and J. Huang, *ACS Nano*, 2013, 7, 1464-1471.
125. Z. Ma, X. Zhao, C. Gong, J. Zhang, J. Zhang, X. Gu, L. Tong, J. Zhou and Z. Zhang, *Journal of Materials Chemistry A*, 2015, 3, 13445-13452.
126. K. H. Kim, Y. Oh and M. F. Islam, *Nat Nano*, 2012, 7, 562-566.
127. J. Min, J. Y. Cai, M. Sridhar, C. D. Easton, T. R. Gengenbach, J. McDonnell, W. Humphries and S. Lucas, *Carbon*, 2013, 52, 520-527.
128. F. Liu, S. Luo, D. Liu, W. Chen, Y. Huang, L. Dong and L. Wang, *ACS Applied Materials & Interfaces*, 2017, 9, 33791-33801.
129. V. Subramanian, H. Zhu and B. Wei, *Electrochemistry Communications*, 2006, 8, 827-832.
130. H. Cheng and H. M. Duong, *RSC Advances*, 2015, 5, 30260-30267.

131. Y. Zhao, J. Liu, N. Wang, Q. Li and M. Hu, *Journal of Materials Chemistry A*, 2018, DOI: 10.1039/C8TA00710A.
132. K. S. Lakhi, D.-H. Park, K. Al-Bahily, W. Cha, B. Viswanathan, J.-H. Choy and A. Vinu, *Chemical Society Reviews*, 2017, 46, 560-560.
133. W.-r. Lee, Y.-S. Jun, J. Park and G. D. Stucky, *Journal of Materials Chemistry A*, 2015, 3, 24232-24236.
134. K. Schwinghammer, M. B. Mesch, V. Duppel, C. Ziegler, J. Senker and B. V. Lotsch, *Journal of the American Chemical Society*, 2014, 136, 1730-1733.
135. A. Javaid, K. Ho, A. Bismarck, M. Shaffer, J. Steinke and E. Greenhalgh, *Journal of Composite Materials*, 2014, 48, 1409-1416.
136. K. D. Fong, T. Wang and S. K. Smoukov, *Sustainable Energy & Fuels*, 2017, 1, 1857-1874.
137. I. Shown, A. Ganguly, L.-C. Chen and K.-H. Chen, *Energy Science & Engineering*, 2015, 3, 2-26.
138. M. Jaiswal and R. Menon, *Polymer International*, 2006, 55, 1371-1384.
139. G. Inzelt, M. Pineri, J. W. Schultze and M. A. Vorotyntsev, *Electrochimica Acta*, 2000, 45, 2403-2421.
140. Q. Meng, K. Cai, Y. Chen and L. Chen, *Nano Energy*, 2017, 36, 268-285.
141. M. Omastová, I. Chodák and J. Pionteck, *Synthetic Metals*, 1999, 102, 1251-1252.
142. G. A. Snook, P. Kao and A. S. Best, *Journal of power sources*, 2011, 196, 1-12.
143. R. B. Choudhary, S. Ansari and B. Purty, *Journal of Energy Storage*, 2020, 29, 101302.
144. S. Suematsu, Y. Oura, H. Tsujimoto, H. Kanno and K. Naoi, *Electrochimica Acta*, 2000, 45, 3813-3821.
145. G. A. Snook, C. Peng, D. J. Fray and G. Z. Chen, *Electrochemistry communications*, 2007, 9, 83-88.
146. H. An, Y. Wang, X. Wang, L. Zheng, X. Wang, L. Yi, L. Bai and X. Zhang, *Journal of Power Sources*, 2010, 195, 6964-6969.
147. E. Zhang, W. Liu, X. Liu, Z. Zhao and Y. Yang, *RSC Advances*, 2020, 10, 11966-11970.
148. R. Ansari, *Journal of Chemistry*, 2006, 3, 186-201.
149. Y. Huang, H. Li, Z. Wang, M. Zhu, Z. Pei, Q. Xue, Y. Huang and C. Zhi, *Nano Energy*, 2016, 22, 422-438.
150. Y. Tan and K. Ghandi, *Synthetic Metals*, 2013, 175, 183-191.
151. J. Torop, A. Aabloo and E. W. Jager, *Carbon*, 2014, 80, 387-395.
152. H. J. Lee and S.-M. Park, *The Journal of Physical Chemistry B*, 2005, 109, 13247-13254.
153. V. V. Tat'yana and O. N. Efimov, *Russian chemical reviews*, 1997, 66, 443.
154. C. Beebee, E. B. Watkins, R. M. Sapstead, V. C. Ferreira, K. S. Ryder, E. L. Smith and A. R. Hillman, *Electrochimica Acta*, 2019, 295, 978-988.
155. A. Davies, P. Audette, B. Farrow, F. Hassan, Z. Chen, J.-Y. Choi and A. Yu, *The Journal of Physical Chemistry C*, 2011, 115, 17612-17620.
156. K. Qi, Y. Qiu and X. Guo, *Electrochimica Acta*, 2014, 137, 685-692.
157. R. K. Sharma, A. C. Rastogi and S. B. Desu, *Electrochemistry Communications*, 2008, 10, 268-272.
158. K. H. An, K. K. Jeon, J. K. Heo, S. C. Lim, D. J. Bae and Y. H. Lee, *Journal of The Electrochemical Society*, 2002, 149, A1058.
159. H. Song, K. Cai, J. Wang and S. Shen, *Synthetic Metals*, 2016, 211, 58-65.
160. R. Xu, J. Wei, F. Guo, X. Cui, T. Zhang, H. Zhu, K. Wang and D. Wu, *RSC Advances*, 2015, 5, 22015-22021.

161. H. Zhou, G. Han, Y. Xiao, Y. Chang and H.-J. Zhai, *Synthetic Metals*, 2015, 209, 405-411.
162. D. N. Taulbee and M. Mercedes Maroto-Valer, in *Encyclopedia of Separation Science*, ed. I. D. Wilson, Academic Press, Oxford, 2000, DOI: https://doi.org/10.1016/B0-12-226770-2/00011-9, pp. 17-40.
163. J. H. Van Gerpen and B. B. He, in *Advances in Biorefineries*, ed. K. Waldron, Woodhead Publishing, 2014, DOI: https://doi.org/10.1533/9780857097385.2.441, pp. 441-475.
164. P.-C. Ma, N. A. Siddiqui, G. Marom and J.-K. Kim, *Composites Part A: Applied Science and Manufacturing*, 2010, 41, 1345-1367.
165. L. Reimer, *Scanning electron microscopy: physics of image formation and microanalysis*, Springer, 2013.
166. D. Li, J. Zhang, Y. He, Y. Qin, Y. Wei, P. Liu, L. Zhang, J. Wang, Q. Li, S. Fan and K. Jiang, *Nano Research*, 2017, DOI: 10.1007/s12274-017-1505-7.
167. K. C. Wong, *Journal of Chemical Education*, 2015, 92, 1602-1603.
168. P. Mohamed Shameer and P. Mohamed Nishath, in *Advanced Biofuels*, eds. A. K. Azad and M. Rasul, Woodhead Publishing, 2019, DOI: https://doi.org/10.1016/B978-0-08-102791-2.00008-8, pp. 181-213.
169. R. M. Silverstein and G. C. Bassler, *Journal of Chemical Education*, 1962, 39, 546.
170. W. Reusch, 2013.
171. A. Polini and F. Yang, in *Nanofiber Composites for Biomedical Applications*, eds. M. Ramalingam and S. Ramakrishna, Woodhead Publishing, 2017, DOI: https://doi.org/10.1016/B978-0-08-100173-8.00005-3, pp. 97-115.
172. E. Mansfield, A. Kar and S. A. Hooker, *Analytical and bioanalytical chemistry*, 2010, 396, 1071-1077.
173. J. P. C. Trigueiro, G. G. Silva, R. L. Lavall, C. A. Furtado, S. Oliveira, A. S. Ferlauto, R. G. Lacerda, L. O. Ladeira, J.-W. Liu and R. L. Frost, *Journal of Nanoscience and Nanotechnology*, 2007, 7, 3477-3486.
174. M. B. Casu and T. Chassé, *Photoelectron Spectroscopy Applications to Materials Science*, 2014.
175. T. Susi, T. Pichler and P. Ayala, *Beilstein J Nanotechnol*, 2015, 6, 177-192.
176. S. Brunauer, *Physical adsorption*, 1945, 1.
177. J.-K. Park, *Principles and applications of lithium secondary batteries*, John Wiley & Sons, 2012.
178. K. S. W. Sing, *Advances in Colloid and Interface Science*, 1998, 76-77, 3-11.
179. W. Rudziński, W. A. Steele and G. Zgrablich, *Equilibria and dynamics of gas adsorption on heterogeneous solid surfaces*, Elsevier, 1997.
180. F. Ambroz, T. J. Macdonald, V. Martis and I. P. Parkin, *Small Methods*, 2018, 2, 1800173.
181. M. Thommes, K. Kaneko, A. V. Neimark, J. P. Olivier, F. Rodriguez-Reinoso, J. Rouquerol and K. S. Sing, *Pure and Applied Chemistry*, 2015, 87, 1051-1069.
182. J. Garrido, A. Linares-Solano, J. M. Martin-Martinez, M. Molina-Sabio, F. Rodriguez-Reinoso and R. Torregrosa, *Langmuir*, 1987, 3, 76-81.
183. Y.-S. Bae, K. L. Mulfort, H. Frost, P. Ryan, S. Punnathanam, L. J. Broadbelt, J. T. Hupp and R. Q. Snurr, *Langmuir*, 2008, 24, 8592-8598.
184. M. Thommes, *Chemie Ingenieur Technik*, 2010, 82, 1059-1073.
185. in *Practical Raman Spectroscopy – An Introduction*, DOI: 10.1002/9781119961284.ch1, pp. 1-38.

186. E. Smith and G. Dent, *Modern Raman spectroscopy: a practical approach*, John Wiley & Sons, 2019.
187. M. S. Dresselhaus, G. Dresselhaus, R. Saito and A. Jorio, *Physics Reports*, 2005, 409, 47-99.
188. P. T. Araujo, I. O. Maciel, P. B. C. Pesce, M. A. Pimenta, S. K. Doorn, H. Qian, A. Hartschuh, M. Steiner, L. Grigorian, K. Hata and A. Jorio, *Physical Review B*, 2008, 77, 241403.
189. A. Jorio, R. Saito, J. Hafner, C. Lieber, D. Hunter, T. McClure, G. Dresselhaus and M. Dresselhaus, *Physical Review Letters*, 2001, 86, 1118.
190. A. R. T. Nugraha, R. Saito, K. Sato, P. T. Araujo, A. Jorio and M. S. Dresselhaus, *Applied Physics Letters*, 2010, 97, 091905.
191. K. Jantharamatsakarn and S. Chaisitsak, *Procedia Engineering*, 2014, 93, 49-58.
192. S. Maruyama, R. Kojima, Y. Miyauchi, S. Chiashi and M. Kohno, *Chemical physics letters*, 2002, 360, 229-234.
193. S. Maruyama, 2018, DOI: http://www.photon.t.u-tokyo.ac.jp/~maruyama/kataura/kataura.html.
194. M. S. Dresselhaus, G. Dresselhaus and R. Saito, *Carbon*, 1995, 33, 883-891.
195. I. Miccoli, F. Edler, H. Pfnür and C. Tegenkamp, *Journal of Physics: Condensed Matter*, 2015, 27, 223201.
196. F. Smits, *Bell System Technical Journal*, 1958, 37, 711-718.
197. A. J. Bard and L. R. Faulkner, *Electrochemical Methods*, 2001, 2, 580-632.
198. C. G. Zoski, *Handbook of electrochemistry*, Elsevier, 2006.
199. M. D. Stoller and R. S. Ruoff, *Energy & Environmental Science*, 2010, 3, 1294-1301.
200. S. Ratha and C. S. Rout, *ACS Applied Materials & Interfaces*, 2013, 5, 11427-11433.
201. P. Sirisinudomkit, P. Iamprasertkun, A. Krittayavathananon, T. Pettong, P. Dittanet and M. Sawangphruk, *Scientific Reports*, 2017, 7, 1124.
202. R. Wang, C. Xu and J.-M. Lee, *Nano Energy*, 2016, 19, 210-221.
203. A. Lasia, in *Modern aspects of electrochemistry*, Springer, 2002, pp. 143-248.
204. N. Wagner and K. A. Friedrich, in *Encyclopedia of Electrochemical Power Sources*, ed. J. Garche, Elsevier, Amsterdam, 2009, DOI: https://doi.org/10.1016/B978-044452745-5.00239-2, pp. 912-930.
205. Q. Liu, Q. Shi, H. Wang, Q. Zhang and Y. Li, *RSC Advances*, 2015, 5, 47074-47079.
206. N. Syahirah, *Int. J. Electrochem. Sci*, 2016, 11, 95-110.
207. S. Zhang and N. Pan, *Advanced Energy Materials*, 2015, 5, 1401401.
208. G. Lee, D. Kim, J. Yun, Y. Ko, J. Cho and J. S. Ha, *Nanoscale*, 2014, 6, 9655-9664.
209. P. Taberna, P. Simon and J.-F. Fauvarque, *Journal of the Electrochemical Society*, 2003, 150, A292.
210. D. K. Kampouris, X. Ji, E. P. Randviir and C. E. Banks, *RSC Advances*, 2015, 5, 12782-12791.
211. C. Lämmel, M. Schneider, M. Weiser and A. Michaelis, *Materialwissenschaft und Werkstofftechnik*, 2013, 44, 641-649.
212. O. J. Guy and K.-A. D. Walker, in *Silicon Carbide Biotechnology (Second Edition)*, ed. S. E. Saddow, Elsevier, 2016, DOI: https://doi.org/10.1016/B978-0-12-802993-0.00004-6, pp. 85-141.
213. Q. Fulian and R. G. Compton, *Analytical Chemistry*, 2000, 72, 1830-1834.
214. P. Connor, J. Schuch, B. Kaiser and W. Jaegermann, *Zeitschrift für Physikalische Chemie*, 2020, 234, 979-994.

215. P. Zhu and Y. Zhao, *RSC Advances*, 2017, 7, 26392-26400.
216. X. Luo, Q. Yang, Y. Dong, X. Huang, D. Kong, B. Wang, H. Liu, Z. Xiao and L. Zhi, *Journal of Materials Chemistry A*, 2020, 8, 17558-17567.
217. C. C. L. McCrory, S. Jung, I. M. Ferrer, S. M. Chatman, J. C. Peters and T. F. Jaramillo, *Journal of the American Chemical Society*, 2015, 137, 4347-4357.
218. O. Kimizuka, O. Tanaike, J. Yamashita, T. Hiraoka, D. N. Futaba, K. Hata, K. Machida, S. Suematsu, K. Tamamitsu, S. Saeki, Y. Yamada and H. Hatori, *Carbon*, 2008, 46, 1999-2001.
219. N. Delaporte, D. B. Ossonon, K. Zaghib and D. Bélanger, *Batteries & Supercaps*, 2020, 3, 638-646.
220. B. J. Landi, M. J. Ganter, C. D. Cress, R. A. DiLeo and R. P. Raffaelle, *Energy & Environmental Science*, 2009, 2, 638-654.
221. T. T. Kerli Liivand, Alar Jänes, and Enn Lust *Electrochemical Society Transactions*, 2015, 64, 41-49.
222. K. Tnurist, T. Thomberg and A. Jänes, *Separator Materials Influence on Supercapacitors Performance in Viscous Electrolytes*, 2014.
223. K. Jost, D. Stenger, C. R. Perez, J. K. McDonough, K. Lian, Y. Gogotsi and G. Dion, *Energy & Environmental Science*, 2013, 6, 2698-2705.
224. H. Lee, M. Yanilmaz, O. Toprakci, K. Fu and X. Zhang, *Energy & Environmental Science*, 2014, 7, 3857-3886.
225. P. Sirisinudomkit, E. Senokos, N. Rubio and M. S. P. Shaffer, *Materials Advances*, 2021, 2, 1981-1992.
226. M. Hervy, F. Bock and K.-Y. Lee, *Composites Science and Technology*, 2018, 167, 126-133.
227. A. Eftekhari, *Energy Storage Materials*, 2017, 9, 47-69.
228. R. Thangavel, A. G. Kannan, R. Ponraj, V. Thangavel, D.-W. Kim and Y.-S. Lee, *Journal of Power Sources*, 2018, 383, 102-109.
229. M. Hervy, A. Santmarti, P. Lahtinen, T. Tammelin and K.-Y. Lee, *Materials & Design*, 2017, 121, 421-429.
230. G. Moreno-Fernández, J. L. Gómez-Urbano, M. Enterría, T. Rojo and D. Carriazo, *Journal of Materials Chemistry A*, 2019, 7, 14646-14655.
231. S. H. Aboutalebi, A. T. Chidembo, M. Salari, K. Konstantinov, D. Wexler, H. K. Liu and S. X. Dou, *Energy & Environmental Science*, 2011, 4, 1855-1865.
232. A. Daraghmeh, S. Hussain, I. Saadeddin, L. Servera, E. Xuriguera, A. Cornet and A. Cirera, *Nanoscale research letters*, 2017, 12, 639-639.
233. C. Y. Lee, H. M. Tsai, H. J. Chuang, S. Y. Li, P. Lin and T. Y. Tseng, *Journal of The Electrochemical Society*, 2005, 152, A716-A720.
234. L. R. F. A.J. Bard, *Wiley Interscience Publications*, 2000.
235. D. P. Dubal, S. H. Lee, J. G. Kim, W. B. Kim and C. D. Lokhande, *Journal of Materials Chemistry*, 2012, 22, 3044-3052.
236. M. Deraman, N. S. M. Nor, N. H. Basri, B. N. M. Dollah, S. Soltaninejad, R. Daik, R. Omar, M. A. Hashim@Ismail and M. A. R. Othman, *Advanced Materials Research*, 2015, 1112, 231-235.
237. Y. J. Lee, S. R. Ham, J. H. Kim, T. H. Yoo, S. R. Kim, Y. T. Lee, D. K. Hwang, B. Angadi, W. S. Seo, B. K. Ju and W. K. Choi, *Scientific Reports*, 2018, 8, 4851.
238. Z. R. Yue, W. Jiang, L. Wang, S. D. Gardner and C. U. Pittman, *Carbon*, 1999, 37, 1785-1796.

239. Y. J. Oh, J. J. Yoo, Y. I. Kim, J. K. Yoon, H. N. Yoon, J.-H. Kim and S. B. Park, *Electrochimica Acta*, 2014, 116, 118-128.
240. L.-x. Li and F. Li, *New Carbon Materials*, 2011, 26, 224-228.
241. M. E. Itkis, D. E. Perea, R. Jung, S. Niyogi and R. C. Haddon, *Journal of the American Chemical Society*, 2005, 127, 3439-3448.
242. D.-W. Wang, F. Li, M. Liu, G. Q. Lu and H.-M. Cheng, *The Journal of Physical Chemistry C*, 2008, 112, 9950-9955.
243. F. Xu, R. Cai, Q. Zeng, C. Zou, D. Wu, F. Li, X. Lu, Y. Liang and R. Fu, *Journal of Materials Chemistry*, 2011, 21, 1970-1976.
244. H.-Q. Li, J.-Y. Luo, X.-F. Zhou, C.-Z. Yu and Y.-Y. Xia, *Journal of The Electrochemical Society*, 2007, 154, A731.
245. C. Young, J. Lin, J. Wang, B. Ding, X. Zhang, S. M. Alshehri, T. Ahamad, R. R. Salunkhe, S. A. Hossain, J. H. Khan, Y. Ide, J. Kim, J. Henzie, K. C.-W. Wu, N. Kobayashi and Y. Yamauchi, *Chemistry – A European Journal*, 2018, 24, 6127-6132.
246. S. Vaquero, R. Díaz, M. Anderson, J. Palma and R. Marcilla, *Electrochimica Acta*, 2012, 86, 241-247.
247. S. Kondrat, C. R. Pérez, V. Presser, Y. Gogotsi and A. A. Kornyshev, *Energy & Environmental Science*, 2012, 5, 6474-6479.
248. Y. Korenblit, M. Rose, E. Kockrick, L. Borchardt, A. Kvit, S. Kaskel and G. Yushin, *ACS Nano*, 2010, 4, 1337-1344.
249. Z. Song, H. Duan, L. Miao, L. Ruhlmann, Y. Lv, W. Xiong, D. Zhu, L. Li, L. Gan and M. Liu, *Carbon*, 2020, 168, 499-507.
250. S. Sakurai, F. Kamada, D. N. Futaba, M. Yumura and K. Hata, *Nanoscale Res Lett*, 2013, 8, 546.
251. M. B. Jakubinek, B. Ashrafi, J. Guan, M. B. Johnson, M. A. White and B. Simard, *RSC Advances*, 2014, 4, 57564-57573.
252. N. Matsumoto, G. Chen, M. Yumura, D. N. Futaba and K. Hata, *Nanoscale*, 2015, 7, 5126-5133.
253. Y. S. Lim, C. W. Lai and S. B. Abd Hamid, *RSC Advances*, 2017, 7, 23030-23040.
254. J. Phiri, J. Dou, T. Vuorinen, P. A. C. Gane and T. C. Maloney, *ACS Omega*, 2019, 4, 18108-18117.
255. Y. Ma, P. Li, J. W. Sedloff, X. Zhang, H. Zhang and J. Liu, *ACS Nano*, 2015, 9, 1352-1359.
256. Z. S. Wu, K. Parvez, X. Feng and K. Müllen, *Nature Communications*, 2013, 4, 2487.
257. H. Yoo, M. Min, S. Bak, Y. Yoon and H. Lee, *Journal of Materials Chemistry A*, 2014, 2, 6663-6668.
258. L. Huang, C. Li and G. Shi, *Journal of Materials Chemistry A*, 2014, 2, 968-974.
259. J.-Y. Hong, B. M. Bak, J. J. Wie, J. Kong and H. S. Park, *Advanced Functional Materials*, 2015, 25, 1053-1062.
260. X. Han, M. R. Funk, F. Shen, Y.-C. Chen, Y. Li, C. J. Campbell, J. Dai, X. Yang, J.-W. Kim, Y. Liao, J. W. Connell, V. Barone, Z. Chen, Y. Lin and L. Hu, *ACS Nano*, 2014, 8, 8255-8265.
261. B. Pandit, S. R. Dhakate, B. P. Singh and B. R. Sankapal, *Electrochimica Acta*, 2017, 249, 395-403.
262. D. N. Futaba, K. Hata, T. Yamada, T. Hiraoka, Y. Hayamizu, Y. Kakudate, O. Tanaike, H. Hatori, M. Yumura and S. Iijima, *Nature Materials*, 2006, 5, 987-994.
263. M. Kebede, *Electrochemical Devices for Energy Storage Applications*, 2020.
264. M. D. Stoller and R. S. Ruoff, *Energy and Environmental Science*, 2010, 3, 1294-1301.

265. T. Chen and L. Dai, *Journal of Materials Chemistry A*, 2014, 2, 10756-10775.
266. A. Borenstein, R. Attias, O. Hanna, S. Luski, R. B. Kaner and D. Aurbach, *ChemElectroChem*, 2017, 4, 2660-2668.
267. B. Andres, A.-C. Engström, N. Blomquist, S. Forsberg, C. Dahlström and H. Olin, *PLoS One*, 2016, 11, e0163146-e0163146.
268. Z. Lei, J. Zhang and X. S. Zhao, *Journal of Materials Chemistry*, 2012, 22, 153-160.
269. T.-W. Chang, L.-Y. Lin, P.-W. Peng, Y. X. Zhang and Y.-Y. Huang, *Electrochimica Acta*, 2018, 259, 348-354.
270. J. Zhou, J. Lian, L. Hou, J. Zhang, H. Gou, M. Xia, Y. Zhao, T. A. Strobel, L. Tao and F. Gao, *Nature Communications*, 2015, 6, 8503.
271. X. Zhang, D. Zhang, Y. Chen, X. Sun and Y. Ma, *Chinese Science Bulletin*, 2012, 57, 3045-3050.
272. Y. Shao, J. Wang, M. Engelhard, C. Wang and Y. Lin, *Journal of Materials Chemistry*, 2010, 20, 743-748.
273. R. Singhal and V. Kalra, *Journal of Materials Chemistry A*, 2015, 3, 377-385.
274. W. Gu, M. Sevilla, A. Magasinski, A. B. Fuertes and G. Yushin, *Energy & Environmental Science*, 2013, 6, 2465-2476.
275. L. Yu and G. Z. Chen, *Front Chem*, 2019, 7, 272.
276. J. M. Klein, E. Panichi and B. Gurkan, *Physical Chemistry Chemical Physics*, 2019, 21, 3712-3720.
277. M. Biercuk, S. Ilani, C. Marcus and P. McEuen, 2007, vol. 111, pp. 455-493.
278. I. Heller, J. Kong, K. Williams, C. Dekker and S. Lemay, *Journal of the American Chemical Society*, 2006, 128, 7353-7359.
279. E. Senokos, V. Reguero, J. Palma, J. J. Vilatela and R. Marcilla, *Nanoscale*, 2016, 8, 3620-3628.
280. D. G. Gromadskyi, J. H. Chae, S. A. Norman and G. Z. Chen, *Applied Energy*, 2015, 159, 39-50.
281. Q. Shao, J. Tang, Y. Lin, J. Li, F. Qin, J. Yuan and L.-C. Qin, *Journal of Power Sources*, 2015, 278, 751-759.
282. K. O. Oyedotun, T. M. Masikhwa, S. Lindberg, A. Matic, P. Johansson and N. Manyala, *Chemical Engineering Journal*, 2019, 375, 121906.
283. B. Pal, S. Yang, S. Ramesh, V. Thangadurai and R. Jose, *Nanoscale Advances*, 2019, 1, 3807-3835.
284. S. A. Hodge, M. K. Bayazit, H. H. Tay and M. S. Shaffer, *Nat Commun*, 2013, 4, 1989.
285. M. Kaempgen, J. Ma, G. Gruner, G. Wee and S. G. Mhaisalkar, *Applied Physics Letters*, 2007, 90, 264104.
286. D. K. Kim, N. D. Kim, S.-K. Park, K.-d. Seong, M. Hwang, N.-H. You and Y. Piao, *Journal of Power Sources*, 2018, 380, 55-63.
287. Z. Niu, H. Dong, B. Zhu, J. Li, H. H. Hng, W. Zhou, X. Chen and S. Xie, *Advanced Materials*, 2013, 25, 1058-1064.
288. C. Yu, C. Masarapu, J. Rong, B. Wei and H. Jiang, *Advanced Materials*, 2009, 21, 4793-4797.
289. X. Li, T. Gu and B. Wei, *Nano Letters*, 2012, 12, 6366-6371.
290. B. Lindemann, U. P. Schröder and W. Oppermann, *Macromolecules*, 1997, 30, 4073-4077.
291. S. Mane, S. Ponrathnam and N. Chavan, *Can Chem Trans*, 2015, 3, 473-485.
292. D. Hecht, L. Hu and G. Grüner, *Applied Physics Letters*, 2006, 89, 133112.

293. Y. Lan, H. Zhao, Y. Zong, X. Li, Y. Sun, J. Feng, Y. Wang, X. Zheng and Y. Du, *Nanoscale*, 2018, 10, 11775-11781.
294. S. Ardizzone, G. Fregonara and S. Trasatti, *Electrochimica Acta*, 1990, 35, 263-267.
295. T.-P. Wang, C.-L. Lee, C.-H. Kuo and W.-C. Kuo, *Ultrasonics Sonochemistry*, 2021, 72, 105444.
296. F. Zhang, T. Liu, J. Zhang, E. Cui, L. Yue, R. Jiang and G. Hou, *Carbon*, 2019, 147, 451-459.
297. R. I. Jafri, T. Arockiados, N. Rajalakshmi and S. Ramaprabhu, *Journal of The Electrochemical Society*, 2010, 157, B874.
298. Y. Zhou, X. Hu, S. Guo, C. Yu, S. Zhong and X. Liu, *Electrochimica Acta*, 2018, 264, 12-19.
299. M. Dhelipan, A. Arunchander, A. K. Sahu and D. Kalpana, *Journal of Saudi Chemical Society*, 2017, 21, 487-494.
300. H. Peng, B. Yao, X. Wei, T. Liu, T. Kou, P. Xiao, Y. Zhang and Y. Li, *Advanced Energy Materials*, 2019, 9, 1803665.
301. C. Cheng, J. Zhu, X. Yang, L. Qiu, Y. Wang and D. Li, *Journal of Materials Chemistry A*, 2013, 1, 9332-9340.
302. X. Yan, Y. Jia, L. Zhuang, L. Zhang, K. Wang and X. Yao, *ChemElectroChem*, 2018, 5, 1874-1879.
303. H. Cho, J. Lee, H. Lee, S.-H. Lee, J. Park, C.-H. Lee and K.-H. Lee, *Materials (Basel)*, 2018, 11, 2170.
304. Q. Liu, M. Li, Y. Gu, Y. Zhang, S. Wang, Q. Li and Z. Zhang, *Nanoscale*, 2014, 6, 4338-4344.
305. T. H. Nam, K. Goto, Y. Yamaguchi, E. V. A. Premalal, Y. Shimamura, Y. Inoue, S. Arikawa, S. Yoneyama and S. Ogihara, *Composites Part B: Engineering*, 2016, 85, 15-23.
306. H. Chen, Y. Chen, H. Zhan, G. Wu, J. M. Xu and J. N. Wang, *Frontiers of Materials Science*, 2019, 13, 165-173.
307. J. Di, D. Hu, H. Chen, Z. Yong, M. Chen, Z. Feng, Y. Zhu and Q. Li, *ACS Nano*, 2012, 6, 5457-5464.
308. D. Qian, W. K. Liu and R. S. Ruoff, *Composites Science and Technology*, 2003, 63, 1561-1569.
309. O.-K. Park, W. Lee, J. Y. Hwang, N.-H. You, Y. Jeong, S. M. Kim and B.-C. Ku, *Composites Part A: Applied Science and Manufacturing*, 2016, 91, 222-228.
310. G. Sun, L. Zheng, Z. Zhan, C. Jiang, R. V. Hansen, Y. Khor and J. H. L. Pang, *Advanced Engineering Materials*, 2014, 16, 961-965.
311. F. Zhang, Y. Feng, M. Qin, L. Gao, Z. Li, F. Zhao, Z. Zhang, F. Lv and W. Feng, *Advanced Functional Materials*, 2019, 29, 1901383.
312. Y. Zare and K. Y. Rhee, *European Polymer Journal*, 2017, 87, 389-397.
313. S. X. Xie, F. Gao, S. C. Patel, J. H. Booske, S. C. Hagness and B. Sitharaman, *Applied Physics Letters*, 2013, 103, 133114.
314. Y. Miyata, K. Mizuno and H. Kataura, *Journal of Nanomaterials*, 2011, 2011, 786763.
315. K. Zhang, J. Wang, J. Zou, W. Cai and Q. Zhang, *Carbon*, 2018, 138, 188-196.
316. M. V. Kharlamova, C. Kramberger, O. Domanov, A. Mittelberger, T. Saito, K. Yanagi, T. Pichler and D. Eder, *physica status solidi (b)*, 2018, 255, 1800178.
317. M. Danish and S. Luo, *Sensors*, 2020, 20, 2904.
318. Y. Gogotsi and P. Simon, *Science*, 2011, 334, 917.

319. Y. Xia, T. S. Mathis, M.-Q. Zhao, B. Anasori, A. Dang, Z. Zhou, H. Cho, Y. Gogotsi and S. Yang, *Nature*, 2018, 557, 409-412.
320. J. Zhao, J. Wu, B. Li, W. Du, Q. Huang, M. Zheng, H. Xue and H. Pang, *Progress in Natural Science: Materials International*, 2016, 26, 237-242.
321. J. Yang, Y. Yang, J. Hou, X. Zhang, W. Zhu, M. Xu and M. Wan, *Polymer*, 1996, 37, 793-798.
322. S. Sadki, P. Schottland, N. Brodie and G. Sabouraud, *Chemical Society Reviews*, 2000, 29, 283-293.
323. L. F. Warren and D. P. Anderson, *Journal of the Electrochemical Society*, 1987, 134, 101.
324. C. M. Bhatt and N. Jampana, 2011.
325. Y. Li, *Journal of Electroanalytical Chemistry*, 1997, 433, 181-186.
326. A. A. Daryakenari, A. Apostoluk, D. Aradilla, S. Sadki and J.-J. Delaunay, *Journal of Solid State Electrochemistry*, 2015, 19, 655-661.
327. Y. Fang, J. Liu, D. J. Yu, J. P. Wicksted, K. Kalkan, C. O. Topal, B. N. Flanders, J. Wu and J. Li, *Journal of Power Sources*, 2010, 195, 674-679.
328. J. Zhu, Y. Xu, J. Wang, J. Wang, Y. Bai and X. Du, *Physical Chemistry Chemical Physics*, 2015, 17, 19885-19894.
329. Y. Han, P. Chen, Y. Xia, S. Huang, W. Chen and W. Lu, *Journal of Solid State Electrochemistry*, 2019, 23, 1553-1562.
330. M. Zhou and J. Heinze, *Electrochimica Acta*, 1999, 44, 1733-1748.
331. J.-C. Vidal, E. Garcia-Ruiz and J.-R. Castillo, *Microchimica Acta*, 2003, 143, 93-111.
332. Y. Yang, D. Xu, Q. Wu and P. Diao, *Scientific Reports*, 2016, 6, 35158.
333. F. Caballero-Briones, J. A. Barón-Miranda, C. Guarneros-Aguilar, O. Calzadilla and F. Sanz, *Materials Research Express*, 2019, 6, 086464.
334. K. S. Khashan, G. M. Sulaiman, R. Mahdi and A. kadhim, *Materials Research Express*, 2018, 5, 105004.
335. J.-H. Han, H. Zhang, P.-F. Chu, A. Imani and Z. Zhang, *Composites Science and Technology*, 2015, 114, 1-10.
336. S. Ahmad, I. Khan, A. Husain, A. Khan and A. M. Asiri, *Polymers*, 2020, 12, 3047.
337. F. N. Ajjan, M. J. Jafari, T. Rębiś, T. Ederth and O. Inganäs, *Journal of Materials Chemistry A*, 2015, 3, 12927-12937.
338. F. Wolfart, D. P. Dubal, M. Vidotti, R. Holze and P. Gómez-Romero, *Journal of Solid State Electrochemistry*, 2016, 20, 901-910.
339. H. Karami and A. R. Nezhad, *International Journal of Electrochemical Science*, 2013, 8, 8905-8921.
340. S.-B. Yoon, J.-P. Jegal, K. C. Roh and K.-B. Kim, *Journal of The Electrochemical Society*, 2014, 161, H207.
341. T.-Y. Wei, C.-H. Chen, K.-H. Chang, S.-Y. Lu and C.-C. Hu, *Chemistry of Materials*, 2009, 21, 3228-3233.
342. M. Hughes, G. Z. Chen, M. S. P. Shaffer, D. J. Fray and A. H. Windle, *Chemistry of Materials*, 2002, 14, 1610-1613.
343. C. Wei, B. Akinwolemiwa, Q. Wang, L. Guan, L. Xia, D. Hu, B. Tang, L. Yu and G. Z. Chen, *Advanced Sustainable Systems*, 2019, 3, 1900065.
344. A. Della Santa, D. De Rossi and A. Mazzoldi, *Synthetic Metals*, 1997, 90, 93-100.
345. K. Fic, M. Meller, J. Menzel and E. Frackowiak, *Electrochimica Acta*, 2016, 206, 496-503.

346. V. Ruiz, R. Santamaría, M. Granda and C. Blanco, *Electrochimica Acta*, 2009, 54, 4481-4486.
347. J. Cherusseri and K. K. Kar, *Journal of Materials Chemistry A*, 2016, 4, 9910-9922.
348. M. S. Kiani, N. V. Bhat, F. J. Davis and G. R. Mitchell, *Polymer*, 1992, 33, 4113-4120.
349. M. Aroyo, *Plating and surface finishing*, 1998, 85, 69-76.
350. J. Chen, Y. Wang, J. Cao, L. Liao, Y. Liu, Y. Zhou, J.-H. Ouyang, D. Jia, M. Wang, X. Li and Z. Li, *Electrochimica Acta*, 2020, 361, 137036.
351. Z. Dai, X. Shi, H. Liu, H. Li, Y. Han and J. Zhou, *RSC Advances*, 2018, 8, 1218-1224.
352. S. Bose, T. Kuila, M. E. Uddin, N. H. Kim, A. K. T. Lau and J. H. Lee, *Polymer*, 2010, 51, 5921-5928.
353. K. Yamani, R. Berenguer, A. Benyoucef and E. Morallón, *Journal of Thermal Analysis and Calorimetry*, 2019, 135, 2089-2100.
354. J. Cao, Y. Wang, J. Chen, X. Li, F. C. Walsh, J.-H. Ouyang, D. Jia and Y. Zhou, *Journal of Materials Chemistry A*, 2015, 3, 14445-14457.
355. J. Tabačiarová, M. Mičušík, P. Fedorko and M. Omastová, *Polymer Degradation and Stability*, 2015, 120, 392-401.
356. J. Kuliček, P. Gemeiner, M. Omastová and M. Mičušík, *Chemical Papers*, 2018, 72, 1651-1667.
357. C. Malitesta, I. Losito, L. Sabbatini and P. G. Zambonin, *Journal of Electron Spectroscopy and Related Phenomena*, 1995, 76, 629-634.
358. X. Chen, X. Wang and D. Fang, *Fullerenes, Nanotubes and Carbon Nanostructures*, 2020, 28, 1048-1058.
359. H. Zhou, G. Han, Y. Xiao, Y. Chang and H.-J. Zhai, *Journal of Power Sources*, 2014, 263, 259-267.
360. X. Fan, Z. Yang and N. He, *RSC Advances*, 2015, 5, 15096-15102.
361. H.-W. Park, T. Kim, J. Huh, M. Kang, J. E. Lee and H. Yoon, *ACS Nano*, 2012, 6, 7624-7633.
362. Z.-H. Huang, T.-Y. Liu, Y. Song, Y. Li and X.-X. Liu, *Nanoscale*, 2017, 9, 13119-13127.
363. N. M. Rosas-Laverde, A. I. Pruna and D. Busquets-Mataix, *Nanomaterials (Basel)*, 2020, 10, 1188.
364. X. Liu, Q. Li, Y. Qin and Y. Jiang, *RSC Advances*, 2020, 10, 28324-28331.
365. C. Xia, M. Leng, W. Tao, Q. Wang, Y. Gao and Q. Zhang, *Journal of Materials Science: Materials in Electronics*, 2019, 30, 4427-4436.
366. Y. Liu, D. Yan, Y. Li, Z. Wu, R. Zhuo, S. Li, J. Feng, J. Wang, P. Yan and Z. Geng, *Electrochimica Acta*, 2014, 117, 528-533.
367. R. Moosaei, M. Sharif and A. Ramezannezhad, *Polymer Testing*, 2017, 60, 173-186.
368. B. Yue, C. Wang, X. Ding and G. G. Wallace, *Electrochimica Acta*, 2012, 68, 18-24.
369. Y. Chen, L. Du, P. Yang, P. Sun, X. Yu and W. Mai, *Journal of Power Sources*, 2015, 287, 68-74.
370. in *Practical Raman Spectroscopy – An Introduction*, DOI: 10.1002/9781119961284.ch4, pp. 61-100.
371. L. Demarconnay, E. Raymundo-Piñero and F. Béguin, *Journal of Power Sources*, 2011, 196, 580-586.
372. P. Sirisinudomkit, P. Iamprasertkun, A. Krittayavathananon, T. Pettong, P. Dittanet, P. Kidkhunthod and M. Sawangphruk, *Sustainable Energy & Fuels*, 2017, 1, 275-279.
373. F. Huang and D. Chen, *Energy & Environmental Science*, 2012, 5, 5833-5841.
374. Y. Su and I. Zhitomirsky, *Applied Energy*, 2015, 153, 48-55.

375. C. Ren, Y. Yan, B. Sun, B. Gu and T.-W. Chou, *Journal of Colloid and Interface Science*, 2020, 569, 298-306.
376. J. Yu, W. Lu, J. P. Smith, K. S. Booksh, L. Meng, Y. Huang, Q. Li, J.-H. Byun, Y. Oh, Y. Yan and T.-W. Chou, *Advanced Energy Materials*, 2017, 7, 1600976.
377. J. Zhu, T. Feng, X. Du, J. Wang, J. Hu and L. Wei, *Journal of Power Sources*, 2017, 346, 120-127.
378. N. Wang, X. Wang, Y. Zhang, W. Hou, Y. Chang, H. Song, Y. Zhao and G. Han, *Journal of Alloys and Compounds*, 2020, 835, 155299.
379. D. P. Dubal, N. R. Chodankar, Z. Caban-Huertas, F. Wolfart, M. Vidotti, R. Holze, C. D. Lokhande and P. Gomez-Romero, *Journal of Power Sources*, 2016, 308, 158-165.
380. R. Kötz and M. Carlen, *Electrochimica Acta*, 2000, 45, 2483-2498.
381. W. Wu, L. Yang, S. Chen, Y. Shao, L. Jing, G. Zhao and H. Wei, *RSC Advances*, 2015, 5, 91645-91653.
382. D. P. Chatterjee and A. K. Nandi, *Journal of Materials Chemistry A*, 2021, 9, 15880-15918.
383. H. Li, J. Wang, Q. Chu, Z. Wang, F. Zhang and S. Wang, *Journal of Power Sources*, 2009, 190, 578-586.